ABSTRACT

INELASTIC PROTON SCATTERING AT 40 MeV
FROM THE EVEN NICKEL ISOTOPES

By

Kenneth M. Thompson

A study of inelastic scattering from the even nickel isotopes has been done using 40 MeV protons from the Michigan State University sector focused cyclotron. Angular distributions from about 15° to 90° were obtained for each nucleus in 5° steps using Ge(Li) charged particle detectors. The best energy resolution achieved was 45 keV. All of the resulting angular distributions are presented in both a tabular and a graphical form.

A high precision goniometer was designed and constructed to facilitate the use of Ge(Li) detectors. The details of the construction of this apparatus are given. Also described in detail are the procedures used in the calibrations of the remotely operated detector support and target positioning mechanisms.

The experimental angular distributions for all of the observed states were compared with calculated distributions using a collective model distorted wave theory. From these comparisons values for the nuclear deformation parameters,

β_L, were obtained. The resulting nuclear deformations, $\beta_L R_o$, were used to calculate the vibrational model parameters and the reduced transition probabilities. The deformations were also compared to results from other experiments. The fractional depletion of an energy weighted sum rule and a sum rule based on the shell-model were also calculated for each state. The dependence of the reduced transition probabilities and sum rule limits on the model used for the nuclear charge density was also examined. The results of these calculations for a uniform charge density with r_o = 1.20F and r_o = 1.31F are given along with those for a Fermi distribution with r_o = 1.10F and a = 0.566F. These are tabulated for all of the observed states.

Comparisons of the calculated quantities were made with results of experimental studies of electromagnetic transitions in the nickel isotopes. There were also comparisons made with the results of calculations using strongly admixed spherical shell model configurations done by N. Auerbach and a modified Tamm-Dancoff approximation done by Ram Raj et al.

INELASTIC PROTON SCATTERING AT 40 MeV FROM THE EVEN NICKEL ISOTOPES

By

Kenneth M. Thompson

A THESIS

Submitted to
Michigan State University
in partial fulfillment of the requirements
for the degree of

DOCTOR OF PHILOSOPHY

Department of Physics

1969

ACKNOWLEDGMENTS

I am greatly indebted to Dr. Charles Gruhn for his guidance, encouragement, and assistance throughout my graduate work and particularly during the work for this thesis.

I am also grateful to Dr. Barry Preedom for his assistance in the understanding and the implimentation of the techniques of the distorted wave analysis needed for this work. I also acknowledge the many helpful discussions with the professional staff of the Michigan State University Cyclotron Laboratory.

Thanks go to many who aided in the design and construction of the goniometer used in this experiment--to Dr. William Johnson, Robert deForest and the staff of the electronics shop for their help in the design and constuction of the electrical and electronics systems; to Norval Mercer, the staff of the mechanical shop, Gunther Stork, David Rozof, and the members of the technical staff for their help in the design, construction, and assembly of the mechanical systems; and to Andrew Kaye for his help in procurring the necessary raw materials.

I am also grateful to my fellow graduate students for their helpful discussions throughout this work but

especially to Carl Maggiore, Tom Kuo, Larry Samuelson, and Bill Seidler for their assistance during the data acquisition for this experiment. Also the aid of the computer personnel is acknowledged as is their provision of the software which established a time sharing computer system which greatly facilitated the analysis of the data.

I also acknowledge the financial support of the research program at MSU provided by the National Science Foundation and the personal support from the NSF during the work for this thesis.

A very special thanks go to Mom and Dad for their support and encouragement during my graduate studies.

TABLE OF CONTENTS

		Page
ACKNOWLEDGMENTS		ii
LIST OF TABLES.		vii
LIST OF FIGURES		ix
Chapter		
I.	INTRODUCTION.	1
II.	HIGH PRECISION GONIOMETER	5
2.1	Design Features	5
2.1.a	The Ge(Li) Detector Package.	7
2.1.b	List of Included Features	10
2.2	Goniometer Construction and Operation.	12
2.2.a	Goniometer Drive	13
2.2.b	Local Electrical System	19
2.2.c	Remote Control Panel	19
2.3	Calibration of the Goniometer	23
2.3.a	Main Arm Angle Calibration	24
2.3.b	Target Angle.	39
2.3.c	Target Height	42
2.3.d	Concentricity Checks	44
2.4	Installation.	45
III.	EXPERIMENTAL PROCEDURES	51
3.1	Cyclotron and Beam Transport System.	51
3.1.a	Cyclotron.	51
3.1.b	Beam Transport System.	51
3.1.c	Alignment of the Beam into the Target Chamber	53
3.1.d	Faraday Cup and Current Integrator	54
3.2	Set up of the Goniometer.	56
3.2.a	Target Chamber	56
3.2.b	Targets	56
3.2.c	Detectors.	56
3.3	Electronics	59
3.4	Data Acquisition	63

Chapter Page

IV. DATA ANALYSIS 69

4.1 Experimental Analysis. 69
4.1.a Computer Programs Used 70
4.1.a.1 Peakstrip 70
4.1.a.2 Reltomon 70
4.1.a.3 Foiltarcal. 71
4.1.a.4 Sigtote. 72
4.1.b Lab Angle Calibration. 73
4.1.c Elastic Cross Sections 75
4.1.d Normalization of the Data to Obtain Absolute Cross Sections. . 76
4.1.d.1 Dead Time 76
4.1.d.2 Ratios of the Monitor Counts to the Integrated Current. . . . 76
4.1.d.3 Method of Normalization . . . 77
4.1.d.4 Corrections 78
4.1.d.5 Final Results. 80
4.1.e Inelastic Angular Distributions . 81
4.1.f Excitation Energies 82

4.2 Theroetical Analysis 88
4.2.a DWBA Theory 88
4.2.b Vibrational Model Parameters and Reduced Transition Probabilities . 95
4.2.c Sum Rules. 98
4.2.d Optical Model Parameters. . . . 99
4.2.e DWBA Calculations 102
4.2.f Extraction of Deformation Parameters, β_L 104

V. DISCUSSION OF THE RESULTS 117

5.1 Comparisons with Other Experiments 120
5.2 Comparison with Theory 126
5.3 Conclusions 128

APPENDICES 133

I. Details of the Construction and Operation of the Goniometer 136

II. Calculations of the Angles in Reference I Used for the Main Arm Calibrations. . . 216

III. Compounding of the Errors in the Points for the Main Arm Reference Angles 218

APPENDICES

Page

IV. Experimental Data 227

IV.1 Tabulated Angular Distributions
IV.2 Plotted Angular Distributions
IV.3 Tabulated Nuclear Deformations
IV.4 Tabulation of Quantities Calculated from the Nuclear Deformation in IV.3

REFERENCES 284

LIST OF TABLES

Table		Page
2.1	The reference I angles and estimated standard errors.	31
2.2	Summary of the results of the calibration of the main arm.	38
2.3	Summary of the results of the calibration of the target angle	41
2.4	Summary of the results of the calibration of the target height	44
2.5	Summary of the results of the concentricity checks.	45
3.1	The self-supporting foil targets used . . .	57
4.1	Excitation energies for ^{58}Ni	84
4.2	Excitation energies for ^{60}Ni	85
4.3	Excitation energies for ^{62}Ni	86
4.4	Excitation energies for ^{64}Ni	87
4.5	Average optical potential parameters used. .	100
4.6	Optical potential strength parameters used .	102
4.7	J^{π} assignments for states in ^{58}Ni and the excitation energies and L-values used in this experiment.	105
4.8	J^{π} assignments for states in ^{60}Ni and the excitation energies and L-values used in this experiment.	106
4.9	J^{π} assignments for states in ^{62}NI and the excitation energies and L-values used in this experiment.	107
4.10	J^{π} assignments for states in ^{64}Ni and the excitation energies and L-values used in this experiment.	108

Table		Page
4.11	Estimated upper limites for the δ_L for the second 2+ states	116
5.1	Tentative L assignments.	119
5.2	Nuclear deformations for ^{58}Ni and comparison with experiments representative of other reactions.	121
5.3	Nuclear deformations for ^{60}Ni and comparison with experiments representative of other reactions.	122
5.4	Nuclear deformations for ^{62}Ni and comparison with experiments representative of other reactions.	123
5.5	Nuclear deformations for ^{64}Ni and comparison with experiments representative of other reactions.	123
5.6	Comparisons of reduced transition probabilities, B(EL; 0→L), in units of F^{2L}. . . .	124
5.7	Experimental surface tension parameters, C_L(MeV)	125
5.8	Experimental mass transport parameters, $D_L/\hbar^2$, in units of (MeV^{-1})	126
5.9	Experimental and theoretical results for B(E2)'s in the nickel isotopes.	127
5.10	Experimental and theoretical results for B(E2)'s for the nickel isotopes. The effective charge assumed in the theoretical calculations was 1.35e	129
III.1	Estimated standard errors for the primary angles in reference I for the main arm due to errors in the linear measurements .	223
III.2	Estimated standard errors for the primary points in reference I due to the error in the central, 90° angle	225
III.3	Total estimated standard errors in the primary points in reference I	225
III.4	Total estimated standard errors in the secondary points in reference I	226

LIST OF FIGURES

Figure		Page
2.1	Vertical cryostat Ge(Li) detector package .	8
2.2	Goniometer drive unit	14
2.3	Local control box	20
2.4	Remote control panel	21
2.5	Floor plan of the geometry for the primary points in reference I	26
2.6	Floor plan of the geometry used in the 90° transfer of the primary angles of reference I.	30
3.1	Experimental area of the Michigan State University Cyclotron Laboratory	52
3.2	Block diagram of the electronics used with the Ge(Li) detectors.	60
3.3	Block diagram of the electronics used with the monitor counter	62
3.4	$^{58}Ni(p,p')^{58}Ni$ spectrum at $\theta_{LAB} = 29.4^{\circ}$ for Ep = 40 MeV.	65
3.5	$^{60}Ni(p,p')^{60}Ni$ spectrum at $\theta_{LAB} = 57.8^{\circ}$ for Ep = 40 MeV.	66
3.6	$^{62}Ni(p,p')^{62}Ni$ spectrum at $\theta_{LAB} = 47.8^{\circ}$ for Ep = 40 MeV.	67
3.7	$^{64}Ni(p,p')^{64}Ni$ spectrum at $\theta_{LAB} = 47.8^{\circ}$ for Ep = 40 MeV.	68
4.1	Comparisons of the experimental, elastic scattering results and the theoretical calculations using the optical potential parameters given in Tables 4.5 and 4.6 .	103

Figure		Page
4.2	Comparisons of the experimental inelastic scattering results and the theoretical DWBA calculations for states in ^{58}Ni with known J^{π} assignments.	110
4.3	Comparisons of the experimental inelastic scattering results and the theoretical DWBA calculations for states in ^{58}Ni with known J^{π} assignments.	111
4.4	Comparisons of the experimental inelastic scattering results and the theoretical DWBA calculations for states in ^{60}Ni with known J^{π} assignments.	112
4.5	Comparisons of the experimental inelastic scattering results and the theoretical DWBA calculations for states in ^{62}Ni with known J^{π} assignments.	113
4.6	Comparisons of the experimental inelastic scattering results and the theoretical DWBA calculations for states in ^{64}Ni with known J^{π} assignments.	114
I.1	Schematic of the structure of the main arm used to calculate the location of the point (A) at which the brace meets the main arm. .	139
I.2	Results of the calculations and measurements of the vertical deflections in the main arm under a load of 100 lbs.	141
I.3	Section view of the 4:1 gear train for the main arm drive.	147
I.4	Plot of the speed factor, X_s, versus angular velocity, RPM	157
I.5	Section view of central column	173
I.6	Section view of the target chamber and sliding vacuum seal.	180
I.7	Remote control panel	195
II.1	Schematic of the geometry used to calculate the angular position of the primary points of reference I used in the calibrations of the main arm	217

CHAPTER I

INTRODUCTION

In recent years there have been many studies done in the $2p_{3/2}$, $1f_{5/2}$, $2p_{1/2}$ region of the periodic table. Of particular interest in this thesis is the work that has been done on the stable even nickel isotopes ^{58}Ni, ^{60}Ni, ^{62}Ni, and ^{64}Ni. Fricke et al. (Fr 67b)*, for example, have used elastically scattered protons and their measured polarization to establish the optical model potentials for ^{58}Ni and ^{60}Ni at 40 MeV. Fricke et al. have also studied the inelastic scattering and the inelastic asymmetries of 40 MeV protons from the highly excited first 2^+ and 3^- states in ^{58}Ni and ^{60}Ni (Fr 67c). There have also been a number of other studies involving these targets: for example (α, α') on ^{58}Ni and ^{60}Ni (Ja 67) (In 68), (d,d') on ^{58}Ni, ^{60}Ni, ^{62}Ni (Jo 69), and (e,e') on ^{58}Ni, ^{60}Ni (Cr 61) and on ^{58}Ni, ^{60}Ni, ^{62}Ni (Du 67). In most of these experiments the emphasis was placed on the strongly excited states.

In addition to these experiments theoretical calculations of the excited levels and reduced transition

*The references are specified by the first two letters of the primary author's surname followed by the year of publication. These are listed alphabetically at the end of the thesis.

probabilities have been made for these isotopes. N. Auerbach has, for example, described the nickel isotopes in terms of strongly admixed spherical shell-model neutron configurations (Au 67). Raj et al. have also done calculations for the even nickel isotopes using a modified Tamm-Dancoff approximation (Ra 67).

As pointed out by Glendenning and Veneroni (Gl 66) the proton is a useful probe of the microscopic structure of the nucleus. They calculate the (p,p') angular distributions of the low lying levels of the nickel isotopes using a microscopic description of the excitations. Comparison of results of the present work with these calculations are not given in this thesis, but these comparisons are expected to be made in the near future.

The nature of these experiments and theoretical calculations revealed the need to do a systematic study. The study which was done for this thesis, therefore, involved the examination of inelastically scattered, 40 MeV protons from the even nickel isotopes. For such a study to render information to test the microscopic interpretations, angular distributions were needed for the weakly excited states as well as for the strong, collective states.

In order to obtain these distributions a detection system was needed which had good resolution and which would minimize the background contributions.

A Ge(Li) charged particle detector was selected for this experiment. In order to facilitate the use of this detector system, a "spider" geometry scattering rig was designed and constructed. The details of the design and construction of this goniometer, i.e., angular measuring device, are given in Chapter II and Appendix I.

The collective model distorted wave theory (Ba 62) (Sa 64) was used in the analysis of the angular distributions obtained in this experiment. This type of analysis has developed into a widely accepted method and therefore provides results which can be readily compared or reproduced if necessary. The optical model parameters used in the calculations were obtained from Fricke et al. (Fr 67b). The analysis of the present data yielded deformation parameters, β_L, for the observed states.

There is evidence that the low lying excited levels of the nickel isotopes are vibrational in character (La 64) (Bo 67a). For this reason the vibrational parameters associated with the observed states were calculated.

Recent studies of electron scattering from the nickel isotopes (Du 67) (Cr 61) yielded values for the reduced transition probabilities for various states; therefore, the B(EL)'s were also calculated for the present experiment to allow comparisons with those earlier experiments as well as with several theoretical estimates.

Using the comparisons between the results of this experiment and other experimental and theoretical studies it was possible to draw some conclusions concerning the extraction of model dependent parameters from the experimental data and the consistancy of several theoretical approaches.

CHAPTER II

HIGH PRECISION GONIOMETER

Before the data for this thesis was acquired, the instrumentation needed for obtaining angular distributions of charged particles using Ge(Li) detectors was designed and built. The form of construction used in the final system is a "spider" geometry similar to that used by others (He68a) (Ca67). This consists of detector positioning elements outside of a central vacuum chamber with the detectors viewing the targets through a sliding vacuum seal. The alternative vacuum pot configuration, in contrast, consists of a vacuum chamber containing the detection instruments and targets. This vacuum pot design, however, was less compatible with our experimental requirements. Since the fundamental purpose of this instrument is to measure the angular positions of detectors, it is called a goniometer.

2.1 Design Features

This device was built to facilitate charged particle, nuclear reaction studies in the energy range of 20-75 MeV. In particular the design was guided by the experimental requirements of inelastic proton scattering and ^{3}He

induced reactions. Among the proposed experiments, there were many which needed to use Ge(Li) charged particle detectors because of their energy resolving capabilities. Such detectors have been successfully fabricated at Michigan State University Cyclotron Laboratory (MSUCL) by a group supervised by C. R. Gruhn (Gr 68). They have been shown to be capable of giving energy resolution of 22 keV FWHM for 40 MeV protons (Gr 68a). Several types of packages were tried by this group for maintaining these detectors at liquid nitrogen (LN_2) temperatures in a vacuum environment. A package similar to the vertical cryostat design of Chasman (Ch 65) was found to be most convenient, and, therefore, the final design of the goniometer was made to be compatible with such a package.

The final configuration of this device is the result of compromising on several points. The results of a number of experiments representative of a variety of reactions were examined. The largest fractional change in the differential cross sections corresponding to an angular variation of 0.01° was estimated in each case. A maximum fractional change of 2% was defined as being acceptable. This required an angular precision of at least 0.02° in the majority of cases examined.

In order to obtain high angular precision as well as to allow for flexibility in the use of this device, the final design incorporated a 4 foot radius detector support called the main arm. This arm can be remotely positioned

with an accuracy of ±0.02° relative to a reference direction. Implementing a support capable of holding a vertical cryostat, detector package at this radius inside a vacuum pot scattering chamber would necessitate a very large vacuum system. The chamber would be prohibitive in cost, and the necessary evacuation times along with the difficulty of reaching the interior points would make this approach unacceptable. The spider geometry, on the other hand, avoids these problems since the detector positioning elements are located outside of a small, central, target vacuum chamber.

2.1.a The Ge(Li) Detector Package--Figure 2.1

The Ge(Li) charged particle detector configurations which have been used at MSUCL have been discussed elsewhere (Gr 68)(Gr 68a). The detector package which was found to be most convenient to use is a vertical cryostat design. The final goniometer design facilitates the use of this type of package. The final configuration does not, however, prevent the use of other choices of detectors or detector packages.

The Ge(Li) detector needs to be kept constantly in a vacuum and at temperatures near the boiling point of LN_2, 77°K. This vertical cryostat design contains an isolated, copper cold finger which is put into LN_2 and is in thermal contact with the detector. The vacuum is maintained inside

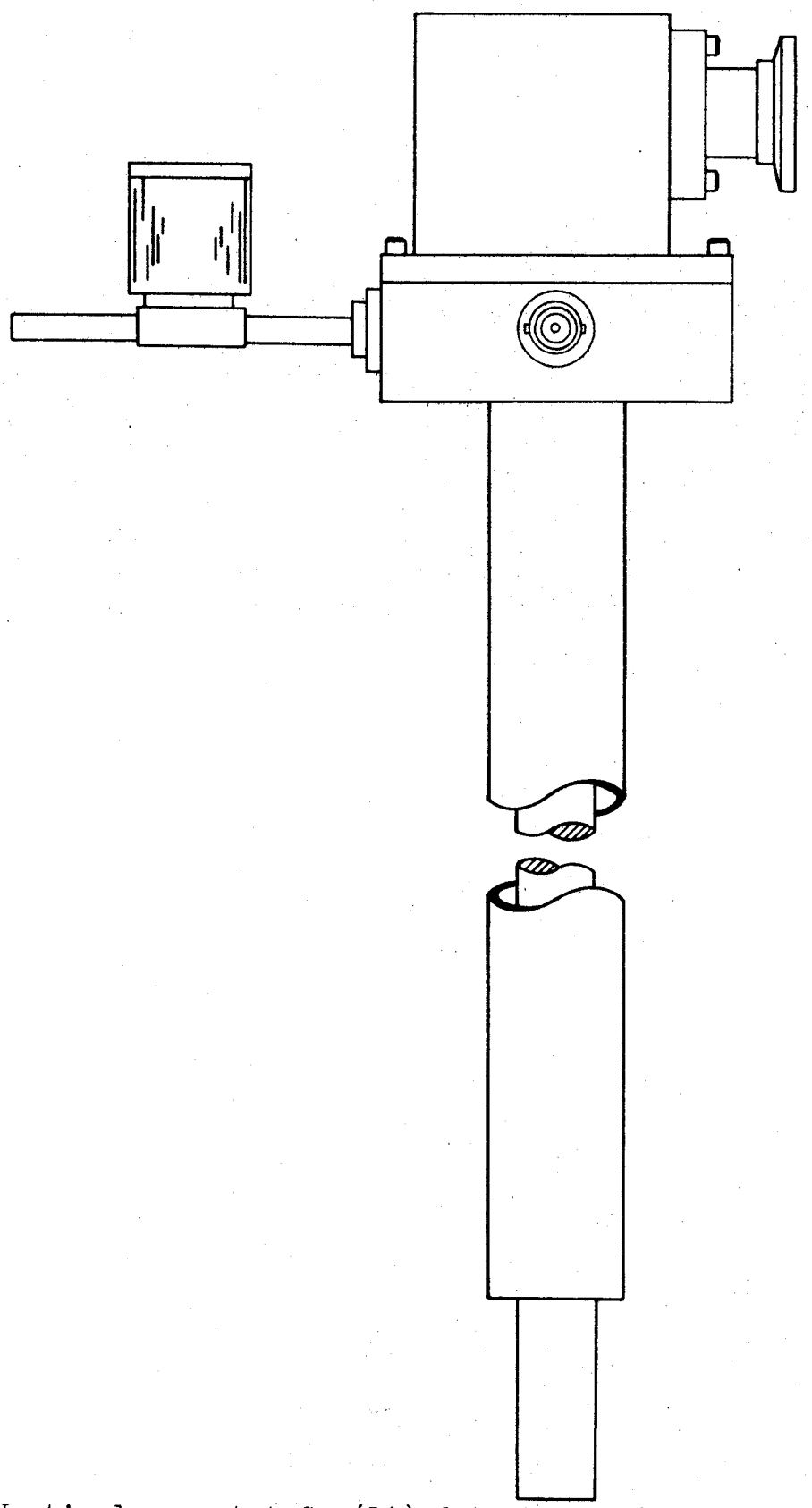

2.1 Vertical cryostat Ge (Li) detector package.

the enclosure by a cryopumping agent. The portion of the package containing the cold finger and cryopump can be inserted into the neck of a standard, 25 liter, LN_2 dewar permitting the storage of the system for up to 2 weeks without refilling.

The detector mount connected to the cold finger contains the collimator which defines the solid angle of the detector system. The package cap which encloses this mount contains an entrance port for the scattered particles. The exact details of this port and of the coupling used between this package and the target chamber depend on the requirements of the experiment. Several possible configurations are described here.

The package itself may contain a thin foil window. This window must be opaque and be able to sustain atmospheric pressures. It must, however, produce a minimum energy straggling contribution in the scattered particles. Windows that have proven successful in covering holes up to 3/8 inch in diameter are 1/10 mil Havar* and 1/4 mil, aluminized mylar. The staggling contributions have been calculated for 40 MeV protons to be about 9 keV and 3 keV respectively. The calculations use a computer program, TARGET, by J. J. Kolata. This program incorporates calculations of the Vavilov distribution of the energy of the transmitted particles. These windows have been glued to the aluminum cap using Eastman 910 adhesive.

*Hamilton Watch Company, Lancaster, Pennsylvania.

The package can be coupled to the foil window of the target chamber (see Appendix I) by using an evacuated tube with a thin foil window on each end. One of these additional windows can be eliminated by coupling the tube directly to the cap through an O-ring seal. A second window can be eliminated by permanently coupling the tube to the cap and removing the window on the cap itself.

The KF-20 Leybold vacuum fitting shown in Figure 2.1 is attached to the cap through an O-ring seal. This fitting allows the convenient implementation of the second arrangement described above. It also provides a means of coupling the detector to the target chamber through a pipe attached to the sliding seal. The window on the cap can also be eliminated by connecting a ball valve, for example, to this fitting. This allows the detector to view the target through the sliding seal in a windowless geometry providing the ultimate conditions for high resolution experiments.

2.1.b. List of Included Features

In addition to the aspects described above there are additional features included in this goniometer which add to its versatility and convenience. The following list enumerates these features as well as those presented above and those of general interest. These are described in detail in section 2.2 and Appendix I.

1. An adjustable stand which permits adjustment of both the vertical and horizontal position, and the levelness.
2. A remotely movable 4-foot radius detector support, the main arm, capable of holding a vertical cryostat for Ge(Li) detectors and the associated LN_2 dewar, or a maximum of 100 lbs at 4 feet.
3. A precision of ±0.02° in positioning the main arm.
4. A manually positioned secondary arm that can be positioned to ±0.1° and can support a maximum of 50 lbs at 2 feet.
5. A central, target vacuum chamber compatible with a sliding vacuum seal or with a thin foil window.
6. A target transfer and hold lock.
7. A target height positioning system with a precision of ±1 mil.
8. An automatic target selection system for three targets.
9. A vernier dial readout for the main arm position capable of being read through a television system to 0.005°.
10. A target rotating system with a precision of ±0.3°.
11. A local control of all functions.

12. Independent, remote digital readouts for the main arm, target angle, and target height positions.
13. A remote, graphic readout system which indicates the relative angular positions of the detector supports, the target, and the incident beam.

2.2 Goniometer Construction and Operation

In order to provide a system which was to be easily modified, the goniometer was designed for a modular construction. The mechanical as well as the electrical assemblies are composed of individual, easily removed sections. This design philosophy permits modifications to be easily incorporated into the total system to satisfy the requirements of a specific experiment.

This goniometer is comprised of three basic units joined by one multiconductor cable and by 48-pin connectors. These units are a semi-portable goniometer drive and two control and power supply assemblies, one at the local station and one at the remote. These can be interconnected in either a retracted or an extended configuration allowing for the system to be easily moved from one location to another and to be conveniently tested.

2.2.a Goniometer Drive

The goniometer drive assembly is shown in Figure 2.2. This includes three remotely controlled drive systems which position the target and the 4 foot radius main arm. These systems are rigidly fastened to an adjustable steel and aluminum base (Figure 2.2A). The four threaded steel legs allow the goniometer to be adjusted so that the main arm is located between 3 and 12 inches below the scattering plane. These also permit alignment such that the main arm remains in a level plane during a complete revolution with its center of rotation intersecting the incident beam line. An X-Y stage is also incorporated to allow for a maximum of 1 inch of adjustment in the horizontal plane.

There are two rotating elements in this system which are used to locate detectors with respect to the beam direction (Figure 2.2C). First there is the 4 foot radius, remotely positioned, main arm. This element has a dual beam, counter balanced construction capable of supporting a maximum of 100 lbs at a radius of 4 feet. The dual beam design allows the vertical cryostat, Ge(Li) detector package along with its LN_2 dewar to be securely supported between the minimum and maximum radial positions.

This arm is driven by a Slo-Syn, SS1800-1005, bifilar stepping motor which is operated in both an AC synchronous mode with a speed of 72 RPM and in a DC stepping mode with 200 steps/revolution at a speed of 20

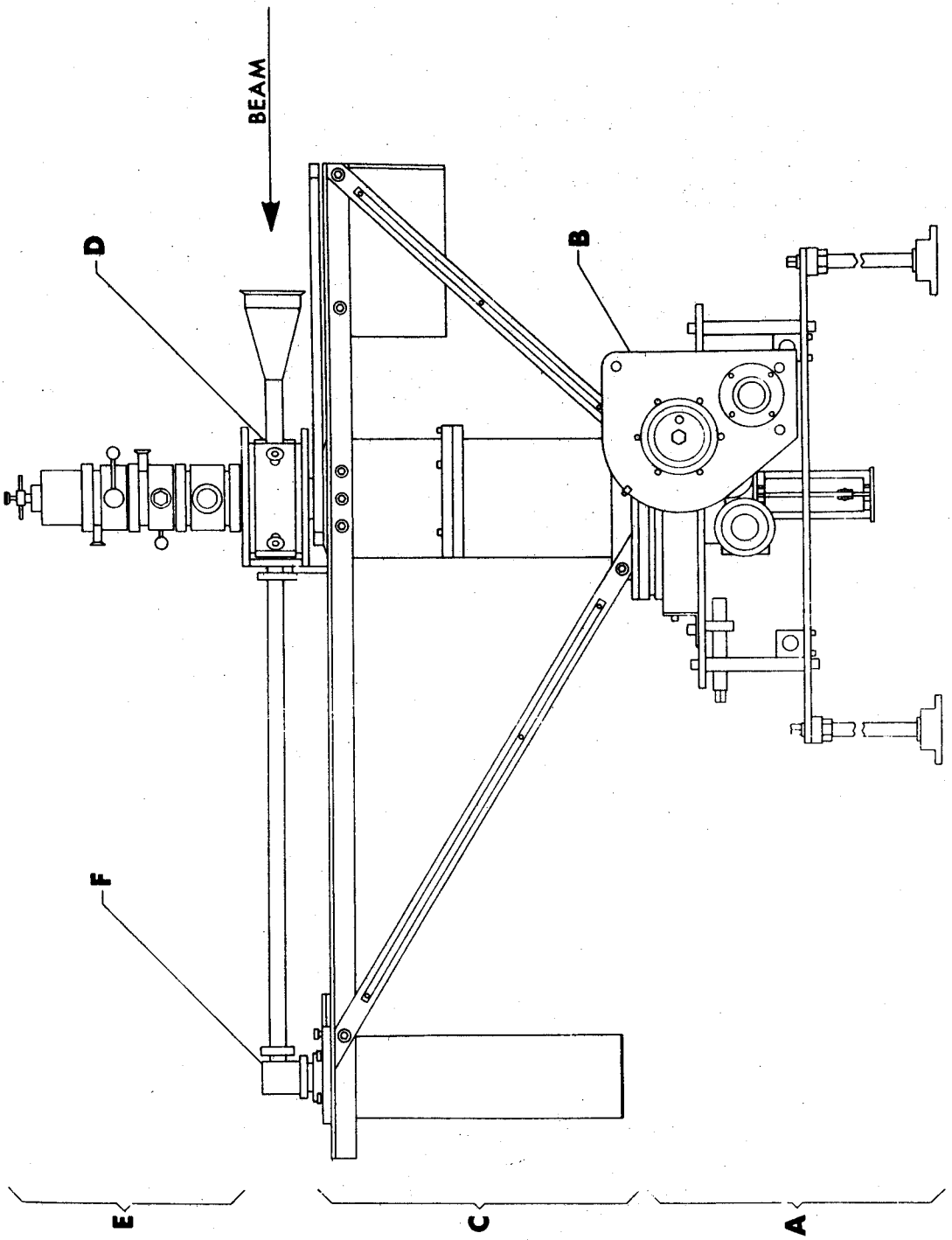

2.2 Goniometer drive unit: A - Base, B - Main arm gear train, C - Main arm, D - Target chamber, E - Target lock, F - Detector carriage.

steps/sec. The motor is connected to the main arm through a 4:1 gear train (see Figure 2.2B) and a 90:1 worm gear. This worm gear mechanism is a Bridgeport, 15 inch, rotary mill table. The resulting rotational velocities of the arm are 72°/min with the motor running in the AC mode and 6°/min for DC operation.

This table is a precision device and precautions were taken to prevent overloading the gears which it contained. To permit the use of the maximum load described above, it was necessary to construct an arm which allowed for a small flex when the angular position of the element was changed. The details of these considerations are given in Appendix I.

The angular position of the main arm is indicated by a vernier scale with a least count of 0.005° and a remote digital readout with a least count of 0.02°. The digital counter is driven by a pair of synchro motors which is connected directly to the Slo-Syn motor shaft.

The second detector positioning element is a 3/4 inch thick aluminum arm located just above the main arm. This manually positioned element has a radius of about 2 feet, and is designed to support maximum loads of about 50 lbs. The angular position is indicated relative to the main arm by a vernier scale with a least count of 0.1°.

The drive mechanisms for the target angle and target height are located below the rotary table. Both of these utilize a worm gear driven by a dual speed motor system.

The position of the target is indicated on two remote digital readouts each of which is driven by a pair of synchro motors which is in turn connected to the drive motor shaft. The least count on the angle readout is 0.02° while the height is 0.2 mil. The gear train used in changing the angular position of the target results in an angular velocity of 432°/min in the fast mode and 36°/min in the slow mode. The target height can be varied at a speed of 1.80 or 0.072 inches/minute. Below the target drive elements are located five microswitches which are activated by a cam on the end of the target shaft. Two of these switches define the target height limits of travel while the remaining define the predetermined positions for three targets in the target holder.

Located just above the arms of the goniometer is the target vacuum chamber (Figure 2.2D), containing a 6 inch high target ladder. The exact configuration of this chamber depends on the experimental needs. These determine, for example, what type of monitor port is incorporated and its position. Also, the experiment dictates the type of beam entrance and exit ports used and the type of coupling needed between the detector and the target vacuum chamber.

The target chamber was designed to be easily modified by providing a replaceable section in the median plane. The first section constructed is 8 inches in diameter and

has two fixed monitor ports at -45° and -135°, a slot for the scattered particles from -15° to 170°, and a single beam port. There is an O-ring seal around the outside of the slot which permits the use of a sliding vacuum seal as well as a thin foil window.

The sliding seal is similar to others (Fe 66) (Bo 67) and was designed to be used with Ge(Li) detectors in a windowless geometry. The seal strap is made of 10 mil stainless steel and is rotated using only the scattered beam port to transfer the torque between the main arm and the strap. The lubrication of this seal which provides a satisfactory operation is Dow Corning, high vacuum, silicone grease. A mixture of vacuum grease and oil with molydenum disulfide powder was also tried but was rejected because it was less convenient to use.

A thin foil window of 1/2 mil Kapton* has also been successfully used in place of the sliding seal on this chamber. Both of these designs are used with an external beam dump located beyond the goniometer. As a result the particle beam must pass through either the foil window or the steel strap. In the latter case serious background radiation is produced and is, therefore, a limitation to the usefulness of this design.

In order to remove this limitation of the 8 inch chamber a 16 inch diameter section was fabricated with the

*E. I. DuPont de Nemours, Wilmington, Delaware.

following features: It includes a sliding seal with a similar construction as the first, and extends from 8° to 110°. This still allows the angular distributions to be obtained, however, from 8° to 172° accomplished by rotating the chamber 180°. It also includes a windowless beam exit port as well as an entrance port, along with two monitor slots with removable thin foil windows of Kapton.

A target transfer and hold lock (Figure 2.2E) is connected to the top of the target chamber through a standard, 4 inch, Marman vacuum coupling. This lock consists of two vacuum valves and a small chamber containing a transfer mechanism. This assembly can be used to insert a target into the central chamber without breaking the chamber vacuum or, if necessary, without exposing the target to the atmosphere.

The detector carriage is shown in Figure 2.2F. The detector packages and the LN_2 dewar are held by this support between the dual beams of the main arm. The radial position of the detector is fixed securely when the detector mount is tightened and the carriage is pinned to the main arm with 1/4 inch, steel dowels. In addition to the single detector mount shown here, a dual mount has been made for holding two detectors side by side. The LN_2 dewar used with this latter system has a pot life of about 10 hours.

2.2.b. Local Electrical System

The local electrical system includes a portable control box connected to a power supply by 30 feet of multiconductor cable. The power supply along with the control relays are completely enclosed in a steel cabinet isolating the contact noise of the relays. The control box shown in Figure 2.3 contains all of the functions found on the remote control panel except an automatic angle increment feature of the main arm which is described below. In addition to these controls, however, there is a main arm limit, override switch permitting the detector to be driven through zero degrees if necessary. This feature was incorporated only into the local control trying to minimize the possibility of an accident and not worrying about the slight inconvenience it might create. The mobility of this local control box greatly facilitates the alignment of the goniometer on the beam line.

2.2.c. Remote Control Panel

The remote control panel is shown in Figure 2.4. The controls on the panel are placed in three verticle groupings. The right hand section contains the controls and digital counter for the target angle. In the center is located the target height controls and counter. The three buttons located in a horizontal row are used for the automatic positioning of three targets in the target chamber. Any one of the targets may be selected by merely pushing the

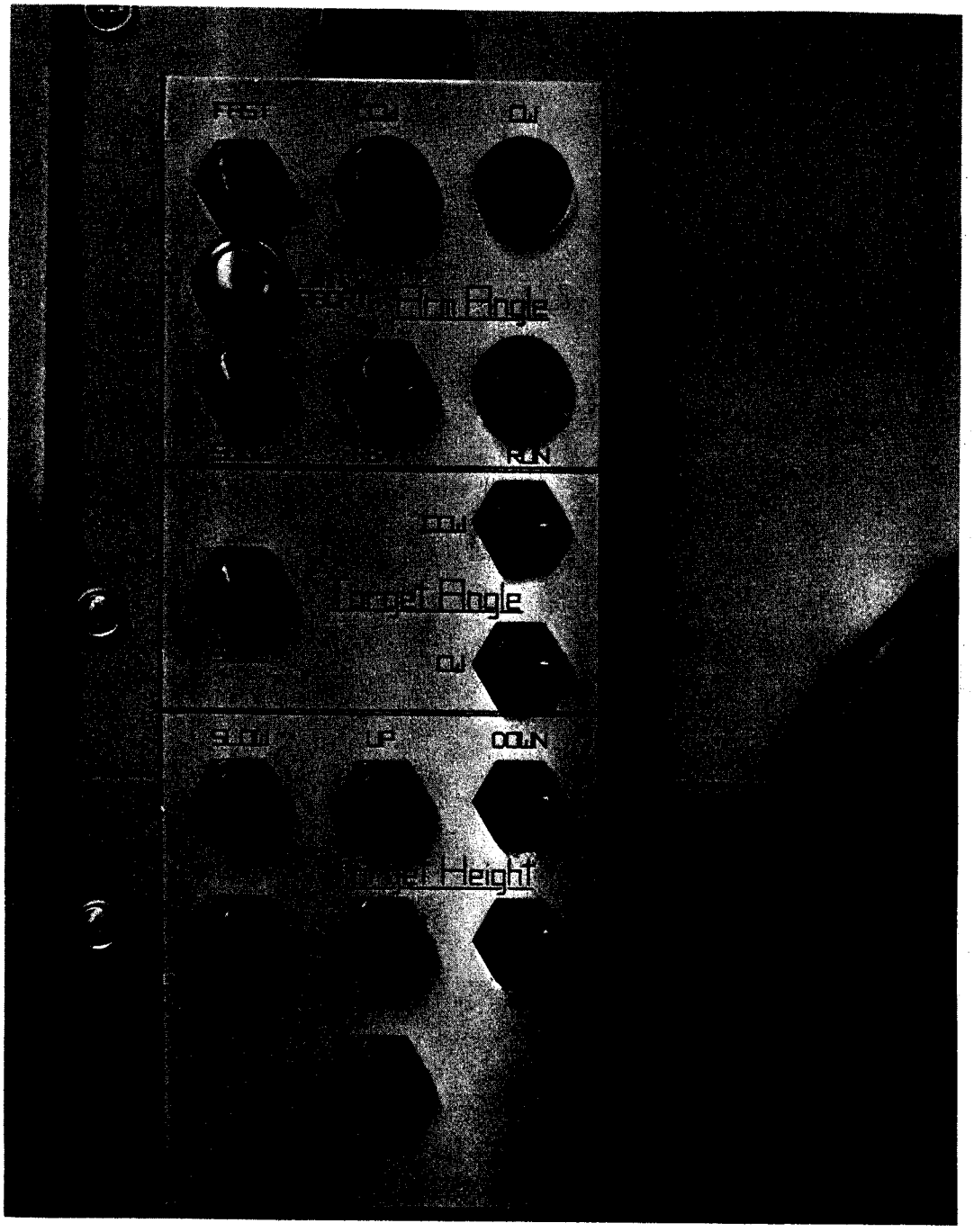

2.3 Local control box.

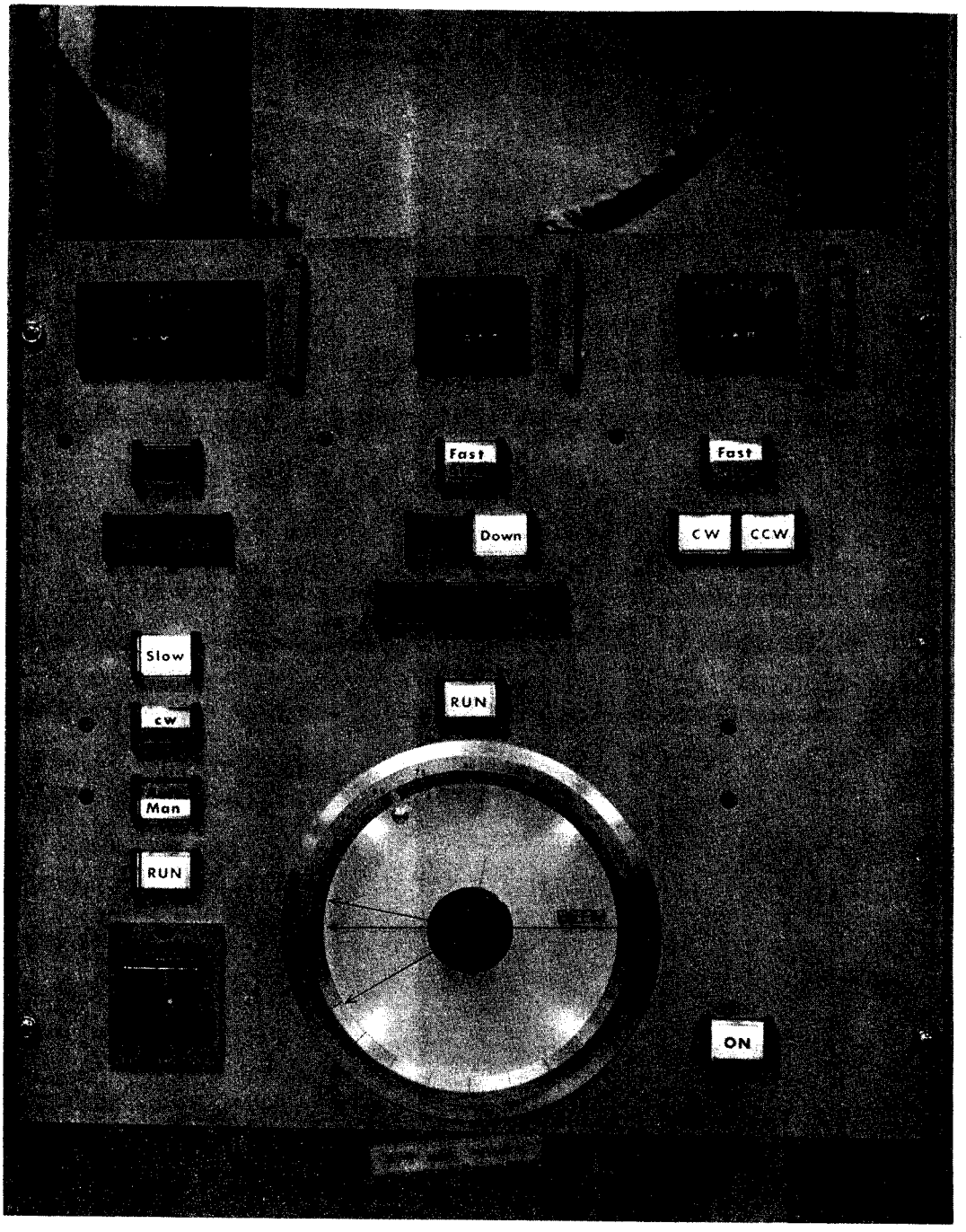

2.4 Remote control panel.

corresponding button. In addition to this automatic feature there is a manual mode which permits, for example, a target uniformity scan.

The last group of controls on the left is for the main arm. The digital counter used for this readout is a dual bank type* which indicates the scattering angle of the detected particles increasing in either direction from 0°. At the bottom of this group is located a predetermined, electromagnetic, digital counter. This counter is used to select the number of steps--0.01°/step--that the main arm is to be moved. In a typical experiment, for example, it is not uncommon to measure an angular distribution in equal angular steps. In such a case the size of the step is set on the preset counter and the motion is automatically completed when the run button is activated.

This remote control panel also contains a graphic display which shows the relative angular positions of the incident beam, the main arm, the target, and the manually positioned arm. This display is in the lower portion of the panel and is coupled to the digital readout system for both the main arm and target by a pair of small synchro motors.

---

*Durant Manufacturing Company, Milwaukee, Wisconsin.

2.3 Calibration of the Goniometer

The calibration of the goniometer involved the measurement of the various quantities which could affect the accuracy of the readout since they are the most direct source of uncertainty in the position of the various elements. There are other aspects, however, which affect the actual positions of the elements. These may include the concentricities of the rotating elements and the levelness of rotation of the main arm. The levelness is a controlable quantity and depends primarily on the care which is taken during the installation of the goniometer. To check the accuracy with which the readouts can indicate the true position of the corresponding element, it is necessary to be able to measure the position of the element independent of the goniometer and with a greater precision than that of the readout system being tested. This independent system of measurement is referred to as the reference in the following sections. To obtain a figure of merit for a readout system, comparisons were made between the reference measurement and the value assigned by the readout. From these comparisons, figures can be obtained which show how well the device can be repositioned to a fixed location, how accurately the element can be positioned at a location, and what size of backlash is involved in the entire system when the drive is reversed.

2.3.a. Main Arm Angle Calibration

2.3.a.1. Construction of the References Geometrics

One reference (reference I) used for calibrating the main arm was a set of points set up about a center point in a large open area. The area above the roof of the shielding at MSUCL offered a large, unobstructed area about 132 feet long and 75 feet wide. The shielding roof made of two layers of 18 inch thick, prestressed, solid concrete beams provided a stable base for the calibration measurements.

Two surveying instruments were used in the setup of this reference, a K & E jig transit with a 30X scope, (TR #1), and a K & E surveying transit, (TR #2), each of which was mounted on an X-Y adjustable stage. TR #1 contained a front surface mirror at the end of its horizontal axis of rotation. This mirror was used to set the two transits such that the lines of sight were perpendicular.

The surface of the mirror on TR #1 was adjusted to be perpendicular to the horizontal axis of rotation. This was done by observing with TR #2 some object that was reflected in the mirror from a distance of about 30 feet. The mirror was adjusted to keep the reflected image fixed in the field of view of TR #2 while the scope on TR #1 was rotated about its horizontal axis.

To obtain an idea as to what effect the levelness of the transit had on the measurements, the following check was made. The transit scope was leveled and a surveying target* was sighted at about 30 feet. The scope was then tilted from level to produce a shift of about 30 mils of the cross hair on the target corresponding to a shift of about 0.005°. During all of the steps used in this calibration, however, the level was repeatedly checked, and the bubble was kept to within 0.03 inch of perfect alignment. Therefore, the errors due to the levelness of the transit were kept to better than 6 mils in 30 feet or 0.001 degree.

Performing a similar test on the level of TR #2 gave the results of 0.003 degree per division on the level. This scope was also kept to within a small fraction of a division of being level throughout the measurements, and, therefore, this also contributed a negligible uncertainty.

According to the specifications of TR #1, the straightness of the line of sight from 8 inches to 100 feet is 1 mil. The specs on TR #2 are unknown but they could be 30 times worse and still contribute a negligibly small error.

The reference points at 0, 90, 180 and 270 degrees--points A C B D in Figure 2.5--were set up first. The 0° and 180° points were located by simply placing two surveying targets on the opposite walls along the larger dimension of the room. TR #1 was set approximately midway

*Keuffel and Esser Company, Hoboken, New Jersey.

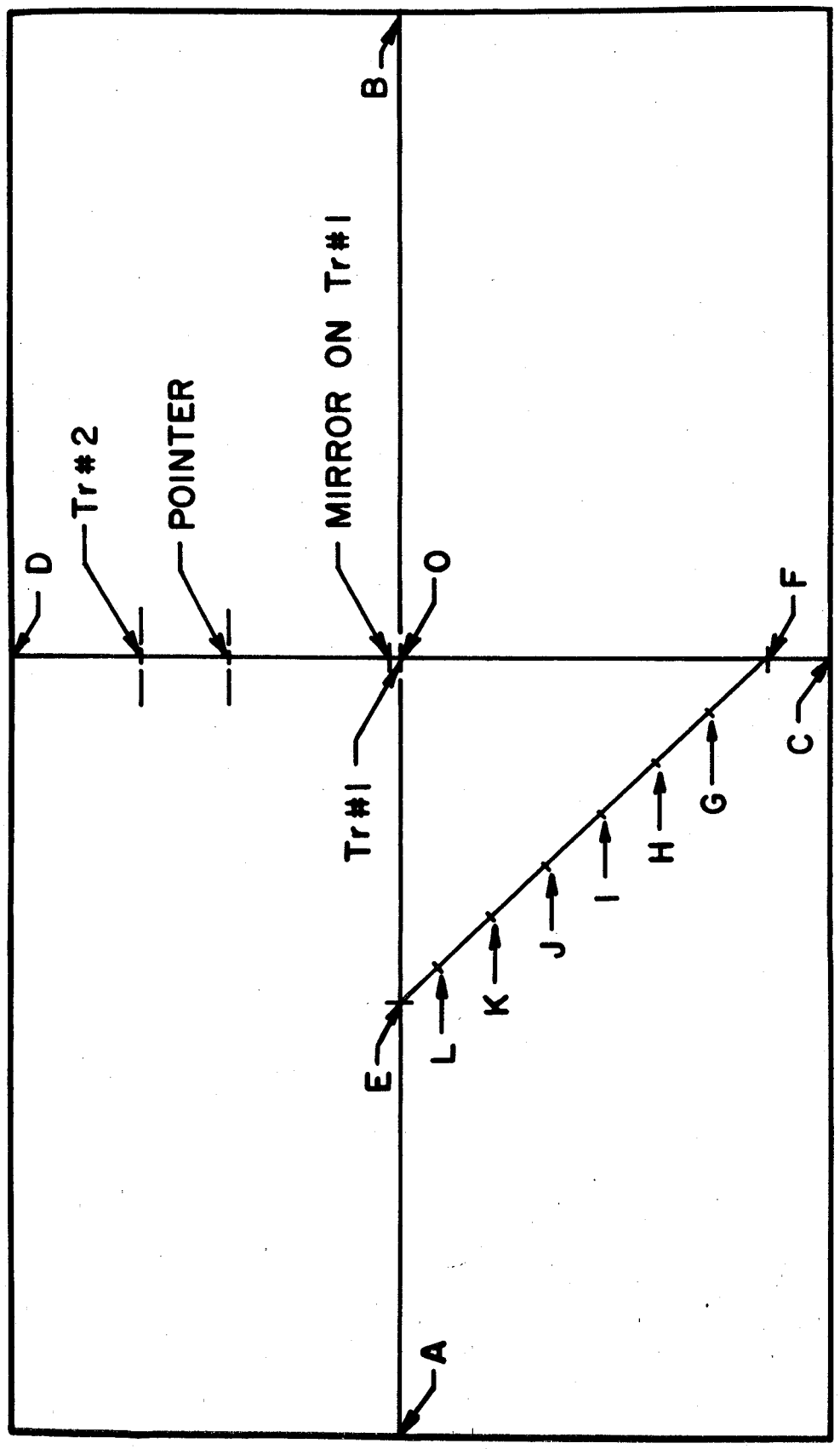

2.5 Floor plan of the geometry for the primary points in reference I.

between these points, leveled, and adjusted such that the two targets could be sighted on the cross hair in the scope by only rotating the scope on its horizontal axis.

The scope was then rotated about its horizontal axis so that the floor beneath it could be viewed through a hole in the transit mount. The scope was then rotated about its vertical axis and adjusted about its horizontal axis until the spot beneath the cross hair remained fixed in the field of view. A target was placed on the floor at the center of the cross hairs and formed the center of the reference, point O.

TR #2 was placed about 24 feet from the mirror on TR #1, which sighted along the AB line (see Figure 2.5). A sharp pointer was placed about 8 feet in front of TR #2. TR #2 and the pointer were adjusted so that the center of the reference, the pointer, the image of the pointer in the mirror, and the internal cross hair in TR #2, were all coplanar. When this was accomplished, the pointer lay on a line through the center and perpendicular to line AB. The scope of TR #2 was rotated about the horizontal axis to determine the positions of targets C and D.

TR #1, still located over the center, was used to place two points, E and F (Figure 2.5), on the floor. These points were located on the two perpendicular lines at a distance of about 32 feet from the center. A 100 foot, Lufkin, chrome-clad, steel measuring tape was used for the linear measurements.

The two targets were located on the two lines in the following way. First, TR #1 was aligned on the line of interest. It was then sighted towards the floor at a point about 32 feet from the center. A target was stuck to the floor at this point, but since the line of sight made a small angle with the floor, there was a problem in aligning the target accurately. To provide a more accurate alignment, a second target was used. The targets have a fine line at the center of each side and intersecting the edge. By placing this target vertically over the target on the floor such that the fine line at the edge is aligned with the center point of the target on the floor, the target on the floor could be accurately adjusted so that its center was on the line of sight.

Next the edge of the measuring tape was placed over the center point, and the same edge was placed over the point located on the line. The tape was held taut, and a sharp pin was used to punch a very small hole in the target surface at an appropriate distance and also on the proper line. The distance OF was 33.500 feet, and OE was 32.000 feet.

TR #2 was lined up so that it could sight along the line between points E and F. The same technique used above was incorporated here to lay out points on the hypotenuse of the 90 degree triangle at distances in multiples of 7.000 feet from point F.

Now TR #1 could be used to transfer this first set of points into the quadrant between points B and C. TR #2 and the sharp pointer were set up as shown in Figure 2.6. TR #2 was aligned to sight along the line between the point on the hypotenuse and the center. TR #1 was then adjusted so that the cross hair of TR #2, the pointer, and the reflected image of the pointer in the mirror were colinear. TR #1 was then used to place a target along its line of sight on a conveniently accessible, stable spot at a distance of about 30 feet from the center. This point is then located 90 degrees from the associated point on the hypotenuse.

The reference angles that resulted from the above procedure are shown in Table 2.1. The details of the calculations used to determine these angles are given in Appendix II. Also shown are the standard error associated with each point as determined in Appendix III.

A second reference (reference II) was used for small angles from 0° to 4°. This consisted of the Lufkin scale fastened to the wall at point A, Figure 2.5. This scale was located at a distance of 71.576 feet from the center. The typical distance that was measured on this tape was 1.50 inches corresponding to 10 steps of the drive system at 0.01°/step. This gave an angle and a standard error (Appendix III) of

$$0.100° \pm 0.001°$$

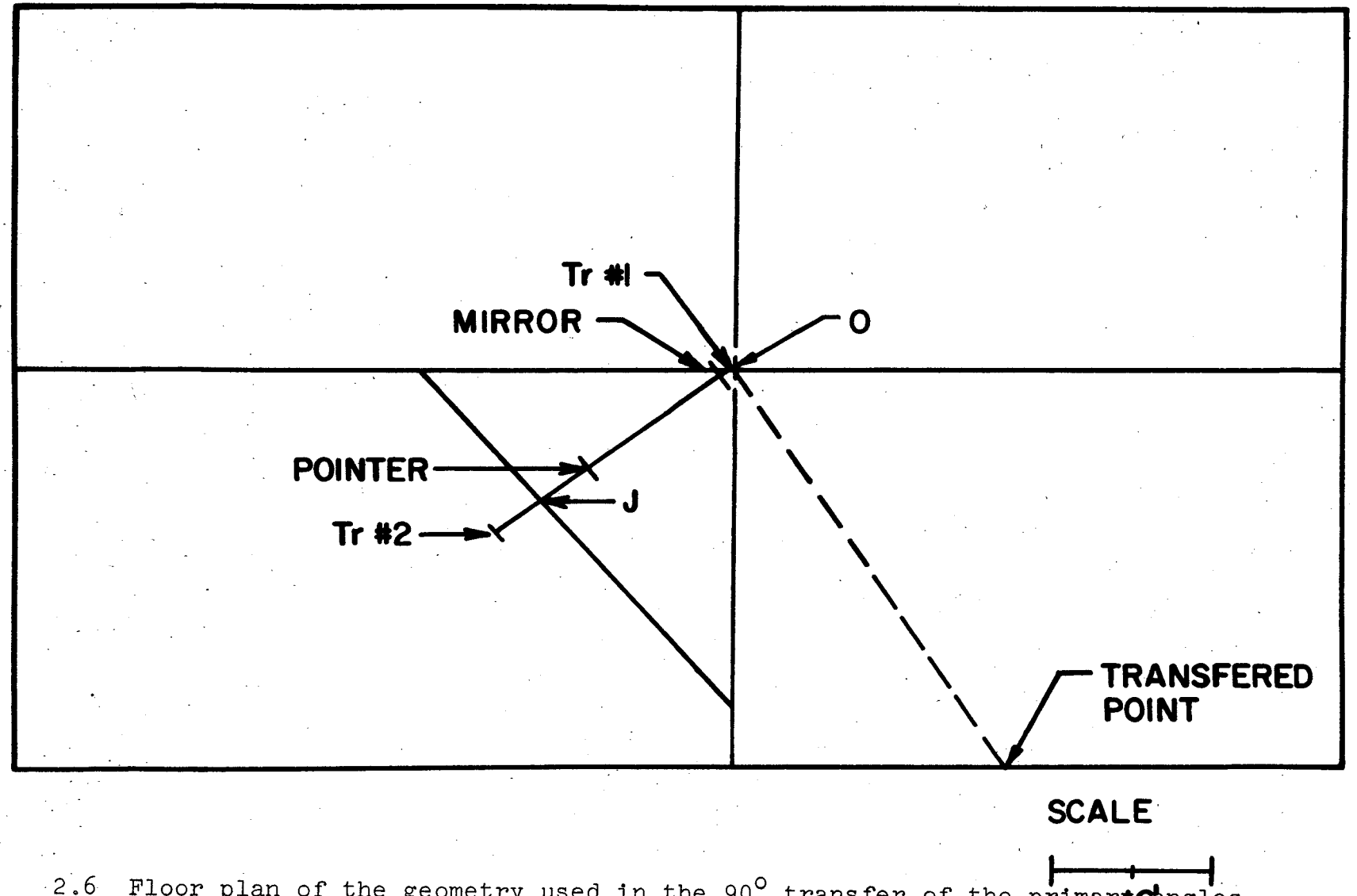

2.6 Floor plan of the geometry used in the 90° transfer of the primary angles of reference I.

TABLE 2.1.--The reference I angles and estimated standard errors.

0.000°	±	0.001°	0.000°	±	0.001°
+9.649°	±	0.007°	-6.155°	±	0.005°
+22.474°	±	0.007°	-18.717°	±	0.005°
+38.379°	±	0.006°	-34.420°	±	0.004°
+55.580°	±	0.005°	-51.621°	±	0.003°
+71.283°	±	0.005°	-67.525°	±	0.003°
+83.844°	±	0.005°	-80.351°	±	0.002°
+90.000°	±	0.004°	-90.000°	±	0.004°
+99.649°	±	0.002°	-96.155°	±	0.005°
+112.474°	±	0.003°	-108.717°	±	0.005°
+128.379°	±	0.003°	-124.420°	±	0.005°
+145.580°	±	0.004°	-141.621°	±	0.006°
+161.283°	±	0.005°	-157.525°	±	0.007°
+173 844°	±	0.005°	-170.351°	±	0.007°
+180.000°	±	0.001°	-180.000°	±	0.001°

With the reference determined, TR #1 was replaced with the goniometer at the center. The goniometer had to be placed so that its axis of rotation was on center and such that the main arm rotated in a level plane.

Having made checks of concentricity of the rotating elements (section 2.3.d) it was felt that the center of the target shaft, Figure I.4s, and the center of the target screw, Figure I.4z, would determine the axis of rotation of the goniometer. To locate this axis, TR #1 was set up on line CD and TR #2 on line AB so that each could view two 90° brass points, one located over each end of the axis. The goniometer was then placed on center to within 1/2 inch by the use of a specially built dolly. The four legs were then used to raise the goniometer to an appropriate height.

At this point the main arm could be leveled approximately by adjustment of the four legs. Then, by using the adjustable X-Y base of the goniometer and the leg adjustments the two pointers located on the axis of rotation were simultaneously brought into coincidence with a vertical line, determined by TR #1 and TR #2, at the center of the reference.

TR #1 was then adjusted to be level at a height such that the cross hair was coincident with the top surface of the main arm at the point where it is fastened to the central column. The bolts in the main arm were loosened and both main arm beams were adjusted so that the top surface, over the entire length was level to ± 2 mils during a rotation of 360°.

The 6 bolts which hold the beams to the upper section of the central column were now securely tightened. The arm was rechecked for any changes. It was noticed that when the braces for the main arm were tightened the ends of the beams on the detector support side of the arm were drawn together. This was found to be caused by a slight twist in the brackets on the lower column section to which the braces were bolted. To prevent this problem, shim stock was placed between the brace and the bracket. All the bolts on the main arm were then tightened and the levelness of the arm was again verified.

With the goniometer arm leveled and the axis of rotation in the center, the X-Y base could be tightened. As the bolts in this base were secured, the main arm was viewed to see if there were any shifts, but there were none.

TR #2, mounted on an X-Y stage, was now fastened to the end of the main arm. A counterbalance of 25 pounds of lead was also put on the arm. The arm was viewed by TR #1 to verify that it had not moved. TR #2 was adjusted to be level and to be on line AB of the reference. This assured that the transit line of sight was through the axis of rotation of the goniometer. TR #1 was readjusted on line CD and was used to monitor that the goniometer remained on center during the calibration.

2.3.a.2. Calibration Procedures

There are two quantities which were used as a measure of the accuracy of the readout system of the goniometer--the RMS deviation, δ, and the backlash. In each case the positions of the elements as indicated by the reference were compared with the corresponding positions as indicated by the goniometer readout system. The δ is defined by the equation

$$\delta = ((X_G - X_S)^2/N)^{1/2}$$

where X_G is the position of the element as read on the goniometer readout system, X_S is the position as read on the

reference system, and N is the number of measurements. There are two different values of δ, one for each direction of motion; therefore, care must be taken not to include backlash effects in this value. For this reason the δ that is considered includes only those measurements in which the system is driven in a fixed direction from a starting location which was initialized in that same direction.

The backlash of the drive systems is found by the following method. During the calibration runs, the drive system of interest is stopped at specific (set) locations as indicated either by the reference or by the digital readout system. This is done at each location a number of times for both directions of motion. The backlash at each of these points is then defined in terms of the deviations of the results of the measurements obtained from the non-set readout system of the set location for the element approaching that point in both directions. The backlash of the readout system is then defined as the RMS of the deviations found for all of the set points.

When considering the actual case of the goniometer, one is concerned with a third quantity, the reproducibility of a position. This reproducibility is a measure of how well a position can be reset when the same number is set on the digital readout. To obtain this figure, the reference values were averaged for each specific location of the

element treating each direction of travel independently. The uncertainties in the reproducibility at the specific location is then defined in terms of the deviations from this mean value.

There are several different operating conditions under which the main arm had to be checked. These include stepping through large angles, stepping through small angles, operating under a light load, and operating near a maximum load. Since there are two methods which can be used to read the position of the main arm (which are independent of each other), the local vernier scale and the remote digital counter, it was necessary to calibrate both.

The scope which was placed on the main arm was used to sight the reference points. All calibrations were made with respect to the 0 degree reference point. When the arm was rotated in the positive, CW, direction from this point the scope was positioned to view the target in the "backward" direction over the axis of the goniometer. When in the negative, CCW, direction, however, the scope was rotated about its horizontal axis, and the targets were viewed in the "forward" direction.

The arm was, in general, driven in a fast mode until it neared the reference point of interest. Then the drive was switched into the stepping mode, and the arm was slowly rotated until the cross hair in the scope coincided with the target point.

When the checks were made for large angle stepping, the arm was set exactly on 0 degrees. The drive was then set to automatically step the arm in 90 degree increments through 360 degrees.

For the measurements of the small angle stepping, the arm was positioned so that the cross hair in the scope was located on a convenient starting point on the tape on the wall. The arm was then automatically stepped through 4 degrees in 0.1 degree increments.

When the arm was run in a loaded configuration an additional 50 lbs was placed at about 3 feet from the center with 75 lbs as the counterweight.

2.3.a.2.a. Total Errors in the Comparisons with the Reference Measurements

The errors which needed to be accounted for in the total errors arise from the centering of the goniometer on the center of the reference, the alignment of the line of sight of TR #2 across the axis of rotation, the sighting of the target with the scope, and the total surveying errors in the reference points themselves.

1) Centering errors
   a) Scope setup lines AB and CD 0.0008°
   b) Goniometer centering 0.0008°
2) TR #2 alignment on line AB 0.0008°

3) Alignment of cross hairs and target (Includes finite motor step size)

   a) Reference I 0.0008°

   b) Reference II 0.002°

4) Errors in standard points

   a) Reference I (Table 2.1) 0.001°-0.007°

   b) Reference II (Appendix IIIB)

The total errors involved in the comparison of the goniometer position to the reference points is the sum in quadrature of (1, 2, 3, 4) above.

The total errors in the measurements range from

±0.002° to ±0.007°

These results of the total errors are 3 to 10 times smaller than the errors that are expected in the ganiometer (0.02°). This verifies that the references that were constructed to test the main arm readout systems had sufficient accuracy.

2.3.a.2.b. Results of the Calibrations

1) Large angle stepping.--This check showed that after stepping through 360 degrees, the arm returned to the same point to within the accuracy of the sighting (0.0008°). This verified that the stepping motor had not lost or gained any steps in the 72,000 necessary for one revolution in this one check.

2) δ and backlash results and conclusions.--The results of the calibrations of the main arm readout systems are shown below in Table 2.2. Included here are the RMS deviations measured, the number of measurements which go into the RMS determination, N, and the maximum deviation, MAX, observed during the measurements.

TABLE 2.2.--Summary of the results of the calibration of the main arm.

	RMS	MAX	N
Digital system deviation, δ:			
1) No load	0.012°	0.024°	77
2) Load	0.011°	0.024°	15
Vernier system deviations, δ:			
1) No load	0.008°	0.018°	77
2) Load	0.009°	0.020°	15
Total deviations, δ, for load and no load discounting backlash effects:			
1) Digital	0.015°	0.038°	149
2) Vernier	0.019°	0.050°	149
Backlash:			
1) Digital	0.020°	0.062°	42
2) Vernier	0.027°	0.060°	42

These figures show that the main arm can be positioned to better than 0.05° even when certain precautions, such as avoiding backlash, have been neglected. When the necessary precautions are observed, however, angular measurements with

an accuracy of 0.02° are shown to be obtainable with this goniometer.

A fact that was noted in the test involving reference I was that the deviations were largely random in nature. This shows that there are no large systematic errors. During the small angle increment tests, however, there did appear a small systematic effect of about 0.01° in a 1.0 degree cycle in the digital readout, but none appeared in the vernier. This indicates a nonlinearity in the digital readout system, which probably accounts for a large part of the errors in the main arm readout. This error could possibly be corrected.

2.3.b. Target Angle

2.3.b.1. The Reference Used and the Calibration Procedures

The reference which was used for the target angle was the main arm itself. This reference has been shown in section 2.3.a. to have a precision of better than ±0.05°, which is about 4 times better than the expected accuracy of the target drive.

A front surfaced mirror was placed into the target ladder. A fine hair was placed in an open frame and was attached to the main arm. The target ladder height was adjusted, and a transit was placed in such a position so that the hair could be viewed by the scope in the mirror.

The target ladder was set at a position such that the corresponding position of the main arm was 0.00°. The target angle digital counter was set for 90.0° at this location. From this initial position the target was rotated to locations between 20° and 160° in 10° steps as indicated by the digital readout of the target position. At each location the main arm was rotated until the hair located on it could be viewed on the scope cross hair. The angular variation of the main arm with respect to its initial position was twice the angular change which was read in the digital readout for the target angle with respect to its 90°, initial position. By comparing the readings of both readouts, an error for the target angle could be determined.

This procedure was used with the target drive operating in the slow mode and in a combined fast + slow mode. Tests were also made, after raising or lowering the target ladder, to determine the effect of the vertical motion on the angular position and to determine how well the target angle could be reset to an initial value after a vertical motion.

The error introduced into these measurements by the method of comparison was negligible because of the factor of two resulting from the use of the mirror. Since this error and the error of the standard itself were small compared to the expected error of the target drive readout system, the calibration was expected to give valid results.

2.3.b.2. Results of the Calibrations

The results of the calibrations of the target angle are given in Table 2.3. The quantities, --RMS, MAX, and N--are defined in section 2.3.a.2.

TABLE 2.3.--Summary of the results of the calibration of the target angle.

	RMS	MAX	N
The deviations, δ, for a $\Delta\theta = 10°$ from an arbitrary point (defined in 2.3.a.2.):			
1) Slow	0.1°	0.3°	66
2) Fast + Slow	0.3°	0.9°	61
The deviations, δ, for any $\Delta\theta$ up to 130°:			
1) Slow	0.3°	0.7°	66
2) Fast + Slow	0.4°	3.9°	50
The reproducibility of the drive system (defined in 2.3.a.2.) With no vertical change			
1) Slow	0.2°	0.4°	70
2) Fast + Slow	0.2°	0.6°	54
With vertical change:			
1) Initial shift	6.0°		1
2) Repositioning with slow drive	0.3°	0.7°	12
Backlash (defined in 2.3.a.2.):			
1) Slow	6.2°	6.7°	11
2) Fast + Slow	5.7°	6.5°	13

It was noted that the deviation from the standard increases as $\Delta\theta$ increases. This tendency is very evident in the fast + slow mode and only slightly apparent in the slow mode.

2.3.c. Target Height

2.3.c.1. The Reference Used and the Calibration Procedures

The reference used for the target height readout system was a 6" vernier height gage with a least count of 1 mil. A dial indicator was attached to the slide of this gage. The dial gage, capable of reading to 0.5 mil, was used to indicate the relative height of the vernier gage to the top of the target shaft.

The vernier gage was held securely on the surface of the secondary arm such that the dial gage could properly contact the top of the target shaft. The target shaft was manually run up and down in a combined fast + slow mode in 0.500 inch steps as indicated on the digital readout. The corresponding changes in the height as shown by the reference were then found. These changes were compared to the 0.500 inch to obtain the deviations for a $\Delta H = 0.500$ inch.

Limit switches were set using the digital readout as the reference. When the target shaft was run UP to its highest position, the limit switch which defines this

upper bound of travel was adjusted so that the bottom of the target ladder was 3.750 inches above the top surface of the main arm. This height corresponds to the beam height for which the system was designed. The digital counter was then set at 9.989 which takes into account a backlash of 11 mils (2.3.c.2) of the drive and allows the bottom of the target ladder to be defined as the 0.000 position for the target shaft traveling DOWN.

The first target at the bottom of the ladder was chosen to be a standard, 0.500 inch high target. The next three targets were chosen as those targets which could be selected automatically. The target frames that were picked to be compatible with the switch locations are 1.125 x 2.000 x 0.06 inch frames. Different sized frames would work but the switches would have to be readjusted. Switches #1, #2 and #3 correspond to the vertical centers of these target frames which are at corresponding distances from the ladder bottom of 1.062, 2.187, and 3.312 inches. One of these distances appear on the digital counter when the corresponding control switch is activated and the search is completed in the proper direction of travel.

The microswitches on the goniometer were adjusted in their vertical as well as their radial positions with respect to the target screw-shaft. The vertical height was defined as satisfactory when the switch stopped the drive to within 5 mils of the proper location with the

drive running DOWN. The radial location of each switch was set so that the switch was activated near the radial peak of the cam on the target screw shaft.

2.3.c.2. Results of the Calibrations

The results of the calibrations of the target height readout system are lsited in Table 2.4. The definitions of the quantities RMS, MAX, and N are given in section 2.3.a.2.

TABLE 2.4.--Summary of the results of the calibration of the target height.

	RMS	MAX	N
The deviations for a $\Delta H = 0.500"$ (defined 2.3.a.2.):	0.6 mil	1.0 mil	55
Total deviations for any ΔH:	1 mil	2 mils	25
Reproducability of the drive system (defined in 2.3.a.2.):			
1) Manual mode	0.4 mils	0.5 mil	38
2) Automatic mode	0.6 mils	1.5 mils	20
Backlash (defined 2.3.a.2.)	11 mils	12 mils	8

2.3.d. Concentricity Checks

The concentricity of two rotating elements can be expressed in terms of total indicator runous (maximum fluctuation of dial gage), TIR. A TIR of 6 mils indicates that the centers of the two elements are separated by 3 mils. To make those tests on the various elements of the goniometer, a dial indicator capable of reading to 0.5

mil was fastened to one element, the base element, and was set in contact with a cylindrical surface on the second element. Table 2.5 shows the results of these tests.

TABLE 2.5.--Summary of the results of concentricity checks.

	Base Element	Second Element	TIR
1.	Secondary Arm	Target Shaft (R)* (Fully extended)	3 mils
2.	Secondary Arm (R)	Target Shaft	3 mils
3.	Secondary Arm (R)	Target Well	1.5 mils
4.	Main Arm (R) with Sec. Arm free (R)	Target Shaft	1.5 mils
5.	Main Arm (R) with Sec. Arm fixed to M. A.	Target Shaft	3 mils
6.	Main Arm (R) with Sec. Arm fixed in space	Target Shaft	3 mils
7.	Main Arm	Target Shaft (R)	4.5 mils

*R = Rotating element

2.4 Installation of the Goniometer on the Beam Line--Figure 3.1

A proper installation of the goniometer on the external beam line is required in order to utilize its precision to the fullest. To obtain the precision of 0.02°, it is necessary that the main arm rotate in a plane containing the beam line to a tolerance of better than

± 16 mils at the full radius of 4 feet. It is also necessary to locate the axis of rotation of the goniometer so that it intersects the beam line to better than ±8 mils.

During the calibration it was found that the main arm rotates about an axis which is within 2 mils of the axis of the target shaft; therefore, an alignment of the center of the target shaft on the beam line defines the axis of rotation of the main arm to within the tolerances. It was also found that the plane of rotation of the main arm could be leveled to within 2 mils over the entire length for one full revolution. Considering these facts, therefore, it can be concluded that the goniometer can be aligned well enough on a beam line to make use of its precision.

2.4.a. Determining the Beam Direction

The limiting factor in the alignment of this precision instrument on the beam line is the accuracy to which the beam direction and the beam location at the center can be determined and reproduced. The beam line elements are shown in Figure 3.1. The alignment procedures were carried out at a beam energy of 40 MeV which was the energy at which this thesis experiment was done.

The beam from the Michigan State University Sector-focused Cyclotron was analyzed by the 90° analyzing system, M3 and M4. The switching magnet M5 was then set

for the field determined by the analysis system and the calibrations for the magnets M3, M4 and M5(Sn 67). The positions of quadrupole magnets, M7 and M8, were adjusted in a direction perpendicular to the beam direction such that the steering effects of these magnets were eliminated. The beam was then focused to a 1/8" wide spot inside of vault #2 at various locations in a 10 foot region about the intended location of the goniometer. At each of these locations a burn was taken on a 1/4 inch thick quartz plate. A plumb line was then used to transfer the center of the burn to the floor. The jig transit, TR #1, described above in section 2.3 was then leveled at the beam height and adjusted such that its line of sight was colinear with the points on the floor. The transit was then used to transfer the beam direction defined by its optical axis to survey targets located on the walls of vault #2.

The beam height was also defined in the above procedures by a burn taken at the intended center location of the goniometer. The center of this spot was transferred to the wall of vault #2 by TR #1 which had been carefully leveled.

The accuracy to which the beam direction was determined for a 40 MeV beam was estimated by how well the centers of the burns could be identified and how well they could be transferred to the floor. The estimated uncertainty was about 1/8 inch in 10 feet or about 0.1°.

2.4.b. Placement of the Goniometer on the Beam Line

A second transity, TR #2, was set up in valut #2 to intersect the intended center location of the goniometer at the beam location. The line of the intersection of the vertical planes determined by TR #1 and TR #2 was then defined as the axis of rotation of the goniometer. The goniometer was placed at the center to ±0.5 inch by using a four wheel dolly. The four legs were then lowered so that the feet rested on four, thin, compressed styrofoam pads on the concrete floor. These pads provide an interface between the floor and the steel feet.

The goniometer was raised so that the beam height, as defined by TR #1 was 3.750 inches above the top surface of the main arm. The distance of 3.750 inches was defined by a sharp scriber point located on a vernier height gage. Using this technique the arm was leveled and adjusted to the proper height.

The center of rotation of the goniometer was defined by a 90° point on the end of a brass sleeve which fit over the upper end of the target shaft. Using the adjustable X-Y base the center was adjusted to the proper location. The arm, however, had to be simultaneously leveled and also adjusted to the proper height.

To level the arm it was necessary to consecutively adjust the base as well as possible and then to adjust the arm braces on the main arm. With enough successive

approximations of the various adjustments, the arm was found to be level to ±2 mils over its entire length, to be at the proper height to within ±2 mils, and to be on center to within ±5 mils.

When the goniometer was aligned, the four feet were held securely to the floor by clamps consisting of 3/4 inch steel plate and a 3/4 inch bolt screwed into the concrete floor. After the goniometer was clamped to the floor, locknuts on the legs and the bolts on the base and arms were tightened, making sure that the alignment was preserved.

2.4.c. Faraday Cup--Figure 3.1.

The Faraday cup which is used with this system is used only as a beam dump and is not intended to be used for measurements of absolute charges. The end of this beam stop is a 1/2 inch thick aluminum cap on the beam pipe about 12 feet beyond the target location. The shielding of the Faraday cup consists of solid concrete and paraffin blocks. The concrete blocks form a stack about 6 feet wide and 7 feet high which extends from the wall of vault #2 behind the stop to a point about 6 feet from the center of the goniometer. The beam stop fits into a hole extending the length of the stack. The region in this hole around the beam pipe and an access hole to the end of the beam pipe are plugged with paraffin. To provide additional shielding for the detectors at small angles from the beam stop, a paraffin ring about 1.5 feet long and 15 inches in

diameter is located around the beam pipe at a distance of about three feet from the target chamber.

Measurements were made to varify the effectiveness of this stack in reducing the neutron background in vault #2. A neutron counter was used to monitor the thermal neutrons around the outside of the stack. Readings were taken in locations which were both shielded and unshielded from the beam dump. The readings at the protected locations were reduced by about a factor of 10.

The beam stop is isolated by a Delrin* beam pipe section from the remaining sections extending from the shield to the target chamber. Another Delrin section is located before the target chamber. These insulators serve to isolate the goniometer from local ground connections, and prevent ground loop problems from occurring as well as to allow the pipe to act as a charge collector of sorts.

---

*E. I. DuPont C.

CHAPTER III

EXPERIMENTAL PROCEDURES

3.1 Cyclotron and Beam Transport System

3.1.a. Cyclotron

The 40 MeV proton beams used in this experiment were produced by the sector-focused cyclotron at Michigan State University (Bl 66). This is a variable energy, isochronous machine designed to accelerate a variety of particles. Protons, for example, can be produced with energies from 20 to 50 MeV. The accelerated particles are extracted at a radius of about 30 inches by a combined electrostatic deflector and magnetic channel system. Typical H^+ internal beam currents used during this experiment were 3μA and typical extraction efficiencies were about 80%. The extracted beam entered the external beam transport system shown in Figure 3.1.

3.1.b. Beam Transport System

Two small, horizontal bending magnets, M1 and M2, and two quadrupole doublets, Q1 and Q2, were used to align the beam parallel to the beam pipe axis and to focus it on the object slit, S1, of the analysis system. The two

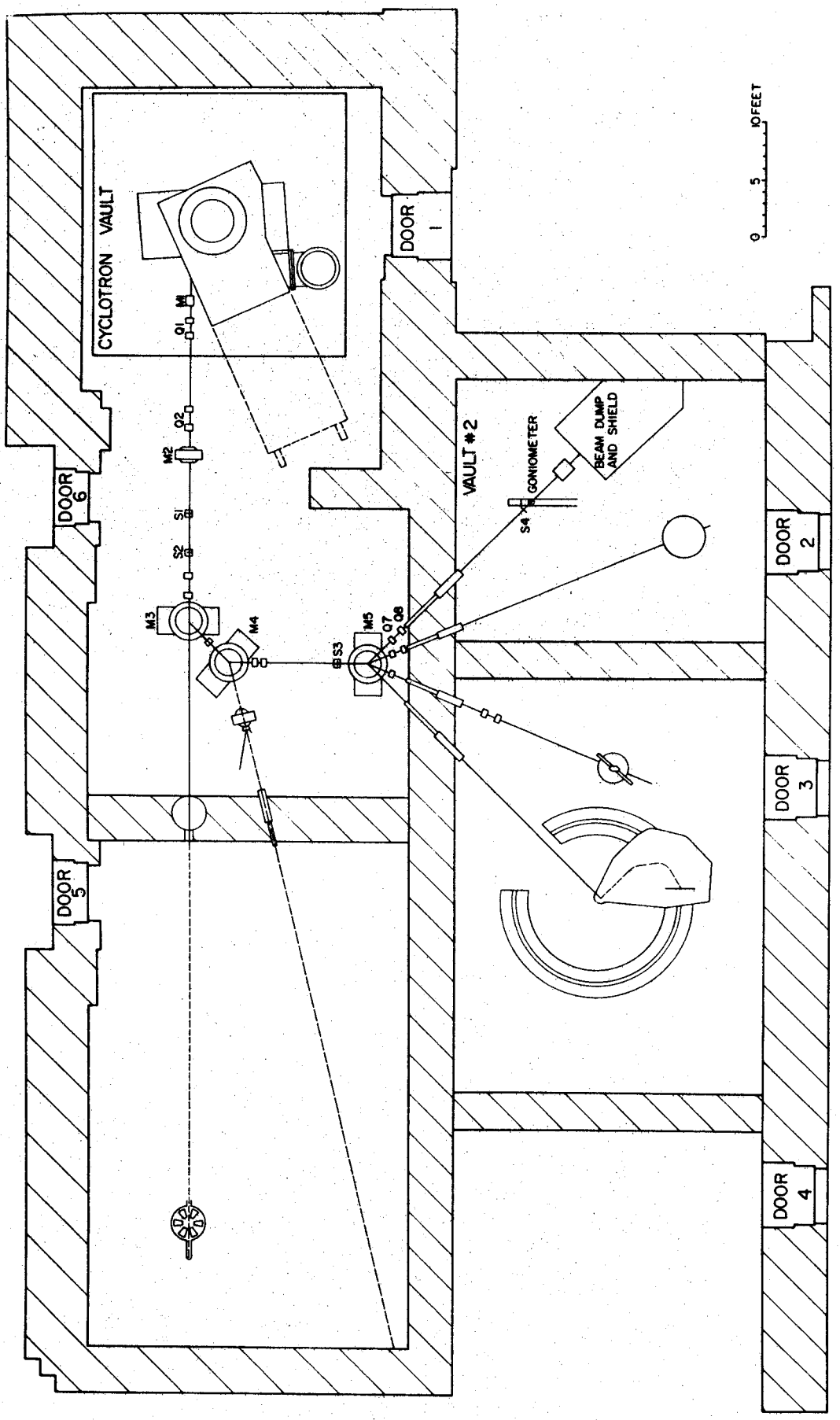

3.1 Experimental area of the Michigan State University Cyclotron Laboratory.

primary elements of the analysis system, M3 and M4, are 45° bending magnets. The properties of this analysis system have been well studied and are described elsewhere (Ma 67) (Sn 67).

Slits S1 and S2 are separated by about 48 inches are used to define the beam divergence. The analyzed beam is focused on slit S3, which is the object for the switching magnet, M5. During this experiment, typical horizontal slit apertures were 70 mils for S1, 150 mils for S2, and 70 mils for S3. These slit settings provide a beam with a calculated resolution of 5.4 parts in 10^4, or 22 keV, and a maximum beam divergence of ±5 mrad.

When the analysing magnets are set up through a standard cycling procedure, the energy of the transmitted beam can be determined to ±100 keV from the decapot settings on the magnet power supplies. These precautions were taken during this experiment to insure that the energy of the protons used were 40 ± 0.1 MeV. Nuclear magnetic resonance fluxmeters in M3 and M4 were also used to verify the energy of the proton beam (Sn 67).

3.1.c. Alignment of the Beam into the Target Chamber

After being analyzed, the proton beam was deflected through an angle of 45° into vault #2. The quadrupoles Q7 and Q8 were adjusted to the settings which were determined during the installation of the goniometer described in

section 2.4. With the detectors removed from vault #2 the beam was allowed to enter the vault, pass through the target chamber and enter the beam dump (Faraday Cup, F.C.).

A 1/8 inch diameter hole was drilled in a tantalum strip which was thick enough to stop 40 MeV protons. This strip was located in the target ladder inside the target chamber such that the hole was along the beam line and on the axis of rotation of the goniometer. With the beam passing through this "hole target" the beam currents were monitored on the annular slit, S4, located in the input coupling to the target chamber (Appendix I) and in the F.C. By slightly adjusting the quadrupoles, Q7 and Q8, and the switching magnet, M5, the current on S4 could be minimized and current on the F.C. could be maximized, thus providing a focus of the beam at the target location. The typical slit settings shown above produced a beam spot of about 1/8 inch in diameter. With a beam current of 30 nA in the F.C. a current of 0.2 nA was read on the annular slit.

3.1.d. Faraday Cup and Current Integrator

The beam stop used in this Faraday Cup is described in section 2.4.c. The beam pipe sections which extend from the paraffin shield around the beam pipe to the target chamber were designed specifically for this experiment.

Just beyond the target chamber was a 12 inch long piece of 3/4 inch copper pipe. This pipe is connected to a 20 inch long, 1-1/4 inch diameter copper pipe which in turn is clamped to a standard beam pipe section containing the paraffin shield ring. This "tapered" construction of the Faraday Cup snout allowed the detector to reach a scattering angle of almost 13°.

The end of this Faraday cup snout next to the target chamber is sealed by a 1 mil Kapton foil glued to the copper pipe. The interior of the entire F.C. assembly was maintained at a pressure of approximately 25 X 10^{-3} Torr during the experiment.

The beam current passing through the target and into the insulated beam dump was measured by an Elcor current integrator model A310B. Since th F.C. was in contact with the paraffin and cement blocks of the shielding, and since the restrictive input snout could provide a loss of charge, the total charge through the target was not measured on an absolute scale. This arrangement, however, did provide the relative numbers for the total incident charge from run to run and served to check the results of the relative normalization as measured by the monitor counter.

3.2 Set Up of the Goniometer

3.2.a. Target Chamber

The target chamber used in this experiment with the goniometer is the 8 inch diameter chamber presented in detail in Appendix I. The foil window was used on this chamber during the experiment and permitted detector angles from about 13° to 160° with respect to the beam. This window consisted of a 1/2 mil Kapton foil glued to an aluminum frame which was bolted to the target chamber through an O-ring seal. The scattered beam as well as the exit beam passed through this window.

3.2.b. Targets

A 1 mil polystyrene target and a target of gold on a 1/4 mil mylar backing were used in checking the detectors. The nickel targets used were isotopicly enriched, self-supporting foils purchased from Oak Ridge National Laboratory. The isotopic purity and areal density for each of these targets is listed in Table 3.1.

3.2.c. Detectors

The monitor detector consisted of an ORTEC silicon surface-barrier detector 270 microns thick and mounted in a transmission geometry. This detector was located outside the target chamber in a mount which contained a 1 mil Kapton window. This mount was clamped to the KF-10 Leybold vacuum fitting at -45°.

TABLE 3.1.--The self-supporting foil targets used.

Target	Purity (%)	Areal Density (mg/cm^2)
^{58}Ni	99.95	0.89 ± 0.3%
^{60}Ni	99.83	0.70 ± 0.4%
^{62}Ni	99.06	0.53 ± 0.4%
^{64}Ni	99.81	0.47 ± 0.4%

Two Ge(Li) detectors were used to obtain angular distributions of the scattered protons during this experiment. These Ge(Li) charged particle detectors were fabricated by C. Maggiore, T. Kuo, and L. Samuelson. The sensitive volumes of these detectors were about 7 mm X 7 mm X 10 mm. Each detector was contained in a package which was described in section 2.1.b.

The collimator located inside the detector package consisted of two slits in a configuration which has been described before (Gr 68). One is a 1/16 by 1/8 inch slit in a sheet of 1/32 inch tantalum. This slit is placed on the back surface of the second slit 1/8 by 3/16 inch in a 1/4 inch thick piece of brass. The edges of this thicker slit were beveled. This type of collimator caused the detected particles, which had gone through slit scattering in the thicker slit, to be degraded by about 10.2 MeV. The result is the removal of the slit scattered events from the region of interest.

These two detectors differed only in the type of structure which was used between the detector cap and the target chamber window. The detector located at the small scattering angle, Det. #1, had a snout about 4.3 inches long made from 3/4 inch copper pipe. This snout was coupled to the aluminum detector cap through an O-ring seal. There was no window on the detector cap but instead the 1/4 mil, aluminized mylar window was glued over a 1/4 inch hole in the end of the snout.

The detector located at the larger angle, Det. #2, contained a 1/10 mil Havar window on the detector cap. A KF-20 Leybold vacuum fitting was fastened to the cap through the O-ring seal. Fastened to this flange was a short brass vacuum pipe which contained a 3/8 inch hole covered with 1/4 mil mylar through which the scattered particles passed. A vacuum valve was also fastened to this section allowing it to be evacuated during the experiment.

These two detectors were securely fastened into the dual detector mount on the detector carriage described in Appendix I. The mounts were adjusted so that the carriage could be pinned to the main arm and at the same time have the ends of the snouts on the detector packages as close as possible to the target chamber wall.

By using a transit which was aligned through the center of the target chamber, each detector was oriented so that the hole in the end of the snout and the center of

the detector cap were along the line of sight of the transit. The internal collimator was also on this line as defined when the detector package was assembled.

When the detector packages were in place, Det. #1 was at a distance of 9.78 ± 0.06 inches from the target with a 0.75 inch air gap between the target chamber window and the window on the end of the package snout. Det. #2 was located at a distance of 9.28 ± 0.06 inches with a 0.40 inch air gap.

Part of the data obtained for ^{58}Ni was taken with only one detector. The detector used at that time was Det. #2 described above. The setup procedures used for this group of data was identical to that described above.

3.3 Electronics

The electronics used with the two Ge(Li) detectors is shown in the block diagram in Figure 3.2. The bias for the detectors was provided by an Ortec Model 210 power supply. The bias applied to Det. #1 was 600V and to Det. #2 was 330V.

The signal from each detector was input to a modified Ortec 109A, charge sensitive preamplifier which gives as output an analog pulse of 2 μsec decay time. Also input were pulses from an Ortec Model 204 pulser coupled to an Ortec Model 422 dual decade attenuator. These pulses were adjusted in amplitude so that they were stored in about channel 100 in the multichannel analyser.

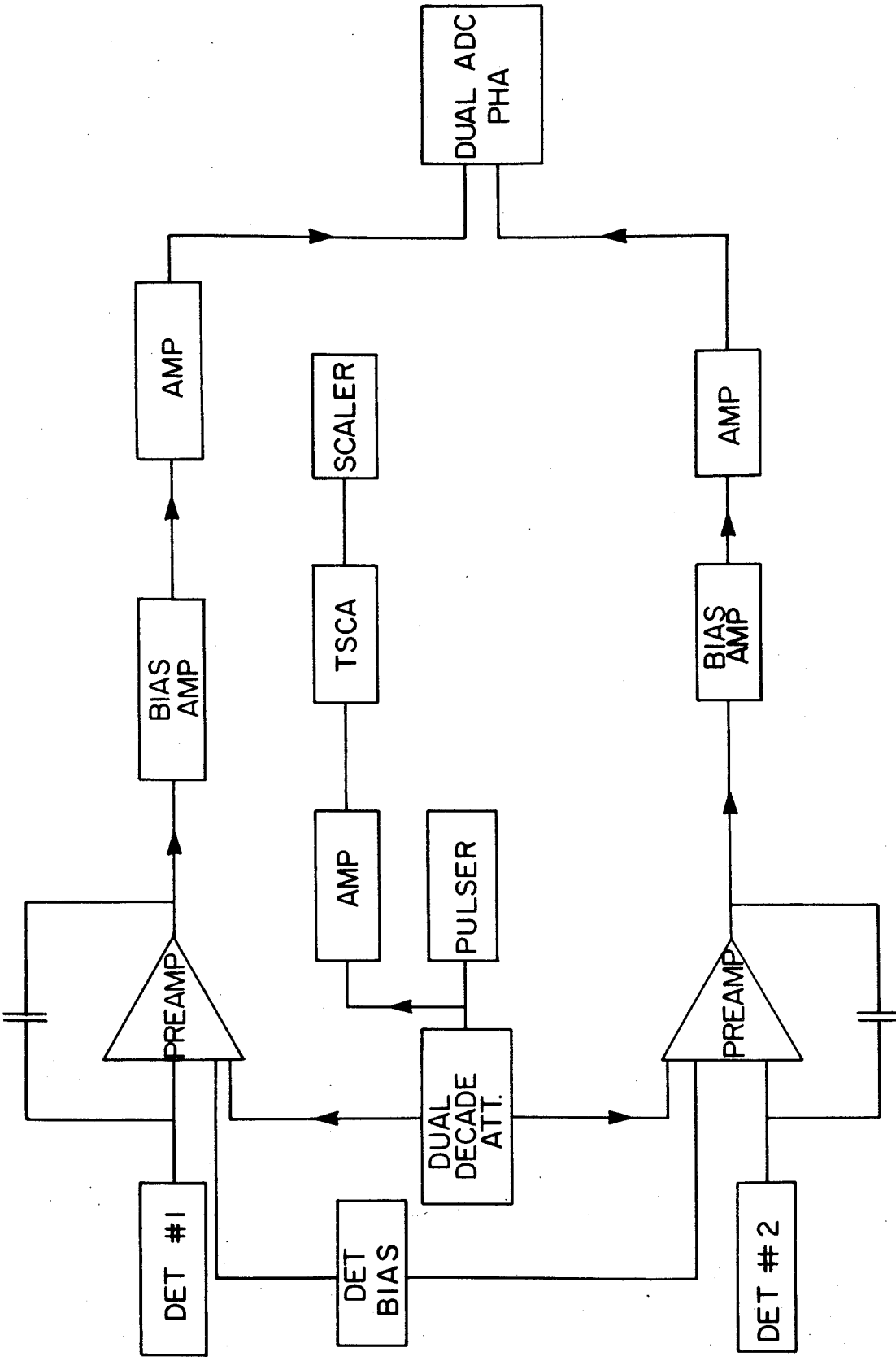

3.2 Block diagram of the electronics used with the Ge(Li) detectors.

The pulses from the preamps were fed into Ortec Model 408 biased amplifiers which were used to cut off the lower 30 MeV of the spectra. From here the pulses entered Tennelec, TC 200 amplifiers. The pulses from these amplifiers were input to a Nuclear Data, dual ADC, 4096 multichannel analyser, ND-160.

The pulser which is in each detector circuit is also counted in an Ortec Model 430 scaler. The Ortec Model 410 multimode amplifier and the Ortec Model 420, timing single channel analyzer, TSCA, shown in this circuit were used to provide the proper pulse shape to drive the scaler.

The electronics used with the monitor counter are shown in Figure 3.3. The 100V of bias used for the counter is provided by the Ortec Model 210 power supply. The pulses from the detector were passed into an Ortec 109A, charge sensitive preamp and from there into an Ortec Model 440 selectable, active filter amplifier, a Model 420 TSCA, and a Model 430 scaler. The remaining elements in Figure 3.3 were used to facilitate the adjustment of the window of the TSCA. This window was set to allow all the pulses from the detector which were greater than or equal to the pulses from the elastically scattered protons to be scaled.

During the early runs only one Ge(Li) detector was used. The electronics during these runs were the same as those described above with the exception that the pulser was not used during the time the data was being taken.

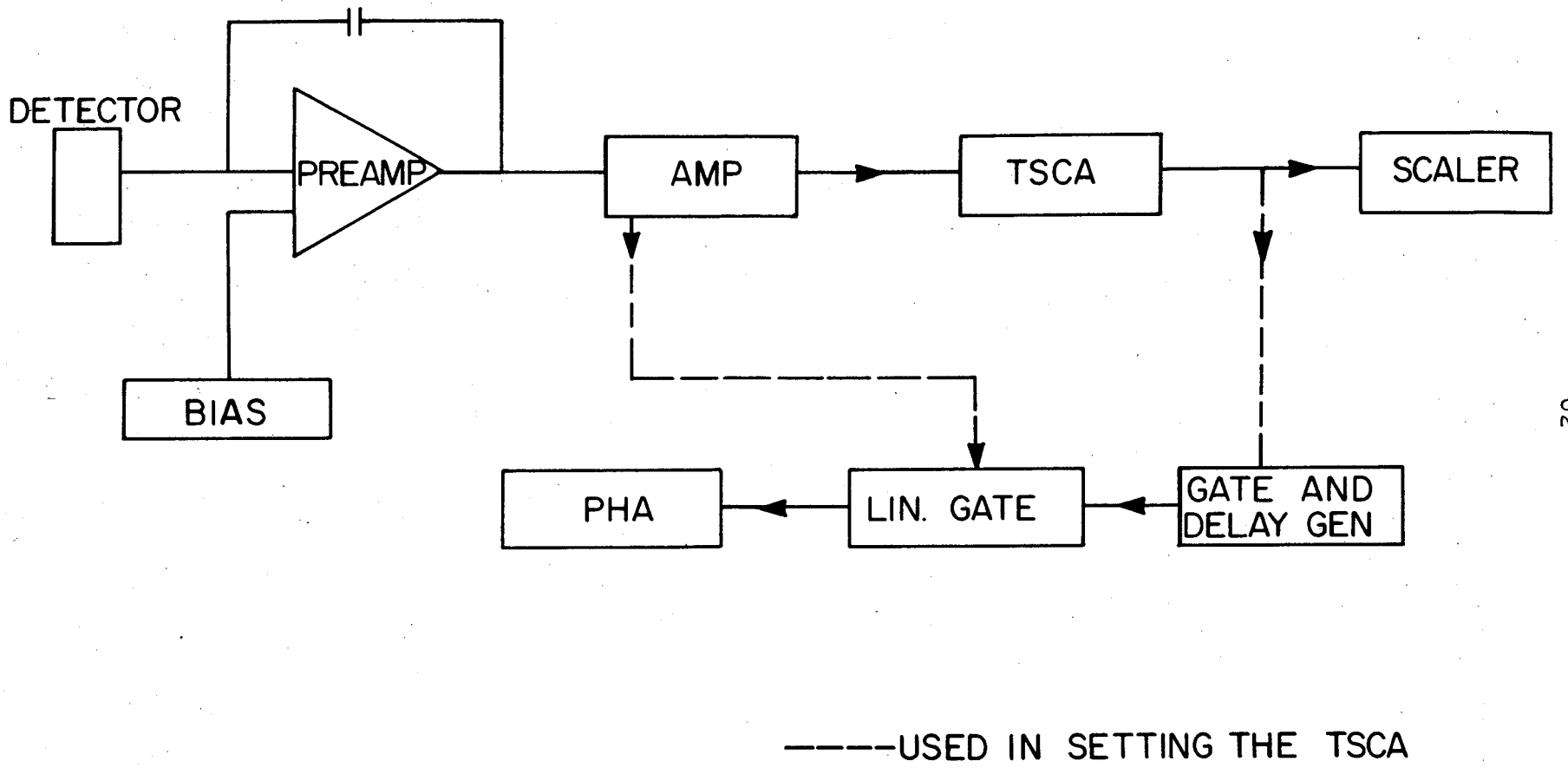

3.3 Block diagram of the electronics used with the monitor counter.

3.4 Data Acquisition

Before the actual data retrieval was begun the electronics were tested with the pulser. The pulses were analyzed in the ND-160 and a measurement of the noise characteristics of the electronic circuits was obtained. A typical value for the full width at half the maximum height of the peak, FWHM, was 6 keV.

The typical times required to obtain the necessary statistics in a spectrum was from 45 minutes to two hours depending upon experimental parameters such as beam current and detector angles. The beam current was limited by analyzer dead time. In order to minimize pile up effects, it was necessary to keep the dead times below about 5%. Following this criterion, beam currents were increased to 400 nA as the detectors were moved to larger angles and the counting rates decreased.

The angular distributions of the nickel isotopes were taken in 5° intervals from about 15° to 90° in the laboratory. The automatic angle increment feature of the goniometer was used during the experiment to increase the angle in the necessary 5° steps. When an angular distribution was finished, the completed target was removed from the target chamber and the new target inserted by use of the target transfer lock. This allowed the target transfer to be completed in about 5 minutes due to the fact that the vacuum in the target chamber was not broken.

The experiment also had to be stopped about every 10 hours to fill the dewar for the Ge(Li) detectors with LN_2. During the experiment it was also necessary to retake a few of the data points due to serious gain shifts in the electronics.

When a run was completed, the data contained in the ND-160 analyzer was dumped into the memory of the Sigma-7 computer and then punched onto computer cards. While accumulating data for the next angle the cards for the previous run were plotted and listed using a Calcomp plotting program written by P. J. Plauger. These plots were then examined for any indication of a new problem which might have arisen.

Representative spectra, one for each of the nickel isotopes, are shown in Figures 3.4-3.7. The resolution obtained in this experiment ranged from 45 keV to 85 keV FWHM. The worst resolutions occurred for the runs with high incident beam currents.

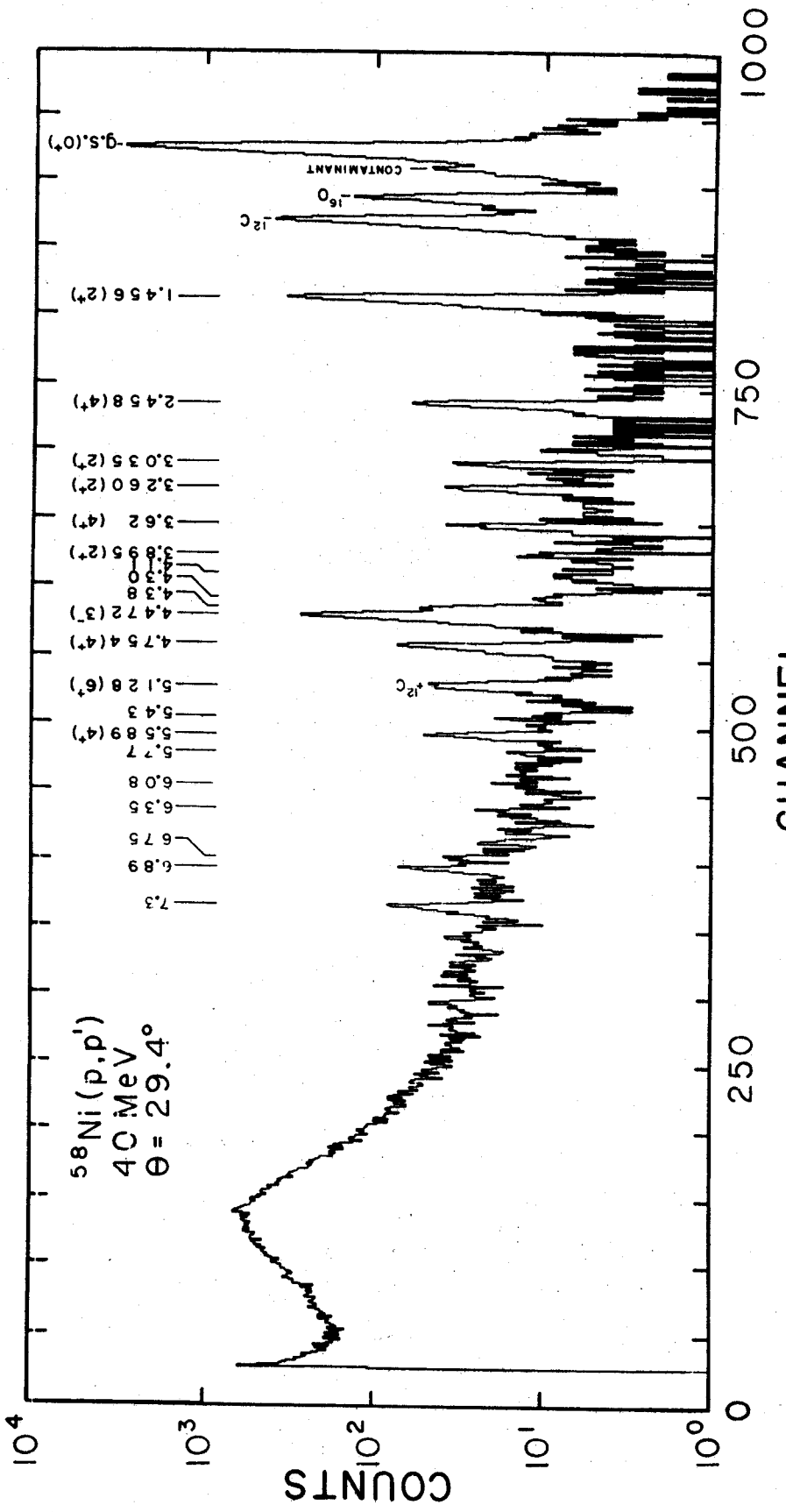

3.4 ^{58}Ni(p,p')^{58}Ni spectrum at θ_{LAB} = 29.4° for Ep = 40 MeV.

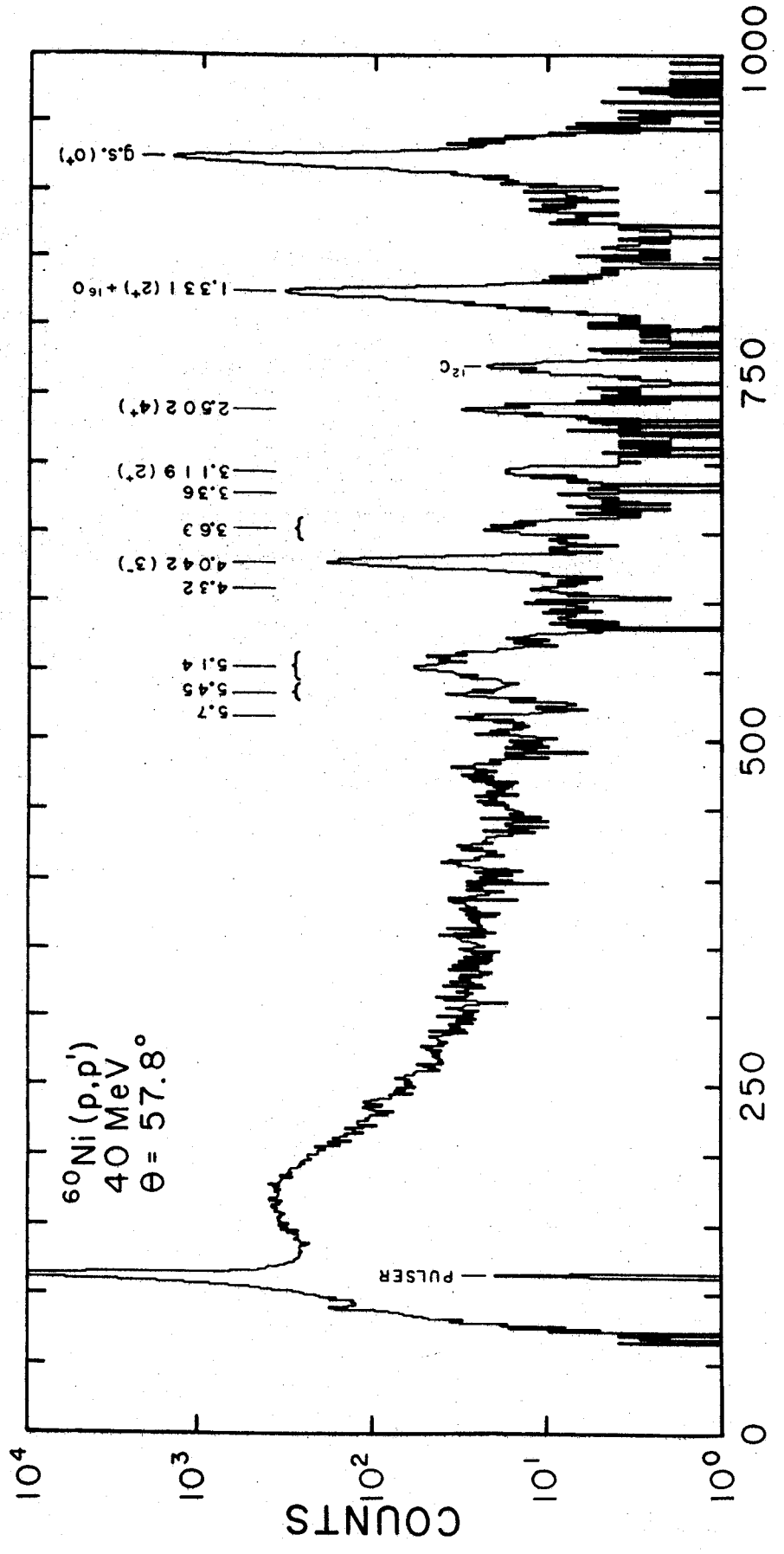

3.5 ^{60}Ni(p,p')^{60}Ni spectrum at θ_{LAB} = 57.8° for Ep = 40 MeV.

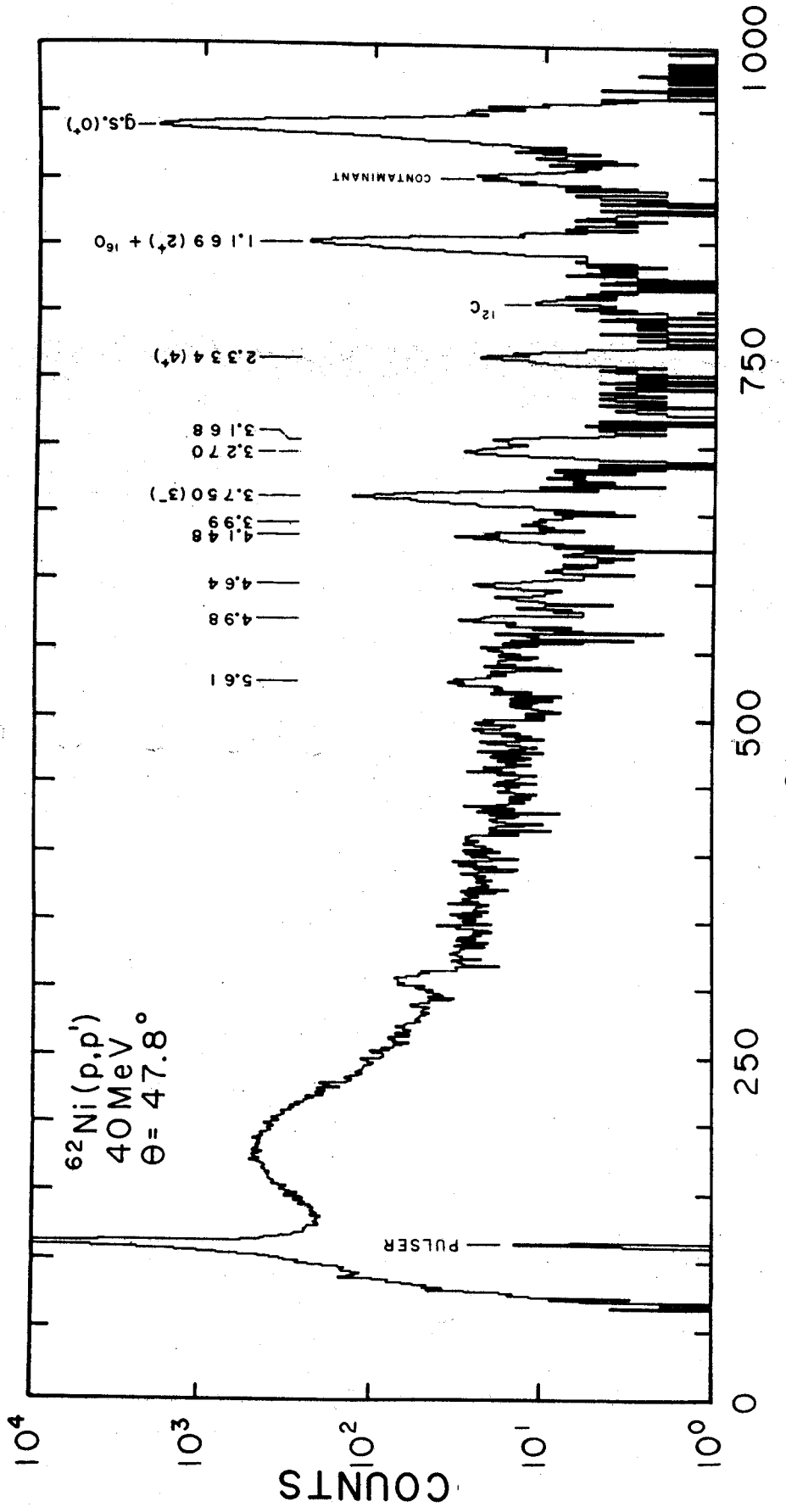

3.6 ^{62}Ni(p,p')^{62}Ni spectrum at θ_{LAB} = 47.8° for Ep = 40 MeV.

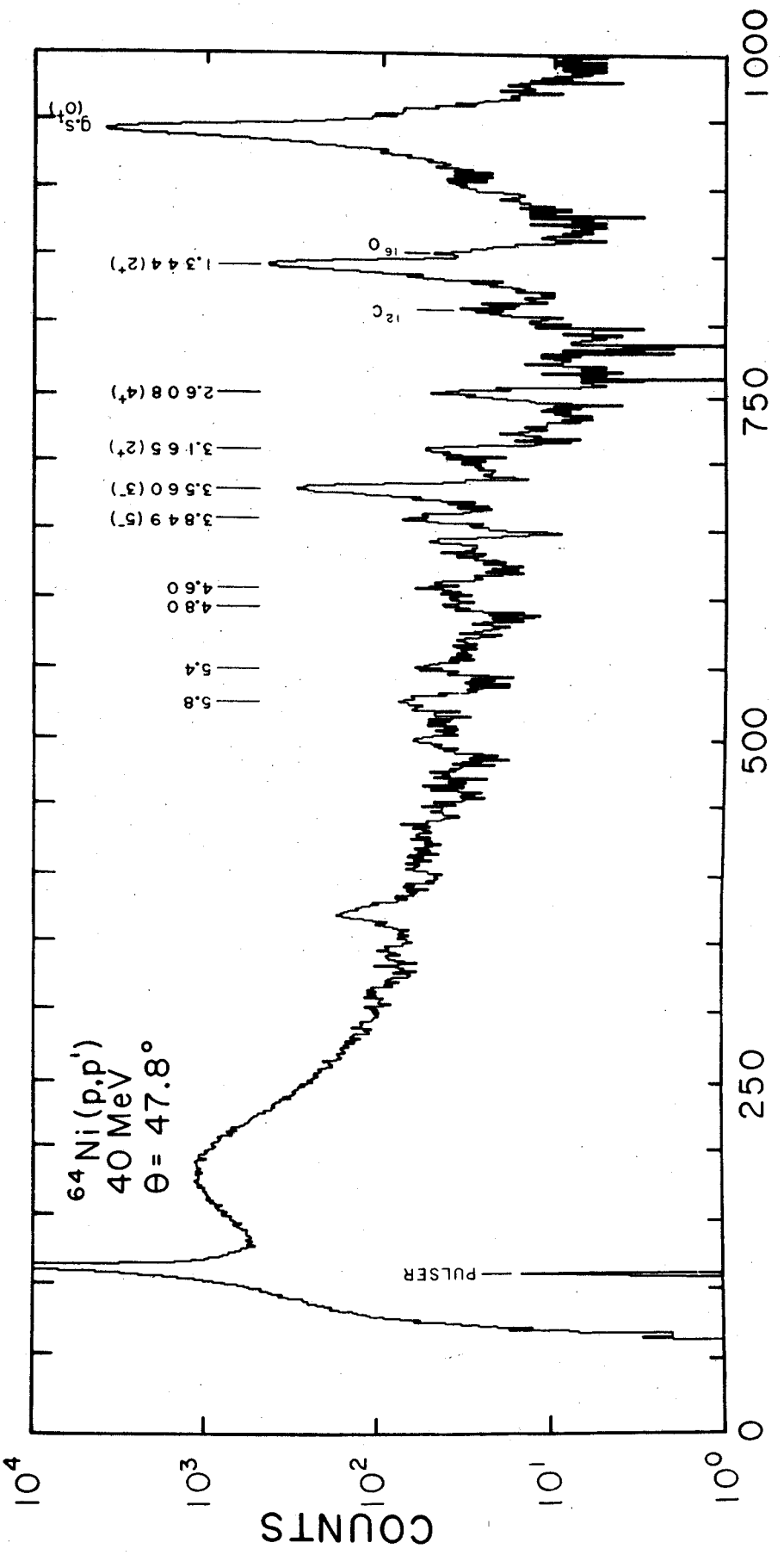

3.7 ^{64}Ni(p,p')^{64}Ni spectrum at θ_{LAB} = 47.8° for Ep = 40 MeV.

CHAPTER IV

DATA ANALYSIS

4.1 Experimental Analysis

Only relative cross sections were obtained in this experiment. To obtain the absolute cross sections, the elastic angular distributions of this experiment were normalized to the results of elastic scattering studies done by M. Fricke (Fr 67a) on ^{58}Ni and ^{60}Ni.

A monitor counter was used to provide the relative normalizations of the runs. This counter, setting at a fixed scattering angle during the entire experiment, monitored the product of charge and target thickness. The existence of this monitor counter eliminated the need to know the exact areal densities of the targets, the exact target angle, and the precise total charge incident on the target.

There are, however, various quantities which did affect the relative results between two data points. First of all, the fact that a multiple counter setup was used requires one to know the relative solid angles of the detectors. It was also observed that there was a need for dead time corrections in those few runs which had unusually large data rates.

4.1.a Computer Programs Used

4.1.a.1. PEAKSTRIP by R. A. Paddock

This program was used to obtain the centroid, the net area, and the statistical error in the area for the peaks in the spectrum. The input required for this program consisted of two boundary channel numbers for each peak along with the background at each of these channels and the identifying number associated with the peak. An option of this program allowed one to choose what fraction of the peak to be used in finding the centroid.

The background used for each channel contained in a peak is the result of the fit of a linear curve between the background given at each boundary channel. The fractional standard error for the net area of each peak is defined by the formula,

$$\Delta N = \frac{(N + 2B)^{1/2}}{N} \qquad 4.1$$

where N is the net yield and B is the total background under the peak.

4.1.a.2 RELTOMON by R. A. Paddock

The input to this program was the output of PEAKSTRIP plus information concerning the reaction involved, the laboratory scattering angle, the monitor counts, and the dead time associated with the spectra. This program calculated the center-of-mass cross section for each peak

at each angle using the monitor counts for the normalization and making allowances for the dead time.

The output of this program was separated into sections, one section for each peak number used. The output for each peak contained the laboratory and center-of-mass scattering angle and cross section.

There was an option in this program which was used during this analysis. This made it possible to multiply the angular distribution obtained for each state by a constant normalization factor. This factor was used to convert the relative angular distributions into absolute distributions.

4.1.a.3. FOILTARCAL by R. A. Paddock

This program was used to determine the excitation energies of various peaks. The input used was the output of PEAKSTRIP plus information concerning the target composition and orientation, the reaction involved, and the detector angle for each spectra.

A further piece of input required for FOILTARCAL was a set of energies for reference peaks (standards). The program used these standards to find a calibration curve of selected order which was then used to determine the excitation energies of the unknown peaks. The effects of target thickness and relativistic kinematics were accounted for in these calculations

4.1.a.4 SIGTOTE

This program was written to extract the deformation parameters, β_L, from the experimental angular distributions obtained for each state. It required as input the experimental and theoretical angular distributions along with identifying numbers which indicated which theoretical distribution was to be compared with the experimental distribution.

All of the data points of a state which occurred at the same angle were combined into one point using a weighted average. The theoretical data was then interpolated to the same angles at which the experimental points occurred using a 6-point Lagrange interpolation. The resulting theoretical distribution and the experimental data were integrated according to the equation,

$$\sigma_{int} = \sum_{i=1}^{N} \sigma(\theta_i) \sin \theta_i \Delta\theta_i \qquad 4.2$$

where $\Delta\theta_i$ is an angular region defined by the equation,

$$\Delta\theta_i = (\theta_{i+1} - \theta_{i-1})/2$$

For the end points in the distributions the angular region was terminated at θ_i.

The ratio of the experimental to the theoretical integrated cross section was found for each state. The

square root of this number resulted in the deformation parameter for the state

An error was calculated for each β^2 resulting from the errors which were input with the experimental distribution only. These input errors produced an uncertainty in the integrated cross section which was calculated using standard propagation techniques (Be 62). This resulting error in β^2 was added in quadrature to an input systematic error due to normalization uncertainties. This resulted in a total uncertainty for β^2.

4.1.b. Lab Angle Calibration

The angular position of Det. #1 relative to the beam direction was defined during the experiment to coincide with the position of the main arm as indicated by the digital readout. The position of Det. #2 relative to Det. #1 was found by sighting the center of one of the detector caps with a transit. The main arm was then rotated until the second cap was aligned in the scope. The relative angle was found to be 20.1°.

The laboratory angles obtained for the detectors during the experiment relative to the beam direction were only approximate. To obtain a better determination for these angles for each detector, measurements were obtained for the cross-over (Ba 64) of the ground states of the carbon and oxygen impurities with some of the more isolated excited states of the nickel isotopes.

The experimental cross-over point was obtained in each case by plotting the centroids of the nickel and contaminant peaks versus the laboratory angle as measured by the goniometer. The centroids used were those determined by the computer program, PEAKSTRIP. The theoretical cross-over angles were determined from calculations of the relativistic kinematics of each target nucleus with the program KINE written by P. J. Plauger. These calculations were done every 0.01°. This allowed the accurate determination of the point at which the apparent excitation energies for the peaks were equal.

Since the kinematics calculations were done every 0.01°, the cross-over points could be determined better than 0.01° for a given incident beam energy. The effect of the uncertainty of ±100 keV in the incident energy was found to be about ±0.07° in the cross-over point.

The errors in the experimental results that were considered included the uncertainties in the shapes of the curves drawn between the points on the centroid vs. lab angle plots and the errors in the centroids themselves.

The total error in each measurement amounted to about 0.3°. There were a number of measurements, however, of the angular correction needed for each of the three detector setups. The resulting standard errors, therefore, in the results ranged from ±0.1° to ±0.2°.

4.1.c Elastic Cross Sections

The absolute cross sections for the experiment were obtained through the normalization to the elastic proton angular distributions on ^{58}Ni and ^{60}Ni obtained by M. Fricke (Fr 67a). Each elastic peak was analyzed by choosing the boundary channels such that the yield at each channel relative to the maximum peak height was consistent with the corresponding results obtained for the other spectra. These tests of consistency were made only between spectra for the same target taken with the same detector setup.

There were several peaks, however, for which one of the boundary channels could not be set at the consistent location as a result of poor peak-shapes caused by pileup or close lying contaminant peaks. In these cases corrections were made in the net areas and estimates of the errors in these corrections were added in quadrature to the statistical errors. There were also uncertainties in the location of the "consistent" channel which produced an uncertainty in the net peak area. These errors were added in quadrature to the errors from above giving a total relative error for the net area of each elastic peak.

4.1.d. Normalization of the Data to Obtain Absolute Cross Sections

4.1.d.1. Dead Time

The average dead time occurring for each spectrum during the later stages of the experiment was found by using the net area of the pulser peak. This peak was generally superimposed onto a smooth background and was easily integrated to obtain the net area. The area of the peak was then divided by the total number of pulses presented to the analyzer as indicated by the scaler (section 3.3). The dead times for these spectra had a mean of 4.2% and a standard deviation of 3.6%.

The spectra obtained in the earlier runs did not contain the pulser peak with which to determine the dead time. Instead the dead time meter on the analyzer was used. These runs were taken with beam currents of approximately 30 nA and with dead times less than 2%.

4.1.d.2 Ratios of the Monitor Counts to the Integrated Current

For each spectrum taken there was a value obtained for both the monitor counts and the total integrated current. The ratio of the monitor to the integrator was calculated for each case. This ratio varied with target angle and with the target used.

The data obtained for ^{58}Ni was taken during two separate times and the ratio was not expected to be the

same. They were, in fact, different, but the values obtained in each set had a fairly constant value shown by the fact that the measurements had a standard deviation of less than 4.0%.

For ^{60}Ni the data was taken at one time, but the target angle was changed after eight data points had been taken. The ratios obtained for the runs after this change had a standard deviation of less than 3%, but the runs before the change had a standard deviation of more than 13%.

The spectra obtained for both ^{62}Ni and ^{64}Ni were taken during the same three-day run, and the target angle was not changed. The standard deviations of the ratios for these targets were 2.9% and 5.1% respectively.

4.1.d.3 Method of Normalization

For ^{60}Ni, ^{62}Ni, and ^{64}Ni, there were two sections of the angular distributions which had to be multiplied by an independent constant factor in order to obtain the absolute cross sections. In each of these distributions, however, there were angles which had been measured by both detectors. By adjusting the relative normalizations of the two parts of each distribution, all of the repeated points were made to simultaneously overlap.

For ^{58}Ni there were no repeated data points and the elastic angular distribution for ^{58}Ni, obtained by Fricke (Fr 67a), was used to find the relative normalization of the two detectors use in the latter run. All of the

resulting factors were averaged to give the relative solid angles for Det. #1 and Det. #2 of,

$$\Delta\Omega_1/\Delta\Omega_2 = 1.08 \pm 0.04 \qquad 4.3$$

The elastic angular distributions obtained in this experiment for ^{58}Ni and ^{60}Ni were normalized to those obtained by Fricke who had estimated absolute errors of from 5% to 9% for the majority of points between 0° and 90°. To obtain an absolute normalization for the ^{62}Ni and ^{64}Ni data, however, the elastic distributions obtained in this experiment by Det. #1 were normalized to the ^{60}Ni elastic distribution of Fricke in the forward angle region between 10° and 20°. Since this region of the distribution is effected predominantly by Rutherford scattering and the mass dependence is small, the results for the different nickel isotopes are expected to be the same. The standard errors for all of these factors were estimated using the total relative errors from this experiment as a guide. Using the factor obtained from Det. #1 in each case and the relation 4.3 the absolute normalizations for the ^{62}Ni and ^{64}Ni data were found.

4.1.d.4 Corrections

During the analysis of the inelastic peaks it was found that the data at a few particular angles in ^{60}Ni, ^{62}Ni, and ^{64}Ni consistently had an improper normalization

relative to the neighboring angles. These discrepancies were attributed to dead time effects and a faulty monitor counter.

It was noted above (section 1.d.2) that the early runs taken for ^{60}Ni had a 13% standard deviation in the values found for the ratios of the monitor counts to the integrated current. A calculation of the expected ratio in these earlier runs was done by using the mean ratio found in the runs taken after the target angle was changed and correcting for the variation. The results showed that the two ratios corresponding to those data points which had a consistently bad normalization differed from the expected value by 23% and 45%. These problems could have been caused by shifts in the monitor electronics during these initial runs. Considering these large discrepancies, it was concluded that the relative normalizations were faulty for these two cases, and the integrated current was used to give the normalization.

There were several spectra in this experiment which had dead times more than one standard deviation from the mean. The corresponding states also were consistently low relative to nearby points in the angular distributions. As a result of these findings it was necessary to make corrections in the results of those spectra.

To estimate the correction factor the results of ^{60}Ni were examined. The results for the 1.33 MeV, 2^+, and 4.04 MeV, 3^-, states obtained by Fricke (Fr 67a) were used as

references. The angular distributions obtained in this experiment were compared with Fricke's results. The points corresponding to those angles with a high dead time were raised in order to be consistent with the Fricke distributions. The correction factor that was required was found to be relatively constant for all points which were taken with high dead times. In addition to this, the high dead time runs were examined for the other targets and the factors which would give smooth results were estimated.

The final correction factor used was an average of the results obtained in the above comparisons with the ^{60}Ni results carrying the largest weight. This averaged factor was then used for all spectra for which the dead time was larger than 8.5%.

An error in this factor was estimated taking into account the errors in the angular distributions that were compared. This error and an estimated error for the monitor correction above were then added in quadrature to all the data points in each of the corrected spectra resulting in total relative errors.

4.1.d.5 Final Results

After the above corrections were made in the monitor counts and in the total relative errors, the final normalization constants were determined for all of the detectors used and for all of the target nuclei. These factors along with the final elastic peak information were then

put into the program RELTOMON which provided an output of the absolute angular distribution along with the total relative errors associated with each point.

The systematic errors in this data were the results of the errors in the constants of normalization of the present data with Fricke's. This error was estimated graphically and added in quadrature to the total relative errors of the data whenever total errors were required.

4.1.e. Inelastic Angular Distributions

After the elastic peaks had been analyzed, the net areas and statistical errors were determined by the program PEAKSTRIP (section 4.1.a.) for each of the inelastic peaks of the nickel isotopes as well as the contaminant peaks. The centroids of these peaks were determined by using the upper 2/3 of the peak. During this analysis special care was taken to provide consistent peak boundaries and consistent backgrounds for each peak considered.

The carbon and oxygen contaminants were removed whereever possible. A laboratory angular distribution was constructed for both oxygen and carbon using only clearly separated peaks and plotting the net counts divided by the associated monitor count. This distribution was then used to estimate the net area of the contaminate located under a nickel peak. This area was subtracted from the net peak area output from PEAKSTRIP and was added to the

background yield, B, in equation 4.1 giving a new statistical error in the net area of the peak.

There were also several multiplet peaks. These multiplets were separated by using a graphical technique of comparing peak shapes. Here again the errors were accounted for in a consistent manner.

The net areas and the statistical errors for each of the peaks along with the monitor counts and the normalization factors were input into the program RELTOMON treating each detector independently. The final results of this analysis were compiled into four decks, one for each target nucleus. These decks were then used in all succeeding calculations. The angular distributions for all of the analyzed states are tabulated in Appendix IV.

4.1.f Excitation Energies

The excitation energies for the states of the nickel isotopes have been determined to ±7 keV by Tee and Aspinall (Te 67) using inelastic proton scattering at 11 MeV. There are states excited in the present experiment, however, which lie in regions of many states. It is necessary, therefore, to determine the excitation energies of those particular states which were excited in this experiment.

In each of the target nuclei there exist two strongly excited states, the first 2^+ state and the first 3^- state. The energies and the centroids of these two states along with the ground state were used as reference

points with a linear calibration curve in the program FOILTARCAL (section 4.1.a.3) to obtain estimates of the excitation energies of the remaining states. The centroids used as input to this program were found in PEAKSTRIP using only the top 2/3 of the peak. These estimates were then compared to the previously determined excitation energies (Te 67). When the estimate was within 15-20 keV of a known state which is separated from its neighboring states by 50-100 keV, the corresponding peak for this experiment was assigned the known energy and added to the list of standard peaks.

The final group of standard peaks was used in FOIL-TRACAL to determine a cubic energy calibration curve and consequently the excitation energies of the unknown states independently for each spectrum. Precautions were taken not to include as a standard any peak which was contaminated by carbon or oxygen. The resulting excitation energies for each unknown peak were then averaged making sure to remove any contaminated or otherwise questionable peaks. These mean energies along with the standard deviations are given in Tables 4.1-4.4. Also presented here are the standard energies which were assigned to peaks observed in this experiment along with the excitation energies determined by Tee and Aspinall. The latter states are listed only up to an energy where the density of states becomes

TABLE 4.1.--Excitation energies for ^{58}Ni.

Ex(MeV) ± 7 keV Te 67	Ex(MeV) Present Data	Ex(MeV) ± 7 keV Te 67	Ex(MeV) Present Data
1.456	1.456*	4.517	
2.458	2.458*	4.538	
2.773		4.578	
2.900		4.754	4.754*
2.940		4.920	
3.035	3.035*	4.965	
3.260	3.260*	5.063	
3.414		5.089	
3.524		5.128	5.128*
3.588		5.165	
3.615	3.62±0.01	5.171	
3.773		5.383	
3.895	3.895*	5.434	5.43±0.01
4.103	4.11±0.02	5.460	
4.290	4.30±0.03	5.475	
4.343		5.506	
4.349		5.589	5.589*
4.380	4.38±0.01	5.706	
4.401		.	5.77±0.02
4.443		.	6.08±0.04
4.472	4.472*	.	6.35±0.08
			6.75±0.02
			6.98±0.08
			7.3 ±0.1

*This state was used to determine the calibration curve in each spectrum.

Note: The highly excited states of Te 67 are not shown since the higher states observed in this experiment cannot be uniquely identified with any single state in this reference.

TABLE 4.2.--Excitation energies for ^{60}Ni.

Ex(MeV) ± 7 keV Te 67	Ex(MeV) Present Data	Ex(MeV) ± 7 keV Te 67	Ex(MeV) Present Data
1.331	1.331*	3.864	
2.156		3.891	
2.284		3.927	
2.502	2.502*	4.011	
2.621		4.021	
3.119	3.119*	4.042	4.042*
}3.187		4.082	
3.271		.	
3.316		.	4.32±0.02
3.390	3.36±0.02	.	}5.14±0.10
3.589			
3.619			}5.45±0.13
3.671	}3.69±0.02		
3.732			5.7 ±0.2

*This state was used to determine the calibration curve in each spectrum.

Note: The highly excited states of Te 67 are not shown since the higher states observed in this experiment cannot be uniquely identified with any single state in this reference.

TABLE 4.3 Excitation energies for ^{62}Ni.

Ex(meV) ± 7 keV Te 67	Ex(MeV) Present Data	Ex(MeV) ± 7 keV Te 67	Ex(MeV) Present Data
1.169	1.169*	3.464	
2.043		3.518	
2.244		3.750	3.750*
2.334	2.334*	3.844	
2.890		.	
3.050		.	3.99 ± 0.02
3.150		.	4.148 ± 0.009
3.168	3.168*		4.64 ± 0.02
3.249			4.98 ± 0.03
3.265	3.270 ± 0.009		5.61 ± 0.06
3.363			

*This state was used to determine the calibration curve in each spectrum.

Note: The highly excited states of Te 67 are not shown since the higher states observed in this experiment cannot be uniquely identified with any single state in this reference.

TABLE 4.4.--Excitation energies for ^{64}Ni.

Ex(MeV) ± 7 keV Te 67	Ex(MeV) Present Data	Ex(MeV) ± 7 keV Te 67	Ex(MeV) Present Data
1.344	1.344*	3.647	
2.275		}3.748	
(2.477)		3.795	
2.608	2.608*	3.808	
2.865		3.849	3.849*
}2.971		3.965	
3.028		.	
3.165	3.165*	.	4.60±0.06
3.273		.	4.80±0.04
3.393			5.4 ±0.2
3.459			5.8 ±0.2
3.483			
3.560	3.560*		

*This state was used to determine the calibration curve in each spectrum.

Note: The highly excited states of Te 67 are not shown since the higher states observed in this experiment cannot be uniquely identified with any single state in this reference.

too dense to be able to make a unique association between states observed in the two experiments.

4.2 Theoretical Analysis

4.2.a. DWBA Theory

The analysis of the data presented in this thesis employs the collective model, distorted wave theory. This theory is described in detail elsewhere (Ro 61) (Ba 62) (Sa 64). For the reactions presented here the distorted wave approximation has been shown to give satisfactory results (Fr 67c). Calculations using this theory were compared with the experimental results and values for the nuclear deformation, $\beta_L R_o$, were obtained for each state observed. The R_o here is the radius of the real well in the optical potential used in this experiment. Some of the basic relationships used in this theory for inelastic scattering are summarized in the following paragraphs.

A general form for inelastic scattering can be written as

$$A(a,a')A^* \qquad 4.4$$

The total Hamiltonian for this system with a projectile, a, and a target nucleus, A, is

$$H = H_\xi + T_o + U(r_o) + V(\underline{r}_o, \xi) \qquad 4.5$$

where

ξ designates the internal coordinates of the target and the projectile.

$\underline{r}_o$ designates the separation vector between the centers of mass of the projectile and the target.

T_o is the relative kinetic energy operator of the two colliding systems.

$U(r_o)$ is the central optical potential describing the elastic scattering.

$V(\underline{r}_o,\xi)$ is the interaction potential producing the inelastic scattering.

The eigenfunctions for this total Hamiltonian, ψ, are solutions of the Schröedinger equation

$$(E - H)\psi = 0 \qquad 4.6$$

The eigenfunctions, $v(\xi)$, of the Hamiltonian, H_ξ, representing the internal states of the target and possibly the projectile are solutions of the equation,

$$(E_n - H_\xi)v_n(\xi) = 0 \qquad 4.7$$

where the subscript, n, can represent either the initial, i, or final, f, states.

The solution of interest for equation 4.6 has an asymptotic form comprised of an incident plane wave and an outgoing spherical wave. This solution with Coulomb effects omitted can be written as

$$\psi^{(+)} \underset{(r\to\infty)}{\longrightarrow} v_i(\xi)e^{i\underline{k}_i \cdot \underline{r}_o} - \sum_f A_{if}\, v_f(\xi)\, (e^{ik_f r_o})/r_o$$

where the cross section for a particular final state in the target is

$$\frac{d\sigma}{d\Omega} = |A_{if}|^2$$

A transition amplitude can then be defined such that

$$|A_{if}|^2 = (\mu/2\pi\hbar^2)^2\, |t_{if}|^2$$

and the cross section for inelastic scattering can be written

$$\frac{d\sigma}{d\Omega} = \left(\frac{\mu}{2\pi\hbar^2}\right)^2 \frac{k_f}{k_i} \sum_{av} |t_{if}|^2 \qquad 4.8$$

The μ is the reduced mass of the system and $\sum_{av}$ designates the average over the spins of the initial states and sum over the spins of the final states.

The transition amplitude, t_{if}, can be represented by the equation,

$$t_{if} = \langle v_f(\xi)\, X_f^{(-)} | V(\underline{r}_o, \xi) | \psi^{(+)} \rangle$$

This is just the matrix element of the interaction potential which connects the total incident wave of the system

with that wave which represents the exit channel of interest. The function $X_f^{(-)}$ is the solution of the Schröedinger equation,

$$[-\nabla_f^2 + \frac{2\mu}{\hbar^2} U_f(r_o) - k_f^2] X_f^{(-)} = 0$$

which satisfies incoming spherical wave boundary conditions.

The total wave function for this system is intractable and, therefore, t_{if} cannot be calculated exactly. The Born approximation makes the assumption that

$$\psi^{(+)} \simeq v_i(\xi) X^{(+)} (\underline{k}_i, \underline{r}_o)$$

which gives,

$$t_{if} \simeq < v_f(\xi) X^{(-)} (\underline{k}_f, \underline{r}_o) | V(\underline{r}_o, \xi) | v_i(\xi) X^{(+)} (\underline{k}_i, \underline{r}_o) > \qquad 4.9$$

The form of $V(\underline{r}_o, \xi)$ is assumed to be central and can be expanded in multipoles as

$$V(\underline{r}_o, \xi) = \sum_{LM} g_L (r_o, \xi) Y_L^M (\hat{\xi}) Y_L^M (\hat{r}_o) \qquad 4.10$$

Each internal nuclear state has a well defined J and m; therefore

$$v_f(\xi) = v_{m_f}^{J_f}(\xi) \text{ and } v_i(\xi) = v_{m_i}^{J_i}(\xi)$$

Using the Wigner-Eckart Theorem (Ro 57) the integration over ξ gives

$$\int d\xi\, v_{m_f}^{J_f *}(\xi)\, g_L(\xi, r_o)\, Y_L^M(\hat{\xi})\, v_{m_i}^{J_i}(\xi) =$$

$$(J_i\ L\ m_i\ M \mid J_f m_f)\, F_L(r_o) \qquad 4.11$$

The cross section can then be written as

$$\frac{d\sigma}{d\Omega} = \left(\frac{\mu}{2\pi\hbar^2}\right)^2 \frac{k_f}{k_i} \frac{2J_f + 1}{2J_i + 1} \sum_{LM} \frac{|B_{LM}|^2}{(2L + 1)} \qquad 4.12$$

where

$$B_{LM} = \int d\underline{r}_o\, X_f^{(-)*}(\underline{k}_f, \underline{r}_o)\, F_L(r_o)\, Y_L^{M*}(r_o)\, X_i^{(+)}(\underline{k}_i, \underline{r}_o)$$

The $F_L(r_o)$ is a radial dependent factor which depends on the model used for the interacting systems.

In the collective model the excited states are attributed to excitations of deformations about a spherical shape. It is assumed, then, that the deformed nucleus has a deformed optical potential associated with it. The total interaction representing the inelastic scattering can be written in the form

$$U_T = U(r - R(\theta')) \qquad 4.13$$

where θ' are coordinates in the body fixed system.

The radius of a deformed nucleus can be written in a multipole expansion,

$$R(\theta') = R_o[1 + \sum_L \beta_L Y_L^o(\theta')] \qquad 4.14$$

if axial symmetry is assumed. The total potential can be expanded in a Taylor series about the spherical shape, $R = R_o$,

$$U_T(r-R) = U(r-R_o) + \Delta R \frac{\partial U}{\partial R}\Big|_{R=R_o} + \frac{1}{2}(\Delta R)^2 \frac{\partial^2 U}{\partial R}\Big|_{R=R_o} \cdots \qquad 4.15$$

where

$$\Delta R = (R - R_o) = R_o \sum_L \beta_L Y_L^o(\theta')$$

The first term in equation 4.15 is the spherical optical potential and describes to first order the elastic scattering. The second term describes to first order the inelastic events. The usual approximation is that the interaction potential of equation 4.5 can be equated to the second term of equation 4.15 giving

$$V(\underline{r}_o, \xi) = -\sum_L R_o \beta_L \frac{\partial U}{\partial r}(r-R_o) Y_L^o(\theta') \qquad 4.16$$

This relation is then transformed from the body fixed system to one that is space fixed by a spherical harmonic addition theorem (Ro 57)

$$Y_L^o(\theta', 0) = (4\pi/(2L+1))^{\frac{1}{2}} \sum_M Y_L^{M*}(\hat{r})\, Y_L^M(\hat{\xi})$$

where $\hat{\xi}$ is the relative angle of the body and space fixed axes, and equation 4.16 becomes

$$V(\underline{r}_o,\xi) = -\sum_L R_o\, \beta_L \frac{\partial U}{\partial r}(r-R_o)\left(\frac{4\pi}{2L+1}\right)^{\frac{1}{2}} \sum_M Y_L^{M*}(\hat{r}_o) Y_L^M(\hat{\xi})$$

This is compared to equation 4.10 for $V(\underline{r}_o,\xi)$ to find an expression for $g_L(r_o,\xi)$ in equation 4.11. For even-even nuclei experiencing a rotational collective motion the nuclear wave functions can be written,

$$v_i(\xi) = Y_o^o(\hat{\xi})\phi_{\text{intrinsic}}$$

$$v_f(\xi) = Y_{J_f}^{M_f}(\hat{\xi})\phi_{\text{intrinsic}}$$

where $\phi_{\text{intrinsic}}$ are parts of the wave function which remain unchanged in a rotational excitation. The angle $\hat{\xi}$ represents the nuclear collective coordinates which are relevant. Using these wave functions along with the $g_L(r_o,\xi)$ found above and the fact that $J_i = 0$ and $m_i = 0$ for an even-even nucleus the form factor (equation 4.11) becomes

$$F_L(r) = -\left(\frac{4\pi}{2L+1}\right)^{\frac{1}{2}} \beta_L R_o \frac{\partial U}{\partial r} \int Y^{M_f *}_{J_f}(\hat{\xi})\, Y^{M}_{L}(\hat{\xi})\, Y^{o}_{o}(\hat{\xi})\, d\xi$$

$$= -(2L+1)^{-\frac{1}{2}} \beta_L R_o \frac{\partial U}{\partial r}\, \delta_{J_f L}\, \delta_{M_f M} \qquad 4.17$$

This form factor is then used in equation 4.12 to determine B_{LM} which is used in turn to give the calculated cross section for inelastic scattering. Then by normalizing these angular distributions to the data, the nuclear deformation, $\beta_L R_o$, can be extracted.

4.2.b. Vibrational Model Parameters and Reduced Transition Probabilities

The spectra of the even nickel isotopes have characteristics of vibrational nuclei (section 5.1). The formal results in the collective, distorted wave calculations for a vibrational model are the same as those shown above for the rotational model. The difference between these two approaches is that for the vibrational case, the nuclear deformation is dynamic in the space fixed coordinate system.

The nuclear deformations for the vibrational model are evaluated from the experimental results in exactly the same fashion as for the rotational case. The vibrational model, however, relates the nuclear deformation, $\delta_L = \beta_L R_o$, to the quantities, D_L and C_L, which appear in

the Hamiltonian describing a system with small oscillations

$$H = H_o + \sum_{LM} H_{LM}$$

where

H_o is the Hamiltonian which describes the static nucleus

and

H_{LM} is the Hamiltonian of the deformation with angular momentum, L, and projection, M.

In terms of generalized coordinates,

$$H_{LM} = \frac{1}{2} D_L \left| \dot{\alpha}_{LM} \right|^2 + \frac{1}{2} C_L \left| \alpha_{LM} \right|^2 + \cdots$$

The D_L is defined as the mass transport parameter and C_L the surface tension parameter. These are related to the excitation energy, $E_L = \hbar\omega_L$, by the relation (La 60)

$$E_L = \hbar (C_L/D_L)^{\frac{1}{2}} \qquad 4.18$$

and to β_L by (Ba 62)

$$\beta_L^2 = (2L + 1)\, \hbar\omega_L / 2C_L$$

or

$$\beta_L^2 = (2L + 1)/2(C_L\, D_L/\hbar^2)^{\frac{1}{2}} \qquad 4.19$$

In the comparisons of experimental results it is more meaningful to compare the nuclear deformations, $\delta_L = \beta_L R_o$, rather than the β_L alone (Bl 63). As a result of this the reduced transition probabilities and the vibrational parameters were derived in terms of the δ_L's or δ_L/R_o where R_o is an interaction radius, $R_o = r_o A^{1/3}$.

The surface tension and mass transport parameter are found from equations 4.18 and 4.19

$$C_L = \frac{(2L + 1)}{2} \frac{R_o^2}{\delta_L^2} E_L \qquad 4.20$$

$$\frac{D_L}{\hbar^2} = \frac{(2L + 1)}{2} \frac{R_o^2}{\delta_L^2} \frac{1}{E_L} \qquad 4.21$$

The reduced transition probability is given by the equation (La 60),

$$B(EL;\ L\to 0) = \left(\frac{Ze(2L + 1) \langle r^{2L-2} \rangle}{4\pi\ R_o^{L-2}}\right)^2 \frac{1}{2(D_L C_L/\hbar^2)^{\frac{1}{2}}} \qquad 4.22$$

Using the fact that $B(EL;\ 0\to L) = (2L + 1)B(EL;\ L\to 0)$(Al 56), and using δ_L and the relation 4.19, equation 4.22 can be rewritten

$$B(EL;\ 0\to L) = \left(\frac{Ze(2L + 1) \langle r^{2L-2} \rangle}{4\pi\ R_o^{L-2}}\right)^2 \frac{\delta_L^2}{R_o^2} \qquad 4.23$$

where (La 60) it has been assumed that the matrix element $\langle r^L \rangle$ is given approximately by:

$$\langle r^L \rangle = \int r^L \rho(r) d\underline{r} / \int \rho(r) d\underline{r} \qquad 4.24$$

where $\rho(r)$ is the charge density distribution. The single particle estimate for the reduced transition probability is defined as (La 60),

$$B_{SP}(EL;\ 0 \rightarrow L) = \frac{(2L+1)}{4\pi} e^2 \langle f | r^L | i \rangle^2$$

but can be estimated by the relation,

$$B_{SP}\ (EL;\ 0 \rightarrow L) = \frac{(2L+1)}{4\pi} e^2 \langle r^L \rangle^2 \qquad 4.25$$

The ratio, G, of the results of equations 4.22 and 4.25 is the reduced transition probability expressed in terms of single particle, Weisskopf units,

$$G = B(EL;\ 0 \rightarrow L) \ /\ B_{SP}\ (EL;\ 0 \rightarrow L)$$

4.2.c Sum Rules

The non-energy-weighted sum rule, NEWSR (La 60), is based on the shell model. This rule gives the maximum value of the sum of the reduced transition probabilities for transitions from the ground state of an even-even nuclei to n states with the spin, L, is given by

$$\sum_n B_n(EL;\ 0 \rightarrow L) = \frac{e^2 Z}{4\pi} \langle r^{2L} \rangle \qquad 4.26$$

A second sum rule is an energy-weighted sum rule,

EWSR, for transitions to states with T = 0. It is (Na 65)

$$\sum_n (E_n - E_o)\, B(EL;\, L\to 0) = \frac{Ze^2\, L\, \hbar^2\, (2L+1)^2}{8\pi\, AM} \langle r^{2L-2} \rangle \qquad 4.27$$

This sum rule is independent of any model of nuclear structure except that it assumes a velocity independent Hamiltonian. It also depends on the charge distribution in the ground state through the quantity $\langle r^{2L-2} \rangle$, but this distribution can be found from electron scattering data (El 61).

The expression 4.27 can be rewritten in terms of the hydrodynamic limit for the mass transport, $(D_L)_{HYD}$ (La 60). $(D_L)_{HYD}$ is written as

$$(D_L)_{HYD} = \frac{2L+1}{L} \frac{AM}{4\pi} \frac{\langle r^{2L-2} \rangle}{R_o^{2L-4}} \qquad 4.28$$

where AM is the total nuclear mass. Using equations 4.28, 4.23, and 4.21 the EWSR can be expressed as

$$\sum_n \frac{(D_L)_{HYD}}{(D_L)_n} = 1 \qquad 4.29$$

4.2.d. Optical Model Parameters

In order to perform the DWBA calculations, the optical potential had to be defined for each target nucleus. The parameters of the potentials used in this analysis were derived from work of Fricke et al. (Fr 67b) who did

elastic polarization studies for eleven targets throughout the periodic table. The optical potential used in this work was of the form

$$V(r) = V_c(r) - V_o f(x) - i(W_o - 4W_D \frac{d}{dx'}) f(x')$$

$$+ (\hbar/m_\pi c)^2 V_s (\frac{1}{r} \frac{d}{dr}) f(x_s) \underline{\sigma} \cdot \underline{\ell}$$

where $V_c(r)$ is the Coulomb potential for a uniformly charged sphere of radius $1.25A^{1/3}$. Also, $f(x) = (e^x+1)^{-1}$ and $x = (r - R_o)/a$. In this study the potential parameters were found for ^{58}Ni and ^{60}Ni, but of more importance a set of average parameters was found for all of the targets. These average parameters are listed in Table 4.5.

TABLE 4.5.--Average optical potential parameters used.

$r_o = 1.16F$	$a = 0.75F$
$r_o' = 1.37F$	$a' = 0.63F$
$r_s' = 1.064F$	$a_s = 0.738F$
$V_s = 6.04$ MeV	

It was concluded in this study that these fixed parameters provide a reasonable optical-model description for elastic scattering and polarization of protons at 40 MeV. As a result of this work, therefore, the average parameters were

used in the present experiment for ^{62}Ni and ^{64}Ni. In addition the values of those remaining parameters found by Fricke et al. for ^{58}Ni and ^{60}Ni were used.

The remaining parameters needed in the present analysis were the potential strengths for ^{62}Ni and ^{64}Ni. To obtain a set of starting parameters, an extrapolation of the form $V_o = K_1 + K_2 (N - Z)/A$ from the ^{58}Ni and ^{60}Ni values was performed for each potential strength (Fr 67b). An optical model parameter search code, GIBELUMP, was used to search on the parameters and obtain fits to the elastic angular distributions. The criterion used to determine the necessary variation of a parameter was the minimization of the quantity X^2 where

$$X^2 = \sum_{i=1}^{N} [(\sigma_{TH}(\theta_i) - \sigma_{EX}(\theta_i))/\Delta\sigma_{EX}(\theta_i)]^2$$

where N is the number of data points, $\sigma_{TH}(\theta_i)$ is the calculated value of the cross section of angle θ_i, $\sigma_{EX}(\theta_i)$ is the experimental value at that angle and $\Delta\sigma_{EX}(\theta_i)$ is its standard error.

The parameters searched on were V_o and W_D. Since changes in W_o and W_D produce about the same effects on the resulting angular distributions, only one needed to be varied. The optical potential depth parameters which were determined in the study by Fricke et al. for ^{58}Ni, ^{60}Ni and those found in this work for ^{62}Ni and ^{64}Ni are

listed in Table 4.6 along with the resulting X^2/N.

TABLE 4.6.--Optical potential strength parameters used.

Target	V_o(MeV)	W_o(MeV)	W_D(MeV)	X^2/N^b	X^2/N^c
$^{58}Ni^a$	45.05	6.63	1.22	3.6	
$^{60}Ni^a$	45.74	5.47	2.50	5.6	
^{62}Ni	44.86	4.38	3.13	2.2	4.8
^{64}Ni	45.25	3.37	3.20	0.55	3.0

[a]Fricke's parameters

[b]Using the final parameters listed

[c]Using parameters that were extrapolated from Fricke's results.

The calculations using these parameters are compared to the data of the present experiment in Figure 4.1.

4.2.e DWBA Calculations

The DWBA calculations were done using a FØRTRAN-IV version of the Oak Ridge computer code JULIE (Ba 62) on the SDS, Σ-7 computer. These calculations included Coulomb excitation with r_c = 1.25F and the deformation of the complete Optical Potential.

The optical potential parameters used in these calculations are those given in Tables 4.5 and 4.6. The

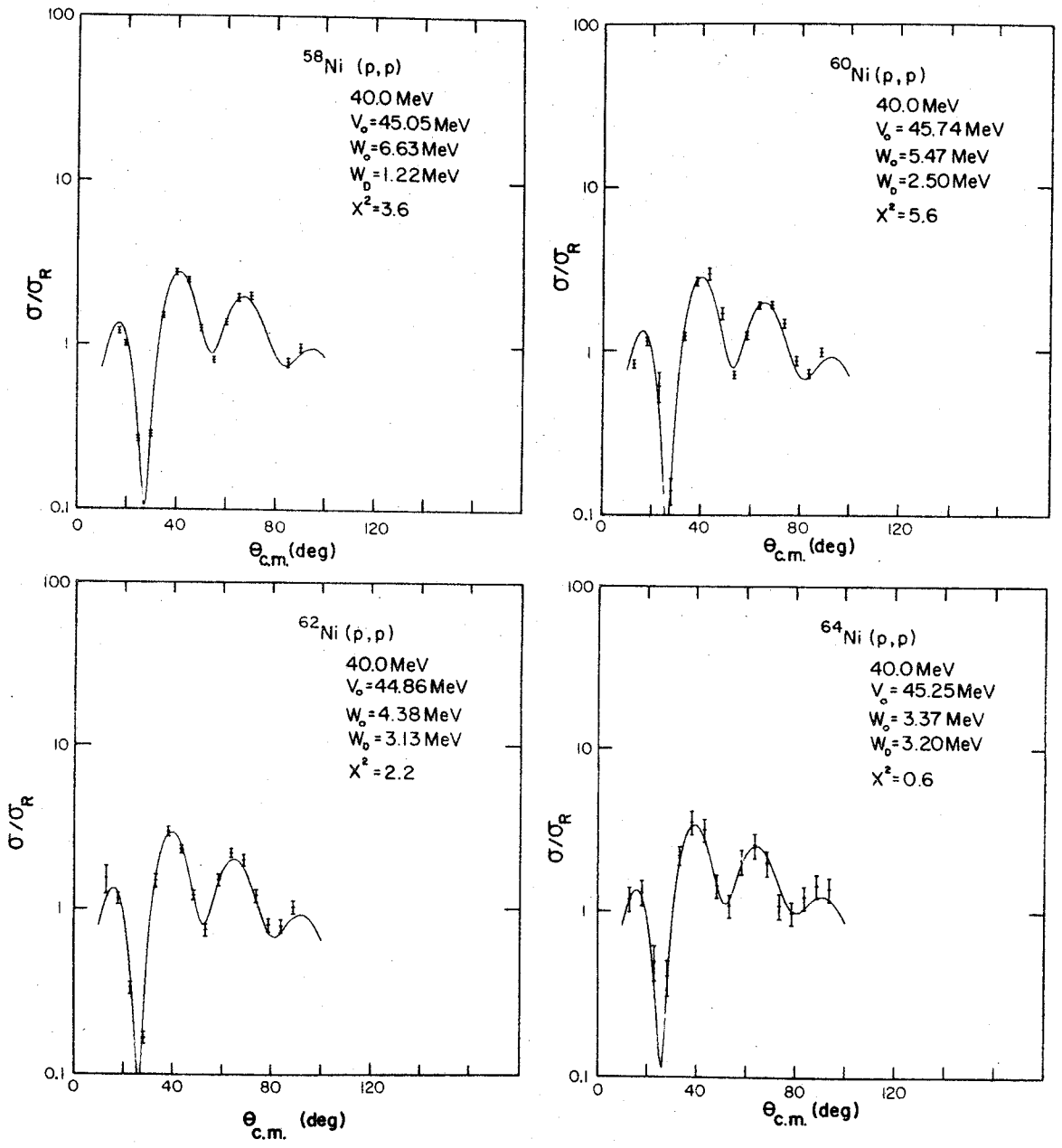

4.1 Comparisons of the experimental, elastic scattering results and the theoretical calculations using the optical potential parameters given in Tables 4.5 and 4.6.

resulting angular distribution, σ_{DW}, for inelastic scattering is related to the experimental distribution by the relation,

$$\frac{d\sigma(EXP)}{d\Omega} = \frac{1}{(2L + 1)} \beta_L^2 \frac{2J_B + 1}{2J_A + 1} \sigma_{DW} \qquad 4.30$$

where L is the transferred orbital angular momentum. For inelastic proton scattering from an even-even target $J_A = 0$ and $J_B = L$; equation 4.30 becomes

$$\frac{d\sigma(EXP)}{d\Omega} = \beta_L^2 \sigma_{DW} \qquad 4.31$$

4.2.f Extraction of Deformation Parameters, β_L

The relation 4.31 was used in the comparison of the theoretical and experimental angular distributions through the computer program, SIGTOTE (section 4.1.a.4). In these comparisons the value of the momentum transfer, L, associated with each state observed was needed in order to extract a definite value for the associated nuclear deformation.

In Tables 4.7-4.10 are tabulated the values of J^π that have been determined for the various states in the stable, even nickel isotopes through other experiments. Also listed here are the L-values that were assigned to the states with the excitation energies shown in the table.

TABLE 4.7.--J^{π} assignments for states in ^{58}Ni and the excitation energies and L-values used in this experiment.

Ex(MeV)	b (α,α') 34.4 MeV J^{π}	c (α,α') 50.2 MeV J^{π}	d (e,e') 183 MeV J^{π}	e (p,p') 8 MeV J^{π}	Values used in Present Work Ex(MeV)	L
1.456[a]	2+	2+	2		1.456	2
2.458a	4+	4+	4	4	2.458	4
2.773a	2+	2+		2		
2.900a		1+				
2.940a		0+				
3.035a	2+	2+		2	3.035	2
3.260a	2+	2+	2	2	3.260	2
3.414q		(3+)				
3.524a		4+				
3.588a		1+				
3.615a	4+	4+	4		3.62	4
3.773a		(3+)				
3.895a	2+	2+			3.895	2
4.103a	(2+)					
4.401a		4+			4.38	4
4.472a	3-	3-	3		4.472	3
4.754a	4+	4+			4.754	4
5.15b	6+				5.128	6
5.40b	4+					
5.60b	4++5+					
5.80b	4+					
6.07b	3-					
6.30b	2+					
6.55b	4+					
6.8-6.9b	3-					
7.15-7.30b	4+					
7.55b,d	3-		4			
7.90b	3-+4+					

[a]Reference Te 67; [b]Reference In 68; [c]Reference Ja 67; [d]Reference Cr 61; [e]Reference Ho 67.

TABLE 4.8.--J^{π} assignments for states in ^{60}Ni and the excitation energies and L-values used in this experiment.

Ex(MeV)	a $J\pi$	b $(\alpha\alpha')$34.4 MeV $J\pi$	Values used in present work Ex(MeV)	L
1.332a	2+	2+	1.331	2
2.158a	2+	2+		
2.286a	0+	0+		
2.506a	4+	4+	2.502	4
3.625a	3+			
3.123a	2+		3.119	2
3.11b		2+(4+)		
3.195a	1+			
3.35b		2+		
3.70b		4+		
4.022a	1+,2+			
4.040a	3-	3-	4.042	3
4.079a	1+,2+			
4.332a	1+,2+			
4.30b		4+		
4.496a	1+,2+			
4.50b		2+		
4.555a	1+,2+			
4.583a	1+,2+			
5.0b		5-		
5.1b				
5.102a	4+	4+		
5.6b		3-		
5.85b		2+		
6.16b		3-		
6.53b		3-		
7.0b		3-,4+		

[a]Reference Ra 68

[b]Reference Ja 67

TABLE 4.9.--J^{π} assignments for states in ^{62}Ni and the excitation energies and L-values used in this experiment.

Ex(MeV)	[a] J^{π}	[b] $^{63}Cu(d,^{3}He)$ J^{π}	Values used in present work Ex(meV)	L
1.172a	2+		1.169	2
2.047a	0+			
2.293a	2+			
2.336a	4+		2.334	4
3.751a	3-		3.750	3
4.02b		( )+		
4.74b		( )+		
4.85b		( )+		

[a] Reference Ve 67

[b] Reference Hi 68

TABLE 4.10.--J^{π} assignments for states in ^{64}Ni and the excitation energies and L-values used in this experiment.

Ex(MeV)	[a] J^{π}	[b] $^{65}Cu(d,^{3}He)$ J^{π}	[c] $(\alpha\alpha')$ 30.5 MeV	Values used in present work Ex(MeV)	L
1.348a	2+			1.344	2
2.272a	0+				
2.605a	4+			2.608	4
2.863a	2+				
3.161a	2+			3.165	2
3.554a	3-			3.560	3
3.79b		( )+			
3.85c			5-	3.849	5
4.29b		( )+			

[a]Reference Ve 67

[b]Reference Hi 68

[c]Reference He 68

There were states observed, however, that could not be associated with a unique state identified in reference Te 67 (see Tables 4.1-4.4). This ambiguity is a result of the errors involved in the determination of the energies. When this was the case, the observed state could not be given a definite L-value. Furthermore, some states in reference Te 62 were given only tentative assignments or no spin assignments at all. In these cases several values of L were used in the comparison of experiment and theory, and the β_L for each case was found. The program, SIGTOTE, described in section 4.1.d, was used for this comparison by the method of normalizing the integrated cross sections for the theoretical and the experimental results. All of the L-values which were used in the calculations are shown in Appendix IV along with the nuclear deformations, $\delta_L = \beta_L R_o$, which were found. The experimental angular distributions of known L are shown in Figures 4.2-4.6 along with the normalized theoretical data. The angular distributions which cannot be associated with an L-value are plotted in Appendix IV. Also in Appendix IV are plots of the DWBA theory. All of these plots of experimental and theoretical data are presented on the same scale to facilitate comparisons.

In addition to this procedure a second method was used to evaluate the nuclear deformations. This method involved comparisons of the ratios of the cross sections

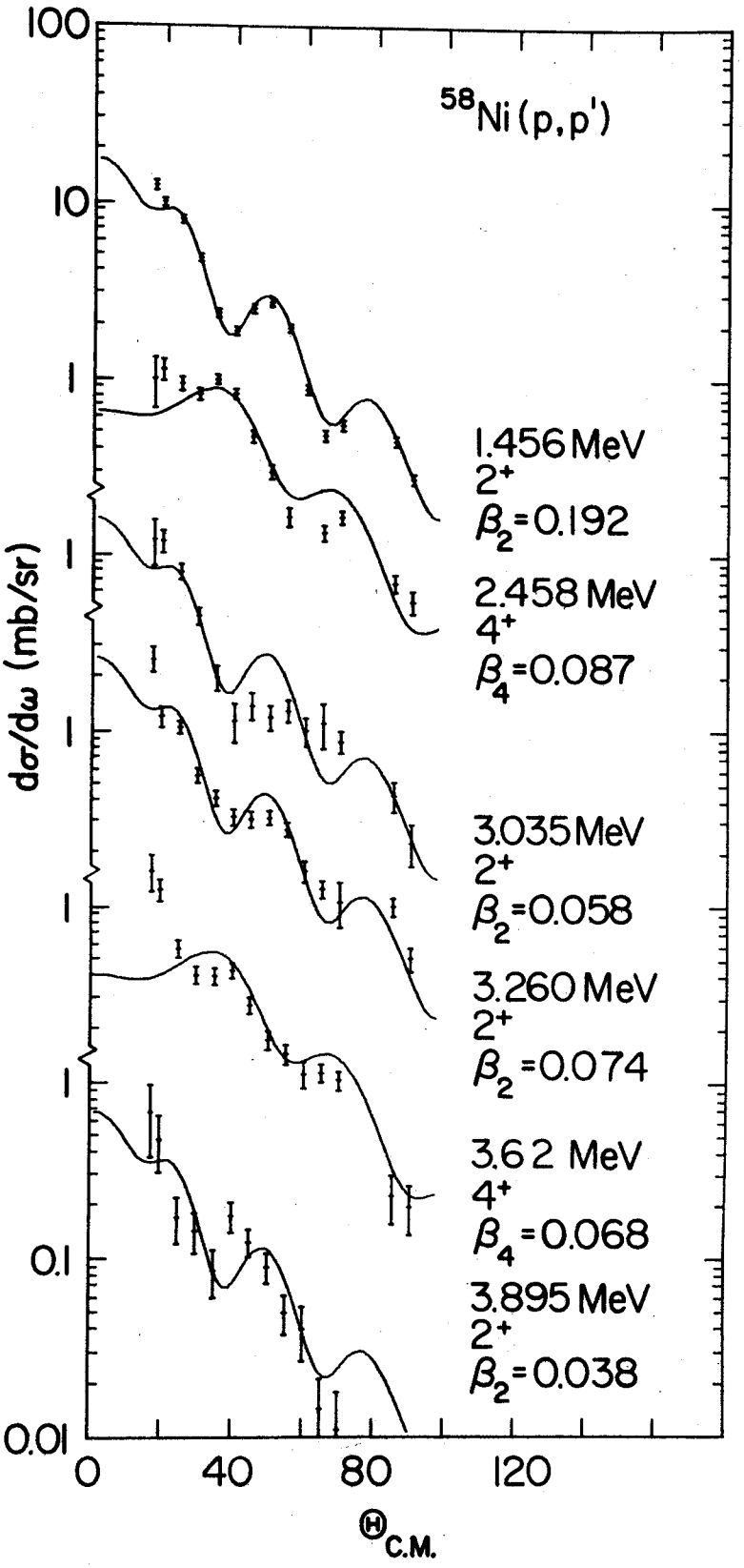

4.2 Comparisons of the experimental inelastic scattering results and the theoretical DWBA calculations for states in ^{58}Ni with known J^{π} assignments.

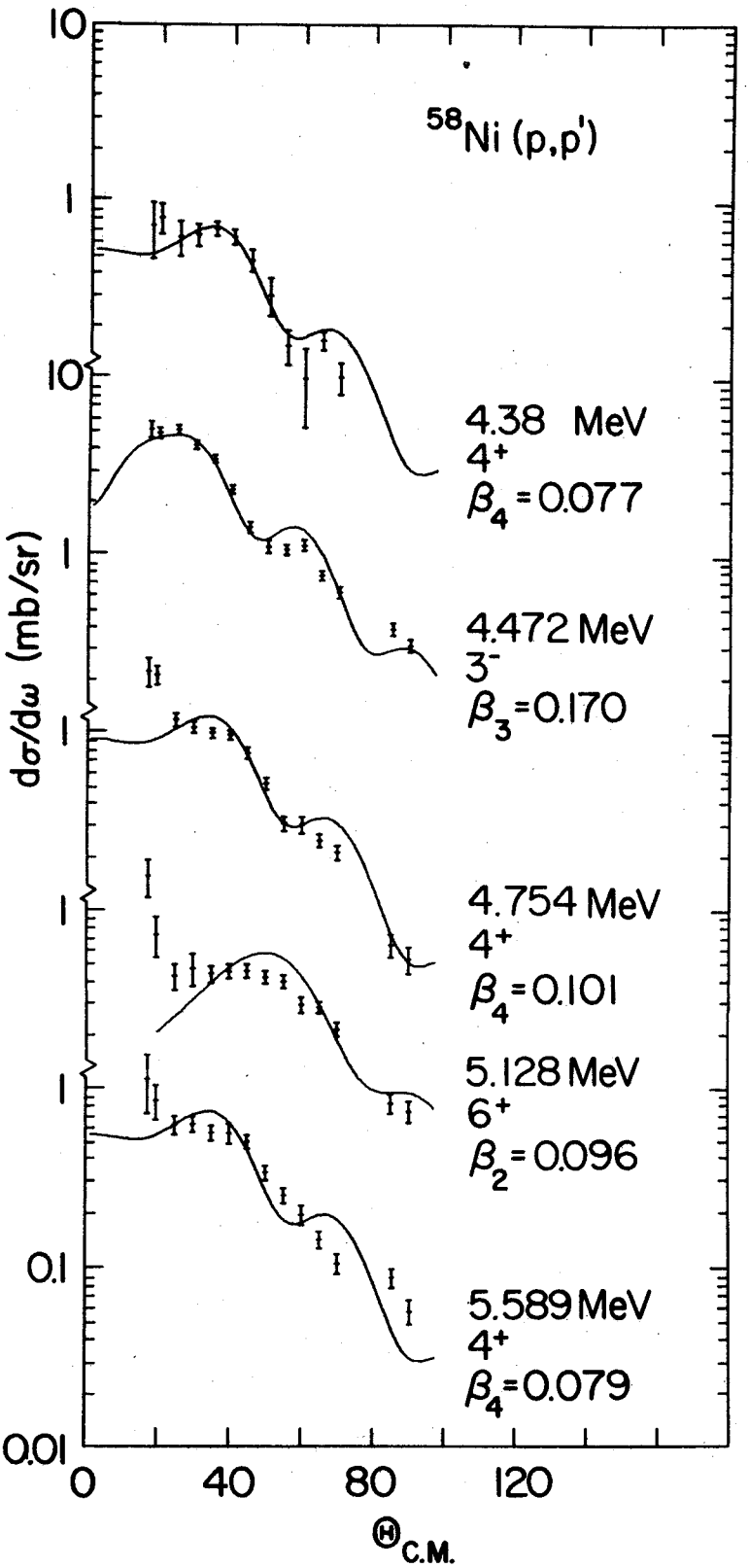

4.3 Comparisons of the experimental inelastic scattering results and the theoretical DWBA calculations for states in ^{58}Ni with known J^{π} assignments.

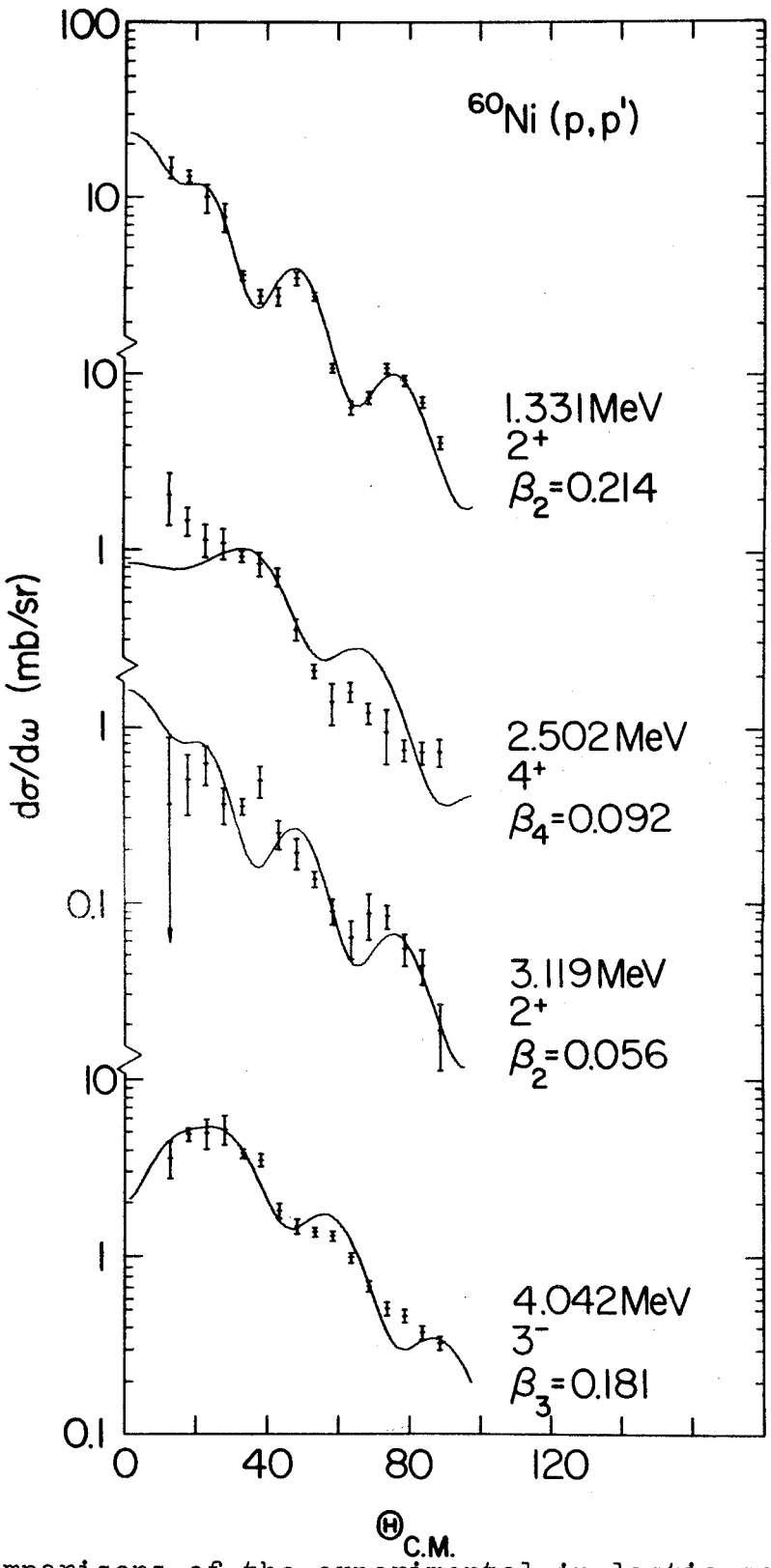

4.4 Comparisons of the experimental inelastic scattering results and the theoretical DWBA calculations for states in ^{60}Ni with known J^{π} assignments.

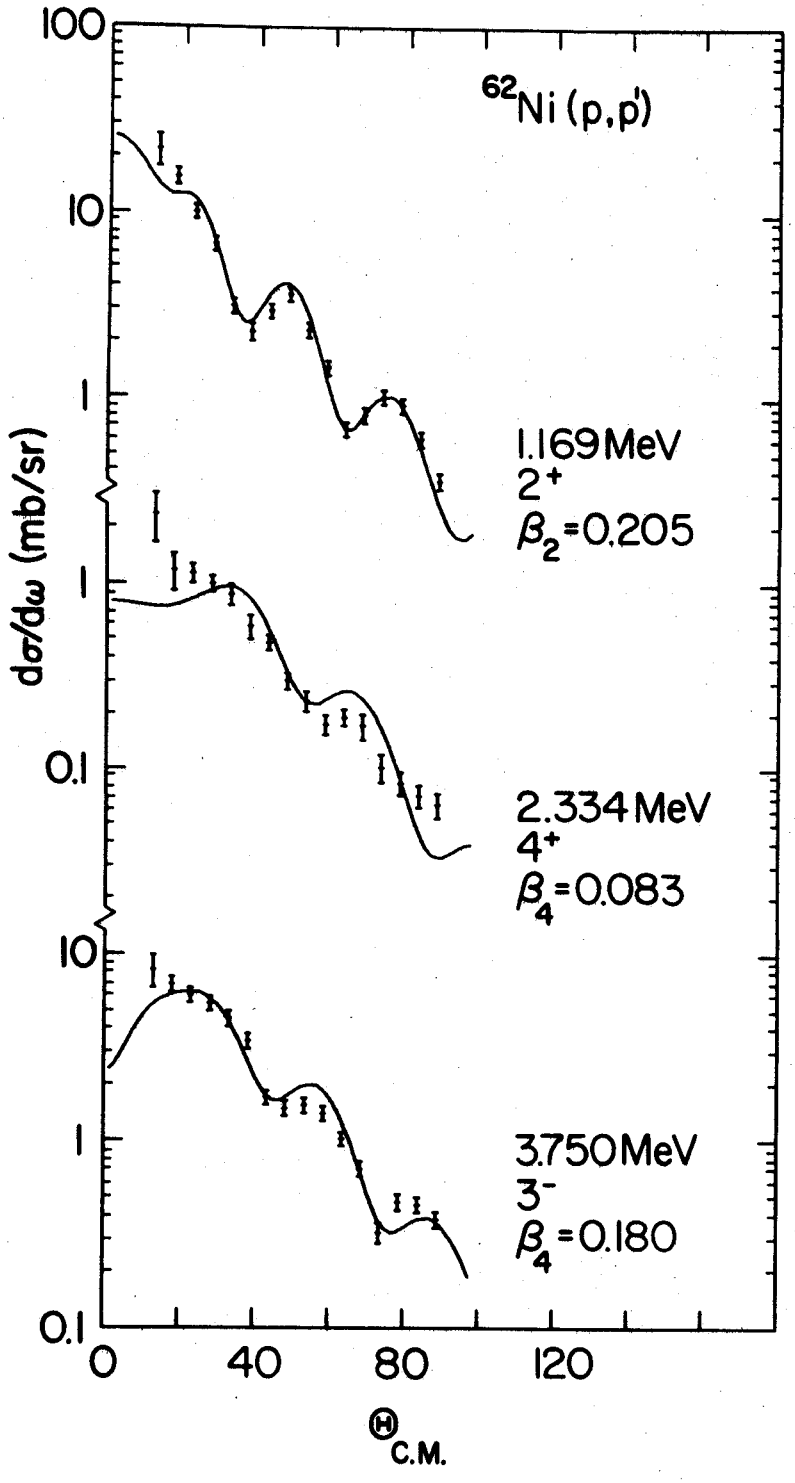

4.5 Comparisons of the experimental inelastic scattering results and the theoretical DWBA calculations for states in ^{62}Ni with known J^{π} assignments.

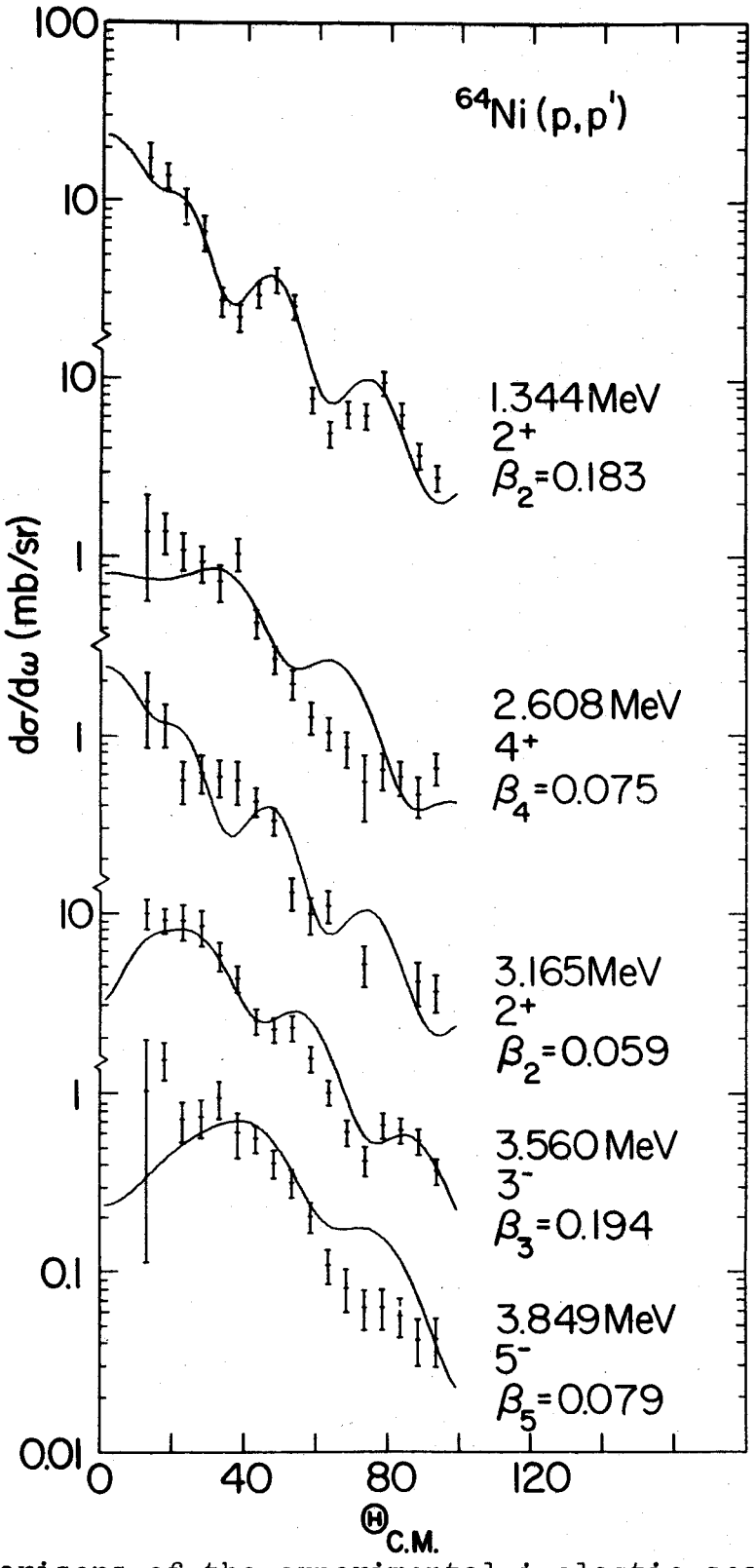

4.6 Comparisons of the experimental inelastic scattering results and the theoretical DWBA calculations for states in ^{64}Ni with known J^{π} assignments.

for the excited states to the ground state for the theory and the experiment. This type of procedure eliminates the need for knowledge of the relative normalization of the data at the various laboratory angles. Since there were normalization problems (see section 4.1.f.2) in this experiment, this method did prove to be helpful. It also has the potential to provide a better measurement of the δ_L's since only the statistical errors contribute to the final error. By the former method, in comparison, there are systematic errors which also contribute.

Involved in the ratio are two statistical errors, one for the ground state and one for the excited state. Furthermore, the angular distributions of the ratios have the general trend of increasing in magnitude with increasing angle. These facts result in a change of the weights of the terms comprising the integrated cross sections in equation 4.2 compared to the first method. The exact nature of this effect was not examined in detail, but the results indicated the larger weight tends to be given to the points at the larger angles. This effect is different from the method involving the absolute cross sections where the forward angles are weighted more.

The result of this change in weighting is that the errors for a particular δ_L as found by the ratio method may in fact be somewhat larger than that found by the more customary method. The results of the ratio method,

however, did agree in general with the values obtained by the customary procedure. This enhances ones confidence that the relative normalizations of the experimental data were correct.

In addition to the observed states upper limits to the differential cross sections for the second 2^+ states were obtained. Several energy spectra at various detector angles for each nuclei were examined at the points at which these states should appear. The statistical fluctuations of the background at these points were compared to the net peak heights for the first 2^+ states. The estimated upper limits are shown in Table 4.11.

TABLE 4.11.--Estimated upper limits for the δ_L for the second 2+ states.

	^{58}Ni	^{60}Ni	^{62}Ni	^{64}Ni
Ex(MeV)	2.773	2.156	2.293	2.863
δ_L	0.103	0.138	0.121	0.102

CHAPTER V

DISCUSSION OF THE RESULTS

A vibrational collective model was used in the distorted wave theory to extract a nuclear deformation for each observed state. These deformations were then used to find reduced transition probabilities and the corresponding parameters of other models.

According to Lane (La 64) transitions which involve "collective" motions exhaust greater than 5% of the sum rule. This is considered to be a rough means of identifying collective motion. The fraction of each sum rule contained in each state is presented in Appendix IV.4. The energy weighted sum rule is deflected by more than 7% for the first 2^+ state in each nuclei and by more than 12% for the first 3^- state. The non-energy-weighted sum rule shows even larger fractions exhausted for these states, and there are a number of additional states which contain more than 5% of the limit. These results indicate that the spectra of the stable, even nickel isotopes contain a number of states which can be associated with collective motions according to the criteria of Lane (La 64).

Vibrational characteristics of the energy level structure of a nucleus include the uniform spacing of the levels and the systematic occurrence of a given type of level in neighboring nuclei (La 64) (Bo 67a).

The low lying energy levels of ^{58}Ni, ^{60}Ni, ^{62}Ni, and ^{64}Ni are approximately evenly spaced as shown by the fact that $E_{2_1} \approx \frac{1}{2}E_{4_2}$ and $E_{2_1} \approx \frac{1}{3} E_{3_1}$. The systematic appearance of the strongly excited 2^+ and 3^- states in even-even nuclei support a collective interpretation of these states.

The optical potential strength parameters used in this analysis for this experiment are shown in Table 4.6. The values of X^2/N indicate that the starting parameters for ^{62}Ni and ^{64}Ni derived from the work of Fricke et al. on ^{58}Ni and ^{60}Ni resulted in reasonable fits. This indicates that the searches on the parameters for ^{62}Ni and ^{64}Ni were probably not necessary.

According to Glendenning and Veneroni (Gl 66) inelastically scattered protons are a valuable tool for examining details of nuclear structure well inside the nuclear surface. This probe, on the other hand, is not conclusive in determining spins and parities as compared to the strongly absorbed particles such as alpha particles.

The results of the collective distorted wave calculations provide very good fits in many cases to the angular distributions for the states of known spins and parities.

As a result of this there is some value in comparing those states of unknown spins and parities to the calculations. This does provide tentative assignments of the orbital angular momenta, L, associated with some of the states.

The tabulated results of such comparisons are presented in Appendix IV.3. The X^2/N can be used here to indicate how the experimental distributions are fit by the calculations for various L-values. Plots of the calculated distributions were also compared with the data to check that the shapes were indeed consistent. The tentative L assignments for various states are given in Table 5.1.

TABLE 5.1.--Tentative L assignments.

^{58}Ni		^{60}Ni		^{62}Ni		^{64}Ni	
Ex(MeV)	L	Ex(MeV)	L	Ex(MeV)	L	Ex(MeV)	L
4.11	(4)	3.67	(4)	4.148	(5)	4.60	(5)
6.89	(3)	5.7	(3)				
7.3	(3)						

The quantity $\langle r^{\lambda} \rangle$ (section 4.2.b) was used in the calculations of the reduced transition probabilities and sum rule limits which gave the results tabulated in Appendix IV.4. The value of this radial moment depends on the type of charge distribution used. These different

distributions were used here. A comparison of the B(EL)'s for these three cases show that there can be factors of 2 variations in the results for the 2^+ states, factors of 4 for 3^- states, and up to factors of 10 for 4^+ states. The conclusion is that the reduced transition probabilities obtained in (p,p') experiments are extremely sensitive to the model used for the matter distribution.

5.1 Comparisons with Other Experiments

The nuclear deformations obtained in this experiment are compared to other experimental results in Tables 5.2-5.5. The quantities shown are mostly for states with a known L-value. For ^{58}Ni and ^{60}Ni, however, there were deformations obtained for states which have uncertain energies and L-values in reference In 68. If the excitation energy determined in this experiment agreed with that in In 68 to within the errors, a value of $\beta_L R_o$ was obtained for the state. The β_L's found for each of these states in the present experiment were, in general, constant to within a few per cent for the different L assignments. An average of the deformations shown in Appendix IV.3 for each of these states of undetermined L is shown in Tables 5.2 and 5.3.

The values obtained for the reduced transition probabilities along with results from other experiments are presented in Table 5.6. Listed here are the results for the three charge distributions given in Appendix IV.4.

TABLE 5.2.--Nuclear deformations for ^{58}Ni and comparison with experiments representative of other reactions.

Ex(MeV)	L	(p,p') 40 MeV Present Work	(p,p') 40 MeV Fr 67a	(p,p') 17.9 MeV Ja 67	(α,α') 50.2 MeV Ja 67	(α,α') 34.4 MeV In 68	(e,e') 65 MeV Du 67	(^{3}He,^{3}He') 25 MeV Ru 68	(^{3}He,^{3}He') 51.3 MeV Bi 68
1.456	2	0.862 ± 2.3%	0.79	0.97 ± 5%	0.997 ± 5%	1.188	0.975±1.7 %	0.970	0.625
2.458	4	0.391 ± 2.5%		0.53 ±36%	0.406 ±12%	0.512			
3.035	2	0.260 ± 3.1%			0.256±10%	0.310	0.347±32%		
3.260	2	0.332 ± 2.8%			0.315 ± 9%	0.310	0.468±9.5%		
3.62	4	0.305 ± 2.9%		0.39 ±38%	0.242 ±10%	0.367			
3.895	2	0.171 ± 5.1%		0.19 ±25%	0.169 ±14%				
4.38	4	0.346 ± 3.4%		0.44 ±33%	0.39 ± 12%				
4.472	3	0.763 ± 2.3%	0.75	0.77 ±12%	0.73 ± 7%	0.986	1.228±1.0%	0.794	0.529
4.754	4	0.453 ± 2.5%		0.53 ±27%	0.39 ±12%	0.449			
5.128	6	0.431 ± 2.7%				0.366			
5.589	4	0.355 ± 2.8%		0.53 ±27%	0.29 ±17%	0.291			
5.43		(0.301)* ±3.3%				0.297			
5.77		(0.198) ± 4.4%				0.335			
6.08		(0.224) ± 3.9%				0.310			
6.35		(0.202) ± 4.6%				0.214			

*The errors for these states do not include the error due to the uncertainty in L.

TABLE 5.3.--Nuclear deformations for ^{60}Ni and comparison with experiments representative of other reactions.

Ex(MeV)	L	(p,p') 40 MeV Present Work	(p,p') 40 MeV Fr 67a	(p,p') 30 MeV Fn 68	(p,p') 13 MeV Ba 68	(α,α') 34.4 MeV In 68	(d,d') 11.5 MeV Jo 69	(e,e') Du 67
1.331	2	0.972 ± 3.3%	0.895	1.055	1.27	1.265	1.120±4%	1.093±1.0%
2.502	4	0.418 ± 3.7%				0.530		
3.119	2	0.254 ± 4.5%				0.374		
4.042	3	0.822 ± 3.2%	0.692	0.938	1.03	1.034	0.790±4%	1.468±2.5%
3.36		(0.163)*± 8.7%				0.249		
3.69		(0.313) ± 4.2%				0.280		
4.32		(0.236) ± 5.6%				0.268		
5.14		(0.699) ± 3.2%				0.498		

*The errors for these states do not include the error due to the uncertainty in L.

TABLE 5.4.--Nuclear deformations for ^{62}Ni and comparison with experiments representative of other reactions.

Ex(MeV)	L	(p,p') 40MeV Present Work	(p,p') 17.5 MeV Mc 66	(α,α') 21 MeV Fu 68a	(d,d') 11.5 MeV Jo 69	(e,e') 65 MeV Du 67	(^{3}He,^{3}He') 25 MeV Ru 68
1.169	2	0.941 ± 4.4%	1.131 ± 3%	1.04	0.992	1.101±0.5%	1.000 ± 4%
3.750	3	0.826 ± 4.3%	0.924 ± 4%		0.631	1.204±2.5%	0.795 ± 4%

TABLE 5.5.--Nuclear deformations for ^{64}Ni and comparison with experiments representative of other reactions.

Ex(MeV)	L	(p,p') 40 MeV Present Work	(p,p') 11 MeV Di 63	(p,p') 17.5 MeV Mc 66	(d,d') 11.5 MeV Jo 69
1.344	2	0.849 ± 7.9	1.155	1.000 ± 7.0%	0.920 ± 4%
2.608	4	0.348 ± 8.3%	1.155		
3.560	3	0.900 ± 7.9%		0.905 ± 5.5%	0.752 ± 4%

TABLE 5.6.--Comparisons of reduced transition probabilities, B(EL; 0→L), in units of F^{2L}.

	Ex(MeV)	L	Coulomb Excitation St 65	ee' Du 67	ee' Cr 61	Present Results a	Present Results b	Present Results c
^{58}Ni								
	1.456	2	1050 ±101	946 ±16	1430 ±200	1030 ±47	1230 ±57	1720 ±79
	3.035	2		102 ±4		94 ±6	112 ±7	156 ±10
	3.260	2		220 ±22		153 ±9	182 ±10	254 ±14
	4.472	3		26780 ±720	27200	17400 ±800	24800 ±1140	68600 ±3160
	2.468	4			1.45×10^5	9.9×10^4 $\pm0.5\times10^4$	1.67×10^5 $\pm0.08\times10^5$	1.34×10^6 $\pm0.07\times10^6$
	3.62	4			2.86×10^5	6.0×10^4 $\pm0.4\times10^4$	1.0×10^5 $\pm0.06\times10^5$	8.1×10^5 $\pm0.5\times10^5$
^{60}Ni								
	1.331	2	1397 ±115	1217 ±13	1790 ±220	1340 ±88	1600 ±106	2200 ±145
	4.042	3		40500 ±922	35300	21200 ±1400	30100 ±1900	80700 ±5200
	2.502	4			2.7×10^5	1.21×10^5 $\pm0.09\times10^5$	2.0×10^5 $\pm0.2\times10^5$	1.6×10^6 $\pm0.1\times10^6$
^{62}Ni								
	1.169	2	1210 ±115	1263 ±16		1290 ± 113	1530 ±135	2080 ±183
	3.750	3		30240 ±778		22300 ±1950	31700 ±2730	82600 ±7100
^{64}Ni								
	1.344	2	1253 ±245			1070 ±180	1270 ±214	1710 ±288

[a] Uniform charge distribution with r_o = 1.20F

[b] Fermi equivalent, uniform charge distribution with r_o = 1.31F

[c] Fermi charge distribution with r_o = 1.10F and a = 0.566F

The force constant, C_L, which was found in this experiment using a uniform charge distribution with r_o = 1.20F is shown for each of the first 2^+ excited states in Table 5.7. Also shown in this table are the results of calculations (Wo 68) of C_L which used the values of the B(E2)'s obtained from studies of electromagnetic transitions (St 65).

TABLE 5.7.--Experimental surface tension parameters, C_L(MeV).

	Wo 68*	Present work**
^{58}Ni	104 ± 9	106 ± 5
^{60}Ni	74.8 ± 5.7	77.7 ± 5.1
^{62}Ni	79.3 ± 6.9	74.4 ± 6.5
^{64}Ni	91.3 ± 14.9	107 ±17

*Using a uniform charge distribution with r_o = 1.20F.

**r_o = 1.20F

Crannel et al. (Cr 61) evaluated the mass transport parameters, D_L. In these calculations the D_L's were calculated from the B(EL)'s found in their experiment with inelastic electron scattering. They used a Fermi charge distribution with $r_o \simeq 1.05$F and $a \simeq 0.57$F. Their results along with those obtained in this experiment are shown in Table 5.8.

TABLE 5.8.--Experimental mass transport parameters $D_L/\hbar^2$ in units of (MeV^{-1}).

	Ex(MeV)	L	Cr 61[a]	Present Work[b]
^{58}Ni	1.456	2	70 ± 9	50 ± 9
	3.260	2	160 ± 38	150 ± 8
^{60}Ni	1.331	2	65.2± 7.8	44 ± 3
^{58}Ni	4.472	3	103 ± 14	29 ± 1
^{60}Ni	4.042	3	88.5± 14	28 ± 2
^{58}Ni	2.458	4	6140 ± 1800	258 ± 12
	3.62	4	1196 ± 270	288 ± 17
^{60}Ni	2.502	4	3400 ± 650	227 ± 17

[a]Using a Fermi charge distribution with $r_o \simeq 1.05F$ and $a \simeq 0.57F$.

[b]$r_o = 1.20F$

5.2 Comparison with Theory

The nickel isotopes have been described (Au 67) by N. Auerbach in terms of strongly admixed spherical shell-model configurations of neutrons in the $2p_{3/2}$, $1f_{5/2}$, and $2p_{1/2}$ orbits. The B(E2) values from these calculations are shown with the present experimental results in Table 5.9. The experimental B(E2)'s shown here were calculated using the uniform charge distribution with

$$r_o = 1.20F.$$

TABLE 5.9.--Experimental and theoretical results for B(E2)'s for the nickel isotopes.

	Theory[a]	Experiment[b]
	$B(E2; 0_1^+ \rightarrow 2_1^+)(F^4)$	
^{58}Ni	585	1030 ± 47
^{60}Ni	1001	1340 ± 88
^{62}Ni	1235	1290 ± 113
^{64}Ni	1129	1070 ± 180
	$B(E2; 0_1^+ \rightarrow 2_2^+)(F^4)$	
^{58}Ni	75	<15
^{60}Ni	30	<27
^{62}Ni	1.4	<21
^{64}Ni	9.0	<15

[a]Au 67

[b]Using a uniform charge distribution with r_o = 1.20F

A modified Tamm-Dancoff approximation has been applied to the even nickel isotopes by Raj et al. (Ra 67). In this work several interaction potentials were used and reduced transition probabilities were found. The results were calculated for the various potentials for transitions between the first and second 2^+ states and the ground state in each nuclei. The results of these calculations and of

the present experiment are shown in Table 5.10. The uniform charge distribution with r_o = 1.20F was used in the extraction of the experimental results.

5.3 Conclusions

From the comparisons made in sections 5.1 and 5.2 between the results of this experiment and other experiments and theoretical calculations it is apparent that certain precautions should be taken. Comparisons of the nuclear deformations, δ_L, in Tables 5.2-5.5 show that the present results agree to within errors for a large number of cases. These comparisons, however, need not necessarily show an agreement for all the reactions considered. The different projectiles used need different optical potentials which are then incorporated into the collective model distorted wave calculations. These potentials commonly have different, real well radii. The effects of this are compensated for by the use of βR_o instead of β alone in the comparisons for different reactions. This procedure has been pointed out, however, to still have its deficiencies (Be 69). The radius which should be used is not well defined in all cases since the β's which are obtained are often the results of calculations which deform both the real and the imaginary well. These wells usually have different geometries. Also the strongly absorbed particles, i.e., deuterons, ^{3}He and ^{4}He, require much more absorption than protons. The fact that

TABLE 5.10.--Experimental and theoretical results for B(E2)'s for the nickel isotopes. The effective charge assumed in the theoretical calculations was 1.35e.

	QQ[a]	EIC[b]		EIA[c]		
		A	B	A	B	Present Results*
	B(E2; $0_1^+ \rightarrow 2_1^+$) (F^4)					
^{60}Ni	949	747	760	756	868	1340 ± 88
^{62}Ni	1124	877	735	937	598	1290 ± 113
^{64}Ni	1059	782	837	892	907	1070 ± 180
	B(E2; $0_1^+ \rightarrow 2_2^+$)(F^4)					
^{60}Ni	5.8	8.1	9.71	7.2	2.0	<27
^{62}Ni	1.0	5.8	41	6.8	148	<21
^{64}Ni	1.0	23	0.29	1.1	9.4	<15

a) Using a quadrupole interaction (Ra 67)
b) Using effective two-body matrix elements extracted in Co 67
c) Using effective two-body matrix elements extracted in Au 60
A) Using the usual procedure to obtain E_a, V_a^2 and U_a^2 (Ra 67)
B) Using the inverse-gap method to obtain E_a, V_a^2 and U_a^2 (Gi 66)
* Using a uniform charge distribution with r_o = 1.20F.

the real and imaginary geometries are quite different could affect the extraction of a deformation.

This problem points out a need for a standardized procedure for the extraction of β or βR. This would make comparisons of the type shown above more meaningful. Unless the interaction radius can be defined more precisely, therefore, comparisons of βR's should be viewed with caution.

It has also been shown that, irrespective of the above problem for β's, there is also the problem of obtaining the reduced transition probabilities and the sum rule limits in an inelastic proton experiment in a manner which is insensitive to the matter distribution. Also the sum rule limits and the mass transport and surface tension parameters found from electromagnetic measurements depend on the model used for the charge distribution. As shown in Table 5.6 and Appendix IV.4 the results of the three models are fairly consistent for the $L = 2$ states, but for the higher spin states the results can differ by factors of more than 10.

The model which gives the most consistent results with electromagnetic measurements can be found by comparing the results in Table 5.6 for all the L-values shown, $L = 2,3,4$. It can be seen that the calculations using a Fermi equivalent, uniform charge distribution are most consistent.

As shown in Tables 5.7 and 5.8 the vibrational parameters, D_L and C_L, obtained from this experiment agree in general, to within experimental errors, with the results of electromagnetic measurements for L = 2 states. The values for the higher spin states in Table 5.8, however, disagree more.

It should be reiterated that for inelastic scattering the values for the mass transport and surface tension are deduced from the experiment in a fashion which is insensitive to the matter distribution in contrast to these parameters as deduced from EM experiments. On the other hand the B(EL)'s found in studies of electromagnetic transitions are insensitive to the charge distribution in contrast to the sensitivity of the B(EL)'s deduced from inelastic proton scattering.

Keeping in mind the above discussion of the model dependent uncertainties for the results of this experiment for the measurements of the B(E2)'s, the results in Tables 5.9 and 5.10 can be compared. Table 5.9 shows that Auerbach's shell-model calculations agree in general with the results of the present work. The calculations for ^{58}Ni, however, do seem to be somewhat inconsistent with the experimental results and yet here the only serious disagreement is in the results for the $0_1^+ \rightarrow 2_2^+$ transition.

The main disagreements in the comparisons made in Table 5.10 involve the $0_1^+ \rightarrow 2_2^+$ transitions. The result of

the EIA(B) theory for ^{62}Ni about 7 times greater than the estimated upper limit. Also the results of the EIC(b) theory for ^{62}Ni and the EIC(a) theory for ^{64}Ni are rather high. In this comparison the most consistent theoretical results are produced by the Q·Q interaction in contrast to its predictions of the excited states (Ra 67).

APPENDICES

APPENDIX I

DETAILS OF THE CONSTRUCTION AND OPERATION OF THE GONIOMETER

Table of Contents

I.1 Goniometer Base

I.2 Main Arm

- I.2.a Construction
- I.2.b Calculations of the vertical deflections

I.3 Rotary Table and Drive Chain for the Main Arm

- I.3.a Rotary Table
- I.3.b Drive Motor
- I.3.c Gear Train
- I.3.d Calculations for the Main Arm Drive
  - I.3.d.1 Motor Requirements
  - I.3.d.2 Gear Strengths
  - I.3.d.3 Strengths of the Pins, Keys, Bearings and Shafts

I.4 Calculations of the Main Arm Configuration

I.5 Readout of Main Arm Position

I.6 Central Column

I.7 Target Drive

I.8 Target Holder

I.9 Target Chamber

I.10 Target Lock

I.11 Detector Carriage

I.12 Local Power Supply

I.13 Remote Control Station

I.13.a Control Panel
I.13.b DC Motor Power Supply
I.13.c Electronics Bin
I.13.d Power Distribution Chassis

I.14 Surface Finishes

I.15 Suggested Improvements

I.16 Documentation

I.17 Assembly and Maintenance Suggestions

I.17.a Backlash Adjustment of the Rotary Table Gears
I.17.b Assembly of Main Arm Drive
I.17.c Installation of Main Arm Synchro Motor
I.17.d Installation of Target Well
I.17.e Assembly of Target Drive and Central Shaft
I.17.f Electrical Fuses
I.17.g Lubrication

I.18 List of the Major Components.

APPENDIX I

DETAILS OF THE CONSTRUCTION AND OPERATION OF THE GONIOMETER

In this section the details are presented of the construction of the goniometer system described in section 2.2. In addition the calculations used in the design and suggestions for maintenance of the system and assembly of the more involved components are given. To facilitate the use of this section a table of contents is provided to aid in the location of the particular topics of interest.

I.1 Goniometer Base--Figure 2.2A

The goniometer is supported entirely on four legs. These legs are constructed from 1 inch diameter, NFT, threaded steel rod. The length of these legs was made sufficiently long to allow the detector support to be positioned at 12 inches below the scattering plane as well as at a typical working distance of 3-3/4 inches.

There was some question about the stability of the system when the longest leg extensions were used. The final design, however, results in a rigid structure. This is insured by using a counterbalanced, load carrying system. This guarantees that there exist only vertical forces on the

legs under static conditions. Under dynamic situations the legs are held securely by threading them into the base plate through 1-1/4 inches of steel and using two lock-nuts to rigidly tighten each leg in place.

Each of the legs is located at the lower end by a foot. The rotating joint between this foot and the leg is close fitting both vertically and radially. This permits the goniometer to be securely located when the feet are fastened rigidly to the floor.

The primary base-plate which supports the goniometer is made of 1/2 inch steel with each corner built up by an additional 3/4 inch of steel to permit a stronger and more rigid leg coupling.

A 1/2 inch thick steel, secondary, base-plate rests on two aluminum spacers which are 7 inches high. To this plate is rigidly fastened all of the drive elements of the goniometer. The spacers are attached to the main plate by 1/2-13 machine screws through slotted holes in the plate. The spacer is fastened to the secondary plate in a similar fashion. Between each spacer and the main plate and between one spacer and the secondary plate are adjustment screws which function like turnbuckles. The position of the goniometer in two perpendicular horizontal directions can then be adjusted by loosening the bolts between the spacer and the plates and then using the turnbuckles to accurately locate the base.

I.2 Main Arm--Figure 2.2C

I.2.a Construction

The rotary mill table (section I.3.a) is securely fastened to the base and the main arm is connected rigidly to the table surface by 8, 1/2 inch bolts and T-nuts. The main arm is supported by a central column constructed from a 22-1/2 inch length of standard 8 inch black pipe.

The main arm is made up of two aluminum beams. Each is a total of 6 feet long and is fastened to the central column such that the portion which supports the detector extends 4 feet from the center of rotation. Each beam of the arm is made of two rectangular bars which are pinned and bolted together. The top bar is 1/4 x 1-1/2 inch and the leg is 1/2 x 1-1/2 inch. Hardened steel drill bushings with 1/4 inch ID are located in the top surface of each beam and are accurately spaced 6 inches apart. These bushings are used to locate the detector mount on the arm.

Between the dual beams of the 2 foot section of the arm opposite the detector support is located an aluminum box used to hold a counterweight if it is needed. This box is large enough to hold at least 8 lead bricks each weighing 25 pounds. Two 3/8 inch bolts and two dowels connect the box to the arm in such a way as to permit the arm to flex a small amount. The need for this flex is given below in section I.4.

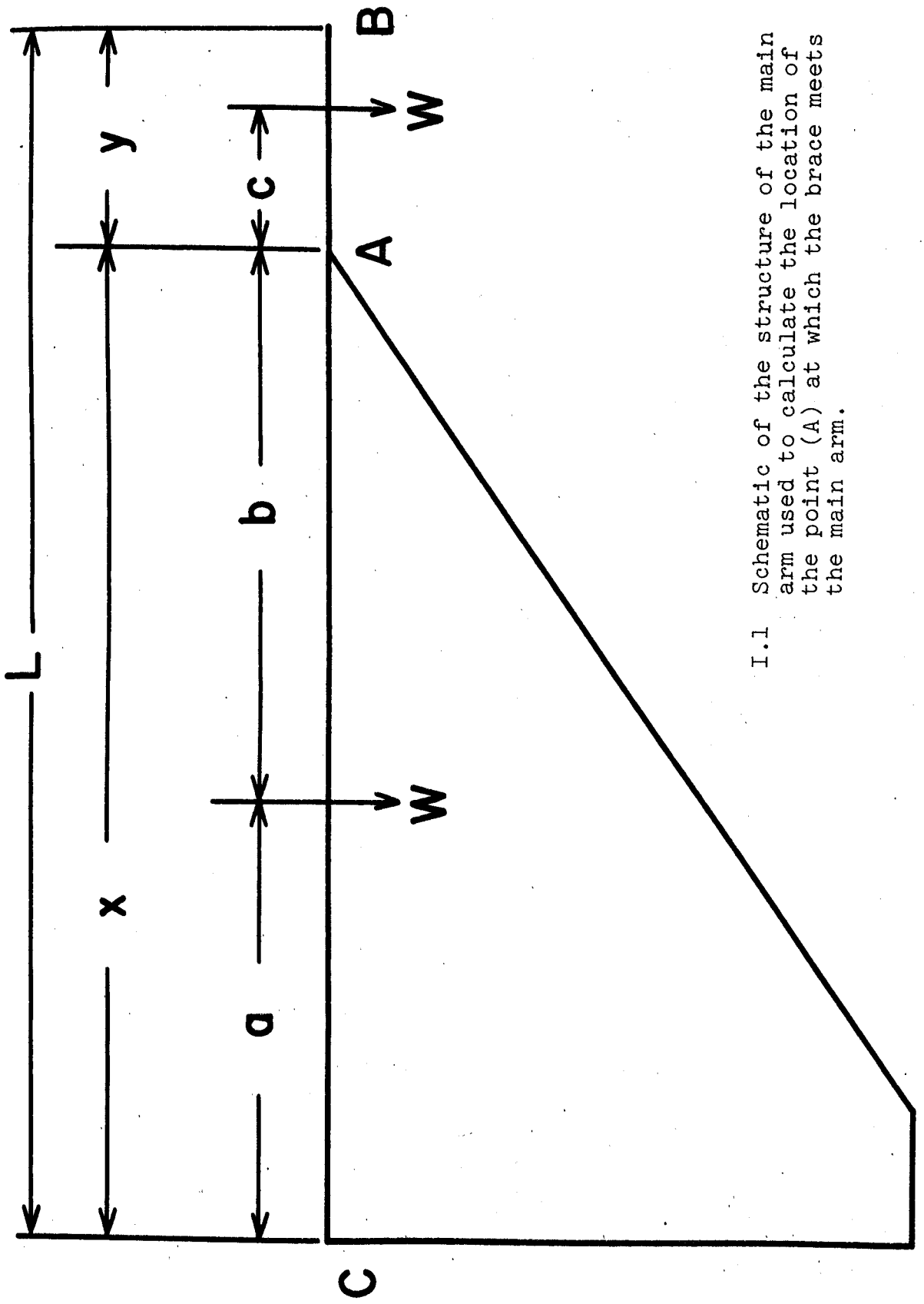

I.1 Schematic of the structure of the main arm used to calculate the location of the point (A) at which the brace meets the main arm.

The end of each beam is supported by a brace which extends to the base of the column. This brace is made of aluminum and consists of a 1/2 x 1-1/2 inch bar with a 1/2 x 1/2 inch bar bolted to it to reduce the bending of the brace under load.

With only the detector support considered Figure I.1 shows the basic configuration of the structure. This schematic was used in the calculations to determine the location of the point at which the brace should meet the arm beam, point (A). For simplicity the beam was assumed to have no vertical deflection under load at point A. The point at which the arm meets the central column, C, is a rigid vertical support, and the beam does not twist about this point since each beam is held to the column at this point by 3, 1/2 inch bolts.

There are two sections of the beam, therefore, which can experience deflections under load--section x which is between the central column and point A, and section y which is beyond point A. Point A can be taken as a pivot point or as rigidly fixed. The criteria which was used to calculate the position of point A was that the maximum deflection of section x be equal to that of section y for a rigid support at A. This calculation is shown below in section I.2.b. and point A was found to be located 9 inches from the end of the arm.

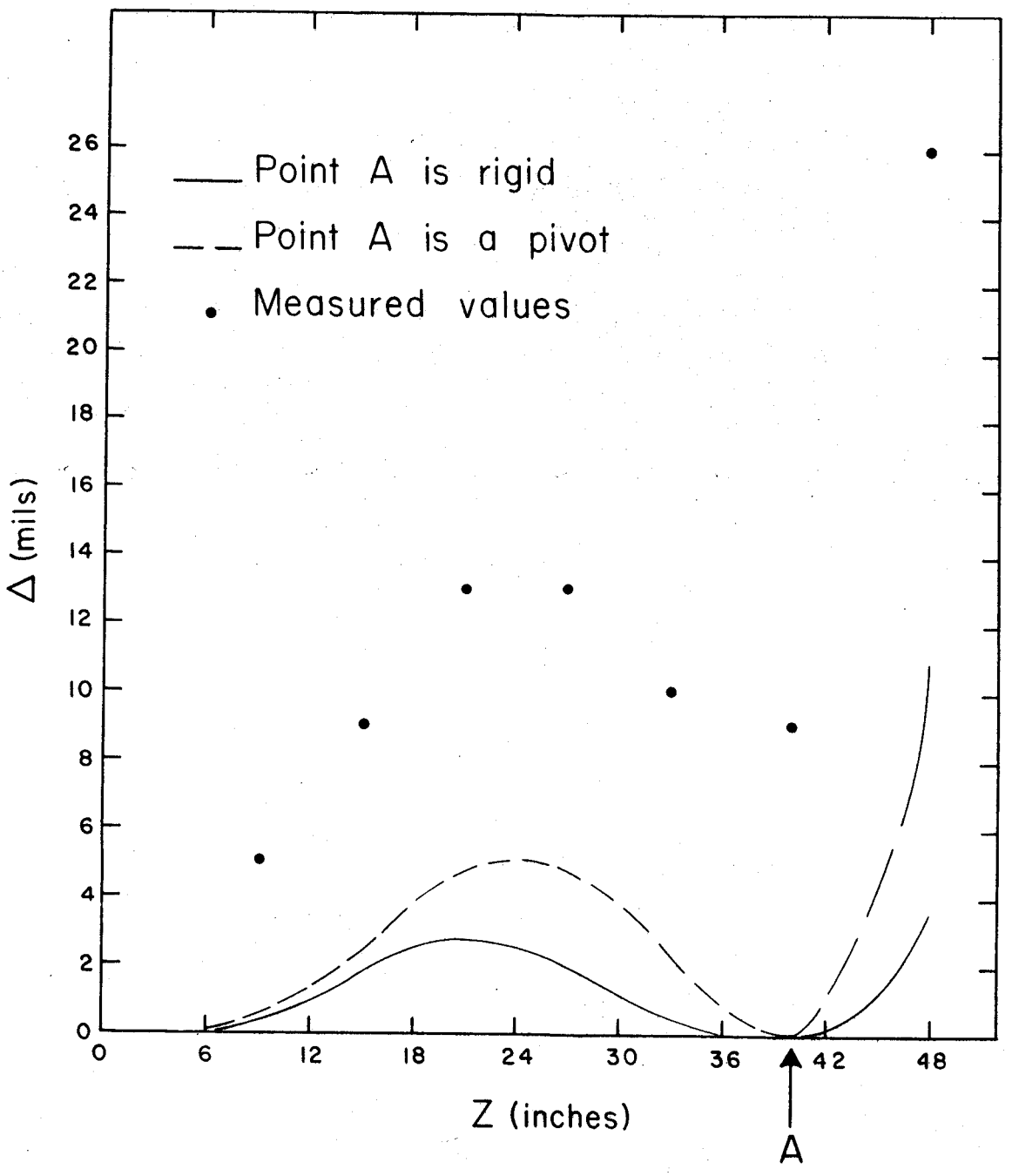

I.2 Results of the calculations and measurements of the vertical deflections in the main arm under a load of 100 lbs.

The deflections of each beam were estimated using equations I.1, I.2, and I.3. The results of these calculations are presented in Figure I.2 where the vertical deflection, Δ, of the arm under 100 lbs load is plotted as a function of the distance, Z, of the load from that point located 4 feet from the end of the arm. Calculations were done for both a rigid and a pivoting connection at A. The deflection for the beam for points beyond A in the second case were estimated by considering the ratios of the deflections calculated for both cases for corresponding points inside of A.

Also shown in Figure I.2 are the results of measurements of the deflections for a 100 lb load. The fact that the value near A is about 9 mils shows that the brace does not provide a rigid vertical support. The comparison of the locations of the peaks in the curves also shows that A is probably a pivot point.

The final dimensions of the dual beams were determined by successive attempts to find a configuration which would satisfy the load and structural requirements discussed in sections 2.1 and I.4. The moment of inertia about the vertical axis of the goniometer for the arm system loaded with the maximum of 100 lbs at 4 feet and 200 lbs at 2 feet was calcualted to be

$$2852 \text{ lbs} - \text{ft}^2$$

This result will be used in some of the succeeding calculations.

I.2.b. Calculations of the Vertical Deflection

The following equations give the deflection, Δ, of sections x and y in terms of the quantities a, b, and c as defined in Figure I.1. For rigid support at A

$$\Delta_x = \frac{Wa^3b^3}{3EI^*x^3} \qquad \text{(Ma 64, p. 397) I.1}$$

$$\Delta_y = \frac{Wc^3}{3EI^*} \qquad \text{(Ma 64, p. 393) I.2}$$

For pivoting at A

$$\Delta_x = \frac{Wa^3b^2(3x+b)}{12\ EI^*\ x^3} \qquad \text{(Ma 64, p. 395) I.3}$$

where E = modulus of elasticity

I^* = Areal moment of inertia of the support cross-section (Ma 64, p. 358)

W = load

The maximum deflections for a given load will occur when the load is in the center of x and at point B for section y; hence, a = b = x/2 and c = L - x.

$$\Delta_x = \frac{Wx^3}{192EI^*} \qquad \text{I.1'}$$

$$\Delta_y = \frac{W(L-X)^3}{3EI^*} \qquad \text{I.2'}$$

$L = 4'-4" = 3.67'$

$x = 2.92'$

This means that A is 9 inches from the end of the 4 foot detector support if the radius of the central column is considered.

I.3 Rotary Table and Drive Chain for the Main Arm-- Figure 2.2B

I.3.a Rotary Table

The primary positioning element for the main arm consists of a 15 inch diameter rotary mill table (1). This table contains an oil reservoir and has an entirely enclosed 90:1 worm gear drive whose center distance of the worm drive is adjustable, thus allowing the backlash to be maintained within tolerable limits. There are also adjustments for all thrust bearings which allow compensation for wear. This table is supplied with a vernier scale on the worm gear shaft which has a least count of 20 seconds, or 0.006°.

In order to use this mill table there was a need to determine if it could operate under loads associated with

its use in the goniometer. The vertical load capability was checked by placing about 400 lbs on the table surface. The worm wheel shaft was then turned and found to have little added resistance compared to the no load condition. The calculations of the limiting strengths of the gears in the table are shown in section I.3.d.2. The details of the main arm construction were then designed so that these calculated limits would not be exceeded under anticipated operating conditions.

I.3.b Drive Motor

In order to have a system that would facilitate anticipated computer control and function accurately and reliably under possibly heavy loads, a bifilar, Slo-Syn motor (2) was chosen. These motors operate with 200 steps per revolution in a DC stepping mode and can also be operated in an AC synchronous mode at a speed of 72 RPM. The motor is connected to the rotary table through a 4:1 gear train resulting in a 1.0 degree change in the main arm position for each motor revolution.

The size of the motor required depends on two aspects of the system--the maximum torque that the motor must supply and the moment of inertia that is rigidly attached to the motor. The maximum torque requirements occur at the moment the system is set in motion. There are two modes of operation which had to be considered--the AC synchronous mode and the DC stepping mode.

The calculations which were done to determine the loads on the motor under various conditions are given in section I.3.d.1. These calculations show that the motor must be able to supply 750 oz-in of torque and must be able to drive a moment of inertia of 10 lbs-in^2.

The Slo-Syn motor that was selected as a result of these calculations is the SS1800-1006. The engineering data needed for this motor was obtained from the Slo-Syn motor catalog #SS1265-2. For the AC mode of operation of the bifilar motor the engineering data for the 3 lead Slo-Syn motor was used. The bifilar motor can supply a torque of 1800 oz-in in the AC mode and 1600 oz-in in the DC mode operating at 20 steps/sec. In addition, the moment of inertia that it can drive is 16 lbs-in^2.

To run this bifilar motor in an AC synchronous mode a 195 Volt, 1KVA, power supply is used with a phase shifting network consisting of a 75 Ohm, 300 Watt resistor and a 25 mf, 460 VAC capacitor. In the AC mode this motor runs at a speed of 72 RPM and drives the main arm at 72°/min. In the DC stepping mode the motor is driven at about 20 steps per second rotating the main arm at a rate of 6°/min.

I.3.c. Gear Train--Figure I.3.

The gear train between the motor and the rotary table has a 4:1 ratio to provide a 1° main arm rotation for each revolution of the motor. The gears that were used are stock, 12 pitch, spur gears. The gears on the motor shaft

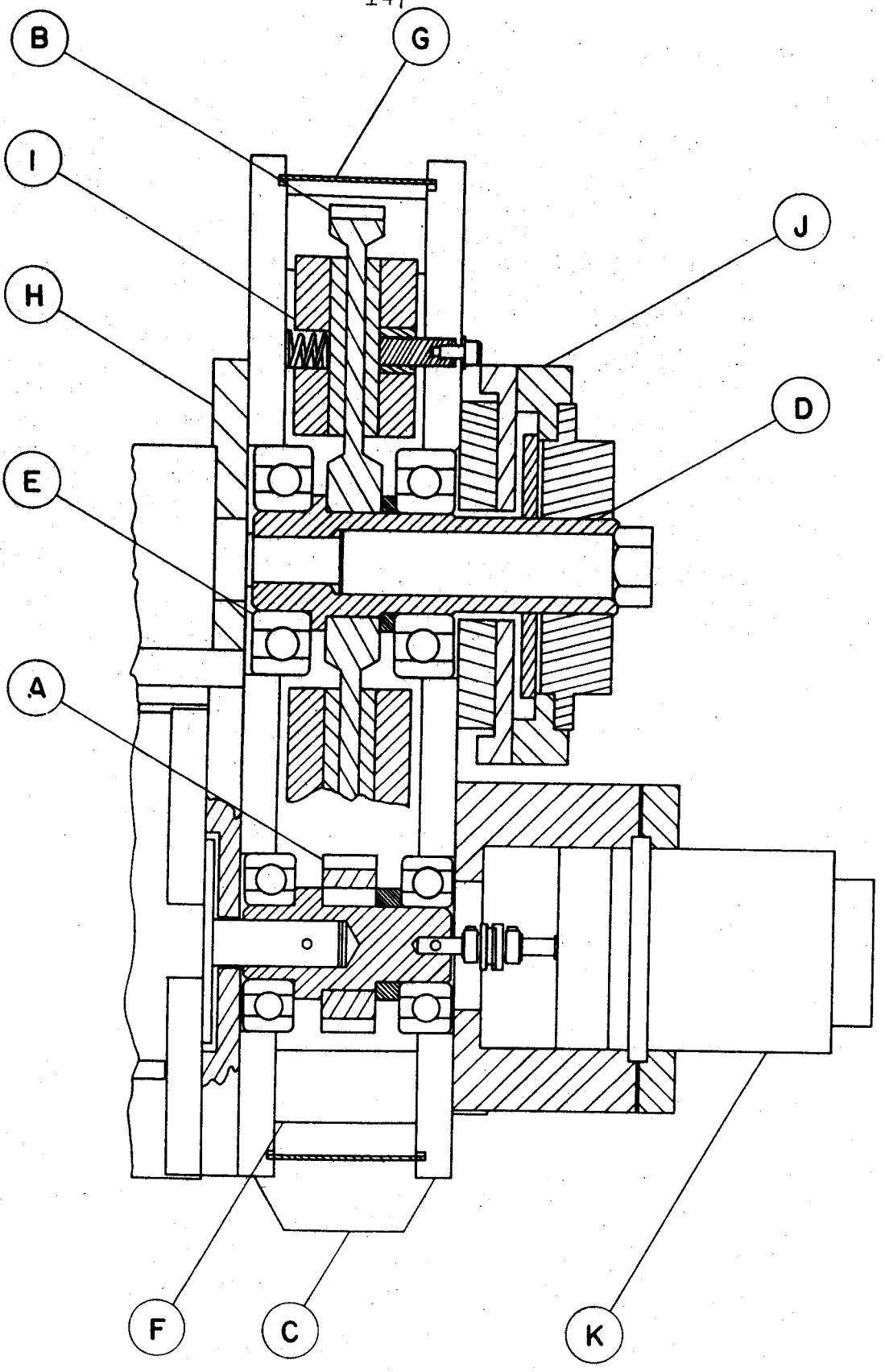

I.3 Section view of the 4:1 gear train for the main arm drive: A - Spur gear, B - Spur gear, C - Gear box sides, D - Gear shaft, E - Ball bearing, F - Box spacer, G - Box cover, H - Bearing cover plate, I - Brake.

(A) and that on the rotary table shaft (B) is a 3/4 inch faced steel spur gear (3) and a cast iron spur gear (4) respectively. These gears are mounted in a box (C) which maintains the center distance for the gears. The center distance for these gears was empirically determined by placing the gears in close contact and measuring the distance between two shafts placed in the gear bores with a micrometer; 1 mil was added to provide for an appropriate backlash. This center distance was then verified by locating two shafts in a block of aluminum at the determined distance and observing that the gears ran smoothly.

These gears were then modified so that they press fit onto two separate shafts, for example (D). A ballbearing, for example (E), is placed on either side of each gear (5) (6). The outside diameter of each of these bearings makes a close, clearance fit in a hole located in the side plates of the gear box. The side plates are bolted together with 1/2-13 bolts and are maintained at the proper spacing with steel spaces (F) over the bolts. A 0.06 inch aluminum sheet (G) is wrapped around the outside of the side plates to provide for a completely enclosed gear train.

The small gear shaft is pinned to the motor shaft with a 1/8 inch diameter, soft steel dowel. The large gear shaft is held to the rotary table shaft utilizing the 1/8 inch Woodruff key supplied with the table. Calculations were done to verify that the pin, key, table shaft and gear

bearings, could take the torque and resulting loads supplied by the motor. These calculations are presented in section I.3.d.3.

When this gear box was first installed and the motor was turned on, it was found that there was a severe rattling. On examination of the gears it was found that there were two problems that produced this effect. First, the stepping action of the Slo-Syn motor, even in an AC synchronous mode, produced an unforeseen problem. The motor makes discrete steps and suddenly stops after each, but the larger gear is allowed to coast a small amount because of the backlash in the gears. When the motor makes the next step the motor gear sharply strikes the table gear like a hammer. Secondly, the large diameter spur gear tended to ring after the hammer-like contacts of the gear teeth.

It was found that a friction drag on the larger gear eliminated the noise and produced a smooth and quiet operation. Two methods were used to provide this drag. First, thrusting screws were placed in cover plates like (H) on either end of the large gear shaft which were in turn securely fastened to the outside of the gear box. These screws were used to apply opposing thrusting loads on the two bearings on the gear shaft. This appeared to provide the necessary affect, but the adjustment of the screws was difficult and not very exact. The actual result was that there was a thrusting load on a bearing inside the rotary

table causing severe wear and ultimate failure of this part.

As a result of this failure, a needle, thrust bearing (7) was placed inside the rotary table to replace the original thrust bearing (Bridgeport #RT-26 and #RT-27). When the thrust screws were used after this modification, it was found that they did not produce the necessary drag on the gear drive.

These thrusting screws were, therefore, replaced by a brake system (I) which constituted the second method. This brake consists of two fiber-covered, spring-loaded, aluminum plates which are located between the gear and gear box sides. The springs for this brake provide a sufficient friction drag to insure a very quiet drive for both the AC and the DC mode of operation.

Calculations were made to determine the safe loads which the various gears in the drive chain could support. These calculations are shown in section I.3.d.2. These computations verify that the spur gears used are strong enough, and that the worm gear in the rotary table can safely supply 67 lbs-ft. of torque.

Also included in this system are two limit switches which stop the clockwise and counterclockwise rotation of the arm. These switches are mounted to the base of the rotary table and are actuated by cams which are located in a groove around the circumference of the rotary table.

I.3.d.1 Motor Requirements

According to Slo-Syn motor specifications for a three-lead, 72 RPM motor, the motor reaches its operating speed within 5° of shaft rotation. Since the main arm is attached to the motor through a 360:1 gear train, however, the arm is brought to speed in 0.014°. The final velocity of the main arm is

$$\omega = \frac{72 \text{ RPM}}{360}$$

$$= 0.021 \text{ rad/sec}$$

The angular acceleration needed to attain this final velocity in a distance $\Delta\theta$ is

$$\alpha = \omega^2/2\Delta\theta$$

$$\Delta\theta = 0.014° = 2.4 \times 10^{-4} \text{ rad}$$

$$\alpha = 0.92 \text{ rad/sec}^2$$

In the stepping mode a rate of 20 steps/sec is chosen--0.1°/sec--for the main arm. It was assumed that during a single step the arm was rigidly attached to the motor. This is, of course, not strictly true, but this is a limiting case and does provide for some safety factor. Therefore, one step moves the arm through an angle of 0.005° in 1/20 sec. This results in an angular acceleration of

$$\alpha = \frac{2\Delta\theta}{\Delta t^2} = 0.07 \text{ rad/sec}^2$$

The above calculations for the accelerations and the moment of inertia of the main arm can then be used to calculate the torque the motor must supply. The largest acceleration of the arm is 0.92 rad/sec^2. A factor of about 5 was then used to account for friction in the drive system and to allow for some safety factor.

Therefore, the torque needed at the arm is

$$T = I\,\alpha$$

$$T(\text{arm}) = 85{,}500 \text{ oz-in}$$

The torque that must be supplied by the motor, however, is effected by the gear ratio, N, shown by the relation

$$T(\text{motor}) = T(\text{arm})/N$$

$$T(\text{motor}) = 240 \text{ oz-in}$$

The moment of inertia seen by the motor is also effected by the gear ratio, N, as shown by

$$I(\text{motor}) = I(\text{arm})/N^2$$

Using the moment of inertia of the arm calculated above

$$I(\text{motor}) = 3.2 \text{ lbs-in}^2$$

Using these results along with the fact that a safety factor of at least 3 should be included, a motor was needed that could drive an inertia of at least 10 lbs-in^2 with a torque of 750 oz-in.

I.3.d.2 Gear Strengths

The safe load for a spur gear is found by using the Lewis formula (Ma 64, p. 715).

Where $W = Fsyc/P_d$ I.4

Wr = safe torque

r = gear pitch radius (in)

F = face width (in)

P_d = diametral pitch = # of teeth/pitch diameter

y = tooth outline factor

c = velocity factor = $600/(600 + v)$

v = pitch line velocity (FPM)

D = pitch diameter

R = RPM

s = safe working stress

For the calculation for the 2.417 inch diameter, 12 pitch gear used at 72 RPM

$P_d = 12$

$F = 0.75"$

$y = 0.32$ for 30 teeth, 14 1/2° (Ma 64, p. 717)

$s > 8000$ PSI

d = 2.417"

R = 72 RPM

v = 45.5 FPM

c = 0.93

r = 0.1'

W = 149 lbs.

And the safe torque is

Wr = 14.9 lbs-ft

For the 9.667 inch diameter gear

r = 0.4'

y = 0.37

Therefore

W = 172 lbs

And the safe torque for this gear is

Wr = 69 lbs-ft.

The calculations for the worm gear contained in the Bridgeport rotary table was a little more involved. The specifications for these gears were supplied by Bridgeport (Bridgeport parts: #RT-4 and #RT-5). The worm gear in the table has the following properties

1. 90 teeth
2. Diametral pitch = 12
3. Pitch diameter = 7.50"
4. Pressure angle = 14 1/2°
5. Addendum = .08"
6. Material is <u>better</u> than gray cast iron.

The worm has the following properties:

1. Axial pitch = .2618
2. Lead angle = 3°49'
3. Pitch diameter = 1.25"
4. Material is hardened steel

Two equations were used to calculate the safe load for this gear. First, the limiting strength load was found by the equation (Ma 64, p. 793)

$$T = 0.625\ S_b X_s\ Q\ m\ D \cos L_a$$

Where

T = torque limit (lbs-in)

S_b = bending stress factor > 6000 PSI (Ma 64, p. 794)

X_s = speed factor

Q = arc length of worm tooth measured along the root

m = .3183 · (axial pitch of worm)

D = pitch diameter

L_a = lead angle

To find the velocity factor for the very slow speeds used, a graph was made of the tabulated valves given for X_s (Ma 64, p. 795). This plot, shown in Figure I.4, shows that for speeds less than 6 RPM, X_s is greater than 0.6.

The valve for Q was found by scaling from the drawings provided by Bridgeport (Bridgeport #RT-4) to be 0.83 inch. Summarizing these values gives

$$S_b > 6000 \text{ psi}$$

$$X_s > 0.6$$

$$Q = 0.83"$$

$$m = 0.083"$$

$$D = 7.5"$$

$$\cos L_a \simeq 1$$

Therefore

$$T > 1160 \text{ lbs-in} = 97.0 \text{ lbs-ft}$$

The strength of the worm wheel is not a limiting factor since it is made of steel and has great strength because of the large effective face width it has. It is not necessary, therefore, to calculate the limiting strength of this drive component.

The second equation that was used to determine the safe load for the worm gear was a modified form of the Lewis formula, equation I.4, used above for spur gears. This modified form is

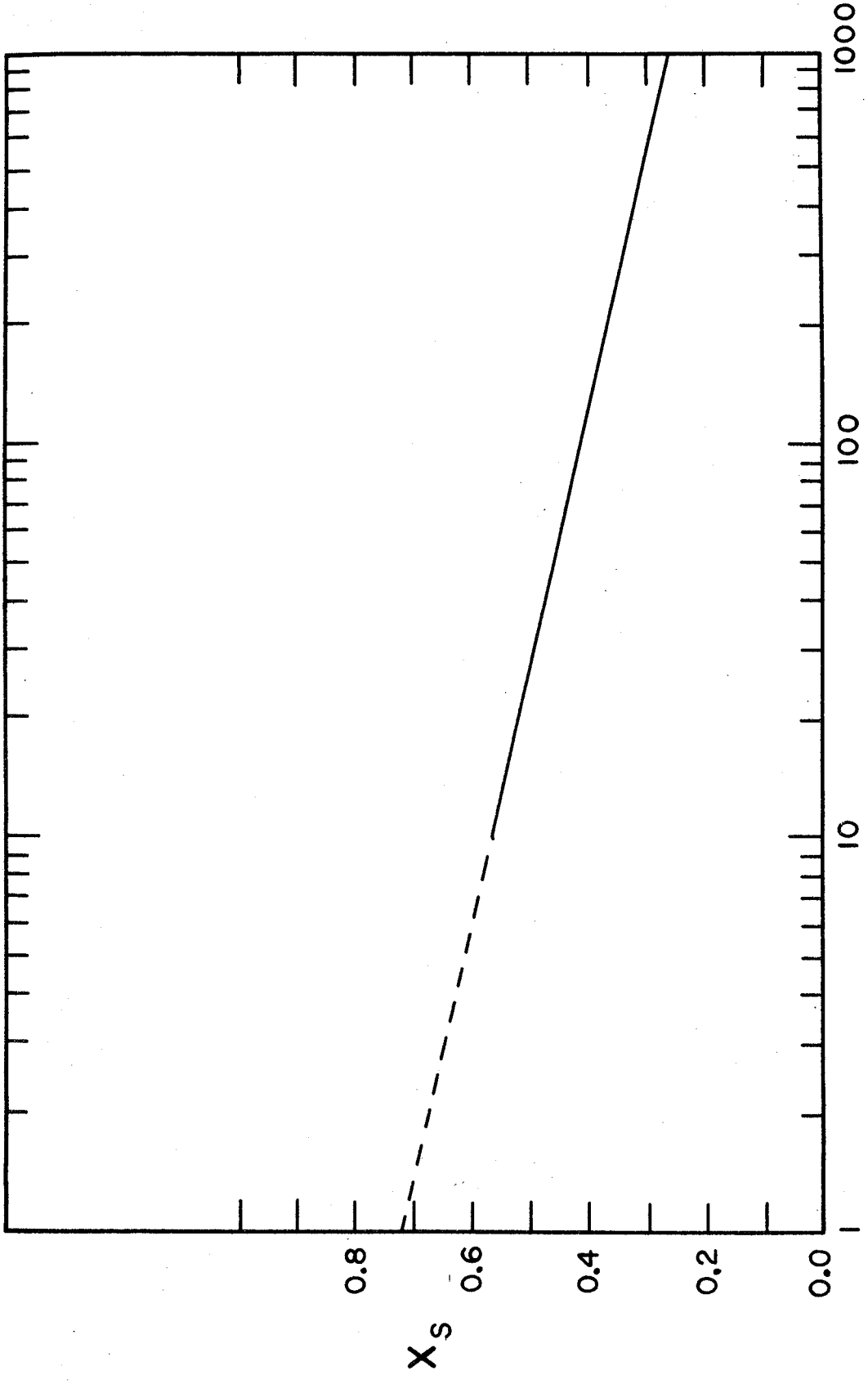

I.4 Plot of the speed factor, X_s, versus angular velocity, RPM.

$$W = F(min)\ syc/P_d$$

Where

$$F(min) = 1.125\ \{(d_o + 2e)^2 - (d_o - 4a)^2\}^{\frac{1}{2}}$$ (Ma 64, p. 776)

d_o = outside diameter of the worm

$= D + 2a$

a = addendum $= 0.3183\ p_n$

e = clearance $= h_t - h_k$

$h_t = 0.7003\ p_n + 0.002$

$h_k = 0.6366\ p_n$

p_n = lead $= \pi D/$ # of teeth

For the rotary table gear

$P_d = 12$

$v \simeq 0$

$c \simeq 1$

$y \simeq 0.37$ for 90 teeth, 14 1/2° (Ma 64, p. 717)

$s \simeq 8000PSI$

$P_n = 0.26"$

$F(min) \simeq 1"$

Therefore

$$Wr \simeq 246\ lbs$$

And the safe torque is

$$Wr = 246\ lbs \times 0.27\ ft = 66.7\ lbs\text{-}ft$$

Considering both of the results, it was decided that 67 lbs-ft would be used as the maximum safe load that the rotary table could support.

I.3.d.3. Strengths of the Pins, Keys, Bearings and Shafts

Shearing torque for a key is (Bl 55)

$$T_s = \frac{wLS_s d}{2} \qquad \text{I.5}$$

The shearing torque for a shaft in rotation is (Bl 55)

$$T_s = \frac{\pi d^3 S_s}{16} \qquad \text{I.6}$$

Where

d = shaft diameter

S_s = elastic limit > 3×10^4 PSI (Bl 55)

w = key width

L = key length

The Woodruff key in the rotary table shaft is 1/8" x 1/2" and the shaft is 5/8 inch diameter. Therefore

T_s = 41 lbs-ft

The pin in the motor shaft is 1/8 inch diameter. The w·L in T_s equation is the cross section of the key

exposed to the shearing forces at the circumference of the shaft. Replacing this cross section with that of a round pin with radius, r, through a shaft of diameter, d, equation I.5 becomes

$$T_s = \pi r^2 S_s d$$

Therefore, for the 5/8 inch diameter motor shaft the safe load is

$$T_s = 12.5 \text{ lbs-ft}$$

For the rotary table shaft

$$T_s = 51 \text{ lbs-ft}$$

All of these values are larger than the torque that the motor can supply--9.4 lbs-ft, on the motor shaft and 37.6 lbs-ft at the table shaft.

The radial load that the ballbearings had to support was also calculated using the equation (Ma 64, p. 726)

$$P = L/\cos \phi$$

Where

L = maximum force supplied by the motor at the gear circumference

ϕ = pressure angle of the gear = 14 1/2°

The motor supplies a maximum of 9.4 ft-lbs of torque to the gear fastened to its shaft; therefore, using the 2.417 inch pitch diameter of the smallest gear in the gear train, there is 94 lbs of force applied at the pitch diameter of this gear. Therefore

$$P = 97 \text{ lbs}$$

For a larger diameter gear this force is less, but these radial forces could easily be met by the ballbearings used.

I.4 Calculations of Main Arm Construction

The construction of the main arm was finalized after the safe load for the rotary table had been determined. The maximum load of the gear is produced when there is a maximum load on the arm (i.e. 100 lbs at 4 ft along with the 200 lbs at 2 ft).

The forces that can appear on the worm gear can arise from various sources. First, there is a force arising directly from the motor. Consdier, for example, the torque that would be applied to the worm gear if the table were prevented from rotating. The torque of the motor is increased by the gear ratio in the gear train (360:1). Therefore, the torque applied to the gear is

$$T = 3380 \text{ lbs-ft}$$

This result shows that the main arm must never be locked or must never run into an immovable object. For this reason the locks that were supplied with the table were removed.

A second load on the worm gear is the main arm itself. Consider what happens when the motor stops. A worm gear system cannot be driven by the worm gear but only the worm wheel. Therefore, when the motor stops, the worm gear is locked in place. Because there is a large amount of energy contained in the loaded main arm while in motion, there will appear large forces on the worm gear which decelerates this motion. Since the Slo-Syn motor can also start in a very short time there is a similar effect when the motor starts. The torque, T, needed to accelerate the arm is

$$T = \frac{\Delta L}{\Delta t}$$

where Δt is very small if the arm is assumed to be rigid. Therefore T is very large.

To reduce the required torque, it is sufficient to increase the time during which the arm is being accelerated. To accomplish this, the arm was made slightly flexible. The calculations presented below show that the final arm design described in section I.2 provides sufficient flex to bring the torque within safe limits.

The following calculations were made for a set of operating conditions which provide for a maximum stress on the drive system. The rotation of the arm very close to the axis of rotation will be assumed to start or stop instantaneously. This assumption is not far from being exact when a Slo-Syn motor and worm gear drive are used. The case that is considered below, therefore, involves the instantaneous stopping of the center of rotation of the main arm from a maximum initial angular velocity of 72 RPM or

$$\omega = 2.1 \times 10^{-2} \text{ rad/sec}$$

The limiting torque that the worm gear in the rotary table can provide is

$$T_G = 67 \text{ lbs-ft} \quad \text{(see section I.3.d.2)}$$

The major source of energy in the rotating arm system will arise from the load on the arm; therefore the contributions of the arm structure itself are neglected. The load on the arm consists of

$$W'' = 100 \text{ lbs} \quad \text{at} \quad L'' = 4 \text{ ft}$$

And

$$W' = 200 \text{ lbs} \quad \text{at} \quad L' = 2 \text{ ft}$$

This configuration has moments of inertia using mass units instead of pound-mass units

$$I'' = 62.5 \text{ slug-ft}^2$$

$$I' = 31.2 \text{ slug-ft}^2$$

The total kinetic energy is

$$KE = KE'' + KE'$$

$$KE'' = \frac{1}{2} I''\omega^2 = 138 \times 10^{-4} \text{ ft-lbs}$$

$$KE' = \frac{1}{2} I'\omega^2 = 68.8 \times 10^{-4} \text{ ft lbs}$$

When the rotation of the axis suddenly stops, this total kinetic energy is converted into potential energy by the flexing of the arm. That is

$$KE = \frac{1}{2} k' (\theta'max)^2 + \frac{1}{2} k'' (\theta''max)^2$$

Where θ represents the angle corresponding to the deflection at the ends of the arm. But

$$|T| = k\theta$$

$$k = |T|/\theta$$

Now a fictitious force, W, is considered to act horizontally at the end of the arm of length L causing the arm to deflect by an angle θ. Then

$$WL = T = k\theta$$

$$\frac{1}{k} = \frac{\theta}{LW} \qquad \text{I.7}$$

The deflection, Δ, caused by the fictitious force, W, on the arm L units long is given by equation I.2

$$\Delta = \frac{WL^3}{3EI^*} \qquad \text{I.2}$$

This deflection can also be given in terms of the arm length and the angle of deflection, if it is assumed that the deflection is small.

$$\Delta = L\theta$$

$$\theta = \frac{\Delta}{L} \qquad \text{I.8}$$

The expression for Δ from equation I.2 is then used in equation I.8 giving a relation for θ which is used in equation I.7,

$$\frac{1}{k} = \frac{\Delta}{L^2W} = \frac{WL^3}{L^2W3EI^*} = \frac{L}{3EI^*} \qquad \text{I.9}$$

Considering only one beam, the kinetic energy before deflection can be equated to the potential energy after deflection giving

$$KE = PE$$

$$\frac{1}{2} I\omega^2 = \frac{1}{2} k \theta^2 \qquad \text{I.10}$$

The preceding equations can now be applied to each end of the beam. From equation I.9 an expression for the ratio of the force constants, k, for each end of the beam can be found. Using the fact that E and I* are the same for both parts

$$\frac{k'}{k''} = \frac{L''}{L'}$$

Taking into account the fact that the beam is held rigidly for 4 inches on either side of its "center"

$$L' \rightarrow 20 \text{ inches}$$

$$L'' \rightarrow 44 \text{ inches}$$

This is not strictly true for all of the L's used in this development, but it will give a result to ± 10%. Therefore

$$\frac{k'}{k''} = 2.2 \qquad \text{I.11}$$

Using equation I.10 for both ends, a ratio of the angles of deflection can be found

$$\theta'/\theta'' = \{(k''/k') \ (I'/I'')\}^{\frac{1}{2}} \qquad \text{I.12}$$

But

$$I'' = 2I'$$

And also using results I.11 equation I.12 gives

$$\theta'/\theta'' = 0.48 \qquad \text{I.13}$$

Now the total kinetic energy before deflection is equated to the total potential energy after deflection

$$KE = \frac{1}{2} k'\theta'^2 + \frac{1}{2} k''\theta''^2$$

$$= \frac{1}{2} k'\theta'^2 \{1 + (k''/k')(\theta''/\theta')^2\}$$

$$k'^2\theta'^2 = 2(KE)k' \{1 + (k''/k') (\theta''/\theta')^2\}^{-1} \qquad \text{I.14}$$

The maximum torque which the rotary table must supply in order to stop the rotary motion of the arm is

$$T_M = k'\theta'_M + k''\theta''_M$$

$$= k'\theta'_M \{1 + (k''/k') (\theta''/\theta')\} \qquad \text{I.15}$$

But this torque is limited such that

$$T_M < T_G$$

$$T_G > k'\theta'_M \{1 + (k''/k') (\theta''/\theta')\} \qquad \text{I.16}$$

where the fact that θ''/θ' = constant has been kept in mine.

Therefore

$$k'\theta'_M < T_G \{1 + (k''/k') (\theta''/\theta')\}^{-1} \qquad \text{I.17}$$

Using I.17 in equation I.14

$$k' < \frac{T_G^2}{2(KE)} \{1 + (k''/k') (\theta''/\theta')\}^{-2}$$

$$x \{1 + (k''/k') (\theta''/\theta')^2\} \qquad \text{I.18}$$

Using this result in equation I.16, θ'_M can be solved for, giving

$$\theta'_M < \frac{2(KE)}{T_G} \{1 + (k''/k') (\theta''/\theta')\} \{1 + (k''/k') (\theta''/\theta')^2\}^{-1}$$

I.19

The value of I* needed to limit the amount of torque the worm gear must supply can now be found. Using equations I.2 and I.8 and eliminating Δ with the maximum values used for W and θ

$$L\theta_M = \frac{W_M L^3}{3EI^*} \qquad \text{I.20}$$

Also

$$W_M L = T_M \qquad \text{I.21}$$

Combining I.20 and I.20 gives

$$T_M = \frac{3I^*E\theta_M}{L}$$

This expression can be applied to both ends of the main arm, giving

$$T'_M = \frac{3I^*E\theta'_M}{L'} \qquad \text{I.22}$$

$$T''_M = \frac{3I^*E\theta''_M}{L''} = \frac{3I^*E\theta'_M}{L'} \{(\theta''/\theta')(L'/L'')\} \qquad \text{I.23}$$

The application of the restriction on the allowable torque which the worm gear can supply is used now to put a limit on the total moment of inertia of the arm structure. This results in

$$T_G > T_M \text{ (total)} = T'_M + T''_M$$

Substituting the results of equations I.22 and I.23 into this relation

$$T_G > \frac{3I^*E\theta'_M}{L'} \{1 + (\theta''/\theta')(L'/L'')\}$$

$$I^* < \frac{L'T_G}{3E\theta'_M} \{1 + (\theta''/\theta')\ (L'/L'')\}^{-1}$$

The expression I.19 for θ'_M can be used in this, along with the expression

$$\frac{L''}{L'} = \frac{k'}{k''}$$

$$I^* < \frac{L'T_G^2 \{1+ (k''/k')(\theta''/\theta')^2\}}{6E(KE) \{1 + (\theta''/\theta')(k''/k')\}}^2 \qquad \text{I.24}$$

Using parameters associated with the final goniometer design,

Total kinetic energy = KE = 206×10^{-4} ft-lbs

T_G = 67 lbs-ft

E = 1.48×10^9 lbs/ft^2 (Ma 64, p. 426)

L' = 1.67 ft

k"/k' = 0.45

θ''/θ' = 2.1

The results of equations I.24, I.19 and I.18 are

$I^* < 3.2 \times 10^{-5}$ ft^4

$\theta'_M < 2.3 \times 10^{-2}$ degree

k' < 8.6×10^4 ft-lbs

And by the relations I.13 and I.11

$\theta''_M < 0.048°$

k" < 3.9×10^4 ft-lbs

Now that a value for k" has been found, the period, τ, for the detector support section of the main arm can be evaluated

$$\tau = 2\pi/\beta$$

Where $\beta = (k''/I'')^{\frac{1}{2}}$

But I" is evaluated above as

$$I'' = 62.5 \text{ slug-ft}^2$$

Therefore

$$\tau = 0.25 \text{ sec}$$

Those results show that the final design of the detector support has an oscillation with a magnitude at the end of the arm of 0.05 degree and a period of 0.25 sec. when it is stopped in the fast mode.

I.5 Readout of the Main Arm Position--Figure I.3

There are two different devices used to indicate the angular position of the main arm. First there is a vernier dial (J). The primary scale is 5-1/2 inches in diameter and is divided every 0.05° of table rotation for a total of 4 degrees. The vernier scale subsequently can be used to divide each of these divisions by ten resulting in 0.005° as the smallest division. This readout is fastened to the worm wheel shaft on the rotary table and provides the most direct readout of the arm position. The second mode of

readout incorporates a synchro-motor (K) (8) which is attached directly to the motor shaft through an Oldham flexible coupling (9).

An estimate of the errors in the digital readout system was made considering only the backlash in the gear systems involved.

1) Main drive spur gears--0.005" (Ma 64, p. 693), 0.0007°
2) Worm gear--0.0010" (I.17.a) 0.016°
3) Digital counter gear train--0.001" (Ma 64, p. 697) 0.0013°

The total error is the algebraic sum of these since backlash errors are accumulative--0.018°.

The error that might be expected is 18 minutes for each synchro motor* or a total error of 25 minutes in the pair. This corresponds to an error for the readout system of 0.0014°. This was added in quadrature to the backlash errors giving an estimate of the total error of the readout system of about 0.016°

I.6 Central Column--Figure I.5

The central column consists of two sections of welded steel construction. The lower section (A) is bolted to the rotary mill table (B). The upper section(AA) is bolted to the lower at the flange (C). An off-set is machined in

*Bendix Synchro Engineering Catalog #25.

I.5 Section view of central column: A - Lower column section, AA - Upper column section, B - Rotary table, C - Flange, D - Tapered roller bearing, E - Tapered roller bearing, F - Secondary arm hub, G - Bearing nut, H - Secondary arm, I - Vernier scale, II - Tapered roller bearing, J - Bearing nut, K - Clamp, L - Clamp housing, M - Clamp, N - Clamp shaft, O - Miter gears, P - Target well, Q - Ball bearing, R - Clamp, S - Target shaft, T - Connecting rod, V - Worm gear, W - Worm gear, X - Limit switch, Y - Central shaft, Z - Target screw.

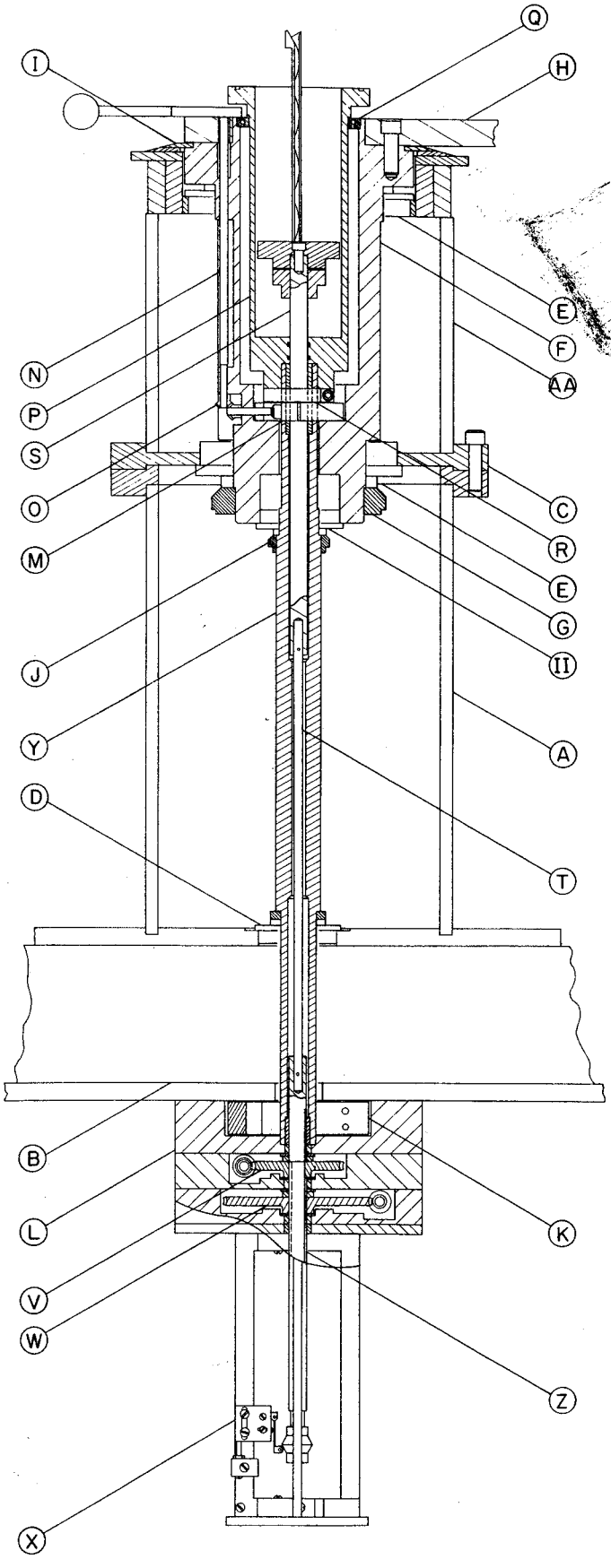
Q
I
H
E
F
N
AA
P
S
O
C
M
R
E
G
J
II
Y
A
D
T
B
K
L
V
W
Z
X

this flange to insure the radial alignment of the two column sections relative to each other. A hardened steel dowel is also located in this flange to provide a secure coupling of the two sections.

In the lower flange of the lower section is located a taper roller bearing (C) (10). The seat for this bearing was machined to be concentric with the alignment seat of the upper flange. The lower surface of the lower flange was also machined to be perpendicular to the axis of the column.

There are two tapered-roller bearings (E) (11) (12) located in the upper column section. The bearing seats are machined to be concentric with each other as well as concentric with the lower flange seat of this column section at (C). These bearings are used to support the secondary arm hub (F). The bearing nut (G) on the lower end of this hub is used to tighten the hub in the bearings.

The secondary arm (H) is fastened to this hub with four 3/8-16 machine screws. This arm is made from a 3/4 inch thick, 6061-T6 aluminum plate. It has a maximum radius of 21.5 inches. There are 1/4 inch, inside diameter hardened-steel, drill bushings inserted into the top of this arm. These bushings are located every 3 inches on three radial lines separated by 15°, each of which intersects the axis of rotation of the arm. This intersection is insured by a close clearance fit of the arm and hub.

The angular position of the secondary arm is indicated relative to the main arm by a vernier scale (I). The scale is fastened to the main arm and is scribed every degree. The vernier contains four indices and is located by a slip joint on the hub allowing the position of the arm to be read to 0.1". This part can be locked in place by a locking screw in the secondary arm plate.

There is located in the bottom of the hub another tapered-roller bearing (II) (10). Between this bearing and the one located in the bottom flange of the lower column section is located the central shaft (Y). The bearing nut (J) is used to adjust these bearings so that there is no radial or axial play of the central shaft. This nut is adjusted through a 1/2 inch hole in the side of the lower column section (A).

The central shaft extends up into the interior of the hub. This shaft is also hollow and contains a 1/2 inch inside diameter, 2 inch long, hardened steel, drill bushing in the upper end. The lower end of the central shaft extends through a 1 inch diameter hole in the rotary table (B) into a 1-1/2 inch thick anchor assembly.

This anchor contains a 4 inch diameter, brass, split collar (K) which is clamped to the shaft. This collar has a tab which is then clamped between two colinear bolts in the aluminum plate (L) which is in turn bolted to the secondary base plate. The result of this assembly is to

provide a shaft (Y) which is fixed to the base and extends up through the center of the central column.

The secondary arm can be clamped to the stationary central shaft by the use of th split clamp (M) located inside the hub. This clamp is activated through the shaft (N) and the miter gears (0) (13).

Located inside the hub is the target well (P) which is a part of the vacuum chamber containing the targets. This well is held in alignment at the top by a ball bearing (Q) (14). At the bottom it is clamped to the central shaft by a split brass clamping collar (R).

There is a hole in the bottom of the target well which contains a double O-ring seal allowing the 1/2 inch diameter target shaft (S) to enter the vacuum system. This shaft is made from drill rod which was specially ground to fit the drill bushing in the top of the central shaft and is straight, to 0.3 mil, over its entire length. A tapered length of drill rod was also made to screw into the top of the target shaft to facilitate the insertion of the shaft through the O-ring seal.

The need for the 2 inch drill bushing is apparent at this point. A certain amount of clearance between the bushing and shaft is necessary in order to have a slip fit. The beam line, however, is 9 inches above the drill bushing in a typical experimental configuration. Since the drill bushing provides the alignment for the target

shaft, there is an amplification at the beam height of the play in the bearing. To decrease this effect for a given clearance it is sufficient to increase the length of the bearing used.

I.7 Target Drive--Figure I.5

The target shaft (S) is pinned to a 1/4 inch diameter shaft (T) which extends to the lower end of the central shaft. At this location the target screw shaft (Z) is pinned to (T). This target screw contains a 1/2-10 Acme thread. There is a keyway located along the side of this screw to accommodate a 1/8 inch square key.

The target drive contains two similar sections, one for the target height and one for the target angle. Each of these sections contains a worm gear assembly. One end of each worm wheel shaft is connected to a drive motor system and the other end is connected to a synchro motor (15).

The target angle, 60 tooth worm gear (V) (16) was modified to contain a 1/2 inch bore with an 1/8 inch keyway. The target height, 100 tooth worm gear (W) (17) was modified to contain a 1/2-10 Acme internal thread.

The drive motor for the target angle is a Slo-Syn #SS50-1001 bifilar motor. This motor is used both in AC synchronous and DC stepping modes. To run this bifilar motor in an AC synchronous mode, a 24 Volt, 1 Amp, power supply is used with a phase shifting network consisting of a 2 Ohm, 25 Watt resistor and a 50 mf, 100 VAC capacitor.

The drive motor assembly for the target height consists of two motors coupled by a magnetic clutch (18). The fast motor is an 1800 RPM, 22 oz-in torque, Globe synchronous motor (19), while the other is a 72 RPM, 50 oz-in torque, Slo-Syn motor #SS50. These two motors use only 110 VAC power. In the AC synchronous mode the bifilar motor drives the target at 432°/min. In DC stepping mode, 20 steps/sec are applied to the motor driving the target at 36°/min.

The Slo-Syn motor in the target height drive moves the target at 0.072 inches per minute. The Globe motor provides a motion of 1.800 inches per minute.

Below the target drive units is located the target position, limit switch assembly (X). This unit consists of five microswitches, two of which define the upper and lower limits of travel and three of which define the vertical positions for three targets. These switches are activated by a cam fastened to the lower end of the target screw (Z). Each switch is mounted so that it can be adjusted in its vertical position as well as in its horizontal position relative to the cam.

I.8 Target Holder--Figure I.5

The target holder consists of two parts fastened to the target shaft. There is a steel collar which is fastened to the target shaft with a brass set screw. This collar has a tongue on it which meets with a groove in the ladder

base and prevents any rotation of the target ladder relative to the target shaft.

The target ladder is a U-frame structure which accepts 6 inches of target frames that are 1/16 inch thick and 2 inches wide. The bottom of this U-frame fits over the target shaft and rests on the steel collar. A short 1/4-28 machine screw goes through a hole in the ladder base and screws into the top of the target shaft. This method of fastening the ladder to the shaft permits the ladder to be easily removed or fastened in place while the target shaft is in its lowest position inside the target well. It also provides a secure location of the ladder on the shaft.

The sides of the ladder contain grooves in which are located bent, phosphor-bronze springs. These springs provide the necessary tension to hold the target against the edge of the groove. The upper ends of the sides of the ladder contain a lead which facilitates the insertion of the targets into the ladder.

I.9 Target Chamber--Figure I.6

The target chamber shown in Figure 2.2D is a section of the goniometer which depends on the experiment for the exact design which is used. For this reason it was constructed in such a way as to facilitate modifications for various requirements.

The target chamber consists of three basic aluminum components. The top and bottom have general usefulness

I.6 Section view of the target chamber and sliding vacuum seal: A - O-ring, B - Ball bearing, C - Spacer ring D - Clamping strap, E - Exit port core, F - Spacer, G - O-ring, H - Spacer, I - Spacer, J - Exit port vacuum flange, K - Exit port clamp, L - Spacing collar, M - Ball bearing, N - Torque coupling.

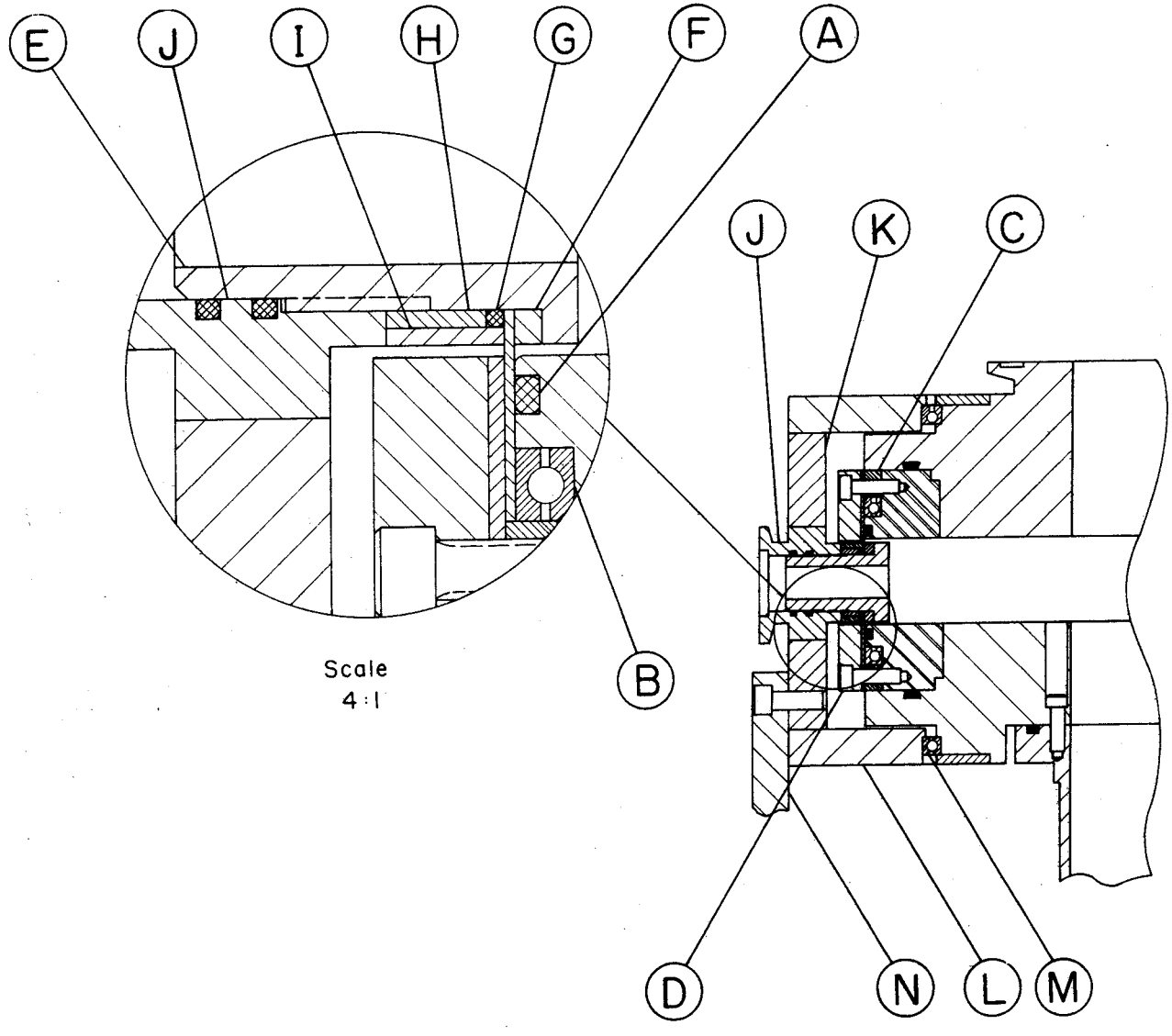
E
J
I
H
G
F
A
J
K
C
B
D
N
L
M
Scale
4 : 1

while the median plane section has a configuration which depends on the experimental requirements. The bottom mates with the top of the target well (Figure I.5P) through an O-ring seal. These two sections are bolted together with four, 10-32 machine screws. On the upper surface of the bottom section there is a 6.625 inch diameter O-ring located in a dovetail groove. This forms the vacuum seal between the bottom and median sections. The top section has a similar construction as the bottom except that it contains a 4 inch Marman flange which is the type of standard coupling used in the beam line.

The center section of the target chamber which was used for this thesis work will be described here. This section is 8 inches in diameter and contains various beam entrance and exit ports. There are two fixed monitor ports--one at -45° and one at -135°. These ports consist of KF-10 Leybold vacuum flanges.

The beam input port consists of a coupling which fastens to the standard beam pipe and tapers down to slip into a 1 inch diameter hole in the target chamber through a double O-ring seal. The inside of this coupling has a 6 inch section of 1/2 inch diameter hole through which the beam must pass. To facilitate the alignment of the beam into the chamber, there is an insulated, 9/16 inch inside diameter, annular, tantalum slit located just before this restricted section.

The final beam port is for the scattered beam. This port is a slot in the side of the chamber extending from -15° to +177°. There is an O-ring groove 1/16 inch outside of this slot on the outside surface of the chamber. This port can be used in two basically different ways. One utilizes a foil window for the beam to pass through while the other incorporates a sliding vacuum seal similar to a type that has been used before (Fe 66) (Bo 67).

The details of the sliding vacuum seal are shown in Figure I.6. Above and below the O-ring groove (A) is located a 1/4 inch wide ball bearing (B) (20). Beyond these bearings are located removable spacing rings (C). The seal strap used is 10 mil stainless steel and covers the entire slot area and the two bearing surfaces.

The clamping strap (D) provides the O-ring compression. This strap contains a slot which has the same dimensions as the slot in the target chamber. There is a piece of 20 mil Teflon sheet between the clamping strap and the stainless steel strap. The clamping strap and Teflon are bolted to the target chamber through holes in the spacing rings (C). When the bolts are tightened this assembly provides the proper O-ring compression. The stainless steel strap is clamped between the Teflon and the ball bearings. The bearings move with the seal strap and the strap slides on the Teflon as the seal is moved.

The scattered beam port coupling is inserted into the stainless steel strap. The necessary torque to move the seal is supplied to the strap through this exit port coupling. To facilitate the replacement of the seal strap, this coupling utilizes an O-ring vacuum seal.

The core of this coupline (E) is made of stainless steel and contains a shoulder on the portion extending inside of the seal strap. Between this shoulder and the strap is a spacer (F) which has an 8 inch diameter. cylindrically curved surface on the side in contact with the seal strap. On the opposite side of the strap is located a 1/16 inch O-ring (G) and beyond that another spacer (H) which has a cylindrically curved surface in contact with the O-ring. Finally, there is a spacer (I) which slides over the spacer, (H) and the O-ring (G) and is in contact with the seal strap on a cylindrically curved surface. The final component is a brass thrusting collar and KF-20 Leybold flange (J). The collar is threaded onto the core (E) and presses against the ends of the two spacers (H) and (I). There is a double O-ring seal between the collar (J) and the core (E).

When this beam port coupling is properly assembled the seal strap is clamped in place and a vacuum seal is formed. The strap is clamped between the spacers (F) and (I). The vacuum seal is formed by the O-ring (G) and the two spacers (H) and (I). The spacer (I) produces the compression of the O-ring against the core while the spacer

(H) produces the compression against the seal strap. This type of coupling limits the smallest obtainable forward angle to about 20°.

The thrusting collar (J) fits into a clamping plate (K) which is then bolted between the two collars (L). These two collars fit over ball bearings (M) (21) which are located on the top and bottom of the target chamber. When the sections (J), (K), and (L) are rigidly bolted together, the exit port coupling is secured at a fixed radius. As a result, one does not have to worry about bending the thin stainless steel strap or breaking the seal by inadvertently moving the exit port.

The torque needed to move the sliding vacuum seal is supplied by the main arm through the coupling (M) to the clamping plate (K). In order to move the sliding vacuum seal, a fair amount of force is necessary. This force can be supplied to the seal strap by the main arm. A counter-torque, however, must also be supplied to the target chamber body to prevent it from rotating with the seal. In the original design this torque was to be supplied through the split ring which clamps the vacuum chamber to the fixed central shaft (see Figure I.5R). It was found, however, that this clamp could not be tightened sufficiently without restricting the movement of the target shaft in the very close fitting bushing located in the upper end of the central shaft.

Since this was the case, the needed torque had to be supplied from some other source. This other source is the coupling between the target chamber and the beam line. There is some play, however, between this coupling and the target chamber, and as a result, the target chamber did rotate a few degrees when the seal strap was moved.

This sliding seal was originally designed to be used with an internal Faraday cup. Some preliminary work, however, showed that this method of charge collection is, in general, not compatible with many types of experiments for which this system is to be used. The alternative method of charge collection for this target chamber is to run the beam through the stainless steel strap into an external beam dump. This method was found to produce background levels that were too high for many types of experiments.

The thin foil, exit port construction is a simple structure in comparison to the sliding vacuum seal. This window utilizes the clamping strap of the sliding seal (Figure I.6D). This strap is clamped to the target chamber through the holes in the spacing ring (Figure I.6C), and the vacuum seal is formed between the O-ring and the inside surface of the strap. A thin foil is glued to the outside of the strap. This is the type of window that was used for this thesis experiment and further details of the particular window that was used will be given in section 3.2.a.

From the above description of this 8 inch diameter target chamber, it can be seen that there are features which limit its usefulness. These features include its fixed monitor ports, its lack of a primary beam, exit port, the limit of 20° as a minimum scattering angle attainable, and the need for additional countertorque for the sliding seal.

In an attempt to improve this system, a 16 inch diameter median plane section was designed (Ma 69). This new chamber has a sliding vacuum seal with an angular range from 8° to 110°. The design of the chamber, however, allows the detectors to cover a range from 8° to 172° if necessary by permitting the inversions of the median plane section for the angles from 90° to 172°. The reduced range of the seal was used in order to keep the necessary torque requirement for moving the seal at approximately the same value as that needed for the 8 inch chamber. There is also a fixed port at the beam exit which has a design that is similar to the input port used for the smaller chamber. Provisions were also made to supply the counter torque for the vacuum seal by coupling the chamber to an anchor post.

Details of this larger target chamber are not given here since this was not included in the original system. It is mentioned here, however, to show the utility of the modular design concept.

I.10 Target Lock--Figure 2.2E

Fastened to the Marman flange on the top of target chamber is the target transfer and hold lock. The lock assembly consists of three aluminum units--a ported vacuum coupling, a vacuum valve, and a small chamber containing a transfer operation.

The next section is a vacuum valve similar in construction to a ball-type valve. This valve has a cylindrical aluminum core which contains a 3/4 x 2-1/2 inch slot which aligns with a similar slot in the valve housing when the valve is opened. At each end of the core there are O-ring seals. There are also two O-ring grooves located on the surface of the core 90° on either side of the slot. These two O-rings are glued in place using Eastman 910 adhesive. These seals are shaped in such a way as to encircle the hole in the valve housing when the valve is closed. This arrangement of O-rings allows the valve to be used in either direction. The only fact that unsymmetrizes this valve is the existence of a KF-10 Leybold vacuum fitting in the valve housing on one side of the valve permitting that side to be evacuated with an external pump. Dow Corning high vacuum silicone grease has been successfully used in these valves.

When this valve is closed and evacuated there is a double O-ring seal between vacuum and atmospheric pressures. This arrangement of O-rings can cause some problem, however, if certain precautions are not taken. To be specific,

there are isolated regions between the valve core and housing when the valve is either fully opened or fully closed. Because of this, the vacuum can be broken when the valve core is turned for the first time after evacuation. To prevent this from occurring, it is sufficient to turn the valve to the half-opened position while evacuating the valve.

Using one valve in the target lock permits the insertion of targets into the vacuum chamber without breaking the vacuum. The use of two valves, on the other hand, permits the transfer of a target without exposing it to the atmosphere.

The third section of the target lock is a small, cylindrical, vacuum chamber. In the top and on the axis of this chamber there is a target transfer mechanism. This mechanism consists of a 3/16 inch steel rod inside of a 5/8 inch steel shaft. The larger shaft enters the top vacuum chamber through a double O-ring seal while the smaller enters the vacuum chamber through a double O-ring seal in the top of the larger shaft.

The part which grasps the target frame is a split, conical, phosphor-bronze jaw. This fits into a conical hole in the lower end of the 5/8 inch shaft. The smaller shaft is screwed into the top of the jaw and is spring loaded to keep an upward pressure on the jaw mechanism.

The transfer of a target into the target chamber is accomplished by placing the target in the transfer jaws while depressing the inner shaft. Releasing this shaft allows the spring to tighten the jaws on the target frame. The chamber is then fastened to the top of the valve and evacuated. The valve is opened and, while being sure that the target is aligned properly, the target is lowered through the hole in the valve and into the target ladder. A clamp around the shaft is provided on the top of the vacuum chamber and prevents the transfer shaft from being unexpectedly drawn into the evacuated chamber.

I.11 Detector Carriage--Figure 2.2F

The detector carriage consists of a base and a LN_2 dewar. The exact configuration of the base depends on the experiment which is to be done. The primary base component consists of an aluminum block which rests on the dual beams of the arm. In that portion of the block which rests on each beam is located 6, 1/4 inch inside diameter, hardened steel, drill bushings spaced at 1 inch intervals. A steel dowel on each side of the base is used to align one of these bushings with one of the bushings located in the beam itself thus fixing the radial position of the detector mount with respect to the target center. The surface of the base which comes in contact with the beam surfaces is covered with a self-adhesive, felt cloth which prevents

the beam surface from being scored while moving the detector carriage over it.

The LN_2 dewar is a welded stainless steel construction large enough to hold two vertical cryostat, detector packages. The inner wall is a 1/32 inch thick tubing and the outer wall is 1/16 inch thick tubing. There is a bellows vacuum valve on the side of the dewar which permits evacuation when necessary. To aid in the thermal insulation of the dewar, the outside is wrapped with two layers of 5 mil polyethylene sheet and heavy aluminum foil. These in turn are wrapped with a heavy, 3 inch wide plastic adhesive tape.

The best performance of the dewar was obtained when it was pumped out with a diffusion pump (D.P.) for several hours. The pressure obtained at the D.P. was about 6×10^{-7} Torr. During the pump down the dewar was also heated with an air gun to permit the outgassing of the inner walls. Having done this, it was found that the dewar had a pot life of about 12 hours which gives a useful lifetime of about 10 hours in an experimental setup using two detector packages simultaneously.

The form of the detector mount support which is used on the base depends on the detector setup used in the experiment. The original support was designed for a single detector package. This consists of a detector clamp which is bolted onto an aluminum block which slides for 1 inch on

two parallel steel rods mounted in the base. This slide in conjunction with the drill bushings permits the detector to have a continuously variable radial position over the useable region of the main arm.

The second detector support is designed to hold two detector packages side by side with a separation of about 20° at a radius of about 9.5 inches. The detector clamps are independently mounted to the base and have a total of one inch of radial adjustment.

I.12 Local Power Supply

The necessary AC electrical power needed for the various driving motors is supplied from a local power supply located in the experimental area. This supply is connected to the goniometer drive unit by three 20 AWG, 15 conductor cables in a bundle and a 48 pin connector.

This power supply along with a power distribution chassis are totally enclosed in a mobile, steel rack. The fact that these are totally enclosed helps to isolate the other electronics in the experimental area from the contact noise arising from the relays in the chassis. These relays are used in the selection of motor speed and direction, in the automatic target selection system, in the limit switch circuits, and in the main 110 VAC control circuit. There are also two time-delay relays used in the fast motor reversing circuits for the main arm and target height drives. These relays are incorporated to prevent

the instantaneous reversal of the motor direction. Instead, there is a two second delay between the time the reversal signal is received and the power is turned off and the time that the power is reapplied in the reverse direction. The contacts of the relays which control the AC power to the main arm and target angle motors as well as those for the main AC power line are all protected with Thyrector diodes.

The electrical chassis ground in the local power supply is provided through the interconnecting cable from the remote power supply. The goniometer itself, however, is not grounded through its control system. All the 110 VAC circuits which are connected to the remote 110 VAC circuits are completely isolated from the local 110 VAC power.

A local control box, Figure 2.3, fastened to about 30 feet of 22 AWG, 25 conductor cable is connected to the local power panel through a 25 pin connector. This control box is grounded in order to isolate the switch contact noise, and it contains all of the controls which appear on the remote control panel except the automatic angle increment feature of the main arm (see section I.13.a.3.a). In addition to these, however, this control box contains a limit switch override which allows the operator to go past the limit switches for the main arm if he desires.

The controls on this box are in the form of momentary push-button, microswitches (22).

The operation of the buttons on this box are the same as those on the remote control panel except for three cases. First, the red, limit abort button must be used if the arm must be positioned beyond the limit switches. This is accomplished by pushing this button while moving the arm over the limit switch. It need not, however, be pushed to return in a CW direction over the switch which limits the CCW motion, etc.

The other two buttons are the target angle, FAST button and the target height, SLOW button. To permit these buttons to provide a choice of speed at the local station, the operator must set the remote controls for the target angle in the SLOW mode and the target height in the FAST mode.

I.13 Remote Control Station

The remote control station is located in an equipment rack in the data room at MSUCL. This station is connected to the local power supply and control circuits by a series of multiconductor cables and 47 pin connectors. This method of connection was found to be very useful since it allows the control panel to be easily connected either locally or remotely to the other system components. This also allows the entire system to be transported in several, easily managed components.

The remote station consists of four interconnected units--the control panel, a DC motor power supply, an electronics bin, and a power distribution chassis. The chassis ground for the entire system is connected at this location to earth ground.

I.13.a Control Panel--Figure I.7

I.13.a.1 Digital Counters and Driving Systems

The front of the control panel is a 1/4 inch aluminum plate. The synchro motors which indicate the positions of the various elements on the goniometer are connected to identical synchros located on a shelf near the top of the control panel. Each of these motors is then connected to the digital counter by a series of gears mounted on 1/4 inch shafts turning in 1/4 inch, inside diameter, ball bearings (23). The main arm system contains a 1:1 gear train connected to a dual-bank, 4 wheel, digital counter (24) giving a least count of 0.02°. The zero on this counter corresponds to a scattering angle of 0.0°. The readings increase in either direction from this point allowing the lab scattering angle to be directly read on the counter.

This counter, as well as the others, are connected to the gear train through a friction coupling (25). This allows a hand-wheel to be attached to the counter shaft permitting the zero to be easily set when necessary.

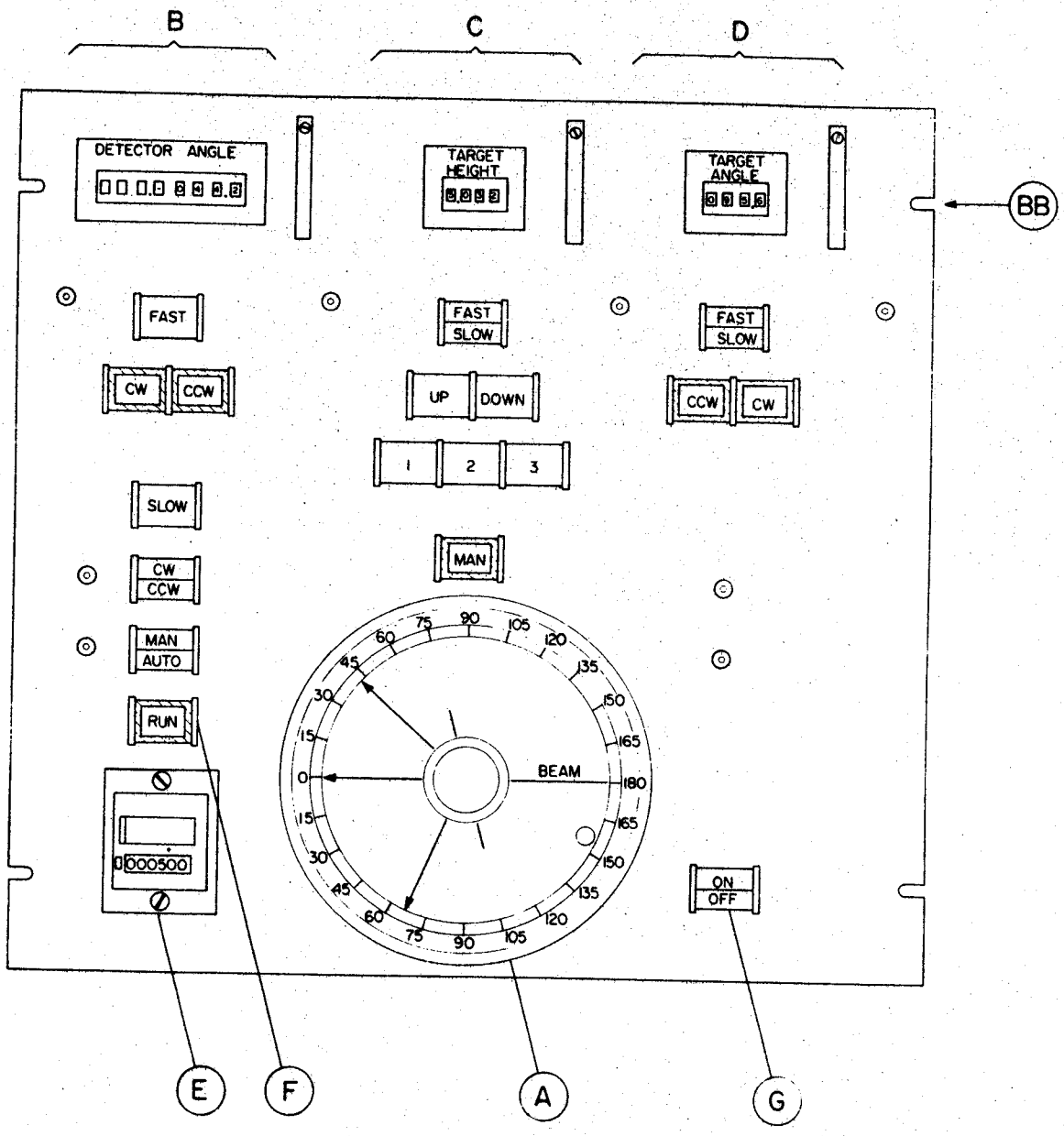

I.7 Remote control panel: A - Graphic display, B - Main arm controls, BB - Digital counter windows, C - Target height controls, D - Target angle controls, E - Preset digital counter, F - Run button, G - Main power switch.

These hand-wheels penetrate the front surface of the control panel by about 1/8 inch, and each has a protective, movable cover to prevent the accidental movement of the wheel.

The target angle system has a 1:6 gear train connected to a 4 wheel digital counter (26) giving a least count of 0.02°. The target height system has a 10:1 gear train connected to a 4 wheel digital counter (26) giving a least count of 0.2 mil. This gear system also contains an electromagnetic brake system. This brake was found to be needed because of the tendency of the synchro motors to go into a free running mode when the drive was started or stopped while using the fast operating mode. This brake is released only when the target height, drive motor is activated and is immediately applied when the drive is stopped. A braking action is also utilized on the goniometer itself in the target height drive system. Here the high residual torque of the Slo-Syn motor used in the drive system is utilized by activating the electromagnetic clutch between the two motors whenever the fast motor is turned off.

The digital counters are viewed from the front of the control panel through cylindrical lenses (27) mounted in blackened frames, (BB), and through blackened masks which incorporate the decimal points. The lens and counter spacings provide for an approximate magnification of 2 for the

numbers on the counter wheels. Each of these digital counter systems includes a 24 VAC incandescent lamp for illumination of the digits.

I.13.a.2 Graphic Display--
Figure I.7A

Coupled into the gear systems which drive the counters for both the arm and target angles are two small sychro motors (28). These motors are used to drive the synchros in a graphic display system located in the control panel (A). This display provides a pictorial view of the relative angular positions of the main arm, the manually positioned arm, the target, and the incident beam direction. Each of these elements is represented in a plexiglass disc by an engraved line which has been filled with India ink. These discs were found to be very soft and easily scratched but could be polished with a buffing wheel. This display also contains four 24 VAC incandescent lamps which provide for the illumination of the elements.

I.B.a.3 Push Button Controls

The front of the control panel is separated into 3 sections, one for each drive system. The controls located on this panel are illuminated switches (22). Those switches which initiate the manually controlled motions of the driven elements are distinguished by a red border around the white switch faces. The remainder of the switches are pale orange except for the main power, on-off switch,

which is red. The switches on this control panel which control 110 VAC have 0.05 mf, 1000 VDC, disc capacitors across them to prevent contact noise.

I.13.a.3.a Main Arm Controls--
Figure I.7B

In this case the slow and fast controls are separated into two separate sections. When running in either mode, only those lights in the section for that mode are lighted indicating at a glance which mode is active.

There is an automatic angle increment feature incorporated into the slow mode drive system of th main arm. In this slow mode the arm is moved by the motor operating in a DC stepping mode. To determine the angular increment, it is sufficient to count the steps of the motor driving circuits. This is accomplished by the use of a pre-determined electromagnetic digital counter (E) (29). Each step on this counter represents 0.01° of main arm rotation.

Implementing this system requires that the arm be set at its starting position using either of the driving speeds. The SLOW button is pushed to activate the stepping circuits. The direction of rotation is set as CW or CCW. The AUTO-MAN button is set in the MAN position. The preset counter is set for the desired angular increment and the reset button on the front of the counter is pushed. When the automatic mode is desired, the AUTO-MAN button is set in the AUTO position. This action may also initiate

the motion of the arm; therefore, it should not be pushed until necessary. When the increment is needed, the RUN button (F) is pushed. To make the next increment the counter is reset and the RUN button activated.

To run in a manual mode, the AUTO-MAN switch must be in the MAN position. When the RUN button is then pushed the motor will make 0.01° steps at a rate of 10/second as long as the button is depressed.

It should be recalled at this point that there is a 2 second time delay incorporated into the fast drive reversing circuits (section I.12). Due to this delay, when the arm has been running in a CW direction, for example, and the CCW button is pushed, there will be a delay of 2 seconds before the arm and the digital counter begin to move in a reverse direction.

I.13.a.3.b Target Height Controls--Figure I.7C

The target height controls include a FAST-SLOW mode switch, an UP switch, a DOWN switch, three automatic target positioning switches--#1, #2, #3--and a manual RUN switch. It may be recalled here that there is a time delay in the reversing circuits. If the target shaft is moving in a downward direction, the DOWN switch will be lighted. If it is now desired to have the shaft move upward, the UP button may be pushed. The light, however,

will not come on nor will the counter move until after a 2 second delay.

The RUN button will produce a motion of the target shaft whenever it is depressed. The motion that is produced depends on the state of the three mode switches discussed above.

The three automatic target positioning switches are used in conjunction with the three limit switches mentioned in section I.7. Whenever one of these switches is pressed, the target shaft will move until it activates the associated microswitch. The microswitches were set initially to be activated when the beam height was 1.062 inches above the bottom of the target ladder for target #1, 2.187 inches for target #2, and 3.312 inches for target #3. These locations were chosen such that the incident beam would pass through the vertical center of standard target frames which are 1.125 inches high. These three targets are the first three located just above a 0.500 inch high standard target which rests on the bottom of the target ladder. These locations are properly defined only when the target shaft is moving DOWN and the reference point correctly determined. This reference point, 0.000, is found by running the target shaft UP until it reaches the upper limit switch. The digital counter should then read 9.989 which allows for the 11 mils backlash in the drive system

(see section 2.3.c). The details of the setup of these switches are given in section 2.3.c.

I.13.a.3.c Target Angle Controls--Figure I.7D

The target angle controls include a mode switch--FAST or SLOW--and two directional switches--CW and CCW. The target angle changes as long as one of the directional buttons is depressed. There are no limit switches in this system.

The fast mode was found to rotate the target at too great a speed for convenient use. The slow speed operation was found to be more useful since only small changes are usually made.

I.13.a.4 Main Power ON-OFF Control--Figure I.7G

The main power control switch is located on the lower right side of the control panel. This switch controls all of the power in the entire system. It turns on the 110 VAC power not only for the remote control panel but also for the local power supply as well.

I.13.b. DC Motor Power Supply

The DC motor power supply is located behind the control panel. This supply has an output of 35 Volts at 6 Amps. It is protected with an MDL-4, 4 Amp slow-blowing fuse on the transformer primary and contains a

switch for the 110 VAC input and a pilot light located between the fuse and the transformer primary.

An AGC-4 fuse on this supply was found to be blown at frequent intervals during the early operation with the goniometer. It was believed that this was a result of surges produced when the AC power is switched on or off. This was corrected when the slow-blowing fuse was installed.

I.13.c. Electronics Bin

The electronics bin is also located behind the control panel. This bin is an Elco Varipak card bin and contains a regulated power supply and the logic and power amplifier circuits necessary to drive the DC stepping motors. The stepping logic for each Slo-Syn, bifilar motor is provided by two DTμL9111, parallel gated, clocked flip-flop, integrated circuits. The clock pulses are provided by an oscillator built around a A710c high speed differential comparator, integrated circuit and a differentiating, RC network. The stepping logic and amplifier for each of the two motors is contained on three cards. The amplifiers for the motors are identical even though the power requirements of the two motors are quite different. This was done to facilitate the construction of the circuits and to permit the swapping of cards if necessary from one drive to the other. The Zener regulated power supply which is in this bin contains outputs of +5VDC, -6VDC, +12VDC, and -12 VDC.

I.13.d Power Distribution Chassis

The remote power distribution chassis is located behind the control panel. There is a plug-in, 24 VAC-DC power supply located here. This supply provides the necessary AC power for the 24 Volt incandescent lamps in the control panel and the DC power needed to drive various reed relays in the electronics circuits and the electromagnetic clutch in the target height drive, section I.7.

Since the clutch is a large load on the power supply, its being switched on caused the lamps in the control panel to dim. To prevent this, a dummy load, equivalent to the clutch load, is put on the power supply whenever the clutch is disengaged.

Also located on this chassis is a plug-in card of miscellaneous electronics and reed relays used in the main arm stepping circuits. There are three momentary relays, one of which is a spare, and one latching relay located here. The contacts of the main power relay are protected with Thyrector diodes and 0.05 mf, 100 VAC capacitors. All the relay contacts which switch 100 VAC have 0.05 mf capacitors across them for noise suppression.

Finally, this chassis has a number of multipin connectors into which are fastened cables from the various components of the system. Not one of these connectors is the same as another except where an interchange would cause no problem; this eliminates any question of the way the components are interconnected.

I.14 Surface Finishes

The exposed steel surfaces of the goniometer base and central column were painted first with a steel primer and then with several coats of enamel. The exposed aluminum surfaces of the goniometer base, which do not come in contact with other components during operation, have a sand blasted finish. This surface is easily cleaned and provides a uniform finish of these parts.

The local control box face contains the identifying lettering for the various bottoms. This lettering is engraved into the surface and filled with black ink.

The surface of the remote control panel is also sand blasted. There is no lettering on this surface, but instead the lettering is located on the digital counter window frames, on the switch faces, and on the graphic display components.

I.15 Suggested Improvements

There are certain difficulties that arise due to some features of the target readout and driving systems. First, the digital counters have a least count which is too small for practical use. Second, the target height drive raises the target by too small a distance for each revolution of the motor, resulting in the need for the 1800 RPM motor and the braking system. Also, the target angle drive rotates the target through too large an angle per revolution of the motor. Finally, the need for a

1:6 gear increasing drive between the synchro and the counter produces a limitation of the usefulness of the fast drive mode for the target angle.

The following changes could be made to remedy these problems. The least count on the digital counters could be increased by a factor of 10 by providing for an additional 10:1 gear train for each system. This would give a 100:1 system for the target height and 5:3 system for the angle. The 5:3 gear reduction would be a great improvement over the 1:6 gear increase. The resulting least count for the target height and target angle would be 2 mil and 0.2° respectively, which are more realistic figures.

The remainder of the difficulties could be removed by a redesign of the gear boxes used in the drive system. The type of change that could be made is to replace the 100 tooth single thread worm gear in the target height box with a 40 tooth, 4 threaded worm gear (30) driven by a 200 RPM Slo-Syn motor (31) or a precision Slo-Syn stepping motor (32). This not only reduces the speed of the motor needed but also increases the travel of the target per motor revolution and eliminates the need for a dual motor system.

The 60 tooth worm gear in the target angle drive could be replaced with a 360 tooth worm gear (33). This would provide for a smaller angular change per revolution

of the motor and would also reduce the problems at the digital counter. The fact that the target screw in the drive system is used for both turning and raising the target can also produce some difficulty. This arises from the fact that the target changes in its vertical position for a change in its angular position. The size of the angular change, however, is less than 90° in a majority of cases, this produces a change in height of 25 mils. This is not a serious problem, however, since this can be compensated for if the operator is aware of the peculiarity. Furthermore, in order to eliminate this problem completely would involve a complete redesign of the target drive system resulting in a much more complicated mechanism.

I.16 Documentation

When the goniometer was completed and operated satisfactorily, all of the mechanical and electrical drawings were updated to insure the existence of a complete set of as-built prints which can be used as reference for future modifications or additions. The mechanical drawings of the goniometer drive unit are filed at MSUCL under the project number HA-110 . . . while the electrical and electronics drawings as well as the control panel mechanical drawings are filed under the project number FC-151 . . . .

I.17 Assembly and Maintenance Suggestions

I.17.a Backlash Adjustment of the Rotary Table Gears

Before this rotary table was assembled into the final system, the proper backlash was set for the worm gear drive. It may be necessary from time to time to check this figure and to readjust the table gears. The technique which can be used to set the backlash is the following: First there can be no endplay in the worm wheel shaft. This can be checked by supplying an alternately CW then CCW torque on the rotary table platform and observing if there is any inward or outward movement of the shaft. If there is a movement, a nut inside the housing around the worm wheel shaft must be tightened.

With the worm wheel shaft secure, a dial indicator can be placed to show any motion at the circumference of the table platform. With the indicator in place a CW and CCW torque can be applied to the table, and the movement of the indicator is observed. A movement of about 2 mils was found to produce a smooth operation. If the movement is not around 2 mils, the backlash is adjusted making sure that the four 1/2 inch bolts holding the table to the secondary base plate are loose. The alteration is accomplished by utilizing the adjustment mechanism on the end of the worm wheel shaft opposite the spur gear drive assembly.

I.17.b Assembly of Main Arm Drive

First the rotary table and central column can be assembled loosely with the central shaft extending through the rotary table and beneath the secondary base plate. The central shaft anchor clamp, Figure I.5K, and anchor housing, Figure I.5L, loosely fastened around the central shaft to confine the center of rotation of the rotary table to an acceptable area.

Next, the motor is hung loosely on its mounting screws, and the rear gear box plate is placed over the motor and table shafts. The large gear shaft containing its two ball bearings is placed on the table shaft and slipped into the bearing hole in the gear box plate. The position of the motor can then be adjusted to allow the small gear shaft with its two bearings to slip over the motor shaft and into the box plate when the two motor mounting screws have been tightened. When this adjustment is completed, the rear box plate should be flat against the mounting plate on the rotary table, the motor mounting plate, and the edge of the secondary base plate. The box plate can then be securely bolted into place.

The gear plate is made to rotate about the worm wheel shaft. If, when all the mounting bolts have been tightened, there is a binding of the ball bearings in their respective seats, the motor must be loosened and readjusted so the bearings slip into their seats with only a slight pressure.

Next the gear shafts can be removed and the "rear" brake plate installed. The gear shafts are placed on the respective shafts. The 1/8 inch pin which couples the motor and gear shafts, is inserted with only a small force and held in place with a small set screw. The rotary table can now be bolted in place. The remainder of the assembly is self explanatory from here.

I.17.c Installation of the Main Arm Synchro Motor

For a proper assembly the synchro housing must be concentric with the motor shaft. Access to the clamp used to fasten the Oldham coupling to the synchro shaft is obtained through a hole in the bottom of the housing.

I.17.d Installation of Target Well (Figure I.5)

The collar (R) on the bottom of the target well (P) contains a #10 socket head, machine screw and is adjusted with a special, long handled, allen wrench. Access to the clamp screw is obtained through a hole in the side of the upper column section (AA) and one in the sides of the secondary arm hub (F). The main arm must be rotated to the appropriate position before the two holes and the screw are aligned properly.

I.17.e Assembly of Target Drive and Central Shaft (Figure I.5)

Before the anchor is attached to the central shaft a dial indicator is used to check to see that the central shaft (Y) assembled in the two central column sections (A)(AA) stays fixed when the rotary table is turned through one revolution. If not, the 8, 1/2 inch bolts which hold the central column to the rotary table must be loosened. Then the central column may be shifted on the table platform to insure that the central shaft does not move when the rotary table is rotated.

Now the central shaft (Y) can be removed from the central column assembly by unbolting the flange (C) and loosening the clamps (J and R). The target screw (Z) which is pinned to the connecting shaft (T) by a tapered pin, which does not extend above the surface of (T), is inserted into the lower end of the central shaft. The target shaft (S) is greased and very carefully inserted into the top of the central shaft being careful not to get any dirt in the grease. Shaft (S) can then be pinned to the shaft (T) through a hole in the side of (Y) using a tapered pin which does not extend above the surface of (S). Making sure that the bearing nut (G) is tightened and the bearings lubricated, the central column can be reassembled at flange (C) making sure that there is no dirt on the flange surfaces.

The clamp ring (K) is attached to the lower end of the central shaft about 1/32 inch below the secondary base plate and tightened securely. The aluminum anchor plate (L) is bolted in the secondary base plate. The same bolt in (L) can be tightened onto (K) now that was loosened during disassembly, preventing any assymmetric loading of the parts.

The two target drives can be assembled straight forwardly. The target angle drive assembly is placed in the proper orientation under the anchor block while the target shaft is in its highest position. It can then be raised so that shaft (Z) goes through the worm gear. The 1/8 inch key, which has well rounded leading and trailing edges, is placed in the keyway in (Z). (Z) is then oriented to permit the key to enter the worm gear. The assembly is then raised to meet block (L) and securely bolted in place taking care not to cause the target screw to bind.

In order to provide enough room for the target height assembly to fit between the fully raised target screw and the main base plate, the secondary table must be loosened and raised a little. Having done this, the target height drive can be located beneath the target screw shaft. The assembly is now raised so that the screw enters the worm gear. By activating the target angle drive, the screw shaft can be slowly screwed through the gear and beyond the bottom of the housing. This assembly can then be raised

bolted to the target angle housing taking care not to cause binding to the target screw.

The 1/4 inch plate of the switch assembly is then bolted to the rest of the drive. The switch mount assembly can finally be placed in position through the hole in the main base plate and bolted to the 1/4 inch mounting plate.

I.17.f Electrical Fuses

		Fuse #
1.	Local Power	
	a. Main power	AGC-10
	b. Main Arm	MDL-6
	c. Target Angle	MDL-1/2
	d. Target Height	MDL-1
2.	Remote Power	
	a. Main Power	AGC-8
	b. 35 VDC Motor Power Supply	MDL-4
	c. Electronics Bin (on back side of bin)	AGC-1
	d. 24 VAC-DC power supply	AGC-1/2

I.17.g Lubrication

The rotary table, section I.3.a, contains a dipstick to check the oil level in the internal reservoir. The oil contained in this table is a heavy oil (Sunoco way oil) and should be checked once a month. There are also three other points which need to be oiled once a month. Two have access through holes on the edge of the table platform, and

the third has access through a hole located on top of the worm wheel drive shaft just outside the table housing.

The lubrication which is used for the target shaft (Figure I.5S) is a 2:1 mixture by weight of Apiazon L vacuum grease and Welch, Duo-Seal, mechanical pump, vacuum oil. Care must be taken when greasing this shaft that no dirt is allowed to get into the grease which could cause a ceasure of the shaft in the hardened bushing in the top of the central shaft.

The target screw shaft (Figure I.5Z) is lubricated with a light, good quality machine grease every two months. This is done by lowering the target shaft to its lowest position and applying the grease to the exposed threads.

When the target drive, worm gear boxes were assembled, grease was packed around the worm gear. The shaft bearings in this mechanism are oil impregnated and, therefore, need not be checked. Once a year grease can be pumped into the worm gear cavities through the hole in the side of each housing containing a small brass plug.

The bearings used in the remote control panel are all either ball bearings or oil impregnated bronze. Therefore, the only lubrication which is necessary is to apply a small amount of light grease to the teeth of the gears once every six months.

Finally, in order to prevent them from rusting, the hardened drill bushings in the main arm, the secondary arm,

and the detector carriage, should be swabbed with a light oil or preferably a rust preventative oil* after every use.

I.18. List of the Major Components

This list contains information concerning those components of special interest mentioned in the text.

Part No.

1. Bridgeport Machines Inc., Bridgeport, Conn.
2. Superior Electric, Bristol, Conn.
3. Boston gear # GD 29
4. Boston gear # GD 116
5. New Departure #3305
6. New Departure # 3307
7. Torrington #NTA 1423, #TRC 1423, # TRD 1423
8. Bendix synchro transmitter, MK.10, Mod. 4, Type 3HG
9. Pic # T3-3
10. Timken #15520B
11. Timken #L624510B
12. Timken #47825B
13. Boston #G462Y
14. Split Ballbearing #45-56-P
15. Henschel synchro transmitter MK.6, Mod. 9, Type 5HG
16. Boston #G1040
17. Boston #G1049
18. Simplatrol #FFK-43

*DoALL, rust preventive mist

19. Globe #CLCLL 142A146
20. Realistim #KA75CP
21. Realistim #KA60XP
22. Micro Switch, Freeport, Illinois.
23. New Departure #R-4
24. Durant #4-4-Y-8823-R-CL
25. Pic #R3-3
26. Durant #4-Y-8823-R-CL
27. Edmond Scientific Co., Barrington, N. J.
28. Arma synchro motor MK.8, Mod. 1B, Type 1F.
29. Hecon #FA-043-6-1-10-12-DC-2-C
30. Boston Q1344
31. Slo-Syn #HS50
32. Slo-Syn #TS50
33. Pic #Q1-13.

APPENDIX II

CALCULATIONS OF THE ANGLES IN REFERENCE I USED FOR THE MAIN ARM CALIBRATIONS

See Figures II.1 and 2.5 for the definitions of the various quantities. Assuming a perfect 90° triangle:

$$\cos(a) = B/H \qquad \text{II.1}$$

$$\sin(a) = A/H \qquad \text{II.2}$$

$$\cot(d) = B'/A' \qquad \text{II.3}$$

$$B' = B - X\cos(a) = X\,B/H$$

$$A' = X\sin(a) = XA/H$$

Therefore:

$$\cot(d) = \frac{B}{A}\left(\frac{H}{X} - 1\right) \qquad \text{II.4}$$

The quantities used in equation II.4 were:

A = 32.000 feet

B = 33.500 feet

H = 46.327 feet

X = n·(7.000 feet) where n = 1 to 6

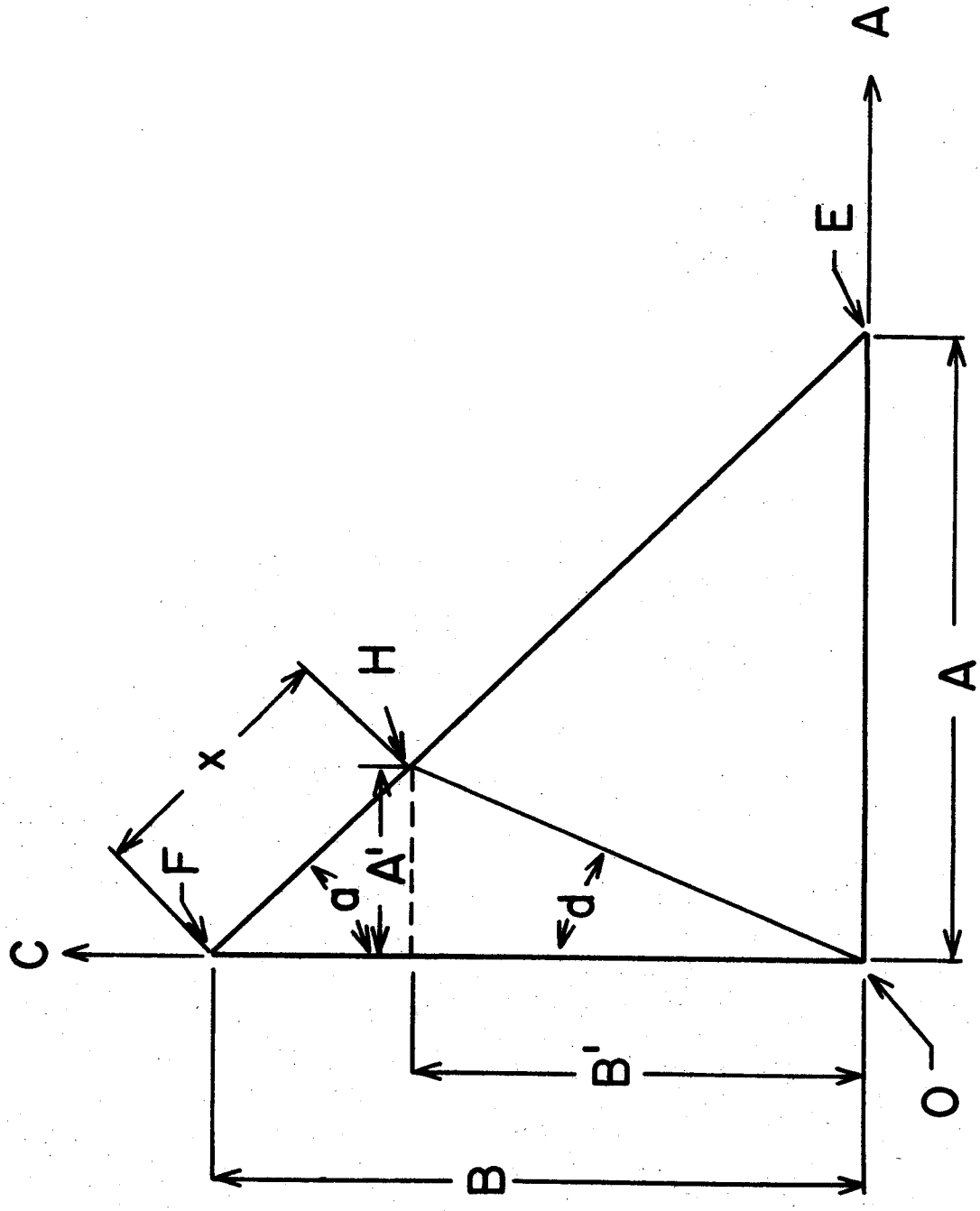

II.1 Schematic of the geometry used to calculate the angular position of the primary points of reference I used in the calibrations of the main arm.

APPENDIX III

COMPOUNDING OF THE ERRORS IN THE POINTS FOR THE MAIN ARM REFERENCE ANGLES

A. The sources of the errors in reference I and the size of the uncertainty in each case is broken down in the following summary. The "adding" of errors was done in quadrature in all cases. It might also be noted here that the errors used in this section are the result of empirical measurements. That is, the errors shown in the majority of the cases are the results of estimates of the maximum errors in the measurements. These errors are hard to compare with standard errors but they will be considered pessimistic estimates of the standard errors.

1. Points A and B, Figure 2.5
   a. Alignment of the scope between the two points 0.021" at 132'
   b. Center point, O, Figure 2.5
      1). 0.010" for transit errors
      2). 0.005" for errors in the placement of the point.

      Total center error is the sum of b(1,2)

      0.011"

Adding the results of 1a and 1b, the total error for points A and B about the center point is:

0.016" at 66' or 0.0012°.

2. Points C and D, Figure 2.5

   a. These points depend on how well the line between points A and B was defined by the line of sight of TR #1.

      0.0012°

   b. Alignment of the cross hair in TR #2 with:

      1). Pointer--0.005" at 8' 0.0031°

      2). Center point--0.005" at 24' 0.001°

      3). Pointer image--0.015" at 40' 0.0018°

      Total error in the perpendicularity of the line of sight of TR #2 to the line of sight of TR #1 is the sum of results of b(1,2,3). 0.0036°

   c. Placement of the targets on the line of sight of TR #2.

      0.020" at 70' 0.0014°

   d. Center point location errors

      0.010" at 35' 0.0014"

      Total error of point C and D about the center point is the sum of 2(a,b,c,d): 0.0043°

3. Point E, Figure 2.5

   a. Error in line AB 0.0012°

   b. Alignment of TR #1 on line AB--0.010" at 66' 0.0008°

c. Transfer of point to the floor--
0.005" at 32' 0.0004°
The total error of point E about the
center is the sum of 3(a,b,d) 0.0015°

4. Point F, Figure 2.5
a. Error in line CD 0.0043°
b. Alignment of TR #1 on line CD--
0.005" at 35' 0.0008°
c. Transfer of point to floor--
0.005" at 33.5' 0.0008°
The total error of point F about
the center is the sum of 4(a,b,d) 0.0044°

5. The 90° angle between lines OE and OF, Figure 2.5. The error about the center in this angle is the sum of the errors in points E and F 0.0047°

6. Checks of consistency of transit and scale measurements---A check was made to see how well the tape and transit measurements compared for the 90° triangle constructed on the floor. Also the sensitivity of the checking procedure used was examined.

The points E and F were located on the floor and the error in the 90° angle was determined---0.0047°

a. Comparing tape and transit measurements---The linear tape was used to measure the distances, A and B, from the center point to points E and F

respectively and the distance H between the points E and F. The source of error which was considered in the linear measurements was that which arises because of different tensions applied to the tape during the measurements. A vernier caliper was used to measure the differences in the measurements due to variations in the tension of the tape. The variations in the measurements in a 32 foot length were found to be ±0.012". This is the error which is associated with each linear measurement. The other sources of errors will be checked in the following paragraphs.

If it is assumed that the central angle is exactly 90° then

$$A^2 + B^2 = H^2$$

$A = 32.000 \pm 0.003$ feet

$B = 33.500 \pm 0.0013$ feet

$H = 46.327 \pm 0.0010$ feet

$A^2 + B^2 = 2146.25 \pm 0.120$ feet^2

H (calc) $= 46.438 \pm 0.001$ feet

This demonstrates that the transit and the tape measurements were of equal quality and that the assigned error is not a bad estimate.

b. Sensitivity of check 6a---In checking 6a it was assumed that the central angle was exactly 90°. The question remains as to what size of error in H might be expected for the size of error determined for the 90° angle.

Considering Figure I.5:

$$H^2 = A^2 + B^2 - 2\,AB \cos\theta$$

Where $\theta = 90° + \phi$ for ϕ small

Also

$$A \simeq B$$

Then

$$H^2 \simeq 2B^2\,(1 + \phi)$$

$$H \simeq \sqrt{2}B(1 + \frac{\phi}{2})$$

Therefore the difference in H due to the error, ϕ, is

$$\Delta H \simeq B\sqrt{2}\,\frac{\phi}{2}$$

For $\phi = 0.0047°$ and $B = 32$ feet

$$\Delta H \simeq 0.022"$$

This shows that the error in the 90° angle determined only by the transits would produce a

change in the H of an amount only slightly larger than the estimated error in H. This verifies that the estimated errors given above are consistent in these tests.

7. Points G, H, I, J, K, L---There are two sources of error in these points. First, there are the errors in the linear measurements of the quantities used in Appendix II. Second, there is an error which arises from the fact that the central angle has an uncertainty. This uncertainty effects the equations II.1 and II.2.

   a. Errors from linear measurements---Using standard procedures for compounding errors in a functional relation of several measured quantities (Be 62), the uncertainties of the points on the hypotenuse were found. The associated error for each point is given in Table III.1.

TABLE III.1.--Estimated standard errors for the primary angles in reference I for the main arm due to errors in the linear measurements.

Point	Error
G	0.0014°
H	0.0025°
I	0.0020°
J	0.0030°
K	0.0025°
L	0.0017°

b. Errors due to central angle---

Equations II.1 and II.2 can be rewritten

$$\cos(a) = \frac{B^2 + H^2 - A^2}{2BH}$$

But:

$$H^2 = A^2 + B^2 - 2AB \cos(90° + \phi)$$

$$\cos(a) = \frac{2B^2 - 2AB \cos(90° + \phi)}{2BH}$$

$$= \frac{B}{H}(1 - (A/B) \cos(90° + \phi))$$

$$\cos(a) = \frac{B}{H}(1 - (A/B)\phi) \qquad \text{III.1}$$

$$\sin(a) = \frac{A}{H} \sin(90° + \phi)$$

$$= \frac{A}{H} \cos\phi$$

$$\sin(a) \simeq \frac{A}{H}(1) \qquad \text{III.2}$$

Using equations III.1 and III.2 in equation II.3

$$\cot(d) \simeq \frac{B - X(B/H)(1 + (A/B)\phi)}{X(A/H)}$$

$$\cot(d) \simeq \frac{B}{A}((H/X) - 1) - \phi \qquad \text{III.3}$$

The ϕ in this case is 0.0047°.

The associated error for each point on the hypotenuse is given in Table III.2.

TABLE III.2.--Estimated standard errors in the primary points in reference I due to the error in the central, 90° angle.

Point	Error
G	0.0017°
H	0.0007°
I	0.0018°
J	0.0032°
K	0.0042°
L	0.0047°

C. Total errors---The total error in these points is the sum of 7(a,b). Table III.3 shows the results using angles relative to line OC.

TABLE III.3.--Total estimated standard errors in the primary points in reference I.

Point	Error
9.649°	0.002°
22.474°	0.003°
38.379°	0.003°
55.580°	0.004°
71.283°	0.005°
83.844°	0.005°

8. Points in quadrant BC, Figure 2.5---The points in this quadrant are the result of the 90° transfer of the points in quadrant AC. The errors in these points are the result of:

   a. Errors in points G ··· L, see Table III.3.

   b. Alignment of TR #2 on the center point and the point, J, on the hypotenuse (see Figure 2.6)

      1). Center 0.010" at 25' 0.0020°

      2). Point J 0.003" at 6' 0.0024°

   c. Alignment of cross hair in TR #2 with

      1). Pointer 0.005" at 12' 0.0020°

      2). Pointer image 0.020" at 58' 0.0020°

   d. Placement of targets on the line of sight of TR #1

      0.010" at 30' 0.0016°

      Note: Center errors are included in 8a.

The total error in these secondary points is the sum of 8(a,b,c,d) and is shown in Table III.5 where the angles are relative to line OA.

TABLE III.5.--Total estimated standard errors in the secondary points in reference I.

Point	Error
96.155	0.0049°
108.717	0.0054°
124.420	0.0054°
141.621	0.0060°
157.525	0.0067°
170.351	0.0067°

APPENDIX IV

EXPERIMENTAL DATA

IV.1 Tabulated Angular Distributions

The following pages contain listings of the center-of-mass differential cross sections and scattering angles for ^{58}Ni, ^{60}Ni, ^{62}Ni and ^{64}Ni. All of the excited states which were observed in this experiment are presented here along with the total relative standard errors (see sections 4.1.d). All shown here is the systematic experimental error which is associated with each distribution. The values of the cross sections are to be read as 1.60E + 03 ≡ 1.60×10^3.

58NI(P,P')58NI* EP=40.0 MEV

THE ERRORS SHOWN ARE THE TOTAL RELATIVE EXPERIMENTAL ERRORS.

THE SYSTEMATIC EXPERIMENTAL ERROR IS 4.5%

EX=0.000 MEV

ANGLE CM (DEG)	SIGMA CM (MB/SR)	ERROR (%)
17.20	1.60E+03	0.43
19.74	7.76E+02	0.34
24.83	8.32E+01	0.71
29.91	4.30E+01	0.84
34.99	1.22E+02	0.35
40.06	1.32E+02	0.33
45.13	7.55E+01	0.43
50.19	2.57E+01	0.73
55.24	1.16E+01	1.08
60.29	1.43E+01	1.12
65.24	1.52E+01	0.67
70.27	1.20E+01	0.76
85.33	2.46E+00	1.74
90.34	2.52E+00	1.72

EX=1.456 MEV

ANGLE CM (DEG)	SIGMA CM (MB/SR)	ERROR (%)
17.21	1.27E+01	4.79
19.75	1.02E+01	3.12
24.84	8.11E+00	2.34
29.92	4.88E+00	2.57
35.00	2.37E+00	2.76
40.07	1.88E+00	3.07
45.14	2.52E+00	3.87
50.20	2.74E+00	2.43
55.26	1.96E+00	2.89
60.31	8.78E-01	4.78
65.25	4.79E-01	5.14
70.29	5.51E-01	4.77
85.35	4.47E-01	4.09
90.36	2.71E-01	5.52

58NI(P,P')58NI* EP=40.0 MEV

THE ERRORS SHOWN ARE THE TOTAL RELATIVE EXPERIMENTAL ERRORS.

THE SYSTEMATIC EXPERIMENTAL ERROR IS 4.5%

EX=2.458 MEV

ANGLE CM (DEG)	SIGMA CM (MB/SR)	ERROR (%)
17.21	1.02E+00	32.30
19.76	1.15E+00	13.31
24.84	9.53E-01	7.83
29.93	8.27E-01	6.70
35.00	1.01E+00	4.78
40.08	8.36E-01	5.08
45.15	4.75E-01	6.44
50.21	2.98E-01	8.03
55.27	1.66E-01	11.11
65.26	1.35E-01	9.13
70.30	1.65E-01	7.68
85.36	6.97E-02	10.37
90.37	5.44E-02	14.04

EX=3.035 MEV

ANGLE CM (DEG)	SIGMA CM (MB/SR)	ERROR (%)
17.21	1.23E+00	29.24
19.76	1.21E+00	13.71
24.85	8.01E-01	9.15
29.93	4.45E-01	9.74
35.01	2.00E-01	15.12
40.08	1.14E-01	24.14
45.15	1.39E-01	16.65
50.22	1.20E-01	15.50
55.28	1.31E-01	13.25
60.33	1.00E-01	17.68
65.27	1.11E-01	27.71
70.31	8.76E-02	12.96
85.37	4.34E-02	18.72
90.38	2.35E-02	26.67

58NI(P,P')58NI* EP=40.0 MEV

THE ERRORS SHOWN ARE THE TOTAL RELATIVE EXPERIMENTAL ERRORS.

THE SYSTEMATIC EXPERIMENTAL ERROR IS 4.5%

EX=3.260 MEV

ANGLE CM (DEG)	SIGMA CM (MB/SR)	ERROR (%)
17.21	2.58E+00	15.29
19.76	1.23E+00	12.72
24.85	1.06E+00	7.28
29.93	5.62E-01	8.57
35.01	4.19E-01	8.73
40.09	3.28E-01	9.63
45.16	3.18E-01	9.49
50.22	3.25E-01	7.77
55.28	2.77E-01	7.92
60.33	1.61E-01	12.77
65.27	1.27E-01	10.02
70.31	1.08E-01	28.21
85.38	1.01E-01	11.06
90.38	5.11E-02	15.14

EX=3.610 MEV

ANGLE CM (DEG)	SIGMA CM (MB/SR)	ERROR (%)
17.22	1.62E+00	22.97
19.76	1.28E+00	13.48
24.85	5.80E-01	10.73
29.93	4.09E-01	10.03
35.01	4.05E-01	9.54
40.09	4.36E-01	8.57
45.16	2.77E-01	9.79
50.22	1.76E-01	11.10
55.28	1.47E-01	11.93
60.34	1.14E-01	16.41
65.28	1.15E-01	10.34
70.32	1.05E-01	11.32
85.38	2.32E-02	30.77
90.39	2.01E-02	30.78

58NI(P,P')58NI* EP=40.0 MEV

THE ERRORS SHOWN ARE THE TOTAL RELATIVE EXPERIMENTAL ERRORS.

THE SYSTEMATIC EXPERIMENTAL ERROR IS 4.5%

EX=3.895 MEV

ANGLE CM (DEG)	SIGMA CM (MB/SR)	ERROR (%)
17.22	6.74E-01	43.80
19.76	4.77E-01	34.87
24.85	1.72E-01	28.76
29.94	1.44E-01	25.52
35.02	8.62E-02	29.39
40.09	1.75E-01	18.49
45.16	1.24E-01	17.44
50.23	8.98E-02	18.56
55.29	4.98E-02	24.32
60.34	4.02E-02	33.11
65.28	1.44E-02	47.07
70.32	1.10E-02	61.25

EX=4.100 MEV

ANGLE CM (DEG)	SIGMA CM (MB/SR)	ERROR (%)
17.22	8.76E-01	45.08
19.76	1.96E-01	75.43
24.85	6.33E-02	63.35
29.94	8.72E-02	33.62
35.02	1.27E-01	23.34
40.09	1.05E-01	22.28
45.17	8.95E-02	21.27
50.23	2.99E-02	44.09
55.29	5.38E-02	35.00
60.34	1.79E-02	67.80
65.29	3.76E-02	23.00
70.32	3.31E-02	25.00
85.39	8.24E-03	69.82
90.40	8.20E-03	66.18

58NI(P,P')58NI* EP=40.0 MEV

THE ERRORS SHOWN ARE THE TOTAL RELATIVE EXPERIMENTAL ERRORS.

THE SYSTEMATIC EXPERIMENTAL ERROR IS 4.5%

EX=4.300 MEV

ANGLE CM (DEG)	SIGMA CM (MB/SR)	ERROR (%)
19.76	3.75E-01	34.49
24.85	1.43E-01	26.34
29.94	8.42E-02	42.86
35.02	1.74E-01	16.80
40.10	1.44E-01	19.63
45.17	5.21E-02	33.33
50.23	6.80E-02	24.00
55.29	1.02E-01	17.11
60.34	4.29E-02	37.50
65.29	4.49E-02	20.90
70.33	3.79E-02	23.60
85.39	1.20E-02	37.50

EX=4.380 MEV

ANGLE CM (DEG)	SIGMA CM (MB/SR)	ERROR (%)
17.22	7.12E-01	34.92
19.76	7.92E-01	18.58
24.85	6.17E-01	21.85
29.94	6.37E-01	13.68
35.02	6.90E-01	7.86
40.10	6.22E-01	8.42
45.17	4.61E-01	13.62
50.23	2.93E-01	23.72
55.29	1.51E-01	21.43
60.34	9.83E-02	47.27
65.29	1.62E-01	11.16
70.33	1.01E-01	19.86

58NI(P,P')58NI* EP=40.0 MEV

THE ERRORS SHOWN ARE THE TOTAL RELATIVE EXPERIMENTAL ERRORS.

THE SYSTEMATIC EXPERIMENTAL ERROR IS 4.5%

EX=4.472 MEV

ANGLE CM (DEG)	SIGMA CM (MB/SR)	ERROR (%)
17.22	4.99E+00	9.23
19.77	4.77E+00	5.30
24.85	4.98E+00	3.94
29.94	4.07E+00	3.33
35.02	3.40E+00	2.49
40.10	2.31E+00	2.91
45.17	1.42E+00	5.45
50.23	1.11E+00	6.97
55.29	1.07E+00	4.63
60.35	1.14E+00	5.19
65.29	7.67E-01	3.85
70.33	6.17E-01	5.70
85.39	3.86E-01	6.80
90.40	3.13E-01	7.38

EX=4.754 MEV

ANGLE CM (DEG)	SIGMA CM (MB/SR)	ERROR (%)
17.22	2.16E+00	17.81
19.77	2.06E+00	11.23
24.86	1.16E+00	7.44
29.94	1.05E+00	6.66
35.02	9.69E-01	5.17
40.10	9.45E-01	4.94
45.17	7.41E-01	5.68
50.24	4.97E-01	6.18
55.30	2.97E-01	7.66
60.35	2.93E-01	9.52
65.29	2.39E-01	6.83
70.33	2.05E-01	7.97
85.40	6.29E-02	13.68
90.40	5.22E-02	16.29

58NI(P,P')58NI* EP=40.0 MEV

THE ERRORS SHOWN ARE THE TOTAL RELATIVE EXPERIMENTAL ERRORS.

THE SYSTEMATIC EXPERIMENTAL ERROR IS 4.5%

EX=5.128 MEV

ANGLE CM (DEG)	SIGMA CM (MB/SR)	ERROR (%)
17.22	1.56E+00	23.46
19.77	7.29E-01	25.00
24.86	4.25E-01	15.50
29.94	4.72E-01	19.75
35.03	4.41E-01	9.55
40.10	4.57E-01	7.98
45.18	4.58E-01	7.73
50.24	4.24E-01	6.90
55.30	4.01E-01	6.61
60.35	2.97E-01	8.98
65.30	2.88E-01	6.07
70.34	2.16E-01	7.67
85.40	8.39E-02	11.29
90.41	7.53E-02	12.87

EX=5.430 MEV

ANGLE CM (DEG)	SIGMA CM (MB/SR)	ERROR (%)
17.22	7.50E-01	52.10
19.77	5.96E-01	26.75
24.86	2.29E-01	25.25
29.95	1.05E-01	34.17
35.03	2.52E-01	13.99
40.11	3.49E-01	12.04
45.18	2.38E-01	13.74
50.25	2.05E-01	12.34
55.31	1.92E-01	10.54
60.36	1.89E-01	12.73
65.30	1.05E-01	13.01
70.34	1.55E-01	10.40
85.41	4.12E-02	19.16

58NI(P,P')58NI* EP=40.0 MEV

THE ERRORS SHOWN ARE THE TOTAL RELATIVE EXPERIMENTAL ERRORS.

THE SYSTEMATIC EXPERIMENTAL ERROR IS 4.5%

EX=5.589 MEV

ANGLE CM (DEG)	SIGMA CM (MB/SR)	ERROR (%)
17.22	1.14E+00	36.15
19.77	8.55E-01	21.59
24.86	6.21E-01	11.32
29.95	6.31E-01	9.41
35.03	5.63E-01	8.21
40.11	5.62E-01	11.96
45.18	5.02E-01	7.33
50.25	3.37E-01	8.36
55.31	2.53E-01	8.54
60.36	1.97E-01	11.99
65.31	1.43E-01	9.60
70.34	1.06E-01	11.40
85.41	8.84E-02	11.18
90.41	5.74E-02	14.75

EX=5.770 MEV

ANGLE CM (DEG)	SIGMA CM (MB/SR)	ERROR (%)
17.22	1.17E+00	36.69
19.77	5.67E-01	29.86
24.86	2.04E-01	26.84
29.95	1.14E-01	31.79
35.03	1.45E-01	23.36
40.11	1.79E-01	17.62
45.18	8.28E-02	28.58
50.25	6.12E-02	29.07
55.31	8.47E-02	19.51
60.36	1.02E-01	21.26
65.31	7.54E-02	16.23
70.35	6.82E-02	17.35
85.41	7.49E-03	76.20
90.42	1.01E-02	56.67

58NI(P,P')58NI* EP=40.0 MEV

THE ERRORS SHOWN ARE THE TOTAL RELATIVE EXPERIMENTAL ERRORS.

THE SYSTEMATIC EXPERIMENTAL ERROR IS 4.5%

EX=6.080 MEV

ANGLE CM (DEG)	SIGMA CM (MB/SR)	ERROR (%)
17.23	1.08E+00	43.16
19.77	4.34E-01	40.74
24.86	3.67E-01	18.32
29.95	1.77E-01	24.73
35.03	1.67E-01	24.55
40.11	1.12E-01	32.17
45.19	1.19E-01	26.33
50.25	9.11E-02	25.28
55.31	1.95E-01	11.56
60.37	1.48E-01	16.82
65.31	1.47E-01	11.08
70.35	1.01E-01	13.35
85.42	2.62E-02	22.69
90.42	1.94E-02	34.38

EX=6.350 MEV

ANGLE CM (DEG)	SIGMA CM (MB/SR)	ERROR (%)
17.23	2.98E-01	131.35
19.77	6.30E-01	29.02
24.87	3.14E-01	20.66
29.95	2.22E-01	21.37
35.04	1.92E-01	23.12
40.12	2.16E-01	20.80
45.19	1.24E-01	24.63
50.26	1.05E-01	20.66
55.32	8.74E-02	20.92
60.37	3.75E-02	47.86
65.32	3.28E-02	34.69
70.35	3.38E-02	29.51
85.42	1.95E-02	34.38
90.43	2.24E-02	30.57

58NI(P,P')58NI* EP=40.0 MEV

THE ERRORS SHOWN ARE THE TOTAL RELATIVE EXPERIMENTAL ERRORS.

THE SYSTEMATIC EXPERIMENTAL ERROR IS 4.5%

EX=6.750 MEV

ANGLE CM (DEG)	SIGMA CM (MB/SR)	ERROR (%)
17.23	6.92E-01	66.19
19.78	5.53E-01	37.79
24.87	6.42E-01	13.53
29.96	5.18E-01	12.27
35.04	2.61E-01	18.06
40.12	2.91E-01	17.01
45.19	1.43E-01	27.76
50.26	1.17E-01	22.55
55.32	1.27E-01	18.32
60.38	7.15E-02	32.20
65.32	6.70E-02	20.74
70.36	5.17E-02	22.75
85.43	3.74E-02	23.16
90.43	2.24E-02	38.74

EX=6.890 MEV

ANGLE CM (DEG)	SIGMA CM (MB/SR)	ERROR (%)
17.23	1.81E+00	34.93
19.78	1.26E+00	21.83
24.87	1.43E+00	7.65
29.96	9.02E-01	7.85
35.04	7.69E-01	8.38
40.12	4.95E-01	11.77
45.20	2.96E-01	14.17
50.26	2.24E-01	13.83
55.32	2.94E-01	9.82
60.38	3.29E-01	14.13
65.32	1.85E-01	9.35
70.36	1.66E-01	9.76
85.43	8.43E-02	14.80
90.44	1.03E-01	11.49

58NI(P,P')58NI* EP=40.0 MEV

THE ERRORS SHOWN ARE THE TOTAL RELATIVE EXPERIMENTAL ERRORS.

THE SYSTEMATIC EXPERIMENTAL ERROR IS 4.5%

EX=7.300 MEV

ANGLE CM (DEG)	SIGMA CM (MB/SR)	ERROR (%)
17.23	3.84E+00	20.52
19.78	2.33E+00	15.17
24.87	1.23E+00	9.12
29.96	1.13E+00	7.64
35.05	8.46E-01	8.46
40.13	5.79E-01	10.58
45.20	5.02E-01	10.46
50.27	4.21E-01	9.73
55.33	3.47E-01	9.16
60.38	2.89E-01	12.83
65.33	2.70E-01	7.91
70.37	1.78E-01	10.18
85.44	1.32E-01	10.26
90.44	9.54E-02	11.48

60NI(P,P')60NI* EP=40.0 MEV

THE ERRORS SHOWN ARE THE TOTAL RELATIVE EXPERIMENTAL ERRORS.

THE SYSTEMATIC EXPERIMENTAL ERROR IS 5.5%

EX=0.000 MEV

ANGLE CM (DEG)	SIGMA CM (MB/SR)	ERROR (%)
12.92	3.39E+03	1.63
18.01	1.25E+03	3.03
23.09	2.50E+02	19.89
28.17	2.62E+01	17.85
33.24	1.21E+02	0.31
38.31	1.50E+02	0.84
43.38	1.04E+02	6.03
48.44	3.94E+01	6.06
53.50	1.16E+01	0.77
58.55	1.44E+01	0.89
63.59	1.63E+01	0.84
68.63	1.25E+01	0.96
73.66	7.52E+00	1.49
78.68	3.55E+00	1.88
83.70	2.42E+00	2.26
88.70	2.72E+00	2.16

EX=1.332 MEV

ANGLE CM (DEG)	SIGMA CM (MB/SR)	ERROR (%)
12.92	1.49E+01	12.76
18.01	1.32E+01	5.67
23.09	1.00E+01	17.96
28.17	7.71E+00	17.84
33.25	3.56E+00	3.03
38.32	2.71E+00	6.75
43.39	2.72E+00	9.72
48.45	3.42E+00	6.97
53.51	2.69E+00	1.96
58.56	1.06E+00	3.98
63.61	6.33E-01	6.26
68.64	7.22E-01	5.36
73.67	1.06E+00	3.97
78.70	8.99E-01	3.71
83.71	6.79E-01	4.28
88.72	4.02E-01	5.64

60NI(P,P')60NI* EP=40.0 MEV

THE ERRORS SHOWN ARE THE TOTAL RELATIVE EXPERIMENTAL ERRORS.

THE SYSTEMATIC EXPERIMENTAL ERROR IS 5.5%

EX=2.502 MEV

ANGLE CM (DEG)	SIGMA CM (MB/SR)	ERROR (%)
12.93	2.07E+00	32.54
18.01	1.48E+00	17.24
23.10	1.15E+00	20.35
28.18	1.11E+00	19.38
33.26	9.20E-01	4.77
38.33	8.36E-01	14.41
43.40	7.08E-01	10.63
48.47	3.55E-01	12.48
53.52	2.08E-01	6.91
58.57	1.40E-01	25.60
63.62	1.60E-01	10.78
68.66	1.22E-01	11.93
73.69	9.49E-02	33.33
78.71	7.54E-02	12.80
83.73	7.35E-02	13.02
88.73	7.40E-02	16.17

EX=3.119 MEV

ANGLE CM (DEG)	SIGMA CM (MB/SR)	ERROR (%)
12.93	3.69E-01	137.80
18.02	5.09E-01	37.32
23.10	6.29E-01	24.35
28.19	3.68E-01	23.11
33.26	3.59E-01	8.87
38.34	5.03E-01	19.80
43.41	2.52E-01	18.02
48.47	1.96E-01	18.86
53.53	1.39E-01	8.86
58.58	9.11E-02	15.83
63.63	6.43E-02	23.74
68.67	8.80E-02	28.95
73.70	8.49E-02	14.00
78.72	5.56E-02	19.49
83.73	4.48E-02	21.86
88.74	1.91E-02	40.53

60NI(P,P')60NI* EP=40.0 MEV

THE ERRORS SHOWN ARE THE TOTAL RELATIVE EXPERIMENTAL ERRORS.

THE SYSTEMATIC EXPERIMENTAL ERROR IS 5.5%

EX=3.360 MEV

ANGLE CM (DEG)	SIGMA CM (MB/SR)	ERROR (%)
12.93	5.90E-01	104.56
18.02	2.64E-01	77.43
23.10	1.39E-01	50.21
28.19	1.49E-01	38.92
33.27	1.14E-01	21.53
38.34	1.11E-01	56.82
43.41	9.23E-02	36.45
48.47	6.05E-02	38.37
53.53	2.28E-02	30.60
58.58	3.41E-02	30.33
63.63	3.44E-02	34.00
68.67	3.71E-02	28.31
73.70	3.41E-02	37.61
78.72	2.60E-02	31.95
83.74	1.62E-02	46.77
88.75	1.40E-02	49.00

EX=3.690 MEV

ANGLE CM (DEG)	SIGMA CM (MB/SR)	ERROR (%)
12.93	1.14E+00	67.58
18.02	1.03E+00	23.44
23.11	4.96E-01	26.68
28.19	4.62E-01	22.25
33.27	3.64E-01	8.99
38.34	5.03E-01	19.80
43.41	3.33E-01	17.02
48.48	2.81E-01	16.49
53.54	1.80E-01	7.90
58.59	1.53E-01	11.84
63.63	1.84E-01	11.16
68.67	1.36E-01	12.70
73.70	1.32E-01	15.02
78.73	6.06E-02	19.04
83.74	3.49E-02	27.21
88.75	1.91E-02	41.67

60NI(P,P')60NI* EP=40.0 MEV

THE ERRORS SHOWN ARE THE TOTAL RELATIVE EXPERIMENTAL ERRORS.

THE SYSTEMATIC EXPERIMENTAL ERROR IS 5.5%

EX=4.038 MEV

ANGLE CM (DEG)	SIGMA CM (MB/SR)	ERROR (%)
12.93	3.61E+00	22.95
18.02	4.92E+00	6.24
23.11	5.03E+00	17.99
28.19	5.27E+00	17.87
33.27	3.85E+00	1.94
38.35	3.52E+00	5.87
43.42	1.81E+00	8.13
48.48	1.48E+00	7.88
53.54	1.37E+00	2.34
58.59	1.30E+00	3.14
63.64	9.74E-01	3.75
68.68	6.68E-01	4.58
73.71	4.98E-01	6.25
78.73	4.52E-01	6.28
83.75	3.65E-01	6.41
88.75	3.17E-01	6.73

EX=4.310 MEV

ANGLE CM (DEG)	SIGMA CM (MB/SR)	ERROR (%)
12.93	8.48E-01	79.57
18.02	4.05E-01	50.67
23.11	4.67E-01	27.16
28.19	4.11E-01	24.85
33.27	2.45E-01	14.05
38.35	2.21E-01	36.91
43.42	1.65E-01	31.05
48.48	1.57E-01	26.32
53.54	7.77E-02	16.38
58.60	8.27E-02	18.82
63.64	5.64E-02	24.82
68.68	6.14E-02	24.25
73.71	4.33E-02	31.73
78.74	3.77E-02	27.34
83.75	4.23E-02	25.65
88.76	2.36E-02	43.08

60NI(P,P')60NI* EP=40.0 MEV

THE ERRORS SHOWN ARE THE TOTAL RELATIVE EXPERIMENTAL ERRORS.

THE SYSTEMATIC EXPERIMENTAL ERROR IS 5.5%

EX=5.150 MEV

ANGLE CM (DEG)	SIGMA CM (MB/SR)	ERROR (%)
12.94	1.99E+00	53.09
18.03	2.58E+00	14.46
23.11	2.09E+00	19.66
28.20	2.33E+00	18.70
33.28	1.92E+00	3.48
38.36	2.50E+00	8.44
43.43	1.71E+00	8.57
48.49	1.46E+00	8.31
53.55	8.75E-01	3.55
58.60	7.25E-01	5.23
63.65	5.93E-01	5.85
68.69	4.62E-01	7.23
73.72	4.04E-01	8.05
78.74	2.98E-01	8.14
83.76	2.61E-01	8.75
88.77	1.84E-01	10.49

EX=5.460 MEV

ANGLE CM (DEG)	SIGMA CM (MB/SR)	ERROR (%)
12.94	1.47E+00	48.48
18.03	8.94E-01	24.17
23.12	6.68E-01	24.94
28.20	6.50E-01	21.89
33.28	4.66E-01	8.21
38.36	2.91E-01	34.60
43.43	2.51E-01	22.42
48.50	3.09E-01	15.36
53.56	2.37E-01	7.80
58.61	2.38E-01	10.28
63.66	2.01E-01	11.49
68.70	1.67E-01	12.73
73.73	1.01E-01	17.77
78.75	1.07E-01	15.14
83.77	5.60E-02	21.42

60NI(P,P')60NI* EP=40.0 MEV

THE ERR0RS SH0WN ARE THE T0TAL RELATIVE EXPERIMENTAL ERR0RS.

THE SYSTEMATIC EXPERIMENTAL ERR0R IS 5.5%

Ex=5.700 MEV

ANGLE CM (DEG)	SIGMA CM (MB/SR)	ERR0R (%)
12.94	1.84E+00	40.50
18.03	1.08E+00	26.19
23.12	7.22E-01	24.69
28.20	3.76E-01	25.55
33.28	3.19E-01	10.56
38.36	3.22E-01	36.44
43.43	2.32E-01	27.69
48.50	1.94E-01	21.41
53.56	1.47E-01	11.78
58.61	1.49E-01	13.80
63.66	9.14E-02	20.99
68.70	7.87E-02	22.01
73.73	5.82E-02	26.34
78.75	3.27E-02	34.08
83.77	2.99E-02	34.38
88.78	4.91E-02	22.86

62NI(P,P')62NI* EP=40.0 MEV

THE ERRORS SHOWN ARE THE TOTAL RELATIVE EXPERIMENTAL ERRORS.

THE SYSTEMATIC EXPERIMENTAL ERROR IS 8.5%

EX=0.000 MEV

ANGLE CM (DEG)	SIGMA CM (MB/SR)	ERROR (%)
13.02	6.14E+03	17.24
18.10	1.25E+03	0.34
23.18	1.35E+02	2.08
28.25	3.08E+01	1.30
33.33	1.45E+02	0.85
38.40	1.69E+02	0.61
43.46	7.88E+01	0.25
48.52	2.82E+01	0.77
53.57	1.19E+01	0.99
58.62	1.74E+01	0.67
63.66	1.87E+01	0.65
68.70	1.30E+01	1.02
73.73	6.15E+00	1.45
78.75	3.25E+00	1.75
83.76	2.61E+00	1.62
88.77	2.83E+00	1.58

EX=1.169 MEV

ANGLE CM (DEG)	SIGMA CM (MB/SR)	ERROR (%)
13.02	2.21E+01	17.83
18.10	1.57E+01	5.43
23.18	1.01E+01	2.36
28.26	6.78E+00	2.06
33.33	3.13E+00	4.77
38.40	2.27E+00	5.90
43.47	2.92E+00	1.44
48.53	3.61E+00	1.62
53.58	2.31E+00	2.77
58.63	1.45E+00	2.79
63.68	6.69E-01	2.75
68.71	7.97E-01	3.93
73.74	1.01E+00	3.76
78.76	9.06E-01	3.11
83.78	5.99E-01	3.47
88.78	3.55E-01	4.67

62NI(P,P')62NI* EP=40.0 MEV

THE ERRORS SHOWN ARE THE TOTAL RELATIVE EXPERIMENTAL ERRORS.

THE SYSTEMATIC EXPERIMENTAL ERROR IS 8.5%

EX=2.334 MEV

ANGLE CM (DEG)	SIGMA CM (MB/SR)	ERROR (%)
13.02	2.35E+00	27.53
18.11	1.19E+00	20.79
23.19	1.14E+00	7.49
28.27	9.99E-01	5.44
33.34	8.76E-01	9.89
38.41	5.90E-01	11.97
43.48	4.82E-01	3.95
48.54	3.00E-01	5.75
53.60	2.33E-01	9.03
58.65	1.74E-01	8.56
63.69	1.90E-01	5.42
68.73	1.71E-01	12.78
73.75	1.02E-01	14.48
78.78	8.44E-02	11.34
83.79	7.22E-02	11.08
88.80	6.44E-02	12.01

EX=3.168 MEV

ANGLE CM (DEG)	SIGMA CM (MB/SR)	ERROR (%)
13.02	7.67E-01	56.90
18.11	6.31E-01	24.75
23.19	3.65E-01	15.47
28.27	4.14E-01	9.30
33.35	3.39E-01	17.79
38.42	2.53E-01	22.78
43.49	2.11E-01	7.82
48.55	1.72E-01	8.76
53.60	8.45E-02	15.79
58.66	8.57E-02	13.60
63.70	7.03E-02	14.46
73.77	4.46E-02	25.71
78.79	3.64E-02	19.79
88.81	1.34E-02	39.48

62NI(P,P')62NI* EP=40.0 MEV

THE ERRORS SHOWN ARE THE TOTAL RELATIVE EXPERIMENTAL ERRORS.

THE SYSTEMATIC EXPERIMENTAL ERROR IS 8.5%

EX=3.270 MEV

ANGLE CM (DEG)	SIGMA CM (MB/SR)	ERROR (%)
13.02	1.72E+00	29.87
18.11	9.32E-01	17.70
23.19	7.83E-01	8.73
28.27	8.47E-01	5.86
33.35	9.18E-01	10.00
38.42	8.89E-01	9.52
43.49	4.84E-01	4.14
48.55	3.27E-01	5.92
53.61	1.47E-01	11.28
58.66	1.29E-01	9.92
63.70	1.24E-01	9.03
73.77	9.44E-02	17.57
78.79	1.02E-01	10.58
88.81	5.94E-02	13.38

EX=3.750 MEV

ANGLE CM (DEG)	SIGMA CM (MB/SR)	ERROR (%)
13.03	8.30E+00	18.32
18.11	6.96E+00	4.89
23.19	6.07E+00	2.49
28.28	5.48E+00	2.08
33.35	4.55E+00	3.91
38.42	3.45E+00	4.02
43.49	1.72E+00	1.69
48.55	1.50E+00	2.46
53.61	1.56E+00	2.95
58.66	1.41E+00	2.57
63.71	1.03E+00	2.01
68.74	7.01E-01	3.37
73.77	3.21E-01	8.73
78.80	4.66E-01	4.51
83.81	4.52E-01	4.12
88.82	3.80E-01	4.54

62NI(P,P')62NI* EP=40.0 MEV

THE ERRORS SHOWN ARE THE TOTAL RELATIVE EXPERIMENTAL ERRORS.

THE SYSTEMATIC EXPERIMENTAL ERROR IS 8.5%

EX=3.990 MEV

ANGLE CM (DEG)	SIGMA CM (MB/SR)	ERROR (%)
13.03	8.96E-01	56.02
18.11	7.90E-01	26.73
23.20	3.23E-01	22.08
28.28	2.79E-01	15.59
33.35	2.45E-01	26.81
38.43	2.21E-01	30.73
43.49	1.77E-01	8.60
48.56	1.37E-01	12.50
53.61	1.37E-01	14.92
58.66	1.48E-01	11.31
63.71	9.99E-02	9.50
68.75	7.69E-02	14.82
73.77	6.38E-02	20.60
83.81	2.74E-02	23.31
88.82	2.54E-02	22.70

EX=4.148 MEV

ANGLE CM (DEG)	SIGMA CM (MB/SR)	ERROR (%)
13.03	4.62E-01	96.28
18.11	3.76E-01	53.63
23.20	3.73E-01	18.49
28.28	3.27E-01	12.26
33.35	4.21E-01	18.32
38.43	5.06E-01	15.91
43.50	4.26E-01	4.44
48.56	3.06E-01	7.09
53.62	2.88E-01	8.55
58.67	1.91E-01	10.06
63.71	1.19E-01	8.15
68.75	7.89E-02	15.15
73.78	6.12E-02	21.25
83.82	4.96E-02	15.25
88.82	3.97E-02	16.83

62NI(P,P')62NI* EP=40.0 MEV

THE ERRORS SHOWN ARE THE TOTAL RELATIVE EXPERIMENTAL ERRORS.

THE SYSTEMATIC EXPERIMENTAL ERROR IS 8.5%

EX=4.640 MEV

ANGLE CM (DEG)	SIGMA CM (MB/SR)	ERROR (%)
13.03	1.52E+00	37.88
18.12	1.19E+00	19.69
23.20	6.10E-01	11.27
28.28	5.77E-01	8.14
33.36	5.00E-01	18.60
38.43	3.44E-01	21.78
43.50	2.18E-01	8.07
48.56	2.64E-01	8.70
53.62	2.70E-01	9.09
58.67	2.30E-01	9.66
63.72	1.80E-01	6.56
68.75	1.40E-01	10.03
73.78	1.25E-01	12.66
78.81	7.52E-02	14.66
83.82	8.10E-02	12.15
88.83	8.26E-02	11.81

EX=4.980 MEV

ANGLE CM (DEG)	SIGMA CM (MB/SR)	ERROR (%)
13.03	3.33E+00	23.68
18.12	1.34E+00	17.40
23.20	9.14E-01	8.67
28.28	8.16E-01	7.24
33.36	6.65E-01	14.43
38.43	6.42E-01	14.84
43.50	3.16E-01	6.30
48.57	2.93E-01	7.50
53.62	2.63E-01	9.68
58.68	1.82E-01	12.38
63.72	1.30E-01	9.32
68.76	1.04E-01	12.91
73.79	1.05E-01	15.99
78.81	9.70E-02	12.19
83.83	8.72E-02	12.45
88.83	7.91E-02	11.37

62NI(P,P')62NI* EP=40.0 MEV

THE ERRORS SHOWN ARE THE TOTAL RELATIVE EXPERIMENTAL ERRORS.

THE SYSTEMATIC EXPERIMENTAL ERROR IS 8.5%

EX=5.610 MEV

ANGLE CM (DEG)	SIGMA CM (MB/SR)	ERROR (%)
13.03	2.74E+00	25.42
18.12	1.40E+00	17.15
23.21	8.80E-01	10.11
28.29	9.25E-01	6.73
33.37	6.19E-01	19.36
38.44	7.77E-01	13.84
43.51	3.44E-01	6.64
48.58	5.26E-01	5.75
53.63	3.65E-01	9.24
58.69	2.38E-01	10.85
63.73	2.41E-01	6.37
68.77	1.52E-01	12.03
73.80	1.63E-01	13.71
78.82	1.65E-01	9.86
83.84	1.46E-01	9.04
88.85	8.12E-02	13.24

64NI(P,P')64NI* EP=40.0 MEV

THE ERRORS SHOWN ARE THE TOTAL RELATIVE EXPERIMENTAL ERRORS.

THE SYSTEMATIC EXPERIMENTAL ERROR IS 15.5%

EX=0.000 MEV

ANGLE CM (DEG)	SIGMA CM (MB/SR)	ERROR (%)
13.01	4.74E+03	9.01
18.09	1.40E+03	9.81
23.16	1.99E+02	18.80
28.24	7.46E+01	18.79
33.31	1.97E+02	1.58
38.38	1.98E+02	0.93
43.44	1.11E+02	0.89
48.50	3.33E+01	0.92
53.55	1.73E+01	1.36
58.60	2.33E+01	9.00
63.64	2.17E+01	9.00
68.67	1.29E+01	9.00
73.70	5.53E+00	9.11
78.72	3.99E+00	2.55
83.73	4.07E+00	1.51
88.74	3.97E+00	2.06
93.74	3.21E+00	2.33

EX=1.344 MEV

ANGLE CM (DEG)	SIGMA CM (MB/SR)	ERROR (%)
13.01	1.73E+01	15.21
18.09	1.39E+01	5.86
23.17	9.47E+00	16.69
28.25	6.67E+00	16.65
33.32	2.73E+00	10.15
38.39	2.21E+00	8.39
43.45	2.96E+00	3.09
48.51	3.61E+00	2.02
53.56	2.55E+00	2.87
58.61	7.66E-01	5.47
63.65	4.92E-01	6.53
68.69	6.40E-01	5.79
73.71	6.23E-01	5.01
78.73	9.63E-01	3.46
83.75	6.36E-01	3.96
88.75	3.72E-01	5.99
93.76	2.80E-01	6.21

64NI(P,P')64NI* EP=40.0 MEV

THE ERRORS SHOWN ARE THE TOTAL RELATIVE EXPERIMENTAL ERRORS.

THE SYSTEMATIC EXPERIMENTAL ERROR IS 15.5%

EX=2.608 MEV

ANGLE CM (DEG)	SIGMA CM (MB/SR)	ERROR (%)
13.02	1.38E+00	57.63
18.10	1.39E+00	20.61
23.18	1.09E+00	18.49
28.25	9.25E-01	17.78
33.33	7.19E-01	17.26
38.40	1.04E+00	14.31
43.46	4.21E-01	9.64
48.52	2.66E-01	7.96
53.57	1.94E-01	9.88
58.62	1.27E-01	13.17
63.66	1.04E-01	13.20
68.70	8.57E-02	15.86
73.73	5.53E-02	37.50
78.75	6.43E-02	16.92
83.76	5.86E-02	14.98
88.77	4.66E-02	20.30
93.77	6.61E-02	12.80

EX=3.165 MEV

ANGLE CM (DEG)	SIGMA CM (MB/SR)	ERROR (%)
13.02	1.56E+00	42.31
18.10	1.18E+00	22.64
23.18	5.64E-01	22.05
28.26	6.25E-01	18.58
33.33	5.91E-01	17.71
38.40	5.62E-01	22.62
43.47	4.27E-01	9.97
48.53	3.32E-01	7.66
53.58	1.31E-01	13.27
58.63	9.92E-02	17.31
63.67	1.11E-01	13.35
73.73	5.23E-02	20.58
88.78	4.19E-02	21.86
93.78	3.68E-02	17.15

64NI(P,P')64NI* EP=40.0 MEV

THE ERRORS SHOWN ARE THE TOTAL RELATIVE EXPERIMENTAL ERRORS.

THE SYSTEMATIC EXPERIMENTAL ERROR IS 15.5%

EX=3.560 MEV

ANGLE CM (DEG)	SIGMA CM (MB/SR)	ERROR (%)
13.02	1.01E+01	10.97
18.10	9.17E+00	4.56
23.18	9.16E+00	16.61
28.26	8.53E+00	16.57
33.33	5.83E+00	9.01
38.40	4.35E+00	6.01
43.47	2.52E+00	3.13
48.53	2.26E+00	2.48
53.58	2.32E+00	2.43
58.63	1.56E+00	2.88
63.67	1.01E+00	3.34
68.71	6.03E-01	5.19
73.74	4.21E-01	9.86
78.76	6.63E-01	4.49
83.78	6.22E-01	4.19
88.78	5.41E-01	5.16
93.78	3.67E-01	6.01

EX=3.849 MEV

ANGLE CM (DEG)	SIGMA CM (MB/SR)	ERROR (%)
13.02	1.04E+00	87.79
18.10	1.53E+00	17.89
23.18	7.05E-01	20.10
28.26	7.34E-01	18.38
33.33	9.38E-01	18.06
38.41	5.98E-01	23.66
43.47	5.60E-01	8.95
48.53	4.04E-01	8.24
53.59	3.14E-01	8.60
58.64	2.04E-01	10.60
63.68	1.09E-01	15.27
68.71	8.14E-02	21.92
73.74	6.32E-02	20.02
78.77	6.33E-02	20.54
83.78	5.68E-02	18.53
88.79	4.19E-02	24.22
93.79	4.22E-02	25.64

64NI(P,P')64NI* EP=40.0 MEV

THE ERRORS SHOWN ARE THE TOTAL RELATIVE EXPERIMENTAL ERRORS.

THE SYSTEMATIC EXPERIMENTAL ERROR IS 15.5%

EX=4.600 MEV

ANGLE CM (DEG)	SIGMA CM (MB/SR)	ERROR (%)
13.02	7.78E-01	112.50
18.10	5.67E-01	40.10
23.19	4.80E-01	23.48
28.26	3.66E-01	23.15
33.34	2.37E-01	27.63
38.41	4.54E-01	26.84
43.48	3.44E-01	14.58
48.54	3.34E-01	8.86
53.59	3.14E-01	9.14
58.64	2.08E-01	11.20
63.69	1.50E-01	12.04
68.72	1.19E-01	17.32
73.75	1.07E-01	14.58
78.77	1.22E-01	13.03
83.79	7.97E-02	35.63
88.79	5.18E-02	23.51
93.79	5.04E-02	21.44

IV.2 Plotted Angular Distributions

In the following pages are contained plots of the experimental center-of-mass angular distributions for which there exists no definite L-value. The initial plot in the group for each target is a plot of the calculated distorted wave distributions for each L-value from L = 2 to L = 6.

All of the plots appearing here as well as those appearing in section 4.2.f are shown on the same scale which allows a direct graphical comparison of the theoretical and experimental data.

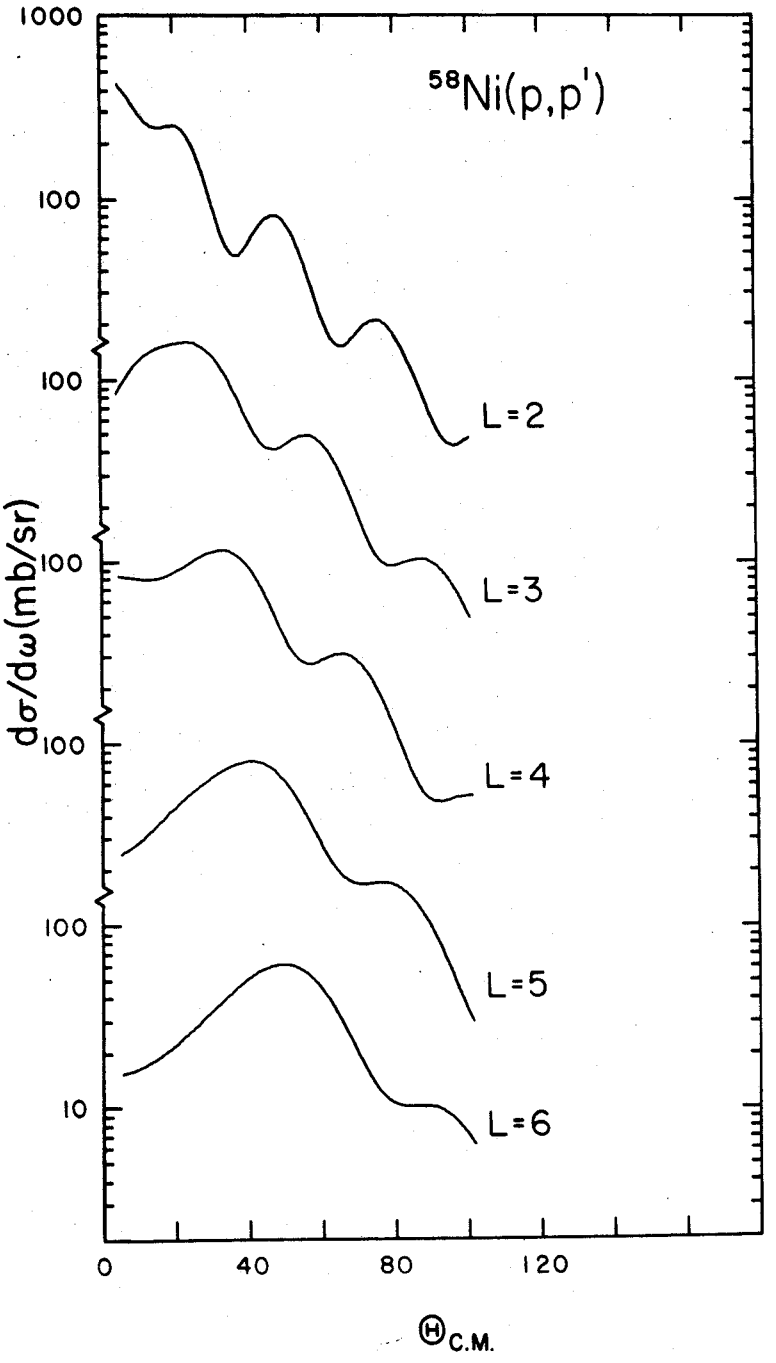
1000
100
100
100
100
100
10
^{58}Ni(p,p')
L=2
L=3
L=4
L=5
L=6
dσ/dω(mb/sr)
0
40
80
120
Θ C.M.

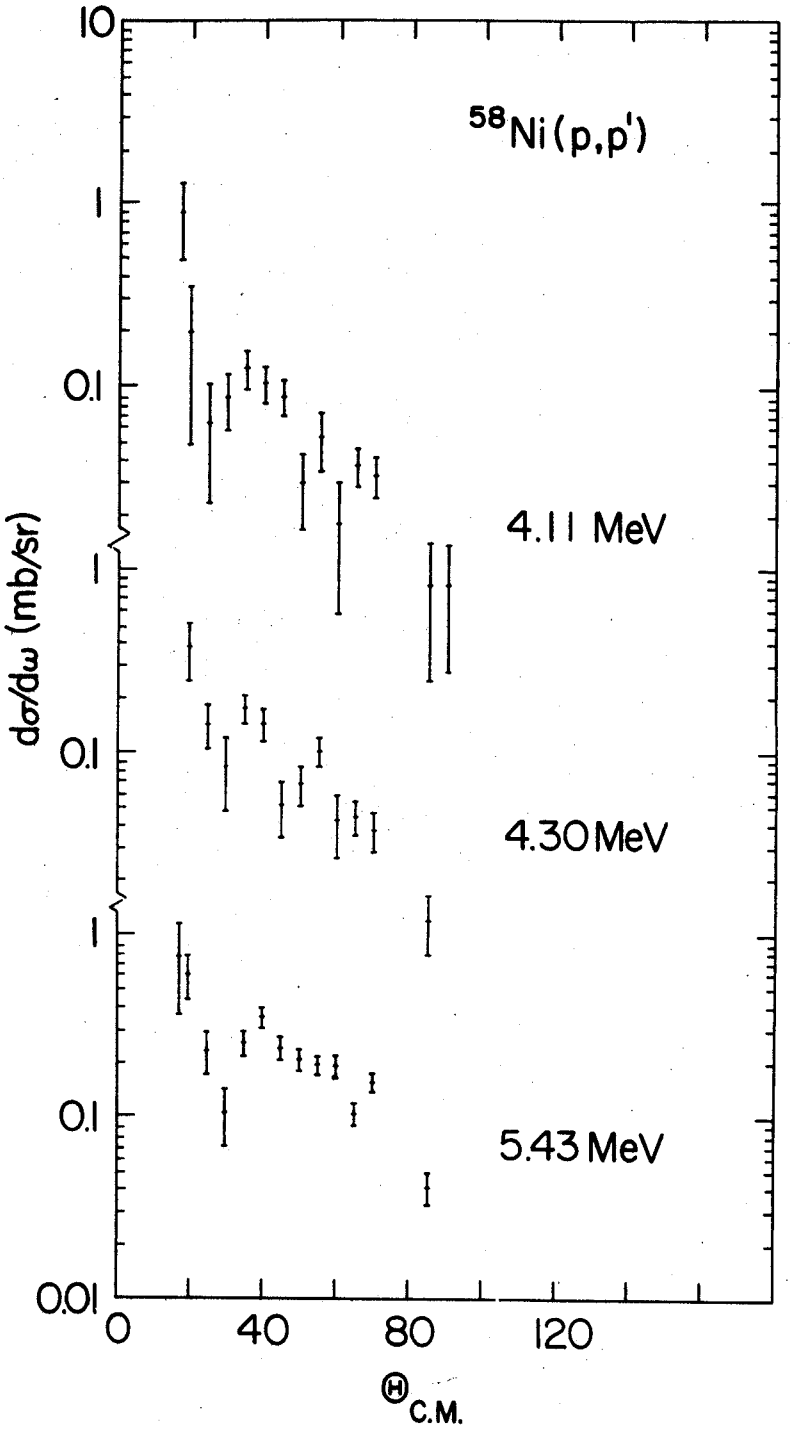
^{58}Ni(p,p')
4.11 MeV
4.30 MeV
5.43 MeV
dσ/dω (mb/sr)
10
1
0.1
1
0.1
1
0.1
0.01
0
40
80
120
Θ C.M.

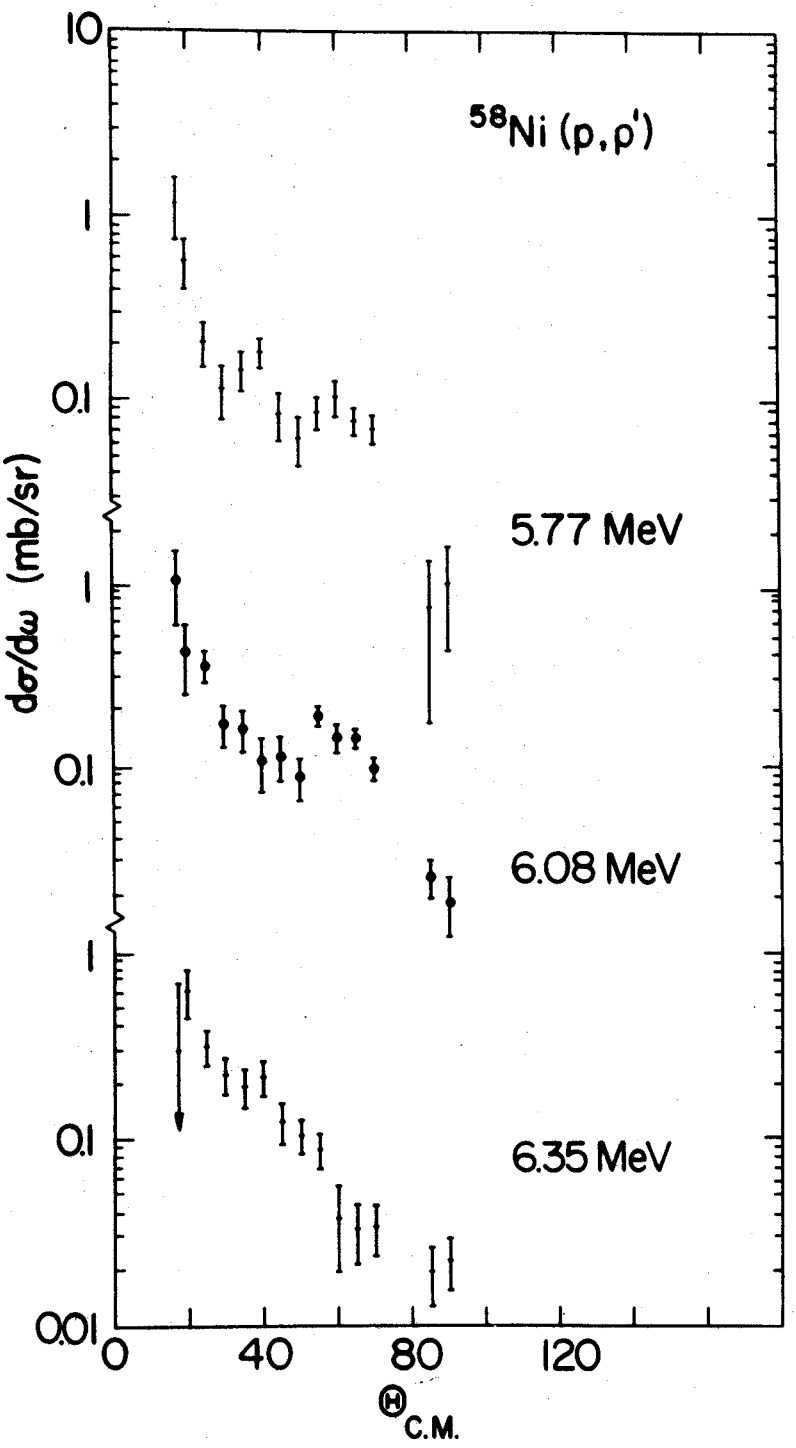
^{58}Ni (p,p')
5.77 MeV
6.08 MeV
6.35 MeV
dσ/dω (mb/sr)
10
1
0.1
1
0.1
1
0.1
0.01
0
40
80
120
Θ C.M.

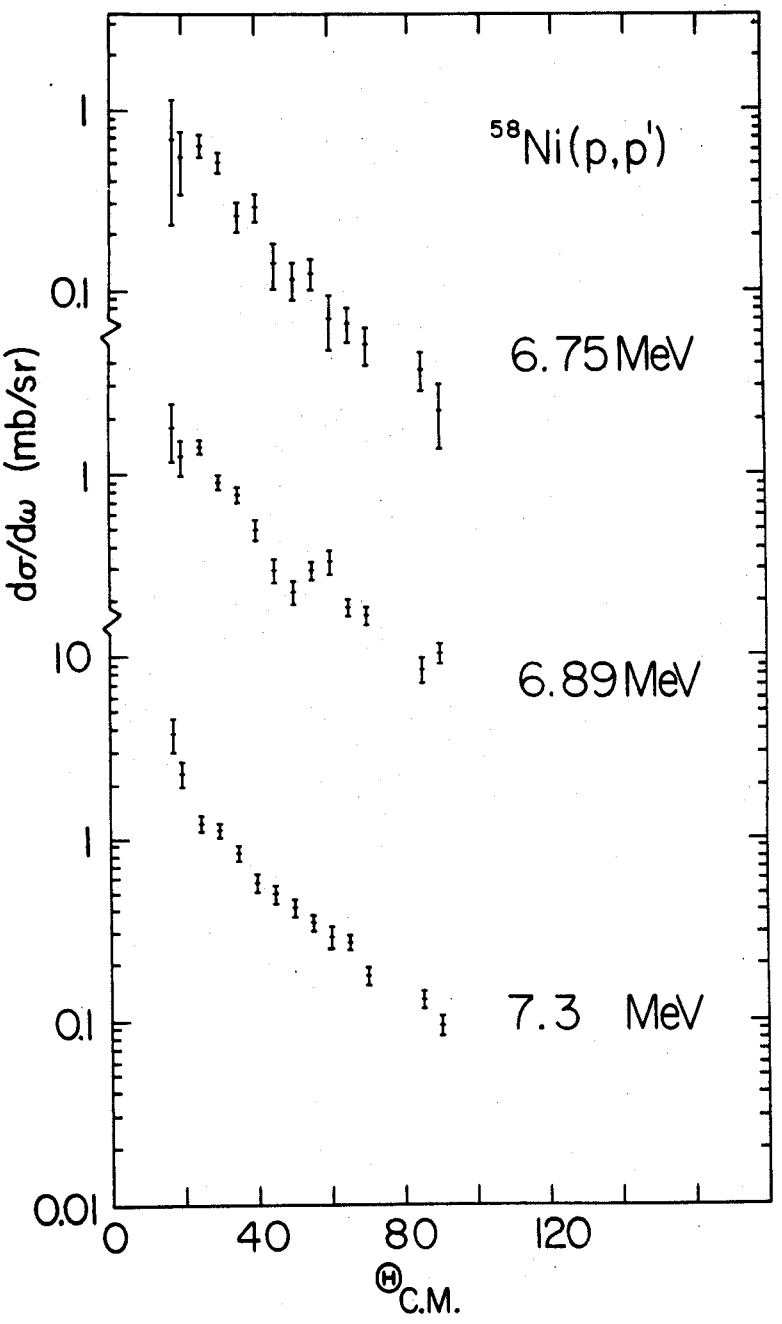
^{58}Ni(p,p')
6.75 MeV
6.89 MeV
7.3 MeV
dσ/dω (mb/sr)
1
0.1
1
10
1
0.1
0.01
0
40
80
120
Θ C.M.

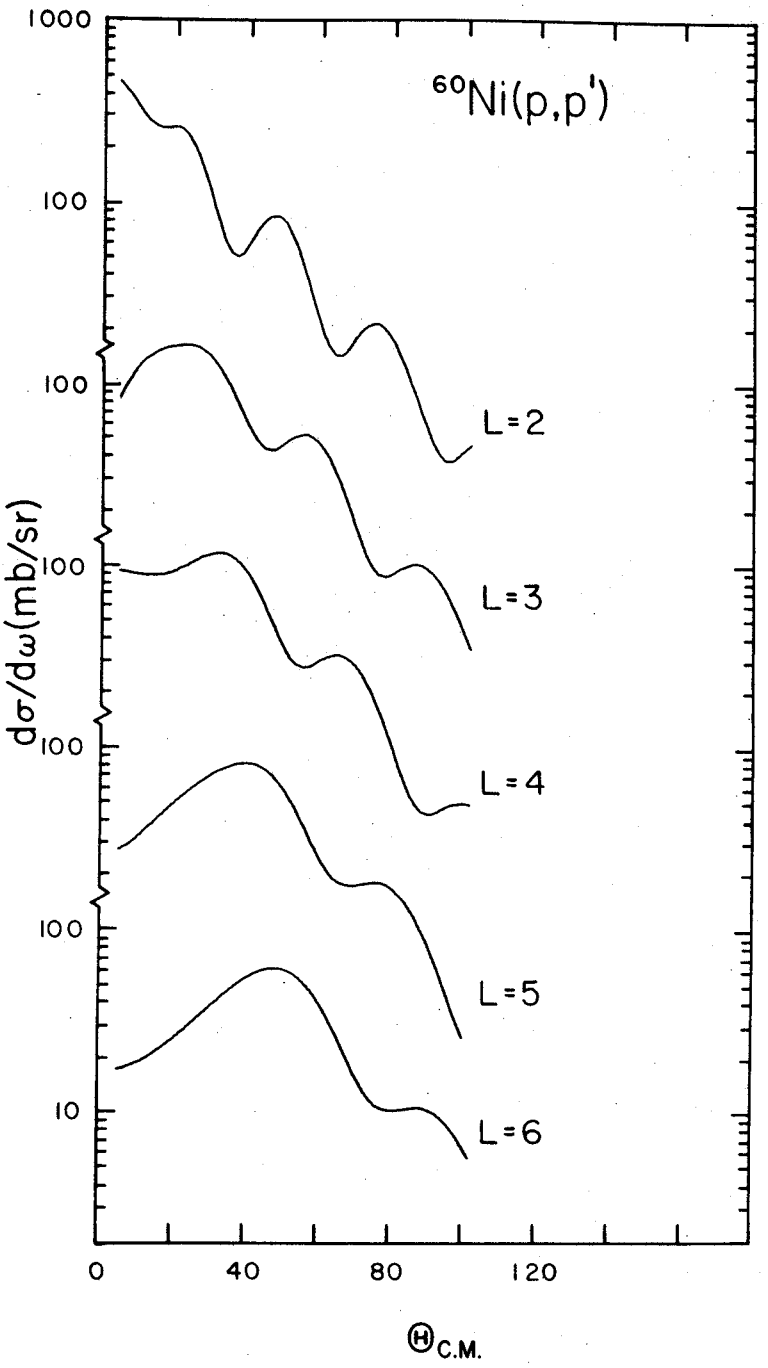
^{60}Ni(p,p')
L=2
L=3
L=4
L=5
L=6
dσ/dω(mb/sr)
1000
100
100
100
100
10
0
40
80
120
Θ C.M.

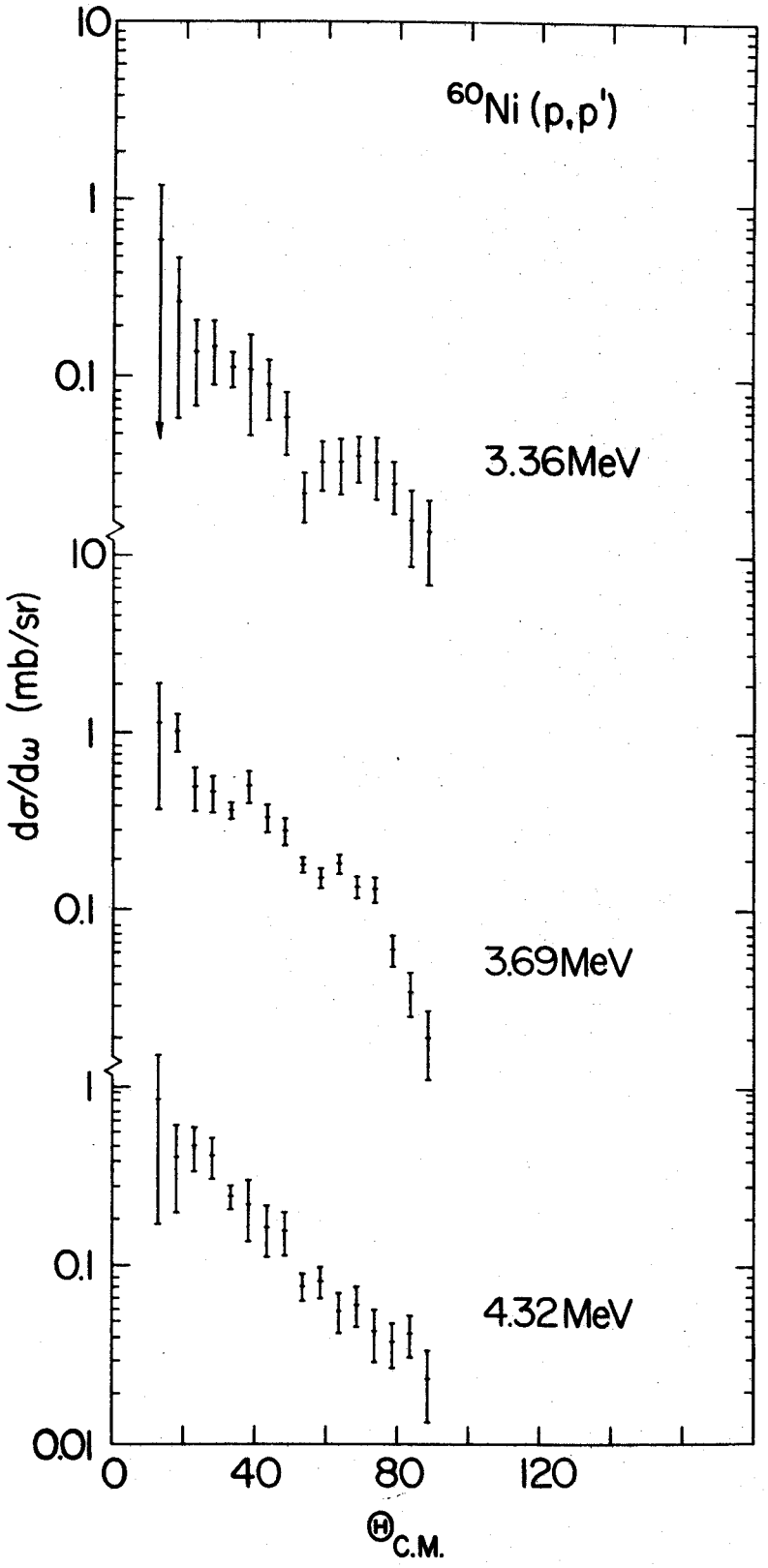
^{60}Ni (p,p')
3.36MeV
3.69MeV
4.32MeV
dσ/dω (mb/sr)
θC.M.
10
1
0.1
10
1
0.1
1
0.1
0.01
0
40
80
120

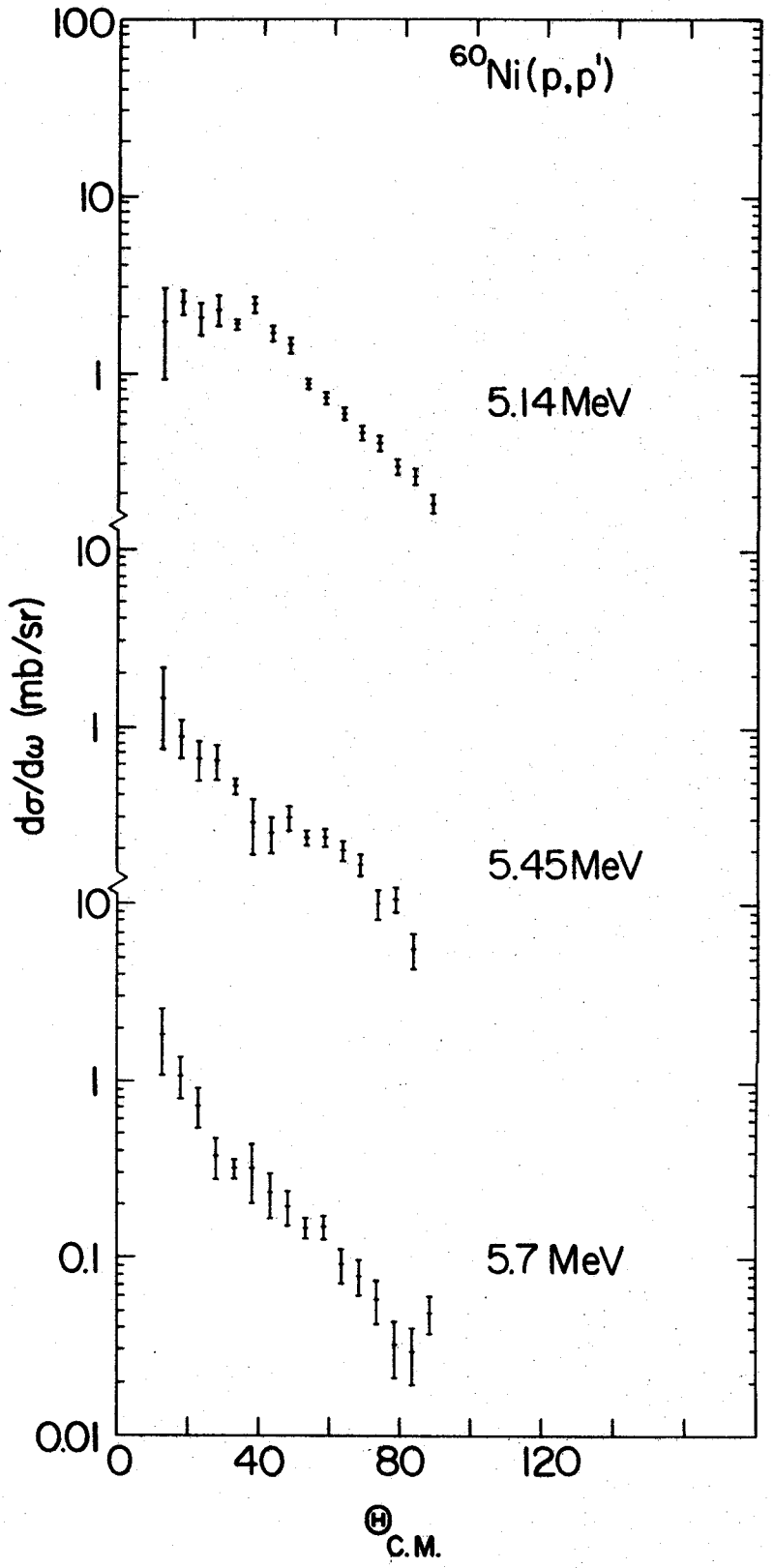
^{60}Ni(p,p')
5.14 MeV
5.45 MeV
5.7 MeV
dσ/dω (mb/sr)
100
10
1
10
1
10
1
0.1
0.01
0
40
80
120
Θ C.M.

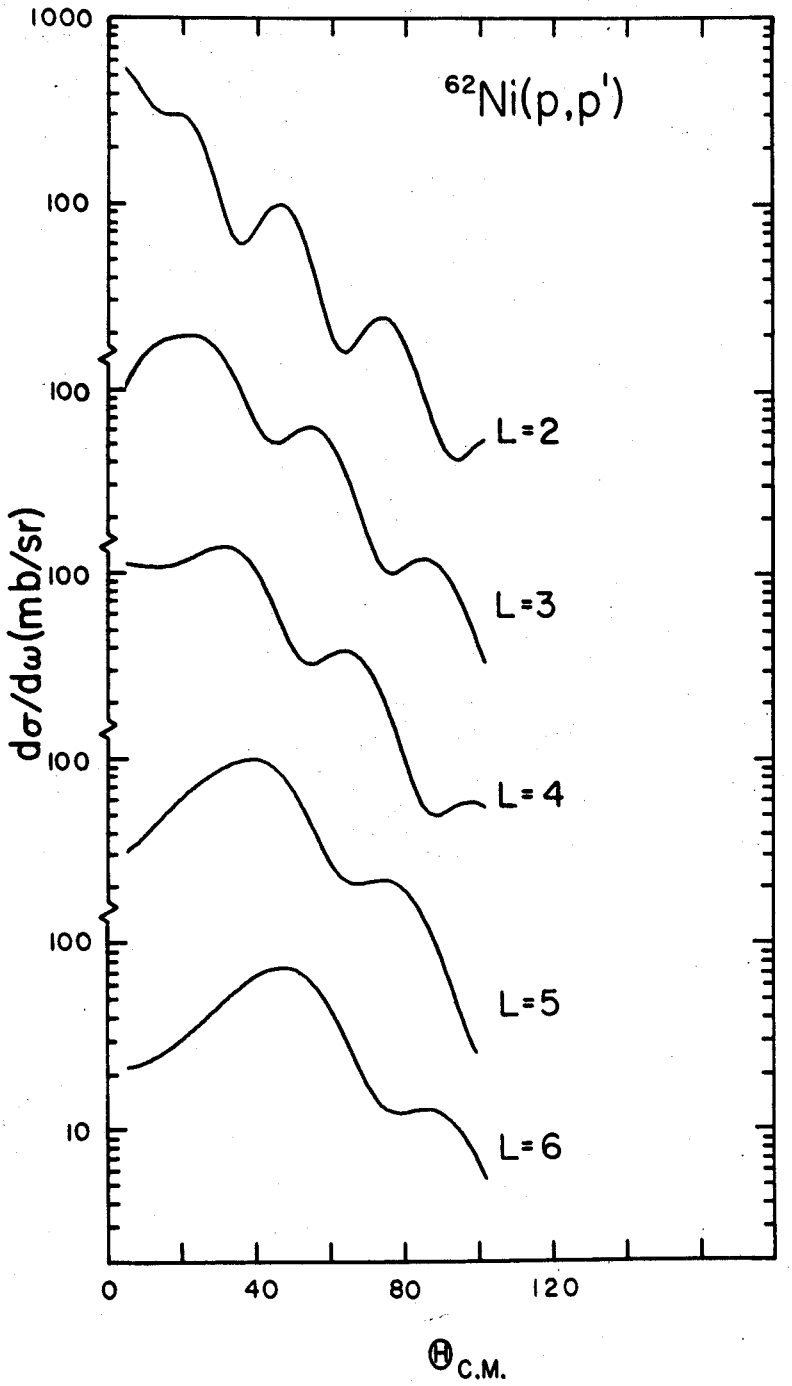
^{62}Ni(p,p')
L=2
L=3
L=4
L=5
L=6
dσ/dω(mb/sr)
1000
100
100
100
100
10
0
40
80
120
Θ C.M.

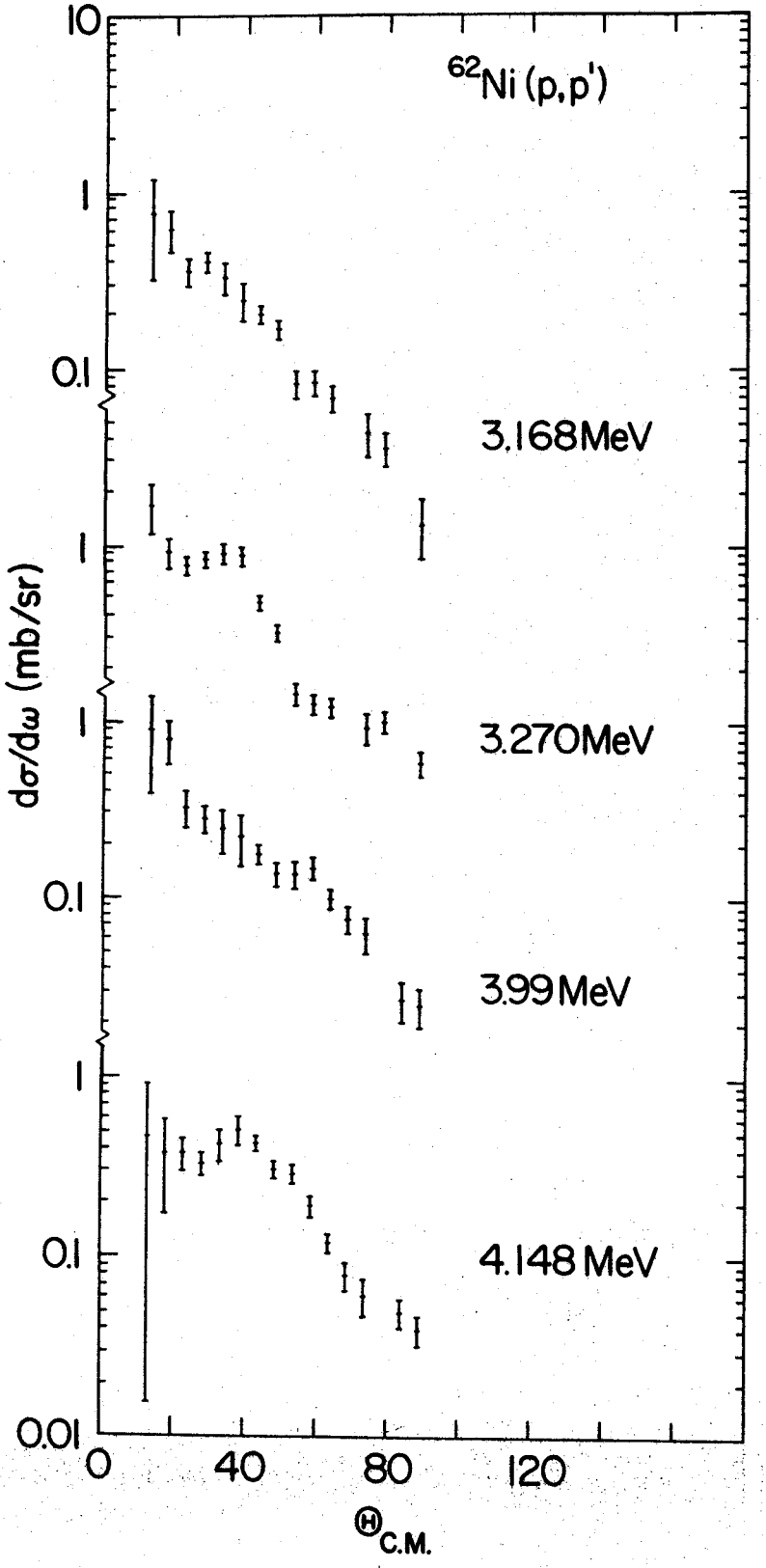
^{62}Ni (p,p')
3.168MeV
3.270MeV
3.99MeV
4.148 MeV
dσ/dω (mb/sr)
10
1
0.1
1
1
0.1
1
0.1
0.01
0
40
80
120
Θ C.M.

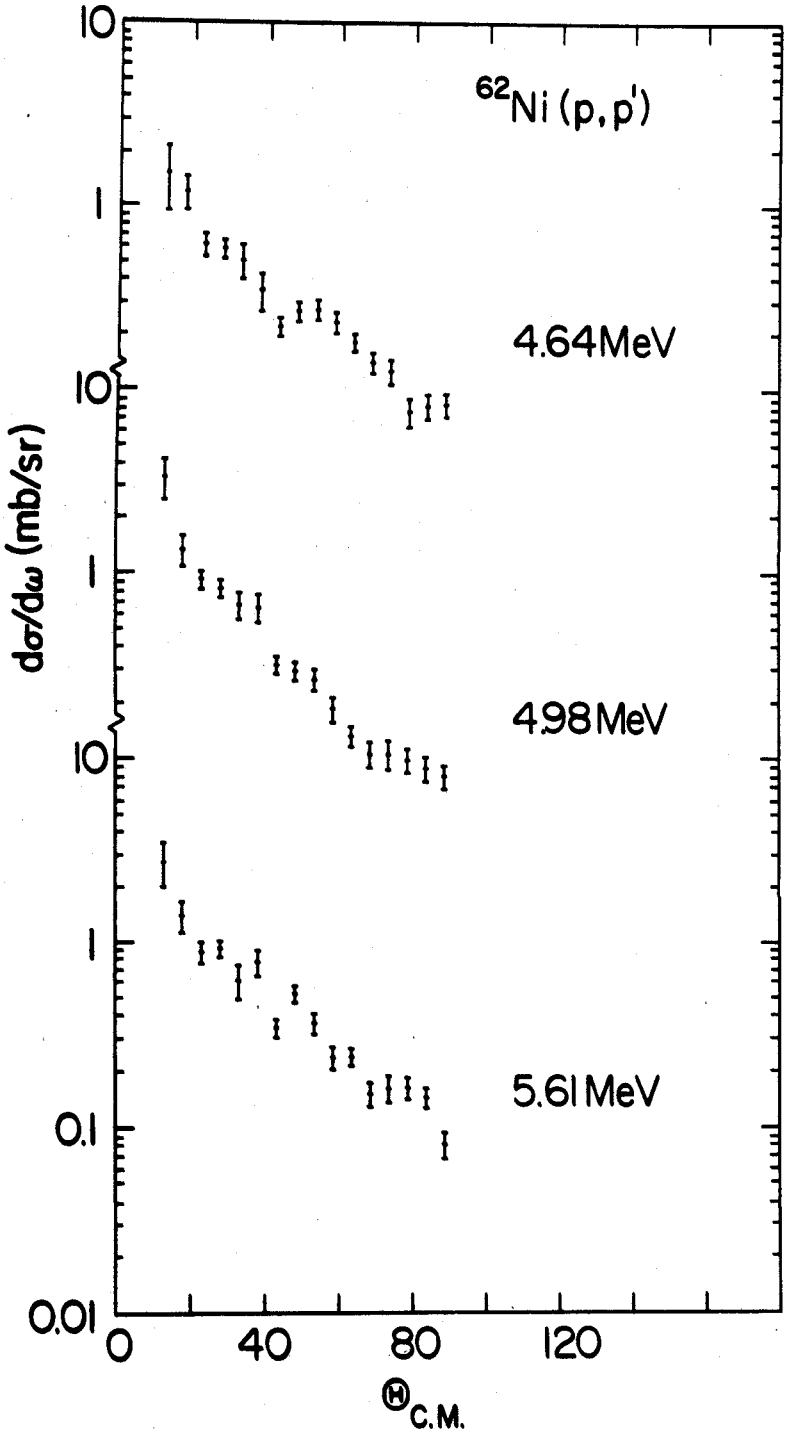
^{62}Ni (p, p')
4.64MeV
4.98MeV
5.61MeV
dσ/dω (mb/sr)
10
1
10
1
10
1
0.1
0.01
0
40
80
120
Θ C.M.

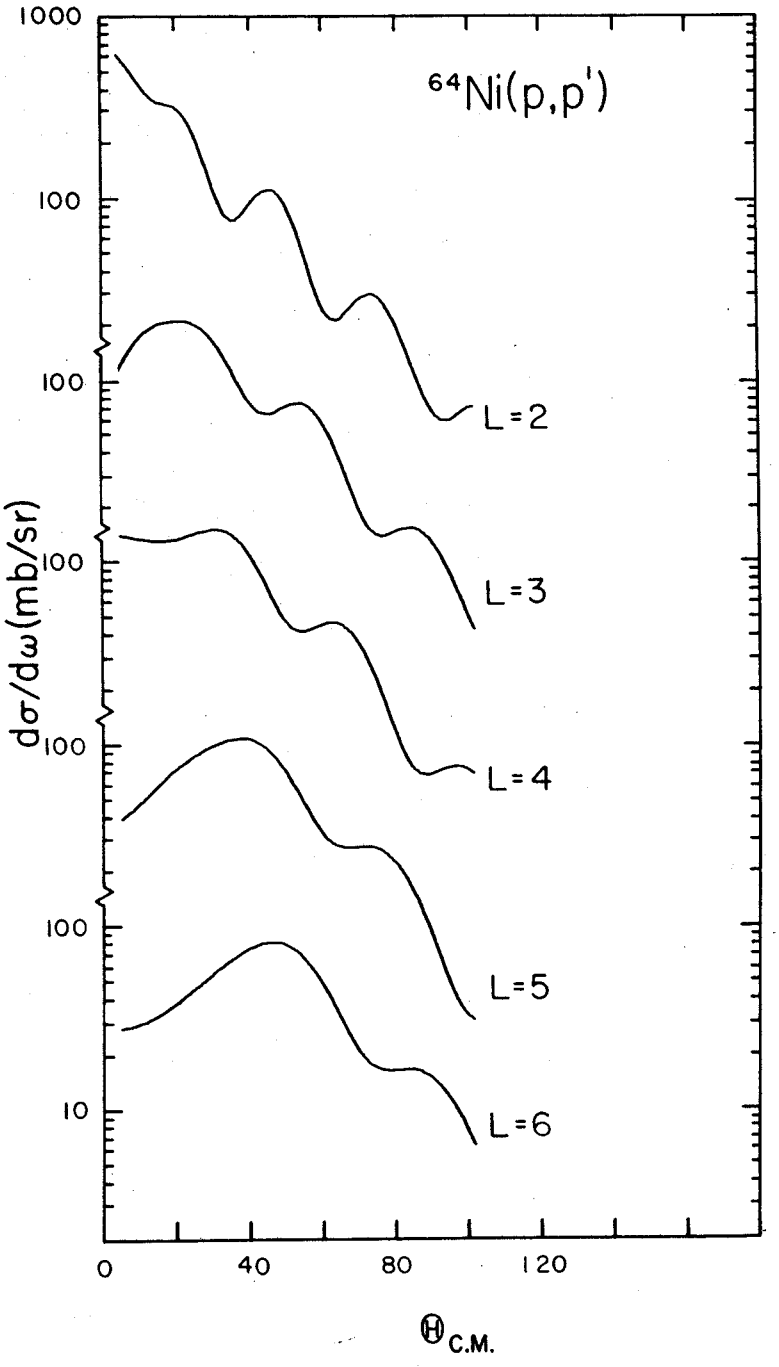
^{64}Ni(p,p')
L=2
L=3
L=4
L=5
L=6
1000
100
100
100
100
10
dσ/dω(mb/sr)
0
40
80
120
Θ C.M.

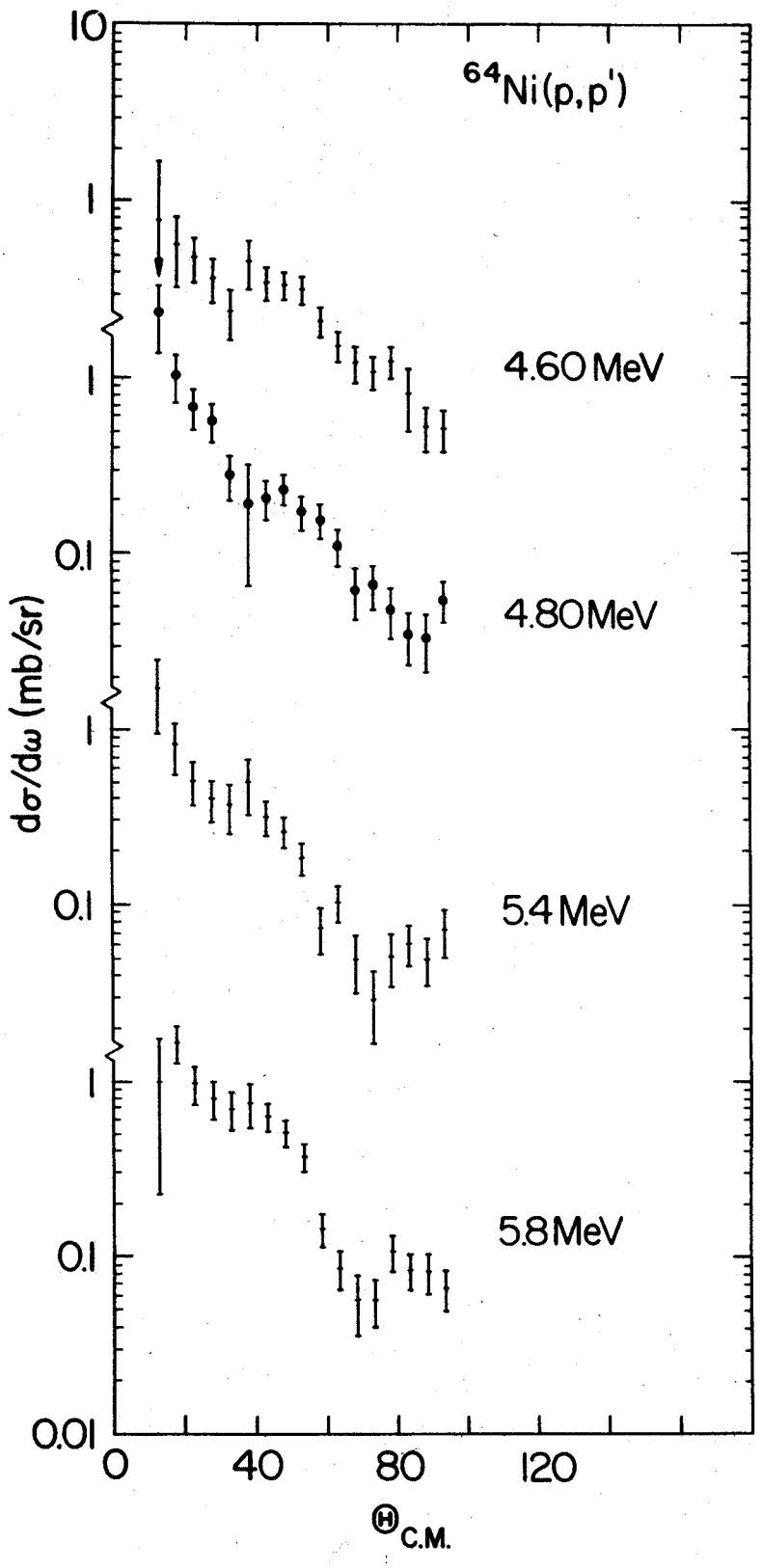
^{64}Ni(p,p')
4.60 MeV
4.80 MeV
5.4 MeV
5.8 MeV
dσ/dω (mb/sr)
10
1
0.1
0.01
0
40
80
120
Θ C.M.

IV.3 Tabulated Nuclear Deformations

All of the values of the nuclear deformations, $\beta_L R_o$ which were obtained from this experiment are tabulated here for ^{58}Ni, ^{60}Ni, ^{62}Ni and ^{64}Ni along with the L-value assigned to the corresponding excited state. The value of R_o used here was $1.16F \times A^{1/3}$ where A is the atomic mass of the target nucleus. Also presented is the X^2/N which is the result of the normalization of the theoretical data to experimental results using the assigned L-value shown

^{58}NI				^{60}Ni			
EX(MeV)[a]	L	$\beta_L R_o$	X^2/N	Ex(MeV)[a]	L	$\beta_L R_o$	X^2/N
1.456	2	0.862 ± 2.3%	6.9	1.331	2	0.972 ± 3.3%	7.0
2.458	4	0.391 ± 2.5%	10.7	2.502	4	0.418 ± 3.7%	13.4
3.035	2	0.260 ± 3.1%	8.2	3.119	2	0.254 ± 4.5%	4.1
3.260	2	0.332 ± 2.8%	5.8	3.36	2	0.154 ± 8.7%	3.8
3.620	4	0.305 ± 2.9%	6.4	3.36	3	0.163	1.2
3.895	2	0.171 ± 5.1%	2.9	3.36	4	0.173	3.8
4.11	2	0.144 ± 6.1%	4.4	3.69	2	0.295 ± 4.2%	8.0
4.11	3	0.148	2.5	3.69	3	0.313	8.6
4.11	4	0.153	1.1	3.69	4	0.327	5.0
4.30	2	0.166 ± 4.4%	5.7	4.042	3	0.822 ± 3.2%	18.5
4.30	3	0.166	2.3	4.32	2	0.223 ± 5.6%	2.8
4.30	4	0.171	2.5	4.32	3	0.236	3.3
4.38	4	0.346 ± 3.4%	2.0	4.32	4	0.245	2.3
4.472	3	0.763 ± 2.3%	13.0	5.14	3	0.645 ± 3.2%	19.0
4.754	4	0.454 ± 2.5%	9.4	5.14	4	0.677	19.2
5.128	6	0.431 ± 2.7%	9.0	5.14	5	0.736	19.1
5.43	3	0.265 ± 3.3%	16.8	5.45	2	0.309 ± 4.1%	7.1
5.43	4	0.274	12.8	5.45	3	0.327	3.7
5.43	5	0.301	8.0	5.45	4	0.341	6.0
5.589	4	0.355 ± 2.8%	9.2	5.7	2	0.272 ± 4.9%	4.0
5.77	2	0.193 ± 4.4%	7.6	5.7	3	0.286	4.0
5.77	3	0.198	3.9	5.7	4	0.304	6.0
5.77	4	0.207	3.9				
6.08	2	0.225 ± 3.9%	9.3				
6.08	3	0.229	5.3				
6.35	2	0.198 ± 4.6%	1.7				
6.35	3	0.202	2.4				
6.35	4	0.211	2.8				
6.75	3	0.251 ± 3.9%	2.3				
6.75	4	0.260	4.6				
6.89	3	0.382 ± 2.9%	3.3				
6.89	4	0.400	14.3				
7.3	3	0.431 ± 2.8%	5.1				
7.3	4	0.449	15.0				

^{62}Ni				^{64}Ni			
1.169	2	0.941 ± 4.4%	38.3	1.344	2	0.849 ± 7.9%	27.8
2.334	4	0.381 ± 4.6%	11.3	2.608	4	0.348 ± 8.3%	21.2
3.168	2	0.220 ± 5.2%	6.0	3.165	2	0.274 ± 8.3%	8.4
3.168	3	0.230	7.8	3.560	3	0.900 ± 7.9%	67.2
3.168	4	0.243	2.6	3.849	5	0.367 ± 8.3	15.1
3.270	2	0.326 ± 4.6%	28.2	4.60	3	0.274 ± 8.5%	5.6
3.270	3	0.344	43.9	4.60	4	0.288	6.7
3.270	4	0.363	15.4	4.60	5	0.311	2.3
3.750	3	0.826 ± 4.3%	32.9	4.80	2	0.251 ± 8.7%	3.0
3.99	3	0.234 ± 5.5%	3.3	4.80	3	0.260	2.2
3.99	4	0.248	4.0	4.80	4	0.274	4.9
3.99	5	0.266	12.3	5.4	2	0.251 ± 8.6%	4.0
4.148	3	0.275 ± 5.0%	19.4	5.4	3	0.260	5.5
1.148	4	0.289	13.3	5.4	4	0.278	7.9
4.148	5	0.312	2.9	5.4	5	0.297	7.4
4.64	2	0.298 ± 4.8%	23.0	5.8	2	0.325 ± 8.2%	5.3
4.64	3	0.312	7.0	5.8	3	0.339	14.8
4.64	4	0.326	16.0	5.8	4	0.362	23.6
4.98	2	0.331 ± 4.7%	17.0	5.8	5	0.385	15.4
4.98	3	0.349	10.9				
4.98	4	0.367	22.9				
5.61	3	0.381 ± 4.6%	13.1				
5.61	4	0.399	22.5				
5.61	5	0.432	35.2				

[a]These are the excitation energies assigned to the excited states observed in this experiment (section 4.1.f).

IV.4 Tabulation of Quantities Calculated from the Nuclear Deformations in IV.3 Above

In the following pages are tabulated the values of parameters calculated from the nuclear deformations. The β_L given here is normalized to an interaction radius of $1.25F \times A^{1/3}$. There are radial moments, $\langle r^\lambda \rangle$ section 4.2.b, which must be evaluated in these calculations and the model used is shown for each set of parameters. There are three models represented below: a uniform charge distribution with $r_o = 1.20F$, a Fermi equivalent uniform charge distribution with $r_o = 1.31F$ (El 61), and a Fermi charge distribution with $r_o = 1.10F$ and $a = 0.566F$ (Du 67).

^{58}Ni(p,p') 40 MeV

Calculated parameters using a Fermi charge distribution with r_o = 1.10F, a = 0.566F

E_x (MeV)	L	β_L	B(EL;0→L) (F^{2L})	G_{SP}	$D_L/\hbar^2$ $(MeV)^{-1}$	C_L (MeV)	$(D_L)_{HYD}/D_L$	B(EL;0→L)/NEWSR
1.456	2	0.178	0.172E+04	12.8	0.419E+02	0.888E+02	0.101	0.322
2.458	4	0.081	0.134E+07	11.7	0.217E+03	0.131E+04	0.066	0.133
3.035	2	0.054	0.156E+03	1.2	0.221E+03	0.203E+04	0.019	0.029
3.260	2	0.069	0.255E+03	1.9	0.126E+03	0.134E+04	0.034	0.048
3.620	4	0.063	0.814E+06	7.1	0.242E+03	0.317E+04	0.059	0.081
3.895	2	0.035	0.675E+02	0.5	0.398E+03	0.604E+04	0.011	0.013
4.472	3	0.158	0.686E+05	18.1	0.244E+02	0.487E+03	0.292	0.322
4.754	4	0.094	0.180E+07	15.8	0.833E+02	0.188E+04	0.173	0.179
5.128	6	0.089	0.316E+11	35.6	0.124E+03	0.325E+04	0.895	0.745
5.589	4	0.073	0.110E+07	9.7	0.116E+03	0.362E+04	0.124	0.109
4.110	2	0.030	0.479E+02	0.4	0.532E+03	0.898E+04	0.008	0.009
4.110	3	0.031	0.258E+04	0.7	0.705E+03	0.119E+05	0.010	0.012
4.110	4	0.032	0.205E+06	1.8	0.848E+03	0.143E+05	0.017	0.020
4.300	2	0.034	0.636E+02	0.5	0.383E+03	0.707E+04	0.011	0.012
4.300	3	0.034	0.325E+04	0.9	0.536E+03	0.990E+04	0.013	0.015
4.300	4	0.035	0.256E+06	2.2	0.649E+03	0.120E+05	0.022	0.025
4.380	4	0.072	0.105E+07	9.2	0.156E+03	0.298E+04	0.092	0.104
5.430	5	0.062	0.886E+08	23.8	0.203E+03	0.598E+04	0.176	0.151
5.430	4	0.057	0.657E+06	5.8	0.200E+03	0.590E+04	0.072	0.065
5.430	3	0.055	0.328E+04	2.2	0.166E+03	0.491E+04	0.043	0.039
5.770	4	0.043	0.375E+06	3.3	0.330E+03	0.110E+05	0.044	0.037
5.770	3	0.041	0.462E+04	1.2	0.281E+03	0.934E+04	0.025	0.022
5.770	2	0.040	0.860E+02	0.6	0.211E+03	0.702E+04	0.020	0.016
6.080	3	0.047	0.618E+04	1.6	0.199E+03	0.736E+04	0.036	0.029
6.080	2	0.047	0.117E+03	0.9	0.147E+03	0.544E+04	0.029	0.022
6.350	4	0.044	0.389E+06	3.4	0.289E+03	0.116E+05	0.050	0.039
6.350	3	0.042	0.481E+04	1.3	0.245E+03	0.987E+04	0.029	0.023
6.350	2	0.041	0.905E+02	0.7	0.182E+03	0.734E+04	0.023	0.017
6.750	3	0.052	0.742E+04	2.0	0.149E+03	0.680E+04	0.048	0.035
6.750	4	0.054	0.591E+06	5.2	0.179E+03	0.815E+04	0.080	0.059
6.890	3	0.079	0.172E+05	4.5	0.631E+02	0.300E+04	0.113	0.081
6.890	4	0.083	0.140E+07	12.3	0.740E+02	0.351E+04	0.194	0.139
7.300	3	0.089	0.219E+05	5.8	0.468E+02	0.249E+04	0.152	0.103
7.300	4	0.093	0.176E+07	15.5	0.554E+02	0.295E+04	0.260	0.175

^{60}Ni(p,p') 40 MeV

Calculated parameters using a Fermi charge distribution with r_o = 1.10F, a = 0.566F

E_x (MeV)	L	β_L	B(EL;0→L) (F^{2L})	G_{SP}	$D_L/\hbar^2$ $(MeV)^{-1}$	C_L (MeV)	$(D_L)_{HYD}/D_L$	B(EL;0→L)/NEWSR
1.331	2	0.199	0.220E+04	15.9	0.369E+02	0.653E+02	0.121	0.401
2.502	4	0.085	0.155E+07	12.8	0.191E+03	0.119E+04	0.078	0.146
3.119	2	0.052	0.150E+03	1.1	0.230E+03	0.224E+04	0.019	0.027
3.360	4	0.035	0.265E+06	2.2	0.830E+03	0.937E+04	0.018	0.025
3.360	2	0.031	0.553E+02	0.4	0.582E+03	0.657E+04	0.008	0.010
3.360	3	0.033	0.317E+04	0.8	0.727E+03	0.821E+04	0.010	0.014
3.690	4	0.067	0.946E+06	7.8	0.211E+03	0.288E+04	0.070	0.089
3.690	3	0.064	0.117E+05	2.9	0.180E+03	0.244E+04	0.041	0.053
3.690	2	0.060	0.203E+03	1.5	0.144E+03	0.197E+04	0.031	0.037
4.042	3	0.168	0.807E+05	20.3	0.238E+02	0.388E+03	0.312	0.364
4.320	4	0.050	0.531E+06	4.4	0.322E+03	0.601E+04	0.046	0.050
4.320	2	0.046	0.116E+03	0.8	0.216E+03	0.403E+04	0.021	0.021
4.320	3	0.048	0.665E+04	1.7	0.270E+03	0.503E+04	0.027	0.030
5.140	4	0.138	0.405E+07	33.5	0.354E+02	0.936E+03	0.418	0.383
5.140	5	0.150	0.531E+09	32.9	0.366E+02	0.968E+03	0.988	0.861
5.140	3	0.132	0.497E+05	12.5	0.304E+02	0.802E+03	0.244	0.224
5.450	3	0.067	0.128E+05	3.2	0.111E+03	0.331E+04	0.066	0.058
5.450	4	0.070	0.103E+07	8.5	0.132E+03	0.391E+04	0.112	0.097
5.450	2	0.063	0.223E+03	1.6	0.891E+02	0.265E+04	0.050	0.041
5.700	3	0.058	0.977E+04	2.5	0.139E+03	0.452E+04	0.053	0.044
5.700	2	0.056	0.172E+03	1.2	0.110E+03	0.357E+04	0.041	0.031
5.700	4	0.062	0.817E+06	6.8	0.158E+03	0.515E+04	0.093	0.077

^{62}Ni(p,p') 40 MeV

Calculated parameters using a Fermi charge distribution with r_o = 1.10F, a = 0.566F

E_x (MeV)	L	β_L	B(EL;0→L) (F^{2L})	G_{SP}	$D_L/\hbar^2$ $(MeV)^{-1}$	C_L (MeV)	$(D_L)_{HYD}/D_L$	B(EL;0→L)/NEWSR
1.169	2	0.190	0.208E+04	14.6	0.458E+02	0.626E+02	0.102	0.369
2.334	4	0.077	0.130E+07	10.1	0.252E+03	0.137E+04	0.060	0.117
3.168	4	0.049	0.528E+06	4.1	0.456E+03	0.458E+04	0.033	0.048
3.168	2	0.044	0.114E+03	0.8	0.309E+03	0.310E+04	0.015	0.020
3.168	3	0.046	0.640E+04	1.5	0.396E+03	0.397E+04	0.019	0.028
3.270	4	0.073	0.118E+07	9.2	0.198E+03	0.212E+04	0.077	0.107
3.270	2	0.066	0.250E+03	1.7	0.136E+03	0.146E+04	0.034	0.044
3.270	3	0.070	0.143E+05	3.4	0.171E+03	0.183E+04	0.045	0.062
3.750	3	0.167	0.826E+05	19.9	0.259E+02	0.365E+03	0.297	0.359
3.990	3	0.047	0.663E+04	1.6	0.304E+03	0.483E+04	0.025	0.029
3.990	4	0.050	0.550E+06	4.3	0.348E+03	0.553E+04	0.044	0.050
3.990	5	0.054	0.696E+08	16.3	0.369E+03	0.588E+04	0.099	0.107
4.148	4	0.058	0.747E+06	5.8	0.246E+03	0.424E+04	0.062	0.068
4.148	3	0.056	0.915E+04	2.2	0.211E+03	0.364E+04	0.036	0.040
4.148	5	0.063	0.958E+08	22.4	0.258E+03	0.444E+04	0.142	0.148
4.640	3	0.063	0.118E+05	2.8	0.147E+03	0.316E+04	0.052	0.051
4.640	2	0.060	0.209E+03	1.5	0.115E+03	0.248E+04	0.041	0.037
4.640	4	0.066	0.951E+06	7.4	0.173E+03	0.372E+04	0.088	0.086
4.980	3	0.071	0.147E+05	3.5	0.109E+03	0.271E+04	0.070	0.064
4.980	4	0.074	0.120E+07	9.4	0.127E+03	0.315E+04	0.120	0.109
4.980	2	0.067	0.258E+03	1.8	0.868E+02	0.215E+04	0.054	0.046
5.610	3	0.077	0.176E+05	4.2	0.815E+02	0.256E+04	0.095	0.076
5.610	4	0.081	0.142E+07	11.1	0.955E+02	0.301E+04	0.159	0.129
5.610	5	0.087	0.184E+09	42.9	0.996E+02	0.313E+04	0.368	0.283

^{64}Ni(p,p') 40 MeV

Calculated parameters using a Fermi charge distribution with r_o = 1.10F, a = 0.566F

E_x (MeV)	L	β_L	B(EL;O→L) (F^{2L})	G_{SP}	$D_L/\hbar^2$ $(MeV)^{-1}$	C_L (MeV)	$(D_L)_{HYD}/D_L$	B(EL;O→L)/NEWSR
1.344	2	0.170	0.171E+04	11.6	0.500E+02	0.902E+02	0.098	0.295
2.608	4	0.070	0.110E+07	8.1	0.276E+03	0.188E+04	0.057	0.095
3.165	2	0.055	0.178E+03	1.2	0.204E+03	0.204E+04	0.024	0.031
3.560	3	0.180	0.994E+05	22.9	0.235E+02	0.298E+03	0.341	0.415
3.849	5	0.073	0.133E+09	29.1	0.205E+03	0.304E+04	0.181	0.196
4.600	5	0.062	0.956E+08	20.9	0.239E+03	0.506E+04	0.155	0.140
4.600	4	0.058	0.751E+06	5.5	0.228E+03	0.483E+04	0.068	0.065
4.600	3	0.055	0.921E+04	2.1	0.196E+03	0.415E+04	0.041	0.039
4.800	3	0.052	0.829E+04	1.9	0.209E+03	0.481E+04	0.038	0.035
4.800	4	0.055	0.680E+06	5.0	0.242E+03	0.557E+04	0.065	0.059
4.800	2	0.050	0.150E+03	1.0	0.160E+03	0.369E+04	0.031	0.026
5.400	3	0.052	0.829E+04	1.9	0.186E+03	0.541E+04	0.043	0.035
5.400	4	0.056	0.700E+06	5.2	0.209E+03	0.609E+04	0.075	0.060
5.400	5	0.059	0.872E+08	19.1	0.224E+03	0.652E+04	0.166	0.128
5.400	2	0.050	0.150E+03	1.0	0.142E+03	0.415E+04	0.034	0.026
5.800	2	0.065	0.251E+03	1.7	0.790E+02	0.266E+04	0.062	0.043
5.800	5	0.077	0.147E+09	32.1	0.124E+03	0.417E+04	0.300	0.215
5.800	3	0.068	0.141E+05	3.2	0.102E+03	0.342E+04	0.079	0.059
5.800	4	0.072	0.119E+07	8.8	0.115E+03	0.386E+04	0.136	0.103

^{58}Ni(p,p') 40 MeV

Calculated parameters using a uniform charge distribution with r_o = 1.20F

E_x (MeV)	L	β_L	B(EL;0→L) (F^{2L})	G_{SP}	$D_L/\hbar^2$ $(MeV)^{-1}$	C_L (MeV)	$(D_L)_{HYD}/D_L$	B(EL;0→L)/NEWSR
1.456	2	0.178	0.103E+04	10.7	0.499E+02	0.106E+03	0.072	0.322
2.458	4	0.081	0.988E+05	2.4	0.258E+03	0.156E+04	0.014	0.058
3.035	2	0.054	0.938E+02	1.0	0.263E+03	0.242E+04	0.014	0.029
3.260	2	0.069	0.153E+03	1.6	0.150E+03	0.160E+04	0.024	0.048
3.620	4	0.063	0.601E+05	1.5	0.288E+03	0.378E+04	0.012	0.035
3.895	2	0.035	0.406E+02	0.4	0.474E+03	0.718E+04	0.008	0.013
4.472	3	0.158	0.174E+05	8.7	0.290E+02	0.580E+03	0.124	0.232
4.754	4	0.094	0.133E+06	3.2	0.991E+02	0.224E+04	0.036	0.078
5.128	6	0.089	0.559E+08	3.3	0.147E+03	0.387E+04	0.024	0.066
5.589	4	0.073	0.814E+05	2.0	0.138E+03	0.431E+04	0.026	0.048
4.110	2	0.030	0.288E+02	0.3	0.633E+03	0.107E+05	0.006	0.009
4.110	3	0.031	0.656E+03	0.3	0.839E+03	0.142E+05	0.004	0.009
4.110	4	0.032	0.151E+05	0.4	0.101E+04	0.170E+05	0.004	0.009
4.300	2	0.034	0.383E+02	0.4	0.455E+03	0.842E+04	0.008	0.012
4.300	3	0.034	0.825E+03	0.4	0.637E+03	0.118E+05	0.006	0.011
4.300	4	0.035	0.189E+05	0.5	0.772E+03	0.143E+05	0.005	0.011
4.380	4	0.072	0.774E+05	1.9	0.185E+03	0.355E+04	0.019	0.045
5.430	5	0.062	0.126E+07	1.5	0.241E+03	0.711E+04	0.015	0.033
5.430	4	0.057	0.485E+05	1.2	0.238E+03	0.702E+04	0.015	0.028
5.430	3	0.055	0.210E+04	1.0	0.198E+03	0.584E+04	0.018	0.028
5.770	4	0.043	0.277E+05	0.7	0.393E+03	0.131E+05	0.009	0.016
5.770	3	0.041	0.117E+04	0.6	0.334E+03	0.111E+05	0.011	0.016
5.770	2	0.040	0.517E+02	0.5	0.251E+03	0.836E+04	0.014	0.016
6.080	3	0.047	0.157E+04	0.8	0.237E+03	0.876E+04	0.015	0.021
6.080	2	0.047	0.703E+02	0.7	0.175E+03	0.648E+04	0.020	0.022
6.350	4	0.044	0.288E+05	0.7	0.343E+03	0.138E+05	0.010	0.017
6.350	3	0.042	0.122E+04	0.6	0.291E+03	0.118E+05	0.012	0.016
6.350	2	0.041	0.544E+02	0.6	0.217E+03	0.874E+04	0.017	0.017
6.750	3	0.052	0.189E+04	0.9	0.178E+03	0.809E+04	0.020	0.025
6.750	4	0.054	0.437E+05	1.1	0.213E+03	0.969E+04	0.017	0.026
6.890	3	0.079	0.437E+04	2.2	0.751E+02	0.357E+04	0.048	0.058
6.890	4	0.083	0.103E+06	2.5	0.881E+02	0.418E+04	0.041	0.061
7.300	3	0.089	0.556E+04	2.8	0.557E+02	0.297E+04	0.064	0.074
7.300	4	0.093	0.130E+06	3.2	0.660E+02	0.352E+04	0.054	0.076

^{60}Ni(p,p') 40 MeV

Calculated parameters using a uniform charge distribution with r_o = 1.20F

E_x (MeV)	L	β_L	B(EL;0→L) (F^{2L})	G_{SP}	$D_L/\hbar^2$ $(MeV)^{-1}$	C_L (MeV)	$(D_L)_{HYD}/D_L$	B(EL;0→L)/NEWSR
1.331	2	0.199	0.134E+04	13.4	0.439E+02	0.777E+02	0.086	0.401
2.502	4	0.085	0.121E+06	2.7	0.227E+03	0.142E+04	0.017	0.065
3.119	2	0.052	0.916E+02	0.9	0.274E+03	0.267E+04	0.014	0.027
3.360	4	0.035	0.207E+05	0.5	0.988E+03	0.111E+05	0.004	0.011
3.360	2	0.031	0.337E+02	0.3	0.692E+03	0.782E+04	0.005	0.010
3.360	3	0.033	0.833E+03	0.4	0.865E+03	0.977E+04	0.004	0.010
3.690	4	0.067	0.740E+05	1.6	0.252E+03	0.343E+04	0.015	0.040
3.690	3	0.064	0.307E+04	1.4	0.214E+03	0.291E+04	0.018	0.038
3.690	2	0.060	0.124E+03	1.2	0.172E+03	0.234E+04	0.022	0.037
4.042	3	0.168	0.212E+05	9.8	0.283E+02	0.462E+03	0.134	0.263
4.320	4	0.050	0.415E+05	0.9	0.383E+03	0.715E+04	0.010	0.022
4.320	2	0.046	0.706E+02	0.7	0.257E+03	0.479E+04	0.015	0.021
4.320	3	0.048	0.175E+04	0.8	0.321E+03	0.599E+04	0.012	0.022
5.140	4	0.138	0.317E+06	7.1	0.422E+02	0.111E+04	0.090	0.170
5.140	5	0.150	0.827E+07	8.9	0.436E+02	0.115E+04	0.087	0.194
5.140	3	0.132	0.130E+05	6.0	0.361E+02	0.954E+03	0.105	0.162
5.450	3	0.067	0.335E+04	1.6	0.133E+03	0.394E+04	0.029	0.042
5.450	4	0.070	0.804E+05	1.8	0.157E+03	0.465E+04	0.024	0.043
5.450	2	0.063	0.136E+03	1.3	0.106E+03	0.315E+04	0.036	0.040
5.700	3	0.058	0.256E+04	1.2	0.166E+03	0.538E+04	0.023	0.032
5.700	2	0.056	0.105E+03	1.0	0.131E+03	0.425E+04	0.029	0.031
5.700	4	0.062	0.639E+05	1.4	0.189E+03	0.613E+04	0.020	0.034

^{62}Ni(p,p') 40 MeV

Calculated parameters using a uniform charge distribution with r_o = 1.20F

E_x (MeV)	L	β_L	B(EL;0→L) (F^{2L})	G_{SP}	$D_L/\hbar^2$ $(MeV)^{-1}$	C_L (MeV)	$(D_L)_{HYD}/D_L$	B(EL;0→L)/NEWSR
1.169	2	0.190	0.129E+04	12.2	0.545E+02	0.744E+02	0.074	0.367
2.334	4	0.077	0.107E+06	2.2	0.300E+03	0.163E+04	0.013	0.053
3.168	4	0.049	0.436E+05	0.9	0.543E+03	0.545E+04	0.007	0.021
3.168	2	0.044	0.702E+02	0.7	0.368E+03	0.369E+04	0.011	0.020
3.168	3	0.046	0.173E+04	0.8	0.471E+03	0.473E+04	0.009	0.020
3.270	4	0.073	0.973E+05	2.0	0.236E+03	0.252E+04	0.017	0.048
3.270	2	0.066	0.154E+03	1.5	0.162E+03	0.174E+04	0.025	0.044
3.270	3	0.070	0.387E+04	1.7	0.204E+03	0.218E+04	0.020	0.045
3.750	3	0.167	0.223E+05	9.7	0.309E+02	0.434E+03	0.130	0.260
3.990	3	0.047	0.179E+04	0.8	0.361E+03	0.575E+04	0.011	0.021
3.990	4	0.050	0.454E+05	0.9	0.414E+03	0.659E+04	0.010	0.022
3.990	5	0.054	0.118E+07	1.1	0.439E+03	0.700E+04	0.009	0.025
4.148	4	0.058	0.617E+05	1.3	0.293E+03	0.504E+04	0.014	0.030
4.148	3	0.056	0.248E+04	1.1	0.252E+03	0.433E+04	0.016	0.029
4.148	5	0.063	0.162E+07	1.6	0.307E+03	0.529E+04	0.013	0.034
4.640	3	0.063	0.319E+04	1.4	0.175E+03	0.376E+04	0.023	0.037
4.640	2	0.060	0.129E+03	1.2	0.137E+03	0.295E+04	0.029	0.037
4.640	4	0.066	0.785E+05	1.6	0.206E+03	0.443E+04	0.019	0.038
4.980	3	0.071	0.399E+04	1.7	0.130E+03	0.323E+04	0.031	0.046
4.980	4	0.074	0.995E+05	2.0	0.151E+03	0.375E+04	0.026	0.049
4.980	2	0.067	0.159E+03	1.5	0.103E+03	0.256E+04	0.039	0.045
5.610	3	0.077	0.475E+04	2.1	0.969E+02	0.305E+04	0.041	0.055
5.610	4	0.081	0.118E+06	2.4	0.114E+03	0.358E+04	0.035	0.058
5.610	5	0.087	0.311E+07	3.0	0.118E+03	0.373E+04	0.034	0.065

^{64}Ni(p,p') 40 MeV

Calculated parameters using a uniform charge distribution with r_o = 1.20F

E_x (MeV)	L	β_L	B(EL;0→L) (F^{2L})	G_{SP}	$D_L/\hbar^2$ $(MeV)^{-1}$	C_L (MeV)	$(D_L)_{HYD}/D_L$	B(EL;0→L)/NEWSR
1•344	2	0•170	0•107E+04	9•8	0•595E+02	0•107E+03	0•071	0•293
2•608	4	0•070	0•953E+05	1•8	0•328E+03	0•223E+04	0•013	0•043
3•165	2	0•055	0•111E+03	1•0	0•242E+03	0•243E+04	0•017	0•030
3•560	3	0•180	0•277E+05	11•3	0•280E+02	0•354E+03	0•151	0•302
3•849	5	0•073	0•244E+07	2•1	0•244E+03	0•362E+04	0•017	0•046
4•600	5	0•062	0•175E+07	1•5	0•285E+03	0•603E+04	0•015	0•033
4•600	4	0•058	0•653E+05	1•2	0•272E+03	0•575E+04	0•016	0•029
4•600	3	0•055	0•256E+04	1•0	0•233E+03	0•494E+04	0•018	0•028
4•800	3	0•052	0•231E+04	0•9	0•249E+03	0•573E+04	0•017	0•025
4•800	4	0•055	0•591E+05	1•1	0•288E+03	0•663E+04	0•015	0•027
4•800	2	0•050	0•934E+02	0•9	0•190E+03	0•439E+04	0•022	0•026
5•400	3	0•052	0•231E+04	0•9	0•221E+03	0•644E+04	0•019	0•025
5•400	4	0•056	0•608E+05	1•1	0•248E+03	0•724E+04	0•017	0•027
5•400	5	0•059	0•160E+07	1•4	0•266E+03	0•776E+04	0•016	0•030
5•400	2	0•050	0•934E+02	0•9	0•169E+03	0•494E+04	0•025	0•026
5•800	2	0•065	0•157E+03	1•4	0•940E+02	0•316E+04	0•045	0•043
5•800	5	0•077	0•269E+07	2•3	0•147E+03	0•496E+04	0•029	0•051
5•800	3	0•068	0•392E+04	1•6	0•121E+03	0•407E+04	0•035	0•043
5•800	4	0•072	0•103E+06	1•9	0•136E+03	0•459E+04	0•031	0•046

^{58}Ni(p,p') 40 MeV

Calculated parameters using a uniform charge distribution with r_o = 1.31F

E_x (MeV)	L	β_L	B(EL;0→L) (F^{2L})	G_{SP}	$D_L/\hbar^2$ $(MeV)^{-1}$	C_L (MeV)	$(D_L)_{HYD}/D_L$	B(EL;0→L)/NEWSR
1.456	2	0.178	0.123E+04	9.0	0.594E+02	0.126E+03	0.072	0.270
2.458	4	0.081	0.167E+06	2.0	0.308E+03	0.186E+04	0.014	0.049
3.035	2	0.054	0.112E+03	0.8	0.313E+03	0.289E+04	0.014	0.025
3.260	2	0.069	0.182E+03	1.3	0.179E+03	0.190E+04	0.024	0.040
3.620	4	0.063	0.102E+06	1.2	0.344E+03	0.450E+04	0.012	0.030
3.895	2	0.035	0.484E+02	0.4	0.564E+03	0.856E+04	0.008	0.011
4.472	3	0.158	0.248E+05	7.3	0.346E+02	0.691E+03	0.124	0.195
4.754	4	0.094	0.225E+06	2.7	0.118E+03	0.267E+04	0.036	0.065
5.128	6	0.089	0.134E+09	2.8	0.175E+03	0.461E+04	0.024	0.056
5.589	4	0.073	0.138E+06	1.7	0.164E+03	0.513E+04	0.026	0.040
4.110	2	0.030	0.343E+02	0.3	0.754E+03	0.127E+05	0.006	0.008
4.110	3	0.031	0.932E+03	0.3	0.100E+04	0.169E+05	0.004	0.007
4.110	4	0.032	0.256E+05	0.3	0.120E+04	0.203E+05	0.004	0.007
4.300	2	0.034	0.456E+02	0.3	0.543E+03	0.100E+05	0.008	0.010
4.300	3	0.034	0.117E+04	0.3	0.760E+03	0.140E+05	0.006	0.009
4.300	4	0.035	0.320E+05	0.4	0.920E+03	0.170E+05	0.005	0.009
4.380	4	0.072	0.131E+06	1.6	0.221E+03	0.423E+04	0.019	0.038
5.430	5	0.062	0.255E+07	1.3	0.287E+03	0.848E+04	0.015	0.028
5.430	4	0.057	0.821E+05	1.0	0.284E+03	0.837E+04	0.015	0.024
5.430	3	0.055	0.299E+04	0.9	0.236E+03	0.696E+04	0.018	0.023
5.770	4	0.043	0.469E+05	0.6	0.468E+03	0.156E+05	0.009	0.014
5.770	3	0.041	0.167E+04	0.5	0.398E+03	0.132E+05	0.011	0.013
5.770	2	0.040	0.616E+02	0.5	0.299E+03	0.996E+04	0.014	0.014
6.080	3	0.047	0.223E+04	0.7	0.282E+03	0.104E+05	0.015	0.018
6.080	2	0.047	0.838E+02	0.6	0.209E+03	0.772E+04	0.020	0.018
6.350	4	0.044	0.487E+05	0.6	0.409E+03	0.165E+05	0.010	0.014
6.350	3	0.042	0.174E+04	0.5	0.347E+03	0.140E+05	0.012	0.014
6.350	2	0.041	0.649E+02	0.5	0.258E+03	0.104E+05	0.017	0.014
6.750	3	0.052	0.268E+04	0.8	0.212E+03	0.964E+04	0.020	0.021
6.750	4	0.054	0.739E+05	0.9	0.254E+03	0.116E+05	0.017	0.021
6.890	3	0.079	0.621E+04	1.8	0.895E+02	0.425E+04	0.048	0.049
6.890	4	0.083	0.175E+06	2.1	0.105E+03	0.498E+04	0.041	0.051
7.300	3	0.089	0.790E+04	2.3	0.664E+02	0.354E+04	0.064	0.062
7.300	4	0.093	0.221E+06	2.7	0.786E+02	0.419E+04	0.054	0.064

^{60}Ni(p,p') 40 MeV

Calculated parameters using a uniform charge distribution with r_o = 1.31F

E_x (MeV)	L	β_L	B(EL;O→L) (F^{2L})	G_{SP}	$D_L/\hbar^2$ $(MeV)^{-1}$	C_L (MeV)	$(D_L)_{HYD}/D_L$	B(EL;O→L)/NEWSR
1.331	2	0.199	0.160E+04	11.2	0.523E+02	0.926E+02	0.086	0.336
2.502	4	0.085	0.205E+06	2.3	0.271E+03	0.169E+04	0.017	0.054
3.119	2	0.052	0.109E+03	0.8	0.327E+03	0.318E+04	0.014	0.023
3.360	4	0.035	0.350E+05	0.4	0.118E+04	0.133E+05	0.004	0.009
3.360	2	0.031	0.401E+02	0.3	0.825E+03	0.932E+04	0.005	0.008
3.360	3	0.033	0.118E+04	0.3	0.103E+04	0.116E+05	0.004	0.009
3.690	4	0.067	0.125E+06	1.4	0.300E+03	0.408E+04	0.015	0.033
3.690	3	0.064	0.436E+04	1.2	0.255E+03	0.347E+04	0.018	0.032
3.690	2	0.060	0.147E+03	1.0	0.205E+03	0.279E+04	0.022	0.031
4.042	3	0.168	0.301E+05	8.2	0.337E+02	0.551E+03	0.134	0.221
4.320	4	0.050	0.703E+05	0.8	0.456E+03	0.852E+04	0.010	0.019
4.320	2	0.046	0.842E+02	0.6	0.306E+03	0.571E+04	0.015	0.018
4.320	3	0.048	0.248E+04	0.7	0.383E+03	0.714E+04	0.012	0.018
5.140	4	0.138	0.536E+06	5.9	0.502E+02	0.133E+04	0.090	0.142
5.140	5	0.150	0.167E+08	7.5	0.520E+02	0.137E+04	0.087	0.163
5.140	3	0.132	0.185E+05	5.1	0.430E+02	0.114E+04	0.105	0.136
5.450	3	0.067	0.476E+04	1.3	0.158E+03	0.469E+04	0.029	0.035
5.450	4	0.070	0.136E+06	1.5	0.187E+03	0.555E+04	0.024	0.036
5.450	2	0.063	0.162E+03	1.1	0.126E+03	0.375E+04	0.036	0.034
5.700	3	0.058	0.364E+04	1.0	0.197E+03	0.641E+04	0.023	0.027
5.700	2	0.056	0.125E+03	0.9	0.156E+03	0.507E+04	0.029	0.026
5.700	4	0.062	0.108E+06	1.2	0.225E+03	0.730E+04	0.020	0.029

^{62}Ni(p,p') 40 MeV

Calculated parameters using a uniform charge distribution with r_o = 1.31F

E_x (MeV)	L	β_L	B(EL;0→L) (F^{2L})	G_{SP}	$D_L/\hbar^2$ $(MeV)^{-1}$	C_L (MeV)	$(D_L)_{HYD}/D_L$	B(EL;0→L)/NEWSR
1.169	2	0.190	0.153E+04	10.3	0.649E+02	0.887E+02	0.074	0.308
2.334	4	0.077	0.181E+06	1.8	0.357E+03	0.195E+04	0.013	0.044
3.168	4	0.049	0.738E+05	0.7	0.647E+03	0.649E+04	0.007	0.018
3.168	2	0.044	0.837E+02	0.6	0.438E+03	0.440E+04	0.011	0.017
3.168	3	0.046	0.246E+04	0.6	0.561E+03	0.563E+04	0.009	0.017
3.270	4	0.073	0.165E+06	1.7	0.281E+03	0.300E+04	0.017	0.040
3.270	2	0.066	0.184E+03	1.2	0.193E+03	0.207E+04	0.025	0.037
3.270	3	0.070	0.550E+04	1.4	0.243E+03	0.260E+04	0.020	0.038
3.750	3	0.167	0.317E+05	8.1	0.368E+02	0.517E+03	0.130	0.218
3.990	3	0.047	0.255E+04	0.7	0.431E+03	0.686E+04	0.011	0.018
3.990	4	0.050	0.769E+05	0.8	0.493E+03	0.785E+04	0.010	0.019
3.990	5	0.054	0.238E+07	1.0	0.524E+03	0.834E+04	0.009	0.021
4.148	4	0.058	0.104E+06	1.1	0.349E+03	0.601E+04	0.014	0.025
4.148	3	0.056	0.352E+04	0.9	0.300E+03	0.516E+04	0.016	0.024
4.148	5	0.063	0.327E+07	1.3	0.366E+03	0.630E+04	0.013	0.029
4.640	3	0.063	0.453E+04	1.2	0.208E+03	0.448E+04	0.023	0.031
4.640	2	0.060	0.154E+03	1.0	0.163E+03	0.351E+04	0.029	0.031
4.640	4	0.066	0.133E+06	1.3	0.245E+03	0.528E+04	0.019	0.032
4.980	3	0.071	0.566E+04	1.5	0.155E+03	0.385E+04	0.031	0.039
4.980	4	0.074	0.168E+06	1.7	0.180E+03	0.447E+04	0.026	0.041
4.980	2	0.067	0.190E+03	1.3	0.123E+03	0.305E+04	0.039	0.038
5.610	3	0.077	0.675E+04	1.7	0.116E+03	0.364E+04	0.041	0.046
5.610	4	0.081	0.199E+06	2.0	0.135E+03	0.426E+04	0.035	0.048
5.610	5	0.087	0.627E+07	2.5	0.141E+03	0.444E+04	0.034	0.055

^{64}Ni(p,p') 40 MeV

Calculated parameters using a uniform charge distribution with r_o = 1.31F

E_x (MeV)	L	β_L	B(EL;O→L) (F^{2L})	G_{SP}	$D_L/\hbar^2$ $(MeV)^{-1}$	C_L (MeV)	$(D_L)_{HYD}/D_L$	B(EL;O→L)/NEWSR
1.344	2	0.170	0.127E+04	8.2	0.709E+02	0.128E+03	0.071	0.246
2.608	4	0.070	0.161E+06	1.5	0.391E+03	0.266E+04	0.013	0.036
3.165	2	0.055	0.133E+03	0.9	0.289E+03	0.289E+04	0.017	0.026
3.560	3	0.180	0.393E+05	9.5	0.333E+02	0.422E+03	0.151	0.254
3.849	5	0.073	0.493E+07	1.8	0.291E+03	0.432E+04	0.017	0.039
4.600	5	0.062	0.354E+07	1.3	0.339E+03	0.718E+04	0.015	0.028
4.600	4	0.058	0.110E+06	1.0	0.324E+03	0.685E+04	0.016	0.025
4.600	3	0.055	0.364E+04	0.9	0.278E+03	0.589E+04	0.018	0.023
4.800	3	0.052	0.328E+04	0.8	0.296E+03	0.682E+04	0.017	0.021
4.800	4	0.055	0.100E+06	0.9	0.343E+03	0.790E+04	0.015	0.022
4.800	2	0.050	0.111E+03	0.7	0.227E+03	0.523E+04	0.022	0.021
5.400	3	0.052	0.328E+04	0.8	0.263E+03	0.768E+04	0.019	0.021
5.400	4	0.056	0.103E+06	1.0	0.296E+03	0.863E+04	0.017	0.023
5.400	5	0.059	0.323E+07	1.2	0.317E+03	0.924E+04	0.016	0.025
5.400	2	0.050	0.111E+03	0.7	0.202E+03	0.588E+04	0.025	0.021
5.800	2	0.065	0.187E+03	1.2	0.112E+03	0.377E+04	0.045	0.036
5.800	5	0.077	0.542E+07	2.0	0.176E+03	0.591E+04	0.029	0.043
5.800	3	0.068	0.557E+04	1.3	0.144E+03	0.485E+04	0.035	0.036
5.800	4	0.072	0.175E+06	1.6	0.163E+03	0.547E+04	0.031	0.039

REFERENCES

REFERENCES

Al 56 Alder, K., A. Bohr, T. Huus, B. Mottelson, and A. Winther. Rev. of Mod. Phys. 28, 432 (1956).

Au 60 Auerbach, N. Phys. Letters 21, 57(1960).

Au 67 Auerbach, N. Phys. Rev. 163, 1203 (1967).

Ba 62 Bassel, R. H., R. M. Drisko, and G. R. Satchler. Oak Ridge National Laboratory Report ORNL-3240 (unpublished, 1962).

Ba 64 Bardin, B. M. and M. E. Rickey. Rev. Sci. Instr. 35, 902 (1964).

Ba 68 Ballini, R., A. G. Blair, N. Cindro, J. Launay, and J. P. Fouan. Nucl. Phys. A 111, 147 (1968).

Be 62 Beers, Y. Theory of Error. Addison-Wesley, 1962.

Be 69 Bernstein, A. M. (To be published in Advances in Nucl. Phys 3).

Bi 68 Bingham, C. R. and M. L. Halbert. Phys. Rev. 169, 933 (1968).

Bl 63 Blair, J. S. "Proceedings of Conference on Direct Interactions and Nuclear Interactions Mechanisms, Padua, Italy, September, 1962," Ed. by E. Clementel and C. Villi. Gordon and Breach, Science Publishers, Inc., 1963, p. 669.

Bl 65 Black, P. Machine Design McGraw-Hill, 1955.

Bl 66 Blosser, H. G., and A. I. Galonsky. IEEE Trans. on Nuclear Science, NS-B, No. 4, 466 (1966).

Bo 67 Borsay, F. L. Nucl. Instr. and Meth. 52, 338 (1967).

Bo67a Bohr, A. and B. Mottelson. Lecture Notes on Nuclear Theory, 1967.

Ca 67 Cameron, J. Unpublished Ph.D. thesis, University of California at Los Angeles, 1967.

Ch 65 Chasman, C. and R. A. Ristiney. Nucl. Instr. and Meth. 34, 250 (1965).

Co 67 Cohn, S., R. D. Lawson, M. H. MacFarlane, S. P. Pandya, and M. Soga. Phys. Rev. 160, 903 (1967).

Cr 61 Crannell, H., R. Helm, H. Kendall, J. Oesar, and M. Yearian. Phys. Rev. 123, 923 (1961).

Dr 63 Dickens, J. K., F. G. Perey, and G. R. Satchler. Nucl. Phys. 73, 529 (1965).

Du 67 Duguay, M. A., C. K. Bockelman, T. H. Curtis, and R. A. Eisenstein. Phys. Rev. 163, 1259 (1967).

El 61 Elton, L. R. B. Nuclear Sizes. Oxford University Press, 1961.

Fe 66 Feldl, E., C. Fetrow, and C. F. Moore. Nucl. Instr. and Meth., 44, 98 (1966).

Fr 67a Fricke, M. P. Unpublished Ph.D. thesis, University of Minnesota. Oak Ridge National Laboratory Report ORNL-1753, 1967.

Fr 67b Fricke, M. P., E. E. Gross, B. J. Morton, and A. Zucker. Phys. Rev. 156, 1207 (1967).

Fr 67c Fricke, M. P., E. E. Gross, and A. Zucker. Phys. Rev. 163, 1153 (1967).

Fu 68 Fulling, S. A. and G. R. Satchler. Nucl. Phys. A111, 81 (1968).

Fu 68a Fulmer, C. B., J. Benveniste, and A. C. Mitchell. Phys. Rev. 165, 1218 (1968).

Gi 66 Gillet, V. and M. Rho. Phys. Letters 21, 82 (1966).

Gr 68 Gruhn, C. R., T. Kuo, C. Maggiore, B. Preedom, L. Samuelson, and J. Chander. IEEE Trans. on Nuclear Science, NS-15, No. 3, 337 (1968).

Gr 68a Gruhn, C. R. Bull. Am. Phys. Soc. 13, 1363 (1968).

Gl 66 Glendenning, N. K. and M. Veneroni. Phys. Rev. 144, 839 (1966).

He 64 Hecht, K. T. In Selected Topics in Nuclear Spectroscopy. Compiled by B. Verhaar. North-Holland Publishing Co., 1964.

He 68 Heymann, G. Phys. Letters 27B, 280 (1968).

He 68a Hendricks, R. H., G. W. Greenlees, J. S. Lilley, and H. Liers. John H. Williams Laboratory of Nuclear Physics Annual Report, 1968.

Hi 68 Hiebert, J. C. and E. Newman. Nucl. Phys. A113, 176 (1968).

Ho 67 Horoshko, R. N., P. F. Hinrichsen, L. W. Swenson, D. M. Van Patter. Nucl. Phys. A104, 113 (1967).

In 68 Inoue, M. Nucl. Phys. A119, 449 (1968).

Ja 67 Jarvis, O. N., B. G. Harvey, D. L. Hendrie, and Jeannette Mahoney. Nucl. Phys. A102, 625 (1967).

Jo 69 Jolly, R. K., M. D. Goldberg, A. K. Sengupta. Nucl. Phys. A123, 54 (1969).

La 60 Lane, A. M. and E. D. Pendlebury. Nucl. Phys. 15, 39 (1960).

La 64 Lane, A. M. Nuclear Theory. W. A. Benjamin, 1964.

Ma 64 Machinery's Handbook, 17th ed. The Industrial Press, 1964.

Ma 67 Mackenzie, G. H., E. Kasky, M. M. Gordon and H. G. Blosser. IEEE Trans. on Nuclear Science, NS-14, No. 3, 450 (1967).

Ma 69 Designed and built by C. Maggiore and T. Kuo.

Mc 66 McCarthy, A. L. and G. M. Crawley. Phys. Rev. 150, 935 (1966).

Na 65 Nathan, O. and S. G. Nilsson. In Alpha- Beta- and Gamma-ray Spectroscopy. Ed. by Kai Siegbahn. North-Holland Publishing Co., Amsterdam, 1965. Chapter X.

Ra 67 Raj, Ram, Y. K. Gambhir, and M. K. Pal. Phys. Rev. 163, 1004 (1967).

Ra 68 Raman, S. Nucl. Data B2, No. 5 (1967).

Ro 57 Rose, M. E. Elementary Theory of Angular Momentum. John Wiley and Sons, 1957.

Ro 61 Rost, E. Unpublished Ph.D. thesis, University of Pittsburg, 1961.

Ru 68 Rundquist, D. E., M. K. Brussel, A. I. Yavin. Phys. Rev. 168, 1287 (1968).

Sa 64 Satchler, G. R. Nucl. Phys. 55, 1 (1964).

Sn 67 Snelgrove, J. L. and E. Kasky. Nucl Instr. and Meth. 52, 153 (1967).

St 65 Stelson, P. H. and L. Grodzins. Nucl. Data. A1, 21 (1965).

Te 67 Tee, R. G. and A. Aspinall. Nucl. Phys. A98, 417 (1967).

Ve 67 Verheul, H. Nucl. Data B2, No. 3 (1967).

Wo 68 Wong, C. Y. Nucl. Data A4, 271 (1968).